UNIVERSITY OF SOUTHAMPTON

FACULTY OF ENGINEERING AND THE ENVIRONMENT

Aeronautics, Astronautics and Computational Engineering

High Collision Probability Conjunctions and Space Debris Remediation

by

Aleksander A. Lidtke

Thesis for the degree of Doctor of Philosophy

December 2016

UNIVERSITY OF SOUTHAMPTON

ABSTRACT

FACULTY OF ENGINEERING AND THE ENVIRONMENT
Aeronautics, Astronautics and Computational Engineering

Doctor of Philosophy

HIGH COLLISION PROBABILITY CONJUNCTIONS AND SPACE DEBRIS REMEDIATION

by Aleksander A. Lidtke

Derelict satellites, rocket bodies, and pieces thereof have been left on orbit. These space debris have been increasing in numbers and simulations of their future evolution have shown that this increase might continue due to collisions between objects. It has been suggested that active debris removal (ADR), i.e. removing objects from orbit by technological means rather than by their natural decay due to drag, might be necessary in order to prevent an excessive increase of the number of debris. Selection of objects to be targeted by ADR is considered important because removal of non-relevant objects will unnecessarily increase the cost of ADR. Collision probability of every object should form part of the metric to select appropriate ADR targets. This work examines how the collision probabilities of all the objects in orbit depend on particular conjunctions, which cannot be forecast far in advance due to increasing orbit propagation uncertainty and variations in solar activity. It is found that conjunctions with high collision probabilities contribute more to the collision probabilities accumulated by objects over a period of time than other close approaches. Objects that are not large in mass and size are found to take part in conjunctions with high collision probabilities. Such objects are not likely to be removed from orbit when using existing ADR target selection schemes, and collisions involving them might not be prevented. Thus, the growth of the number of debris might continue in spite of ADR because collision fragments will continue to be generated. A complementary solution to constraining the number of debris in orbit, i.e. prevention of collisions between derelicts (just in-time collision avoidance, JCA), is thus investigated. It is found that fewer than ten JCA actions per year could constrain the number of objects in orbit. However, certain objects will repetitively take part in conjunctions with high collision probabilities. Permanently removing such objects from orbit via ADR may be more cost-effective than mitigating their collision risk via JCA. The finding that conjunctions with relatively high collision probabilities are the reason why ADR may be insufficient to constrain the number of debris, and analysis of JCA using an evolutionary debris model are the main novel contributions of this work.

"Haiku on debris"

Pieces of space junk
Disabling our satellites...
Should we do something?

Contents

List of Figures

List of Tables

Declaration of Authorship

I, Aleksander A. Lidtke , declare that the thesis entitled *High Collision Probability Conjunctions and Space Debris Remediation* and the work presented in the thesis are both my own, and have been generated by me as the result of my own original research. I confirm that:

- this work was done wholly or mainly while in candidature for a research degree at this University;
- where any part of this thesis has previously been submitted for a degree or any other qualification at this University or any other institution, this has been clearly stated;
- where I have consulted the published work of others, this is always clearly attributed;
- where I have quoted from the work of others, the source is always given. With the exception of such quotations, this thesis is entirely my own work;
- I have acknowledged all main sources of help;
- where the thesis is based on work done by myself jointly with others, I have made clear exactly what was done by others and what I have contributed myself;
- parts of this work have been published as: [73], [82], [83], [84] and [85]

Signed:.....

Date:.....

Acknowledgements

First and foremost I would like to express my gratitude to my first supervisor, Dr Hugh G. Lewis, for provision of the DAMAGE results that formed part of the IADC comparison study, and the DAMAGE executable. Also, I would like to thank him and my other supervisors, Dr Roberto Armellin and Dr Adrian Tatnall, for their support in completion of this work.

I would also like to thank the ESA Space Debris office for allowing me to use the MASTER 2009 and MASTER 2013 reference populations. Dedicated thanks go to Dr Holger Krag and Dr Tim Flohrer for their extremely valuable feedback and discussion regarding operational collision avoidance, and help in validating the collision probability algorithms by provision of the set of estimated TLE covariances.

Sincere thanks to Dr David Vallado for distribution of the SGP4 propagator code, without which this research would never be possible in the timeframe available. I would also like to express gratitude to Dr T.S. Kelso for useful comments regarding the collision probability, maintaining the CelesTrak website, and provision of the objects' physical radii database. I would like to express my gratitude to Dr Darren McKnight for provision of the objects' masses database and important comments regarding this work. Similarly, I would also like to than the Join Space Operations Center for providing me with Special Perturbations state vectors, which allowed me to assess currently achievable ephemeris accuracies.

The author would also like to acknowledge the use of AGI's Systems Toolkit in the verification process of the developed simulation framework. I would also like to acknowledge the use of the IRIDIS High Performance Computing Facility, and associated support services at the University of Southampton, that enabled completion of this work. Specifically, I would like to thank Elena Vataga, who has enabled me to run DAMAGE on the Iridis 3 supercomputer, which has allowed me to conduct a large portion of this work. Also, I would like to thank the Astronautics Research Group of the University of Southampton and the Engineering and Physical Sciences Research Council (EPSRC) for funding my project.

Abbreviations and acronyms

ADR - active debris removal

AGI - Analytical Graphics Incorporated

CAT - Conjunctions Assessment Tool (a tool within STK)

DAMAGE - Debris Analysis and Monitoring Architecture to the Geosynchronous Environment, the debris environment simulation tool developed by Dr Hugh Lewis, Astronautics Research Group, University of Southampton

DEB - debris

GEO - geostationary orbit

GTO - geostationary transfer orbit

IADC - Inter-Agency Space Debris Coordination Committee

LEO - low Earth orbit

MASTER - Meteoroid and Space Debris Terrestrial Environment Reference

MC - Monte Carlo

MEO - medium Earth orbit

MOID - minimum orbit intersection distance

MRO - mission related object

PDF - probability density function

PIB - particles in a box (debris model)

P/L - payload

R/B - rocket body

RIC - radial, in-track, cross-track frame of reference

RTC - radial, transverse, cross-track frame of reference (same as RIC)

SGP4 - special perturbations propagator

STK - Systems Toolkit

SSC - space surveillance catalog number

SST - space surveillance and tracking

TCA - time of the closest approach

TLE - two-line element set

USD - U.S. dollars

UTC - Coordinated Universal Time

Nomenclature

Symbol	Meaning	Unit
$N(t)$	Number of objects at time t (in a PIB debris model)	No. objects
A	Object deposition coefficient in a PIB debris model	No. object per unit time
B	Object decay coefficient in a PIB debris model	
C	Object collision coefficient in a PIB debris model	
F	Debris flux	$m^{-2}s^{-1}$
Σ	Combined cross-sectional area of two objects in a debris model	m^2
Δt	Time step in a debris model	days
P_C	Collision probability	unitless
R	Pearson correlation coefficient	unitless
σ	In Chapter 4: ephemeris accuracy	unit-less
σ	Outside Chapter 4: standard deviation	corresponding unit
m	Object mass	kg
X_i	Cartesian position component used in interpolation	km
$\dot{X}_i$	Cartesian velocity component used in interpolation	$km\ s^{-1}$
$X(t)$	Cartesian position interpolated at time t	km
$V(t), \dot{X}(t)$	Cartesian velocity interpolated at time t	$km\ s^{-1}$
A_j	Interpolating polynomial coefficient	corresponding unit
P_i	Lagrange interpolation coefficient	km
h_{ij}	Hermite basis polynomial	corresponding unit
ΔT	Time step of conjunction detection and assessment	seconds
m_{ij}	Coefficients used to interpolate i-th component of relative motion	corresponding unit
$\overrightarrow{r(t)}$	Relative position between two objects at time t	km
$\overrightarrow{\lvert r\,(t)\rvert}$	Relative range between two objects at time t	km

Symbol	Meaning	Unit
$v(t)$	Relative range rate between two objects at time t	$km\ s^{-1}$
$a(t)$	Relative acceleration between two objects at time t	$km\ s^{-2}$
r	Collision radius	m
$P_C\|^{TRUE}$	Collision probability computed using un-scaled covariance matrices	unit-less
$P_C\|^{MAX}$	Maximum collision probability	unit-less
C	Covariance matrix	corresponding units squared
R_{1to2}	Rotation matrix from reference frame 1 to frame 2	unit-less
p_{mean}	Nominal relative position at the TCA projected onto the B-plane	km
k	Covariance scaling factor	unit-less
ζ	Criticality ($P_C \times m$)	kg
$\zeta\|^{TRUE}$	True criticality ($P_C\|^{TRUE} \times m$)	kg
$\zeta\|^{MAX}$	Maximum criticality ($P_C\|^{MAX} \times m$)	kg
ϵ	Contribution of of the P_C or ζ of a given conjunction to the final vale accumulated by a given object over a period of time	%
ϵ_{env}	Contribution of of the P_C or ζ of a given conjunction to the value accumulated in the entire debris environment over a period of time	%
m_{TH}	Minimum mass of an object that has to be exceeded for JCA of its conjunction to be considered	dimensionless or kg
$P_{C,TH}$	Minimum P_C of a conjunction that has to be exceeded for JCA to be considered	unit-less or dimensionless
h	Maxmum altitude of a conjunction that has to be exceeded for JCA to be considered	km
$X_{ECI}, Y_{ECI}, Z_{ECI}$	Axes of an inertial reference frame	
X, Y, Z	Axes of a B-plane reference frame	
σ_R,σ_I,σ_C	Radial, in-track and cross-track position standard deviation	km or m
$\vec{x}$	Vector of model inputs that was evaluated	kg, unit-less, dimensionless
$\vec{y}$	Value of a given parameter obtained by direct evaluation of a model	corresponding unit
$\vec{y}_{REG}$	Value of a given parameter obtained using a surrogate model	corresponding unit

Chapter 1

Introduction

This work tests whether it is possible to prevent the expected growth of the number of space debris by selective removal of certain objects, which are going to be involved in collisions. It then tests if it is possible to mitigate the collision probabilities of conjunctions, which cannot be foreseen far in advance, to limit the number of orbital collisions and, consequently, reduce the rate at which collision fragments are added into the environment.

This chapter identifies the origins of the space debris issue. Next, work of other authors, which shows that the number of debris is predicted to increase and thus actions should be taken to prevent such a situation from happening, is reviewed. The approaches to modelling the evolution of the space debris population are then described, and the origins of the associated uncertainties are given. Current approaches to identifying objects that are likely to be involved in collisions in the future, and thus should be removed from orbit, are reviewed next. It is then hypothesised why the existing methodology may be unsuccessful at preventing the number of debris from increasing. Lastly, the objectives of this work, which investigates the set hypothesis and its implications, are defined and the contents of the remaining chapters of this thesis are outlined.

1.1 Space debris

1.1.1 Origins and the current state

The space era dawned on 4 Oct 1957 with the launch of Sputnik 1 [40]. Since then, many great achievements have been accomplished in space. Spaceflight has also brought countless benefits to the whole of humanity, such as global telecommunication, advanced materials or novel medical procedures. Furthermore, a completely new branch of industry worth over 300 billion USD annually [141] has emerged.

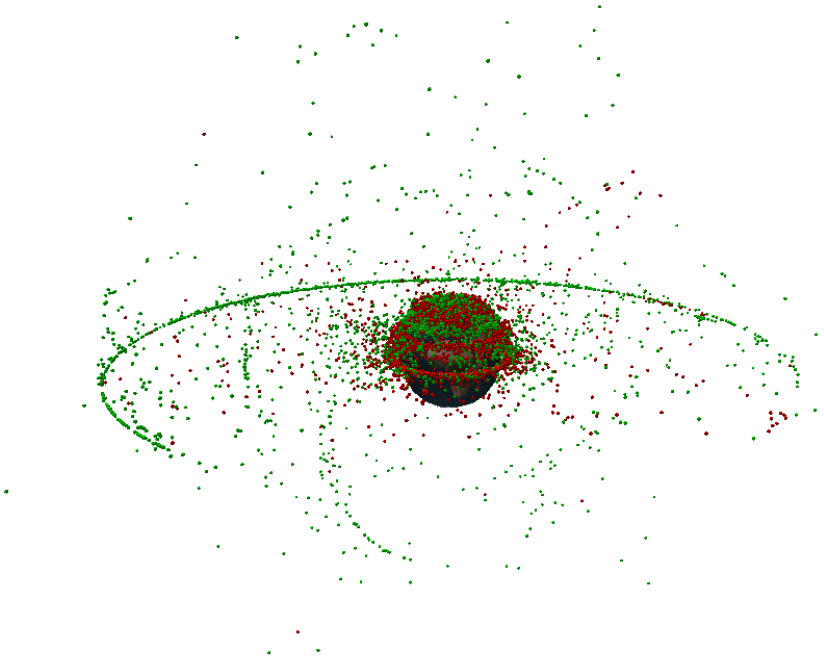

Figure 1.1: Objects in the public two-line element set (TLE) catalogue from 23 Oct 2013 available through Space-Track [135]. Objects classified as debris (9821) marked in red, the remainder (5096), including operational spacecraft, in green. The minimum size of the objects is approx. 10 cm in diameter. The size of the objects is not to scale with the size of the Earth or positions of the objects.

Space launches have continued since Sputnik 1 and more are expected to occur in the future. This has led to a build-up of objects in Earth orbit. The number of derelict objects exceeded that of operational satellites in the early nineteen-sixties [52], i.e. within only several years of spaceflight. Approximately a decade later, it was realised for the first time that space debris would accumulate in Earth orbit and potentially create more debris through mutual collisions [58]. Until end of October 2013, when this work started, the catalogue of space objects that can be tracked and whose positions were made publicly available through Space-Track [135] had grown to 14 917. These objects are shown in Fig. 1.1.

Only approximately 1000 objects currently in orbit are operational satellites and 2600 are derelict [69], and approximately 66% of all these objects are small pieces of debris. This abundance of smaller debris can be attributed mainly to two fragmentation events that took place in 2007 and 2009, which can be seen as rapid increases in the number of debris in Fig. 1.2. The current state of the debris environment agrees with forecasts made by Kessler and Cour-Palais [58], who stated that "unless significant changes are made in the method of placing objects into space, fragments from inter-collisions will probably become a source of additional space debris by the year 2000, perhaps much earlier".

Debris are typically much smaller than operational satellites but they pose a threat of damaging or disabling spacecraft [41]. However intact, derelict satellites, spent rocket bodies etc. can also be classified as debris. Even objects that are too small to be tracked can still pose a threat to active satellites - Cougnet et al. [24] have found that particles with sizes between 2 and 4 mm have the highest probability to cause a failure of their reference missions, mainly due to the high fluxes of such small particles. And even small, low-mass debris can still cause much larger objects to break up and generate many new fragments if the collision energy is high enough [51].

One can imagine a situation where countless small debris are orbiting the Earth and every new satellite gets disabled due to an impact shortly after it is launched. This is an extreme example, but it shows that spaceflight might not be sustainable. This is to say that, if many new collisions take place, space activities will not be "able to be maintained at a certain rate or level" [115], which is the definition of sustainability in the Oxford Dictionary of English.

1.1.2 Future accumulation of debris

It is impossible to predict with confidence how many new satellites or completely new space systems will be launched in the future because human activity is uncertain. Even less confident predictions can be made regarding the orbital regimes that those systems will occupy [62]. However, since the beginning of spaceflight, every year there were new spacecraft being launched. Even though most of the objects currently in orbit are classified as debris and originated in major recorded fragmentations, involving Iridum 33, Cosmos 2251 and Fengyun 1C, launches continue to take place. The continued launches are visible as monotonic increases of the number of rocket bodies and payloads in orbit shown in Fig. 1.2.

The future launch traffic has major implications on how numerous the space debris population will be [7, 62, 94]. Specifically, White and Lewis [152] have shown that the future space debris population sizes can vary by as much as an order of magnitude depending on, amongst others, how many spacecraft are launched. It is unlikely that all the objects launched into space will naturally decay due to atmospheric drag because high-altitude orbits present insufficient air density. Therefore, unless space launches cease completely, certain objects will be left in orbit and so the total number of man-made objects in space will increase.

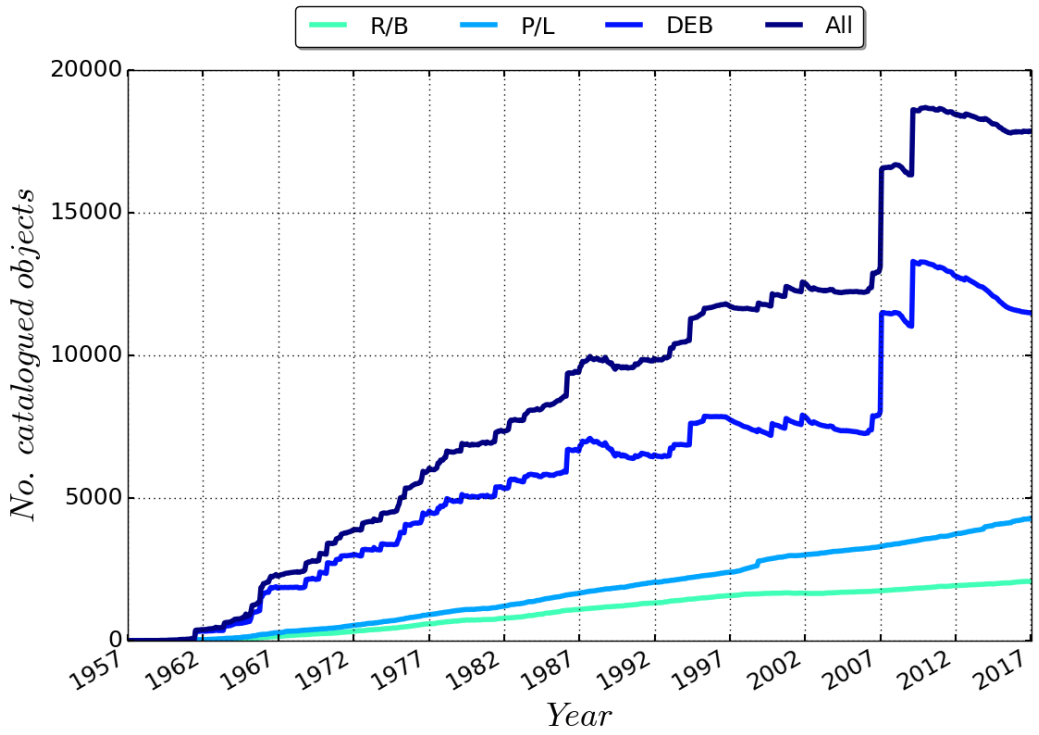

Figure 1.2: The number of objects that Space-Track [135] classifies as rocket bodies (R/B), payloads (P/L), and debris (DEB) present in the public catalogue of the US space surveillance network since 1 Jan 1957 until 20 Nov 2016. Source: Space-Track [135]

Once the space debris issue was realised, the Inter-Agency Debris Coordination Committee (IADC) was founded in 1993 to tackle the problem. In 2002, the IADC published space debris mitigation guidelines that are intended to limit the number of debris added to the environment and thus reduce the rate of the build-up of objects in orbit [139]. These guidelines are, by themselves, not legally binding but they have been incorporated into national legislation in several countries [122], e.g. through the Outer Space Act in the United Kingdom [143] and the French Space Operations Act no. 2008-518 [144]. This means that satellites owned by these countries have to comply with the debris mitigation but others do not.

Perhaps the most effective IADC guideline [79] states that LEO objects should be deorbited or manoeuvred into orbits that limit their lifetime after the end of their mission. Limiting the remaining orbital lifetime to 25 years was recommended by several studies and incorporated into national guidelines [139], which is why this IADC guideline is often referred to as the "25-year rule". This is not to say that the "25-year rule" can solve the issue of orbital collisions and generation of new debris - collisions might still happen between objects that comply with this guideline before they deorbit. Limiting the lifetime of objects in orbit should reduce the potential for catastrophic collisions

nonetheless. However, only approximately 80% (42 out of 53 in 2010/2011) rocket bodies and 36% (17 out of 47 in 2010/2011) spacecraft comply with the "25-year rule" [64]. These compliance rates are particularly bad at high altitudes, where more fuel is needed to achieve compliance with the guideline [64]. Ironically, it is at those altitudes where objects have long natural lifetimes and thus are expected to accumulate. Thus, the "25-year rule", at current compliance rates, does not help in preventing the increase in the number of debris by a huge factor.

Even if all spacecraft and rocket bodies are designed to comply with the "25-year rule", derelicts are likely to keep accumulating in the Earth orbits [64]. This is because some of the spacecraft and rocket bodies will fail and hence will not be able to leave their orbit, even if this was initially intended, as in case of Itelsat2, for example [8]. The derelicts resulting from such failed missions will not always naturally decay due to little atmospheric drag that is present in some orbital regimes, e.g. the geostationary ring.

1.2 Predicted evolution of the debris environment

1.2.1 Expected increase in numbers

It was stipulated by Kessler and Cour-Palais [58] that a situation where objects accumulate in orbit would result in debris colliding with debris and hence creating new debris that would lead to more collisions. This self-sustaining effect is often referred to as the "Kessler syndrome" or the collision cascade. More attention has been paid to the debris issue recently as Liou and Johnson [88] suggested that the collision cascade might be inevitable even if no future launches take place. Soon after their work was published, the collision between Cosmos 2251 and Iridium 33 took place in February 2009, which only increased the concerns about the future of the debris environment.

Currently, most of the objects in orbit are derelict and, therefore, cannot evade potential collisions. Modelling studies have been performed to assess whether the debris environment will indeed continue to grow in numbers. One of such studies was conducted by Lewis et al. as part of the IADC comparison study [86], which compared the results obtained by different debris models. A subsequent study, which compared various debris mitigation strategies, was then conducted by the IADC with more up-to-date population and launch traffic assumptions. According to the latter study, it is expected that the total number of the objects will grow as shown in Fig. 1.3 even if 90% of spacecraft are de-orbited after the end of their lives. This shows that debris mitigation, i.e. limiting the number of debris added to the environment, might not prevent the growth of the number of objects in orbit. Authors of both studies agree that orbital collisions will generate new debris and the total number of objects in orbit will grow, with the debris generated during collisions of large derelicts being the main constituent of the environment [86].

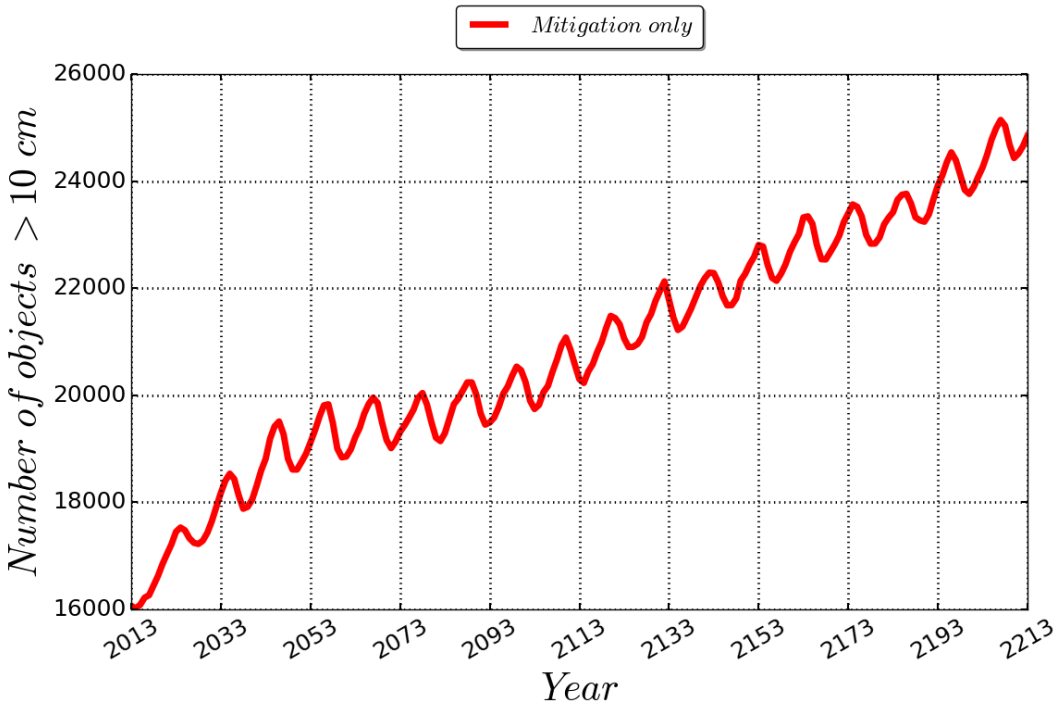

Figure 1.3: Evolution of the number of objects in orbit for the "mitigation only" scenario from Table 1.1. The curve is a mean of the Monte Carlo sample of 140 runs obtained as part of an IADC comparison study, which followed the study by Liou et al. [86]. Data provided by Dr Hugh G. Lewis.

At present, however, it is difficult to assert whether the cascade of collisions predicted by Kessler and Cour-Palais [58] will take place at all. Liou [89] states that 59% of the future collisions in the 30 Monte Carlo runs in his study involved fragments resulting from collisions or explosions. However, most of the collision debris in the final population came from collisions between intact objects. Therefore, even though the total number of objects is predicted to increase, the impact of debris generated during collisions causing new collisions and thus producing new debris may not be the driving force behind the growth of the debris population. Moreover, the forecasts of the number of objects in orbit 200 years from now, performed using similar debris environment models, may vary by as much as an order of magnitude if uncertainties in e.g. the launch traffic or solar activity are included in the forecasts [152]. However, the likely increase in the number of objects in orbit [58, 86, 89] has caused a worldwide interest in development of solutions to stop it.

1.2.2 The need for debris remediation

The Inter-Agency Debris Coordination Committee in [86] suggested that "to stabilise the LEO environment, more aggressive [than only mitigation] measures, such as active debris removal, should be considered". Removal of large, derelict, uncontrolled objects, i.e. active debris removal (ADR), has been suggested by several authors [17, 39, 93, 98, 118, 157] as a means to prevent the growth of the total number of objects in the environment. If five such objects are removed every year, the total number of objects in orbit is believed to increase at a lower rate than if no debris remediation is performed, as shown in Figure 1.4.

This suggestion of removing derelicts has sparked a worldwide interest in the development of technologies to perform active debris removal [17, 20, 44, 113, 127]. Related research in optimisation of trajectories that the removal vehicles could follow [19, 160] and development of business models for ADR companies [150] is also being undertaken.

It appears to be a general belief, both in the space debris community and beyond, that "removal of five heavy LEO debris per year, like spent satellites or launcher upper stages, is mandatory to stabilise the debris population" [19] [17]. By this logic, performing ADR is a necessary condition for the debris environment not to increase in numbers [92], hence the interest in the development of the associated technologies. In order to make judgements about the effects of ADR and the incentive to perform it, however, one should look into the nature of the evolutionary debris models and appreciate the conclusions that can be drawn based on their results.

1.3 Space debris modelling and simulation

1.3.1 General approach

One of the first debris models, devised by Kessler and Cour-Palais [58] and based on the work by Oepik [110], used the kinetic theory of gases to compute the average number of collisions per unit time for the objects in the debris environment, i.e. the collision rates [59]. Possibly the most significant assumption made by Kessler [59] was that the volume where the collision probabilities between objects were computed was small compared to the uncertainties on the orbits of the objects. The effects of this assumption on long-term debris forecasts are discussed by Blake and Lewis [16], whereas section 4.2 compares this assumption and the resulting collision probabilities found in orbit to what can be achieved operationally. In an extreme case, if this volume is large enough to include all Earth-orbiting objects, this assumptions means that every satellite could collide with any other. Even if this volume is smaller, it is impossible to predict which objects *are going to be* involved in collisions, because the objects could be located anywhere in the small volumes of space.

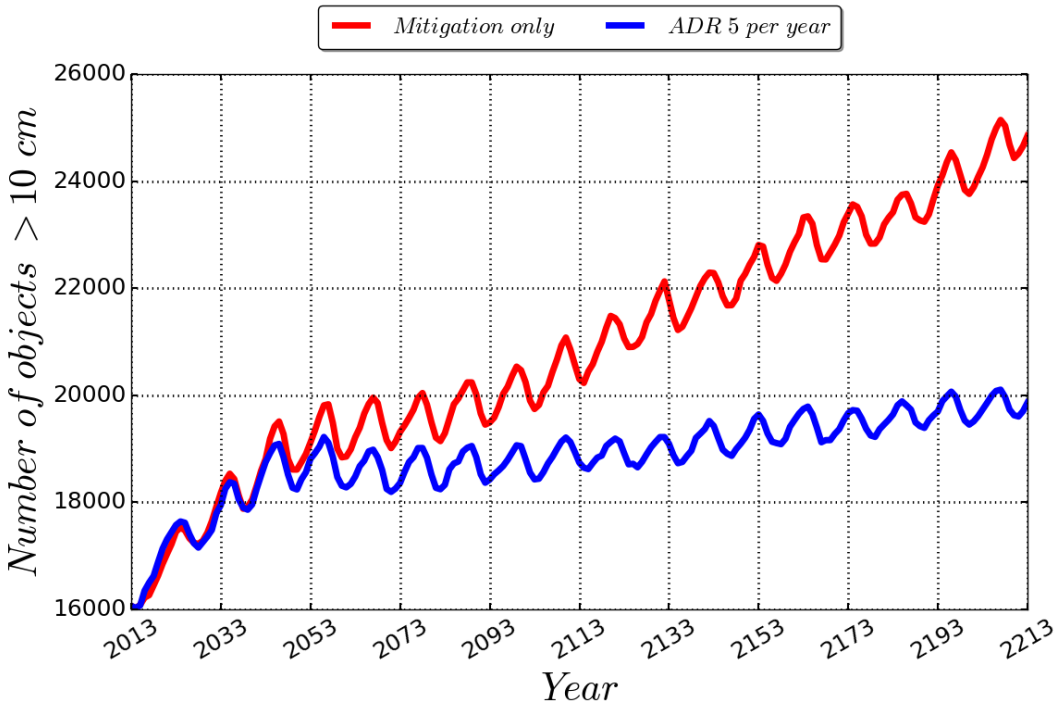

Figure 1.4: Evolution of the number of objects in orbit for "mitigation only" (red) and "ADR 5 per year" (blue) scenarios from Table 1.1. The curves are means of the Monte Carlo samples of 140 and 91 runs, respectively. The results have been obtained as part of an IADC comparison study, which followed the study by Liou et al. [86]. Data provided by Dr Hugh G. Lewis.

Predicting the actual close approaches between objects, and estimating the associated collision probabilities based on the uncertainties of their states at the times of the closest approaches, is impossible on time scales of hundreds of years. This is because the positions of the objects are subject to orbit determination uncertainties, which grow during propagation under the influence of orbital dynamics [147]. Therefore, modelling the evolution of the space debris population on such long time scales cannot rely on actual collision forecasts. Instead, collision rates, computed using approaches based on the work by Kessler and Cour-Palais [58], are used. Specifically, two different types of derived debris models are in use today: particles-in-box (PIB) and semi-stochastic approaches. The latter models use deterministic prognoses of e.g. the solar activity, but they simulate collisions in a stochastic fashion, which will be covered in detail in this section, and so they require the use of Monte Carlo (MC) analyses.

The PIB models, for example by Farinella and Cordelli [33], Talent [137], Kebschull et al. [55] or Lewis et al. [76], describe the evolution of the number of objects on orbit (N) with differential equations. This set of equations expresses the rate of change of N as a function with coefficients corresponding to deposition (A), decay (B), and collisions (C) of objects [137]:

$$\frac{dN}{dt} = A + BN + CN^2. \tag{1.1}$$

Integrating Eq. 1.1, starting at some initial conditions, yields the number of objects in orbit at the end of the integration period. Fundamentally, the kinetic theory of gases manifests itself in the CN^2 term, which states that any object can collide with any other. These models were further improved by, for example, only allowing objects from distinct altitude bins to collide with each other [55]. However, the assumption of the kinetic theory of gases has been retained.

The other group of models, i.e. the semi-stochastic codes, also uses the kinetic theory of gases assumption, however at a different spatial scale. These models examine every object separately and compute the collision probability for the examined object (target) using the flux of other objects at that target [14, 62, 89]. This flux F, in $m^{-2}s^{-1}$ (or other units of length and time), is computed by assuming uniform probability of existence of two objects in small volumes of space, which uses the kinetic theory of gases assumption in these volumes [62]. Different shapes of these volumes are used, e.g. Liou [89] and Lewis et al. [77] use cubes in Cartesian orbital elements, Ariyoshi and Hanada [10] spheres, and Bastida-Virgili [14] bins in right ascension-declination-altitude space. The volumes of space are small relative to the PIB models - Liou [89] recommends using cubes with edge length less than 1% of the average semi-major axis of all the objects (specifically 10 km). However, if the volumes were increased to include all the Earth orbiting objects, the particles-in-box model would be recovered [89]. When the flux F is known, the collision probability for every object, P_C, is computed as per Eq. 1.2:

$$P_C = F\Sigma\Delta t, \tag{1.2}$$

where Σ is the combined cross-sectional area of the objects and Δt is the time step [62]. To get accurate representation of P_C at any point in the simulation time, Δt should be equal to the time the objects spend in the small volume of space. However, the smaller the Δt, the more computational time the simulation requires. Thus, due to computational time restrictions, larger time steps are normally used.

A random number is generated for every conjunction and a collision simulated if the random number is lower than P_C [87]. The number of fragments resulting from every collision is then computed using the NASA Standard Breakup Model [51] or a similar empirical model. The breakup model introduces randomness into the simulations through the use of random samples drawn from probability distributions describing fragment characteristics.

The Debris Analysis and Monitoring Architecture to the Geosynchronous Environment (DAMAGE), the evolutionary model developed at the University of Southampton [77], was used in this work. Collisions in every Monte Carlo run of DAMAGE, and the corresponding numbers of fragments, were generated based on random numbers. This made every MC run unique. Moreover, close approaches, for which P_C was computed, were found by randomising the mean anomaly of all the objects and identifying pairs of objects that were within a certain distance threshold from one another. This introduced a further source of variability between different MC runs.

Close approaches are found at regular intervals of time, typically every five days, in order to simulate collisions. The process of finding close approaches at a given point in time is often referred to as taking a "snapshot". Many such snapshots may be taken at the beginning of a given year for the upcoming year. Objects are ranked according to a chosen metric, e.g. collision probability times mass [93], computed using these snapshots in order to identify the objects to be removed from the environment to simulate active debris removal. All the snapshots, from all the Monte Carlo runs, can also be assembled and the objects ranked according to the chosen metric. This can then be used to select the objects to be actively removed in reality, i.e. for ADR target selection. If collision probability is included in the metric of choice, the objects found in this way are the ones that are the most likely to be involved in a collision in the long-term.

This forms a basis on which DAMAGE works. The algorithms used to simulate collisions implemented in DAMAGE are similar to those used by LEGEND (LEO-to-GEO Environment Debris) and SDM (Space Debris Mitigation), but their specifics are different from LEODEEM (LEO Space Debris Environment Evolution Model), LUCA (Long Term Utility for Collision Analysis) and DELTA (Debris Environment Long-Term Analysis), for example [86]. Even though the details of all the models are different, the number of objects on orbit in 2209 predicted by them agrees to within 10% (error relative to the mean of all the models) [86]. What is more, collision rate calculation in LUCA is also based on the work by Oepik [110] [124], and DELTA also uses flux of the objects to compute the P_C [14]. Thus, it is believed that analysing the results of DAMAGE is important to understand the conclusions that can be drawn using other semi-stochastic debris models, specifically the ones used by the IADC. Settings of DAMAGE that were used to generate the results discussed in this work, which were similar to the IADC comparison study [86] except for the updated reference population and launch traffic assumptions, are summarised in Table 1.1.

1.3.2 Space debris simulation uncertainties

Space debris simulations are associated with uncertainties, which originate from the finite precision of the used numerical schemes, as well as the accuracy of the input data and algorithms.

Table 1.1: Simulation settings for DAMAGE used in an IADC comparison study that followed the previous study by Liou et al. [86]. Two scenarios are titled by the names they are referred to in text and in figures. They are supposed to investigate the outcome of trying to preserve the debris environment by not polluting it any further, i.e. good compliance with debris mitigation, and the effects of additional active removal of five large objects per year.

Parameter	**"Mitigation only"**	**"ADR 5 per year"**
Active Removal rate (objects per year)	0	5
Number of snapshots used to select objects to be removed in a given year	N/A	200
Fraction of objects that comply with post-mission disposal guidelines	90%	
Simulation start epoch	1 Jan 2013	
Simulation end epoch	31 Dec 2213	
Modelled launch traffic	Repeated 2005-2012 launch traffic	
Modelled objects	≥ 10 cm from MASTER 2013 reference population	
Conjunction threshold distance	$\sqrt{300} \approx 17.32$ km	
Time step between Kernel algorithm snapshots used to simulate collisions	5 days	

1.3.2.1 Sources of uncertainty

Multiple sources of uncertainty, both dependent and independent of the implementation details, exist in the evolutionary debris models. These factors are reviewed by Dolado-Perez et al. [26] and influence the number of objects in orbit and how well this can be predicted. The uncertain, model-independent parameters, e.g. the solar activity or the future launch traffic, can be included in the Monte Carlo analyses as done by e.g. White and Lewis [152]. Model-dependent parameters include propagators, the way in which collisions are predicted, breakup models etc. Both sets of uncertain parameters, particularly the use of random numbers to simulate collisions and their outcomes, mean that the predictions of the future debris environment generate a distribution of

the possible number of objects in orbit rather than a deterministic answer. However, *if sufficiently many MC runs are analysed*, these distributions can be estimated. Research questions can be answered based on those, for example the relative effectiveness of various debris mitigation or remediation measures can be compared and decisions whether to implement any can be taken.

It was mentioned in section 1.3.1 that collisions cannot be foreseen far in advance. If the conjunction geometry is kept constant, the probability of the two objects colliding, which we can forecast, typically reduces the larger the uncertainty in their positions [4]. This phenomenon is often referred to as "probability dilution" [4]. This means that long-term ($o(100)$ years) debris simulations have to use collision probability estimation algorithms described in section 1.3.1 instead of orbital positions of the objects propagated to the times of the closest approaches.

The occurrence of collisions has been found to be the source of the largest variability between different Monte Carlo runs [26, 76], and thus results in large uncertainties in the number of objects in the debris simulations. It is the kinetic theory of gases assumption and the use of random numbers, described in section 1.3.1, which give rise to this variability because they affect the collisions that take place in every run and make their occurrence dependent on random numbers. This signifies that models using such a semi-stochastic approach cannot predict *exactly* how many collisions are going to take place in the future, let alone which objects are going be involved in them or how many debris these collisions will be generate.

1.3.2.2 Effects of the uncertainty on long-term debris simulations

It was explained in section 1.2.2 that active debris removal is believed to be necessary. Such conclusions have been drawn primarily by examining means of Monte Carlo samples, which can have significant spread, for the reasons described in section 1.3.2.1.

As shown in Fig. 1.5, the 1σ standard deviation bands around the means of the MC samples simulating the "ADR 5 per year" and "mitigation only" scenarios overlap. These Monte Carlo simulations did not include variability in many significant parameters, e.g. the solar activity or the launch traffic; the resulting variability was only due to different collisions in various MC runs (number of collisions, involved objects, numbers of resulting fragments, epochs and altitudes). If more uncertain parameters are included, the numbers of objects at the end of a 200 year projection within the Monte Carlo sample can vary by as much as an order of magnitude [152], i.e. the spread in the data is even larger and the difference between the "ADR 5 per year" and "mitigation only" scenarios is even harder to discern.

The overlap between potential outcomes of active debris removal and only mitigation can be better seen when analysing the final distributions of the number of objects in all the Monte Carlo runs, as shown in Fig. 1.6a. What is more, the theoretical normal distributions and the empirical distributions of the MC runs differ. For example, few MC runs of "ADR 5 per year" predict the number of objects in 2213 to be 17 000, which is nearly at the peak of the probability density of the theoretical distribution. Thus, it is uncertain whether the numbers of MC runs were sufficient to correctly represent the final distributions.

It can be deduced from the probability plots of the final distributions shown in Fig. 1.6b that the distributions in the "ADR 5 per year" and "mitigation only" scenarios appear to be normal. This conclusion is further justified by the relatively high $p - values$ of the Shapiro-Wilk normality tests of both samples presented in Fig. 1.8 [25, 65, 104]; similar $p - value$ is obtained when numbers are seeded from a normal distribution using a random number generator. Note that the initial distribution of the number of objects in the MC sample is uniform; the distribution changes due to the occurrence of collisions and so the Shapiro-Wilk $p - value$ evolves over time. However, when the probability plots are made with theoretical log-normal distributions, as shown in Fig. 1.7b, the final distributions of the numbers of objects are represented equally well by such theoretical distributions ($R = 0.99787$ c.f. $R = 0.9974$).

If the distributions of the numbers of objects in the MC samples are not reliable, quantitative comparison of "ADR 5 per year" scenario to "mitigation only" is unreliable. More Monte Carlo runs that would represent the underlying distributions unambiguously are required to draw definite conclusions. Still, in the current samples, approximately 81% of Monte Carlo runs in Fig. 1.6a saw the total number of objects in the environment increase despite ADR remediation. This is not an artefact present in the final distribution only - it can be seen in Fig. 1.9b that the number of objects in many Monte Carlo runs was consistently increasing throughout the simulation. ADR clearly reduces the rate at which the number of objects grows c.f. "mitigation only", which is shown in Fig. 1.9a, but the means of the final populations are smaller by only approximately 5000 objects.

This leads to a conclusion that active debris removal may not only be unnecessary to reduce the growth rate of the environment. ADR of five objects per year, which was claimed to be mandatory by e.g. Cerf [19] or Braun et al. [17], is *could be insufficient*. In point of fact, 4.26 as many Monte Carlo runs saw the number of objects increase rather than decrease in spite of ADR.

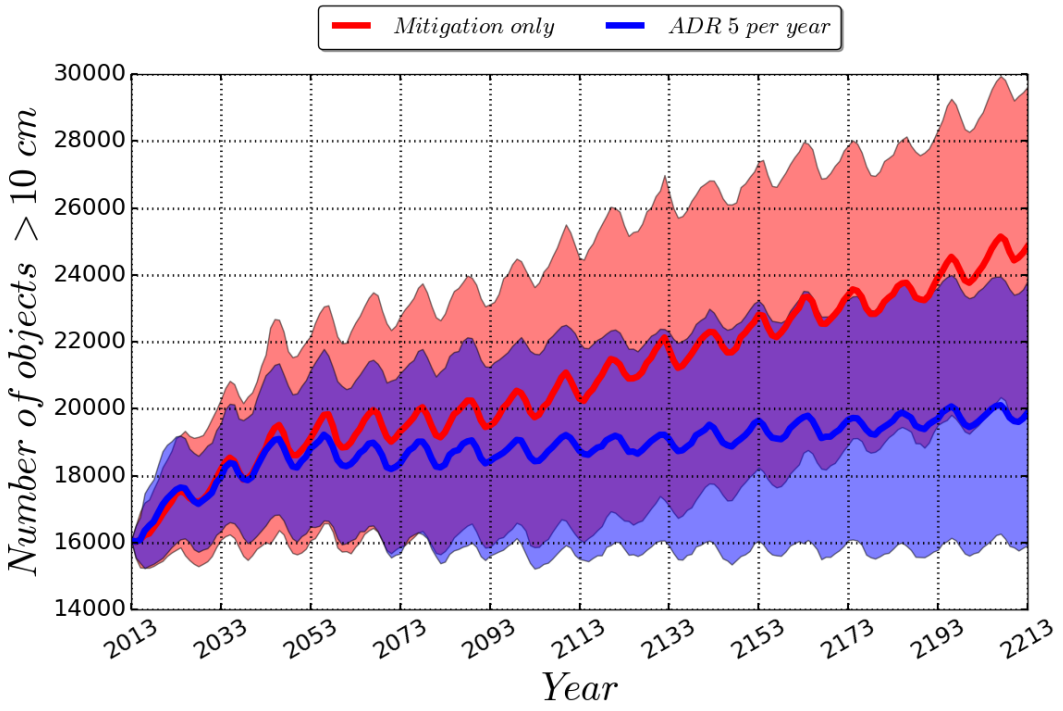

Figure 1.5: Evolution of the number of objects in orbit for "mitigation only" (red) and "ADR 5 per year" (blue) scenarios from Table 1.1. The curves are means of the Monte Carlo samples with 140 and 91 runs, respectively. One standard deviation bands around every Monte Carlo mean are shown. Data provided by Dr Hugh G. Lewis.

Why might active debris removal be unsuccessful? What can we do to change it? How will we know that what we are doing will successfully reduce the growth rate of the number of objects in orbit? Clearly, if all the objects that will be involved in collisions in the future are removed from orbit, no collisions will take place. This will prevent the generation of new fragments and so the number of orbiting debris will not increase by more than what is launched into orbit. Could it be that the objects, which take part in collisions are not targeted by ADR in all the Monte Carlo runs? The ADR target selection metrics will now be reviewed to answer this.

1.4 Current approaches to Active Debris Removal target selection

Some of the first ADR target selection methodologies, such as the one by Ash et al. [12], are based on manually selecting objects that seem likely to be involved in a collision with high severity. This reduces the target selection problem to identifying large-mass objects with large cross-sectional areas and located in densely populated orbital regimes. The object's mass correlates with the severity of the effects of its potential collision,

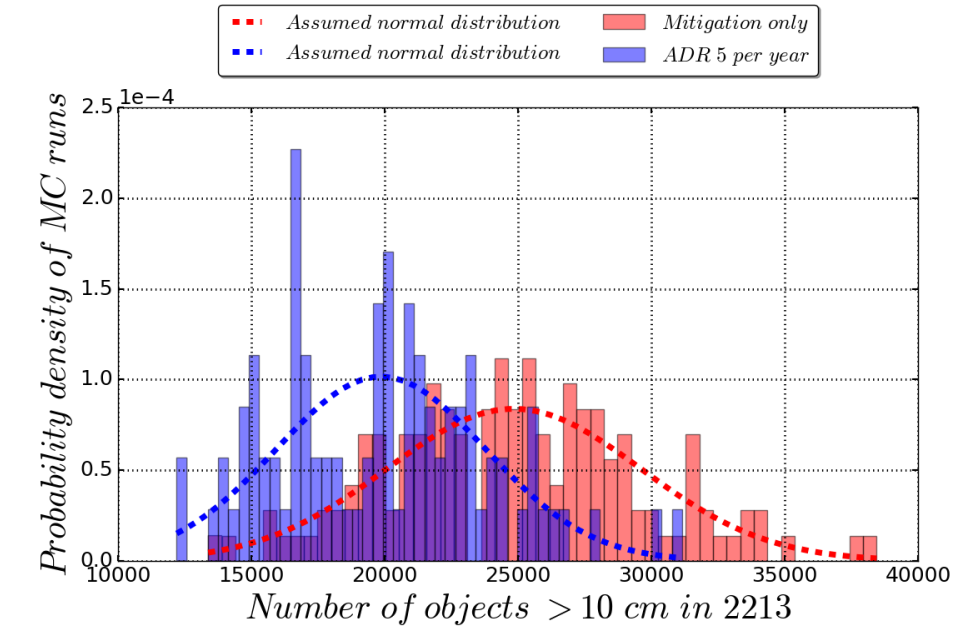

(a) Histograms

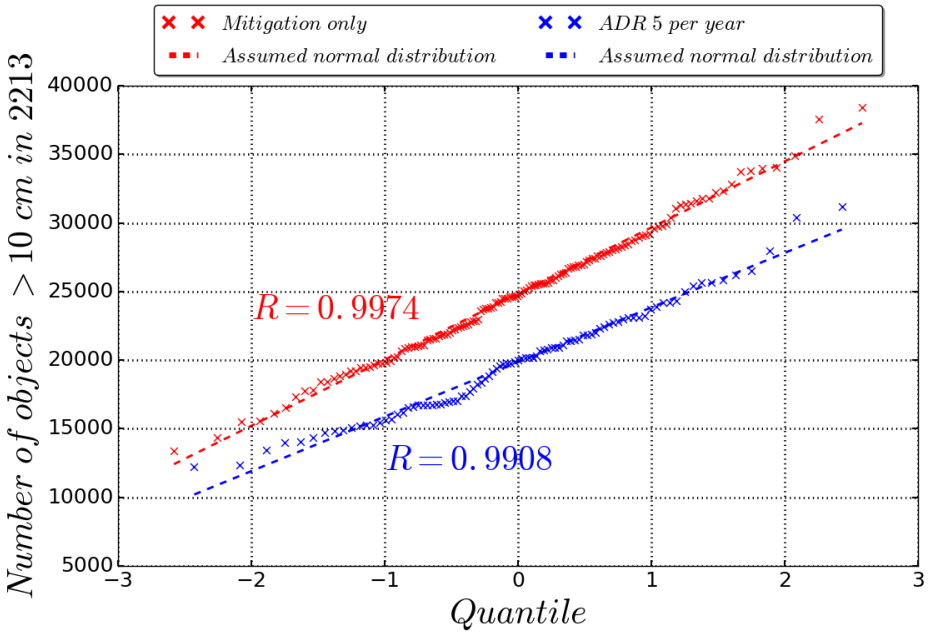

(b) Normal probability plots

Figure 1.6: Histograms and normal probability plots of the distributions of the number of objects larger than 10 cm in orbit at the end of the projection (2213) in the Monte Carlo runs of the "mitigation only" (red) and the "ADR 5 per year" (blue) scenarios from Table 1.1. Theoretical normal distributions are also shown.

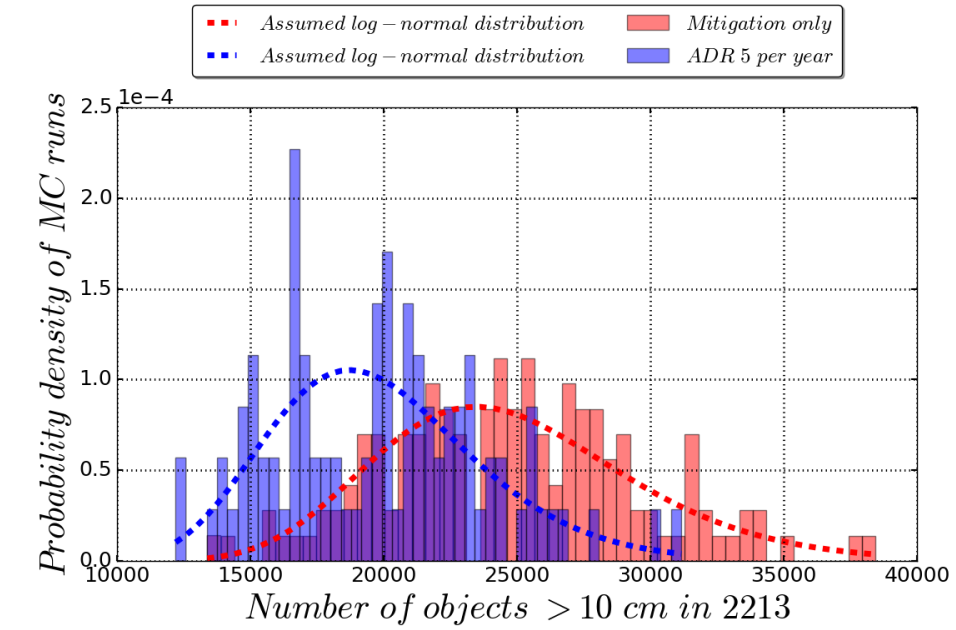

(a) Histograms

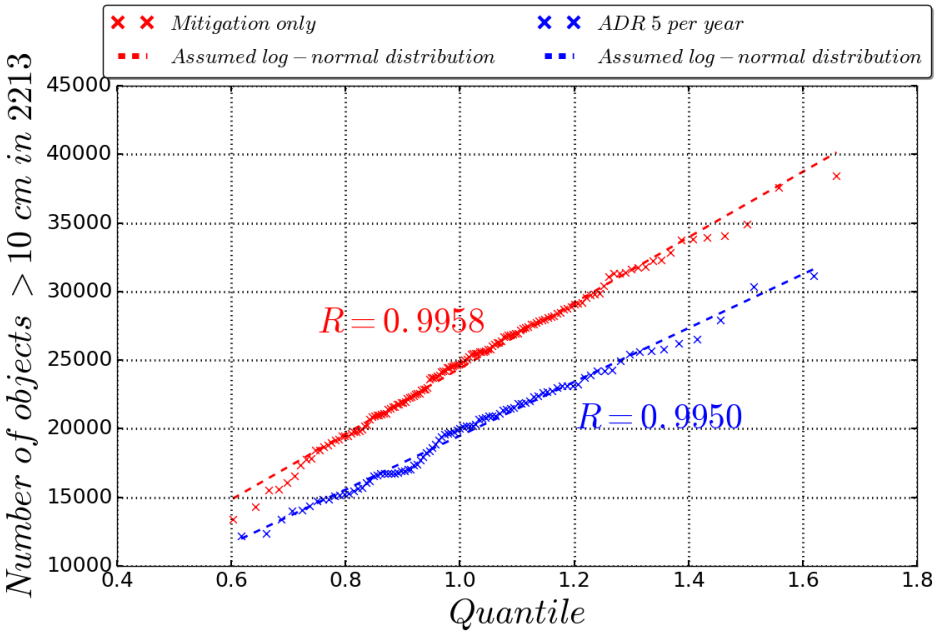

(b) Normal probability plots

Figure 1.7: Histograms and normal probability plots of the distributions of the number of objects larger than 10 cm in orbit at the end of the projection (2213) in the Monte Carlo runs of the "mitigation only" (red) and the "ADR 5 per year" (blue) scenarios from Table 1.1. Theoretical log-normal distributions are also shown.

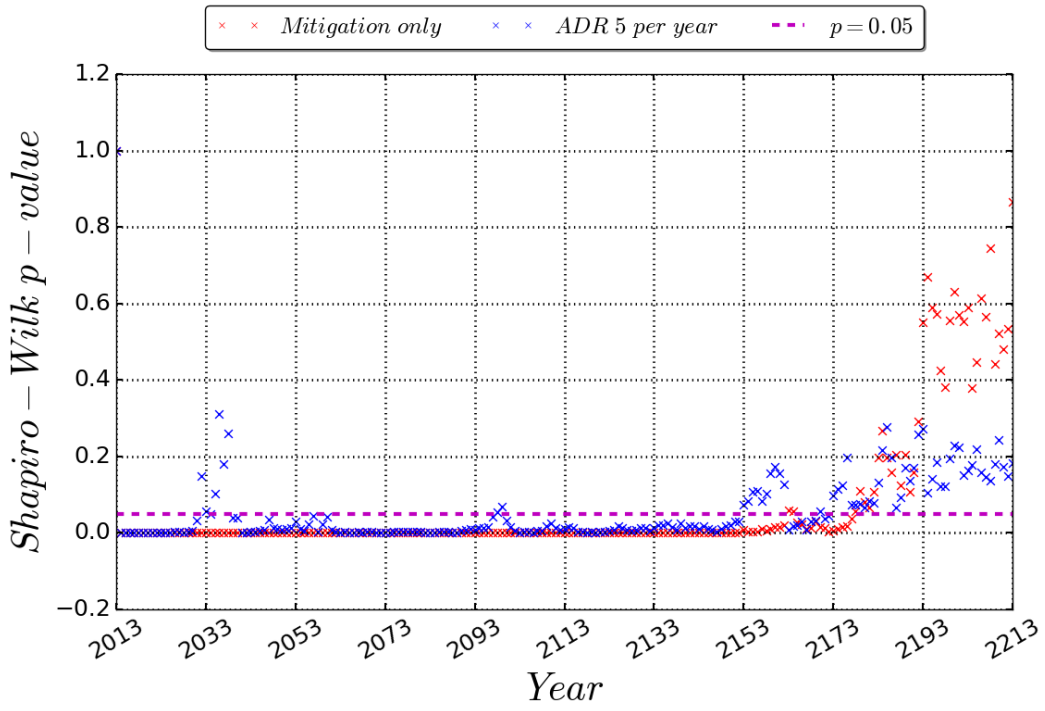

Figure 1.8: Shapiro-Wilk test results, showing the $p - value$ of the null hypothesis that the data had come from a normal distribution at all the analysed epochs. Monte Carlo samples of the "mitigation only" (red), and "ADR 5 per year" (blue) scenarios from Table 1.1. Data provided by Dr Hugh G. Lewis.

i.e. the number of fragments that could be generated, which could then disable or damage active satellites. Large cross-sectional area and frequent conjunctions, which are expected to take place in densely populated orbital regimes, increase the collision probability of the object [12]. Additional selection criteria can also be included, for example examining only physically similar, undamaged objects located in similar orbits, which makes devising missions to remove them relatively easy. The study by Ash et al. [12] found that Cosmos C-lB rocket bodies make good ADR targets of opportunity. These objects are relatively easy to reach and the fact that many objects of the same type exist in similar orbits makes removal of many of them low cost, relative to removal of different types of objects located in different orbital regimes, which would require larger fuel masses.

Objects that are likely to be involved in a collision that will produce many fragments are still being proposed as ADR targets. However, the analyses are now conducted primarily using evolutionary debris models, most of which are briefly described in [86], rather than by manually studying the data. Work by Liou [91] explicitly uses collision probability, P_C, accumulated by different objects and their mass, m, to compute the target selection metric as $P_C \times m$.

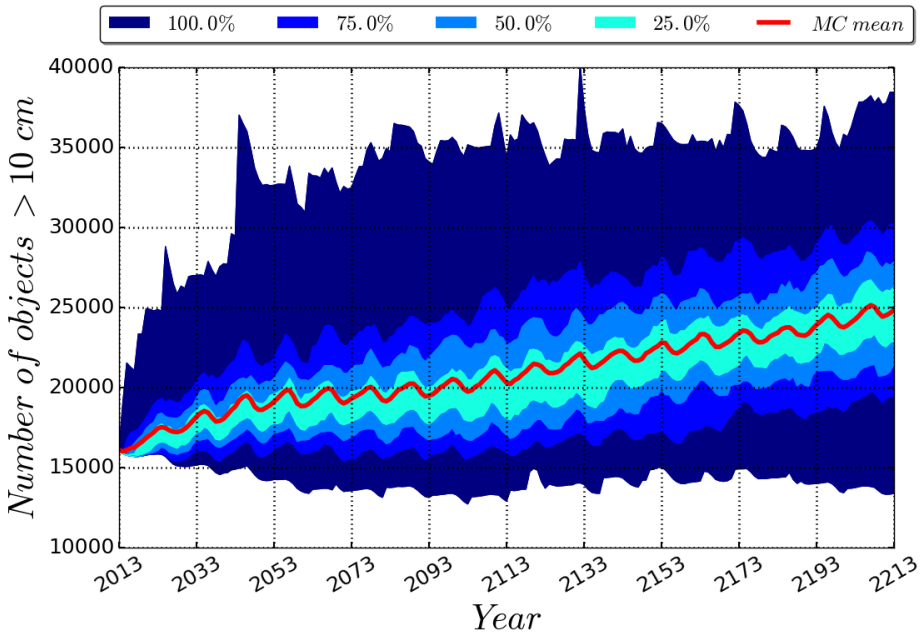

(a) "mitigation only"

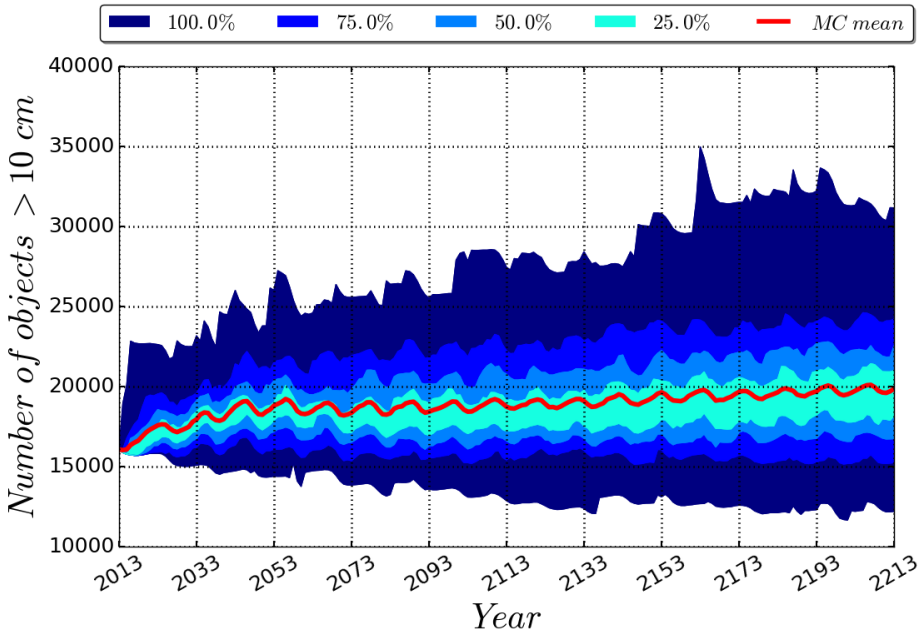

(b) "ADR 5 per year"

Figure 1.9: Evolutions of the number of objects larger than 10 cm in the Monte Carlo samples of "mitigation only" and "ADR 5 per year" scenarios, summarised in Table 1.1. Showing the number of objects in a given fraction of the Monte Carlo runs, centred on the median. Also showing the means of the samples. Data provided by Dr Hugh G. Lewis.

Utzmann et al. [145] as well as Yasaka [158] proposed similar metrics, namely the P_C from Eq. 1.2, where the Δt was made equal to the remaining orbital lifetime. Utzmann et al. [145] multiplied the P_C by $m^{0.75}$, while Yasaka [158] by αm, where α is given by a breakup model and gives the maximum expected number of fragments generated in the fragmentation of mass m.

A similar metric was also used in a study by Braun et al. [17]. However, Braun et al. [17] only examined the probability of a catastrophic collision. Also, they used flux of the objects to estimate the collision probability of every potential target, not the collision probability estimated using the evolutionary debris models.

The approach to finding the "criticality" of every object, by looking at the probability of its collision as well as the effects that the related fragmentation would have, is being continued by Radtke et al. [125] and Rossi et al. [128]. Both groups simulate fragmentations of certain objects and compare these scenarios to a reference one. The reference scenario is based on "assumptions that represent a good, standard hypothesis that are well suited to produce an 'average' reliable future environment appropriate for the purpose of" those studies [128]. These comparisons yield the effect that the fragmentations of representative satellites might have on the evolution of the number of objects in orbit, i.e. severity. By including spatial density [128] or flux [125] of all the remaining objects in the orbit, where the representative satellite resides, the severity of its fragmentation can be combined with the probability of the fragmentation occurring, thus giving a criticality metric. The criticality of any other satellite can then be approximated by examining the representative object it resembles.

Both of the mentioned [125, 128] criticality metrics use future predictions that are based on the results of 200 year projections by evolutionary debris models. Due to the fact that the variance of the Monte Carlo samples is large, the effects of individual fragmentations are difficult to discern after approximately 50 years from the fragmentation epoch, even if relatively large-mass objects break up in densely populated orbital regimes. This is because the variability between the runs in the Monte Carlo samples obscures the differences that fragmentations of individual objects make, and so discerning the difference between scenarios with fragmentations and the reference scenario is difficult. The same difficulty arises when comparing the number of objects in the environment [128] or the collision rate [125] in scenarios with fragmentations to the reference one.

Letizia et al. [71] also computes the "criticality" of every object by finding the increase in the collision probability of operational spacecraft that the fragmentation of a given object would cause. The objects found to be the most appropriate candidates for ADR are large in mass, cross-sectional area and located in densely populated orbital regimes, as in the case of using other ADR target selection approaches [71]. One advantage of this work is the fact that it does not depend on the results of evolutionary debris models. However, it only examines the severity of the fragmentation of every object, not its probability.

Dominguez-Gonzalez and Sanchez-Ortiz [27] also ranked the objects according to their "criticality". They used spatial density of objects to compute collision probabilities for all the objects in the public TLE catalogue. In this case, there was no Monte Carlo analysis involved, and thus the differences in collision probabilities of various objects were more distinct. This target selection method identifies objects that are large in size and reside in densely populated orbital regimes as top-priority targets. These are not necessarily the objects that *are going to be* involved in collisions, however, merely the ones that are *likely* to be involved in a collision. For the sake of brevity, this work will refer to such objects as *statistically* important.

A conceptually different approach was adopted by Lewis et al. [75], who treated the objects in orbit as vertices of a network and their conjunctions as edges, i.e. connections between the vertices. By building such a network of connections using results of an evolutionary debris model, DAMAGE, they were able to find the objects that have many connections to other objects, i.e. act as "hubs" in the network. If any objects fragment, the resulting debris will propagate through the network via the hubs. If sufficiently many hubs are removed, however, the network will become disjoint and even if certain objects do collide or fragment, the resulting debris will not be able to affect most of the satellites in orbit [75]. Even though conceptually different, this study was still based on the results of an evolutionary debris model and, as such, suffered from the uncertainties associated with finding the conjunctions over the 40 year time period [75].

Actively removing the objects likely to be involved in collisions and hoping to contain the growth of the number of objects assumes that it is those objects that are going to be involved in most, if not all, of the future orbital collisions. Removal of those objects should, therefore, limit the number of collisions to a point when the number of objects in the environment does not increase beyond acceptable levels. This assumption is also made in the work by Lewis et al. [75], who claim that removal of the hubs of the "debris network", i.e. reducing its resilience, is going to prevent collision fragments from propagating across the network and causing more collisions.

As stated by Liou [91], the best approach to remediation of the problem of space debris depends on what the end goal is. The optimum actions that lower the risk to operational spacecraft in the near-term or maintain the total number of objects in the environment centuries ahead are likely to be different. This is visible when examining the work by Rossi et al. [128] and Radtke et al. [125], who suggest that short-term risk is highly influenced by individual collisions, but the effect of single fragmentations on the long-term evolution of the number of objects is hard to distinguish due to the variance of the samples.

For some of the goals set for ADR, selecting statistically important objects may be sufficient, but for other objectives of debris remediation this may not suffice. If enough objects are removed from orbit, we can hope to have prevented enough future collisions to halt the growth of the number of debris. But this may not be the case, as in the majority of the Monte Carlo runs described in section 1.3.2.

Ultimately, it is the collisions that are responsible for the future increase of the number of debris as well as the short term increases in the collision risk to operational spacecraft. Thus, our debris remediation efforts should aim to prevent collisions from occurring.

1.5 A different look at debris remediation

It has been shown that objects are likely to accumulate in orbit. Currently, the population of space debris consists mainly of relatively small fragments, but intact spacecraft and rocket bodies have also been left in orbit. Large derelicts might collide, thus producing more small debris. These debris, even though small, might damage or disable satellites. Therefore, they have to be actively avoided by the spacecraft capable of manoeuvring [64], if the debris are large enough to track.

The space debris problem can therefore be split into two issues. Firstly, it is the small debris that can eventually cause damage to spacecraft and disrupt their operations. The minimum size of objects that can be tracked in Low Earth Orbit is often quoted to be 10 cm [62], meaning that there are objects that are difficult or impossible to track. This renders actively avoiding collisions, by moving the spacecraft when a conjunction is forecast, insufficient to fully protect them [63] because untracked objects could still damage or destroy the satellites.

The exact minimum size of an object that can be tracked depends on its altitude as well as its physical properties. The smaller the object, the more difficult it is to track and certain small objects cannot be tracked at all [42]. They can, nevertheless, disable operational spacecraft [24].

The abundant small debris have different sources. They can be generated during nominal spacecraft operations, as e.g. NaK droplets [154] or aluminium oxide slag [49], and debris mitigation guidelines and technology advancements can tackle their generation. However, as was shown in Fig. 1.2, many small fragments have been, and most likely will be [86], generated by fragmentations of large, intact objects. The current trend to reduce the growth rate of the number of small objects appears to be active removal of large derelicts and thus trying to prevent catastrophic collisions, which are the source of the problem. This is primarily because, even though up to 95% of future collisions are going to involve objects smaller than 10 cm, 98% of these events will be non-catastrophic and so will not contribute to the increase in the number of debris [67]. "Non-catastrophic collisions between small impactors ($<$ 10 cm) and large targets ($\leq$ 10 cm) are by far the dominant mode of collisions in the modelled environment. In reality these events would be unlikely to be observed, as the effect is a destruction of an untracked impactor and some crater damage to a much larger target." [67]. Discrepancies in the order of magnitude are present between different debris models in the 1 mm to 1 cm size regime [66]. Thus, it is impossible to confidently quantify the fraction of the future debris population that will be generated by collisions involving small objects because their current number is unknown. Still, the proliferation of all debris in orbit, including the small objects, will be caused by collisions involving large derelicts [86].

It appears reasonable to combat the origins of the issues, rather than treating the symptoms. But how many objects that are likely to be involved in a collision should be removed per year to guarantee that the investment in ADR will bring the expected returns? Which objects should we remove and in what order, especially given the uncertainties that were described in section 1.3.2.2? And how much will all this cost?

This makes one ask what other options to contain the number of objects in the environment exist. Could forecasting and prevention of collisions, thus stopping the production of small, untraceable objects, as suggested by McKnight et al. [99], be sufficient? If so, how many conjunctions have to be prevented to ensure zero growth of the number of debris given that, realistically, not all the collisions can be prevented due to our inability to predict the future with absolute certainty? And how many of these conjunctions will involve low-mass objects, which would not be removed by ADR but still catastrophic breakups?

It has been suggested by Lewis and Lidtke [73] that particular conjunctions might give rise to the most of the collision probability that certain space objects accumulate over short (order of months) periods of time. This creates the potential to prevent those relatively few events and remedy most of the collision probability in the entire debris environment, and thus reduce the probability of the growth of the debris population.

Active removal of a single, large derelict object is likely to be expensive, probably in the order of \$10 to \$50 million per object [103]. It was shown in Fig. 1.9b that, if debris model uncertainties are accounted for, potentially more than five objects per year have to be removed to halt the increase of the number of debris, which will cost more than $\$50 - 250$ million per annum. This yearly cost of active removal of five objects equates to only 1.4% of NASA'a and 6.6% of ESA's annual budgets [32, 108], which suggests that active debris removal could be implemented, if need be, but it would strain the space agencies worldwide.

However, the outcome of ADR, as well as the incentive to perform any space debris remediation in order to prevent the increase in the number of objects in orbit, remain uncertain. Unless these are addressed, active debris removal is unlikely to gain sufficient backing to be funded. It is difficult to argue against performing ADR and removing mass from orbit. However, ADR missions are associated with non-negligible cost and they could cause a collision in orbit [85], or increase the number of objects in densely-populated orbital regimes should they fail [74]. Therefore, performing ADR on a large scale may not be the most optimal, from the cost-risk-benefit point of view, strategy to remedy the debris environment.

1.6 Goals and objectives

It was argued here and by many other authors that space debris are an issue that should be dealt with. It may not be necessary but reducing humanity's impact on the space environment and making spaceflight sustainable can be argued for. Besides, it may well be that this could be the only way future generations will be able to access space.

However, it remains unclear how the space debris issue can be tackled beyond the implementation of sensible mitigation measures. One of the widely suggested measures to deal with the debris problem, namely active debris removal, was questioned due to its uncertain outcomes and non-negligible cost. It was argued that it is impossible to predict collisions far in advance and so the involved objects cannot be targeted by ADR with absolute certainty. At least 9.5 derelicts had to be removed to prevent a single collision in a study by Liou and Johnson [93]. This means that selecting ADR targets based on long-term collision probability estimates increases the number of the removed objects beyond the number of collisions that are expected. This also implies that, unless all the uncontrolled objects are removed, the number of space debris might still increase despite the ADR efforts because not all the collisions will be prevented.

Previous work by Lewis and Lidtke [73] has shown that most of the collision probability of certain objects in orbit may be caused by infrequent (one in thousands) conjunctions with collision probabilities several orders of magnitude higher than the rest. This suggests that it is those events that could ultimately lead to most of the collisions. Also, such close approaches could give rise to the fact that collisions occur in projections by evolutionary debris models in spite of ADR, because different sets of objects are involved in collisions than are selected for removal.

It is therefore considered important to analyse the impact of the rare conjunctions with extremely high collision probabilities on the collision probability accumulated by every object individually as well as the entire debris environment. Sensitivity of the collision probabilities of all the objects to key factors, such as solar activity and object attitude, which cannot be reliably predicted far in advance, is also of interest. Assessing this sensitivity could help us understand whether we can even aspire to identify all the objects that are going to be involved in collisions and remove them.

Two outcomes of the above investigation are possible: either any object could be involved in a collision, or there is a limited subset of objects that are going to cause collisions. In the latter case, it should suffice to remove those objects to reduce the collision risk in the debris environment. In the former scenario, different measures that address particular conjunctions at a relatively short notice need to be pursued. This is because it is possible to estimate the collision probability of a conjunction several days in advance [147], but removing the involved objects from orbit will require more time [20]. Perhaps a mixed approach is optimal from the cost and benefit point of view.

To address the issues associated with ADR target selection uncertainties highlighted above, the following research objectives were set for this work:

1. Test whether particular conjunctions with high collision probability are experienced by all objects in orbit or only a subset.

2. Determine whether these particular conjunctions give rise to a large portion of the probability of any collision taking place in orbit.

3. Test whether variations in external conditions, which cannot be forecast far in advance, e.g. solar activity, change the objects that have the highest collision probability in a given period of time by introducing new conjunctions with relatively high collision probabilities.

4. Demonstrate that such conjunctions with extremely high collision probabilities also take place in evolutionary debris models and result in more collisions than other close approaches with lower collision probabilities.

5. Correctly capture the underlying distribution of the future number of objects in a DAMAGE projection to provide a reliable reference scenario, on which the effects of preventing only excessive growth of the number of debris (tail of the distribution) can be tested.

6. Corroborate the thesis that preventing collisions between objects on an *ad hoc* basis is a viable means of reducing the growth rate of the number of debris.

7. Determine the number of conjunctions that need to be prevented annually to achieve a given result on the debris environment, to enable financial viability of an *ad hoc* collision prevention framework to be assessed.

8. Identify characteristics of the objects, collisions of which should be prevented to stop the number of debris from increasing.

In order to achieve these goals, a debris simulation framework that can identify individual conjunctions as well as estimate their collision probabilities needed to be developed. In order to discern individual conjunctions, it had to have relatively fine spatial and temporal resolutions compared to the current debris models. The details of this framework are given in Chapter 2.

The developed framework was then applied to analyse how particular conjunctions with high collision probaility contribute to the collision probability accumulated by individual objects over a given time interval. The contribution of such events to the collision probability in the entire debris environment was also examined. The unpredictability of such events, due to the uncertainty in e.g. object attitude or solar activity, was then investigated in a sensitivity study. These investigations address the research objectives 1, 2, and 3, and are described in Chapter 3. This chapter also covers the investigation addressing the research objective number 4, which was carried out using DAMAGE.

Another solution that could potentially help improve the sustainability of space activities by preventing collisions in an *ad hoc* fashion, just-in-time collision avoidance (JCA) [99], was then analysed. It was investigated whether it is sufficient to stop the growth of the number of objects in the debris environment, regardless of the uncertainties in predicting collisions. The parameters that should be included in JCA target selection were also be analysed and suggestions made. Lastly, the rate of JCA false alarms, which will govern the cost of JCA and thus its economic feasibility [99], was quantified with current ephemeris uncertainties. All of this is covered in Chapter 4 and addresses the remaining research objectives of this work (5, 6, 7, and 8).

The preceding discussion of the space debris issue, limitations of ADR target selection and suggested hypothesis that *ad hoc* collision prevention can halt the increase of the number of objects in orbit, together with the upcoming topics of this thesis, are presented in Fig. 1.10. The chapters in Fig. 1.10 are numbered as in this work, however, the boxes summarise the topics that are covered, which sometimes span more than one subsection. The utilisation of the tools developed in this work, as well as the relationship between the set hypotheses and the investigations that test them is also indicated in Fig. 1.10. Due to the multitude of the topics covered here, the Reader is encouraged to consult Fig. 1.10 to orientate themselves when progressing through this work.

1.7 Relevance of the research

The journal publications associated with the research presented in this work are:

- Lidtke, A.A., Lewis, H.G. and Armellin, R., "Actual results may vary: interpreting results of evolutionary debris models", submitted to Advances in Space Research in 2016.
- Lidtke, A.A., Lewis, H.G., Armellin, R. and Urrutxua, H., "Considering the collision probability of active debris removal missions", Acta Astronautica 131, 10–17, 2016.
- Lidtke, A.A., Lewis, H.G. and Armellin, R., "Impact of high-risk conjunctions on Active Debris Removal target selection", Advances in Space Research 56(8), 1752–1764, 2015.

The corresponding conference presentations are:

- Lidtke, A.A. and Lewis, H.G., "Representing modelling outputs - part 2 ", in Proceedings of the 34th Inter-Agency Space Debris Coordination Committee Meeting, Harwell, United Kingdom, 2016.
- Lidtke, A.A. and Lewis, H.G., "Collision Probability Assessment for Active Debris Removal Missions", in Proceedings of the 65th International Astronautical Congress, Toronto, Canada, 2014.
- Lidtke, A.A., Lewis, H.G. and Armellin, R., "A deterministic approach to active debris removal target selection", in Proceedings of the Advanced Maui Optical and Space Surveillance Technologies Conference, Wailea, HI, USA, 2014.
- Lidtke, A.A., Lewis, H.G. and Blake, R., "Deterministic method for Active Debris Removal target selection", in Proceedings of the 3rd European Workshop on Space Debris Modelling and Remediation, Paris, France, 2014.

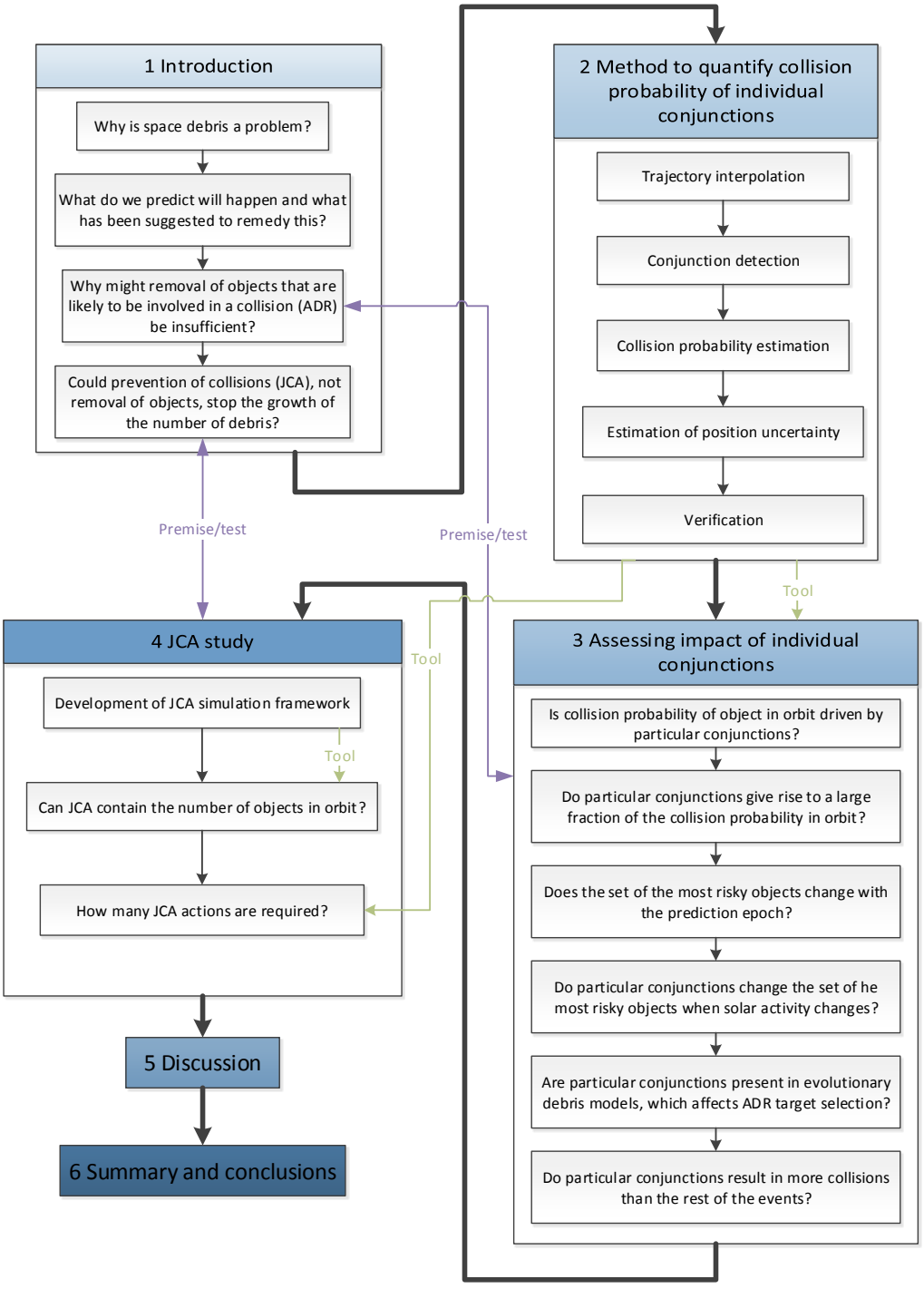

Figure 1.10: The flow of the topics covered in this thesis, including the development of simulation tools and the questions raised. Grey arrows indicate the chronological order, in which the indicated topics are discussed. Green arrows indicate utilisation of the simulation tools developed in this work, whereas purple arrows show the premises that lead to different investigations, which then test the set theses and hypotheses.

The novel contributions of this work, as determined by the topics of the published articles and feedback from conferences, are:

- Demonstration of the importance of particular conjunctions in the scope of collision probability accumulated by individual objects in orbit and the entire debris environment.
- Proof that conjunctions with high collision probabilities lead to more collisions in evolutionary debris models than the rest of close approaches.
- Generation of a reliable distribution of the number of objects in orbit for the "mitigation only" scenario.
- Analysis of the currently achievable ephemeris accuracies and quantification of the associated number of conjunctions that exceed a given collision probability threshold.
- Proof that JCA is a viable means of preventing the long-term growth of the number of space debris.
- Development of a state-of-the-art conjunction detection and assessment framework, which combines ephemeris interpolation with conjunction detection, and uses a range of collision probability estimation algorithms to increase the overall computational speed while retaining accuracy.

While working on this thesis, the author also published the following work:

- Lidtke, A.A., Gondelach, D., Armellin, R., Colombo, C., Lewis, H.G., Funke, Q., and Flohrer, T., "Processing two line element sets to facilitate reentry prediction of spent rocket bodies from geostationary transfer orbit", in Proceedings of the International Conference on Astrodynamics Tools and Techniques, Darmstadt, Germany, 2016.
- Lidtke, A.A., Rumpf, C., Tatnall, A., Lewis, H.G., Walker, S.J., Taylor, M., Fear, R.C., Weddell, A.S., Maunder, R.G. and Bantock, J.R.B., "Enhancing spaceflight safety with UOS3 cubesat", in Proceedings of the 1st Symposium on Space Educational Activities, Padova, Italy, 2015.
- Lidtke, A.A., "Solar Power Satellite: an alternative concept: System study of a spacebased solar power system", 9783659631993, LAP LAMBERT Academic Publishing, 2014.

and co-authored the following:

- Gondelach, D., Armellin, R., and Lidtke, A.A., "TLE-based reentry predictions for upper stages in geostationary transfer orbit", submitted to Advances in Space Research in 2016.

- Gondelach, D., Lidtke, A.A., Armellin, R., Colombo, C., Lewis, H.G., Funke, Q. and Flohrer, T., "Reentry prediction of spent rocket bodies in GTO", in Proceedings of the 26th AAS/AIAA Space Flight Mechanics Meeting, Napa, CA, USA, 2016.

- Rumpf, C., Lidtke, A.A., Weddell, A.S. and Maunder, R.G., "Enhancing microelectronics education with largescale student projects", in Proceedings of the 11th IEEE European Workshop on Microelectronics Education, Southampton, UK, 2016.

- Lewis, H.G. and Lidtke, A.A., "Active Debris Removal: Consequences of Mission Failure", in Proceedings of the 65th International Astronautical Congress, Toronto, Canada, 2014.

- Lewis, H.G. and Lidtke, A.A., "A Collision Conundrum: Investigation of Envisat Collision Hazard", in Proceedings of the 32nd Inter-Agency Space Debris Coordination Committee Meeting, Beijing, China, 2014.

Chapter 2

Conjunction Detection and Assessment

This chapter describes the method that was developed to identify individual conjunctions between objects, i.e. times when they get within a certain distance from one another. The algorithms used to compute the associated collision probabilities, P_C, including estimation of the uncertainty of the publicly available state vectors (positions and velocities of the objects) i.e. two-line element sets (TLEs), are also described here. Such a conjunction detection and assessment framework was needed in order to test whether particular conjunctions affect the collision probability accumulated by objects more than most of the close approaches, i.e. to address research objectives number 1, 2 and 3 from section 1.6. The same framework was also used to determine the number of conjunctions that need to be prevented annually to achieve a given result on the debris environment, i.e. objective number 8.

In order to keep this chapter brief, only the algorithms developed by the author are described in detail; the algorithms adopted from the literature are only summarised unless modifications were made to them. For the same reasons, most of the numerical studies are presented in the companion Chapter A of the Appendix.

At the time of the development of the algorithms, the exact format of the ephemerides, which were used in this work, was not known. Therefore, a trajectory interpolation method that could support ephemeris tables generated with any orbital propagator was used. Such an approach also provided computational time savings with respect to using an orbital propagator directly to find conjunctions [6]. The interpolation method is described first, followed by description of the methods specific to conjunction detection and their P_C assessment.

2.1 Trajectory interpolation method

Most of the schemes used to interpolate ephemerides are based on polynomials that interpolate Cartesian state vectors [42], with the Hermite and Lagrange schemes of 3^{rd} to 7^{th} order being the most prevalent [42, 111, 138]. The time intervals by which the interpolation nodes are separated are normally in the order of several minutes [131]. However, optimal (in terms of lowest error for least computational time required) interpolation node placement strategies depend strongly on the characteristics of the orbit at hand, e.g. its eccentricity [111].

Because this work is concerned with studying the space debris environment, not developing ephemeris interpolation schemes, a simple approach with interpolation nodes uniformly distributed in time was decided upon. This could affect the accuracy of the interpolation, but a study was conducted in section A.1 to assess the inaccuracies of the method and their impact on the final results. Moreover, using such an approach to interpolation also simplified building a conjunction detection algorithm that uses the interpolated ephemerides. This made the combined set of algorithms faster, which enabled more extensive studies to be performed in the timeframe of this project. If interpolation was conducted in mean or true anomaly, which could make interpolation itself more accurate for a given number of the interpolation nodes, the code would need to convert between the mean/true anomaly and time domains anyway to perform conjunction prefiltering. Having to perform these operations at all the interpolation steps for all the objects would reduce the overall computational speed of the developed software. Quantitative assessment of the computational speed of the entire conjunction and assessment framework, which uses the chosen interpolation scheme, is presented in section A.2.3.

Different approaches to formulating the interpolating polynomials were investigated. Those can be split into two groups: those that use only the function value, i.e. position along a given coordinate in this case, to define the interpolating polynomials and those that also use gradient, i.e. velocity, data. Several interpolation methods were investigated, namely Lagrange and power series from the former kind, and Hermite and modified power series from the latter. The details of the interpolation schemes will be presented first. The different interpolation techniques will then be compared on several representative test cases, and an appropriate method selected.

2.1.1 Available interpolation methods

The methods described here are generic and can be used with interpolating polynomials of any order. Any polynomial interpolation should find the same polynomial when given the same input data, if it is applied correctly [123]. It was eventually decided to use an interpolation scheme that uses velocity as well as position data to interpolate the states of the objects. This is why generic forms, for an arbitrary polynomial order, of the Lagrange and power series interpolation schemes will be given here. On the other hand, the modified power series and Hermite will be described based on an example of a cubic polynomial because these are the forms in which they were used.

2.1.1.1 Power series

Perhaps the simplest method to formulate and interpolating polynomial is, given N Cartesian position coordinates X_0, X_1, $X_2 \ldots X_i \ldots X_{N-1}$, to find an order $N-1$ polynomial, with coefficients A_0, A_1, $A_2 \ldots A_j \ldots A_{N-1}$, interpolating these points by solving the following system of equations [123]:

$$\begin{bmatrix} t_1^{N-1} & t_1^{N-2} & \ldots & t_1^j & \ldots & t_1^2 & t_1 & 1 \\ t_2^{N-1} & t_2^{N-2} & \ldots & t_2^j & \ldots & t_2^2 & t_2 & 1 \\ \vdots & & & \vdots & & & & \vdots \\ t_i^{N-1} & t_i^{N-2} & \ldots & t_i^j & \ldots & t_i^2 & t_i & 1 \\ \vdots & & & \vdots & & & & \vdots \\ t_N^{N-1} & t_N^{N-2} & \ldots & t_N^j & \ldots & t_N^2 & t_N & 1 \end{bmatrix} \begin{pmatrix} A_{N-1} \\ A_{N-2} \\ \vdots \\ A_j \\ \vdots \\ A_2 \\ A_1 \\ A_0 \end{pmatrix} = \begin{pmatrix} X_1 \\ X_2 \\ \vdots \\ X_i \\ \vdots \\ X_N \end{pmatrix}, \tag{2.1}$$

where t_i^j are the epochs, i.e. the free variable, corresponding to the interpolation nodes X_i taken to the power j. Solving this system of equations gives the polynomial coefficients explicitly. Those coefficients can then be used to find the value of the function of interest for any time t:

$$X(t) = A_{N-1} \times t^{N-1} + \ldots + A_j \times t^j + \ldots + A_1 \times t^1 + A_0. \tag{2.2}$$

Coefficients A_j can also be used for further analysis, e.g. to formulate an analytical relative distance function. They can also be used to interpolate the velocity of the object, which is the rate of change of the position, e.g. $\dot{X}(t)$ for the X coordinate, as it can be obtained analytically based on the same coefficients:

$$V(t) = \dot{X}(t) = (N-1) \times A_{N-1} \times t^{N-2} + \ldots + j \times A_j \times t^{j-1} + \ldots + 2 \times A_2 \times t^1 + A_1. \tag{2.3}$$

The additional analyses enabled by having the interpolating polynomial coefficients directly were considered advantageous due to the computational time savings they provided, and hence this interpolation scheme was preferred. In order to obtain a cubic polynomial, four interpolation nodes are necessary to provide enough information to solve the system of equations in Eq. 2.1 if only the function values, i.e. positions, are known.

This set of equations has a special Vandermonde form and so dedicated solver algorithms, faster than the generic ones, are available to solve it [123]. However, the propagation computational time was considered equally important as the time taken to interpolate the ephemerides. Hence using four interpolating nodes and a classical power-series interpolation was not deemed highly advantageous because more nodes, and hence computational time compared with e.g. the Hermite scheme, were required to formulate a polynomial of the same order.

2.1.1.2 Lagrange

It is also possible to find the polynomial of degree $N-1$ by interpolating N data points using a so-called Lagrange scheme. This consists of computing Lagrange coefficients, P_i, for every known data point X_i and the value of the free parameter, t, at the point of interest [123]:

$$P_i(t) = X_i \prod_{\substack{k=1 \\ k \neq i}}^{N} \frac{t - t_k}{t_i - t_k}. \tag{2.4}$$

The Lagrange coefficients are then summed for all the known data points whenever the function value X is to be interpolated for some value of the free variable t:

$$X(t) = \sum_{i=1}^{N} P_i(t). \tag{2.5}$$

This scheme also requires four data points in order to obtain sufficient information to be able to find four coefficients of a cubic polynomial interpolating the points. Its main disadvantage is the time taken to compute the Lagrange coefficients, which need to be recomputed every time the function is to be interpolated for a new value of the free parameter t.

Moreover, this scheme does not explicitly give the interpolating polynomial's coefficients and hence any further analysis based on those is impossible. This creates a need to interpolate velocity and position separately, which increases the computational time even further.

2.1.1.3 Hermite

Another classical interpolation scheme that was examined was Hermite interpolation. Given the values of a function and its derivative at two points, a cubic polynomial can be fitted to the data. For numerical stability, this interpolation was performed in a dimensionless time domain, i.e. with the free parameter $t \in [0, 1]$ [123]. For the example of a cubic polynomial, four Hermite basis polynomials h are computed:

$$\begin{aligned} h_{11}(t) &= 2t^3 - 3t^2 + 1, \\ h_{21}(t) &= t^3 - 2t^2 + t, \\ h_{12}(t) &= -2t^3 + 3t^2, \\ h_{22}(t) &= t^3 - t^2. \end{aligned} \tag{2.6}$$

Given known function values at the ends of the interval, X_1 and X_2, and the corresponding gradients, $\dot{X}_1$ and $\dot{X}_2$, the coefficients from Eq. 2.6 can be combined to interpolate the function value for a given t:

$$X(t) = h_{11}(t) X_1 + h_{21}(t) \dot{X}_1 + h_{12}(t) X_2 + h_{22}(t) \dot{X}_2, \tag{2.7}$$

The main disadvantage of this scheme is that it does not explicitly provide the polynomial's coefficients. Also there exists the computational time burden associated with interpolating position and velocity separately, recomputing the basis polynomials for any t, and converting between the time and dimensionless time domains. The largest advantage of the Hermite interpolation is that it conserves the gradient of the function between the interpolation intervals.

2.1.1.4 Modified power series

A classical power series expansion was combined with Hermite interpolation. The former gives interpolating polynomial coefficients explicitly, which can be used to reduce the overall computational time of finding the conjunctions between objects. The latter ensures that the velocity is interpolated correctly, which increases accuracy of P_C estimation. This is because objects' velocities influence the orientation of the uncertainty regions where two conjuncting objects are located, and thus the collision probability that is of interest.

The following set of equations defining a 3^{rd} order polynomial based on function values, X_1 and X_2, and gradients, $\dot{X}_1$ and $\dot{X}_2$, specified at two interpolation nodes 1 and 2, was written [123]:

$$\begin{bmatrix} t_1^3 & t_1^2 & t_1^1 & t_1^0 \\ t_2^3 & t_2^2 & t_2^1 & t_2^0 \\ 3t_1^2 & 2t_1^1 & t_1^0 & 0 \\ 3t_2^2 & 2t_2^1 & t_2^0 & 0 \end{bmatrix} \begin{pmatrix} A_3 \\ A_2 \\ A_1 \\ A_0 \end{pmatrix} = \begin{pmatrix} X_1 \\ X_2 \\ \dot{X}_1 \\ \dot{X}_2 \end{pmatrix}, \tag{2.8}$$

where A_3, A_2, A_1 and A_0 are the coefficients of the interpolating polynomial and t is the time, i.e. the free parameter. Unlike the case of ordinary power series interpolation, only two nodes are necessary to uniquely define a 3^{rd} order polynomial thanks to the use of gradient information.

As for the power series case, the set of equations 2.8 can be solved for the unknown polynomial coefficients $(A_3, A_2, A_1, A_0)^T$. The position and velocity can then be interpolated using Eq. 2.2 and Eq. 2.3. Unfortunately, no special solution methods exist for Eq. 2.8. However, the computational burden of solving Eq. 2.8 using general equation-solving approaches was considered acceptable given the advantages of this scheme. Because the interpolation was conducted in dimensionless time domain with constant time spacing between the interpolating nodes, LU decomposition was used to reduce the time required to solve Eq. 2.8 for new $\left(X_1, X_2, \dot{X}_1, \dot{X}_2\right)^T$ [123].

2.1.2 Choice of the interpolation scheme

The different interpolation schemes described in section 2.1.1 were tested on two objects located in different orbits. Specifically, Envisat located in a near-circular low-Earth orbit (LEO), and a Delta 1 rocket body in a highly-eccentric geostationary transfer orbit (GTO) were investigated. Most of the objects crossing the LEO volume, where collisions are expected to occur in the future [89], will have eccentricities bound by these two exemplar objects (0.00 and 0.71). Thus, Envisat and Delta 1 R/B make for extreme test cases in this orbital element, which affects orbit interpolation accuracy [111]. They also have different semi-major axes, which makes accurately interpolating both orbits using the same scheme with the same settings even more challenging. The three-line element sets of these test cases are given in Table 2.1.

The orbits of both test cases were propagated over one orbital revolution with the SGP4 propagator at 1 second intervals, which was treated as the "truth" data [3, 111]. SGP4 is a fast, analytical propagator intended for use with two-line element sets (TLEs) [48]. The orbits were then interpolated and the differences between the "true" positions and velocities, and the interpolated ones were analysed.

Table 2.1: Three-line element sets (two-line elements sets, i.e. double-averaged classical orbital elements [48], with the common names of the objects) used for interpolation testing. Source: Space-Track [135]

Case	**Three-line element set**
LEO	0 ENVISAT 1 27386U 02009A 13296.16551405 .00000100 00000-0 47533-4 0 8339 2 27386 098.4160 001.9229 0001126 079.5538 280.5787 14.37637337609529
GTO	0 DELTA 1 R/B 1 00862U 64047B 13295.21685803 -.00000267 00000-0 73107-2 0 5879 2 00862 015.7331 219.7670 7129815 071.8006 033.2597 02.05096770163617

The effects of varying the interpolating polynomial order and interpolating node spacing were tested, which is described in detail in section A.1. It was discovered that low-order polynomials retain accuracy comparable to the higher-order schemes for interpolating nodes located up to 400 s apart. Including the velocity information in the formulation of the interpolating polynomials, through the use of Hermite or modified power series schemes, improves the interpolation accuracy for the same polynomial order and interpolating node spacing. It also ensures that the velocities of the objects are continuous between the interpolating intervals, thus providing a continuous representation of objects' state vectors in the entire interpolation domain. This is desired because discontinuities in velocity could produce numerical instabilities in the algorithms that search for the time of the closest approach.

Low order of the interpolating polynomials was desired to simplify the development of the conjunction detection code and increase its computational speed, therefore a third-order scheme was decided upon. Modified power series was used because it explicitly gave interpolating polynomial coefficients and improved interpolation accuracy relative to a classical power series or Lagrange scheme of the same order. This scheme enabled representation of the relative range between two objects, as a function of time, as a 6^{th} order polynomial and allowed efficient numerical schemes to be employed when searching for the time of the closest approach (TCA) [3, 142]. This interpolation technique is not commonly used for ephemeris interpolation, and applying it to interpolate the relative range between two objects by using their individual interpolating coefficients is novel in this field. Even though interpolation accuracy was directly tested on only two objects, this interpolation scheme was used to find conjunctions between all objects in orbit and their details were in agreement with AGI's STK, which is presented in section 2.5.2. This shows that the interpolation scheme was accurate.

Moving the interpolating nodes further apart reduces the number of propagations, thus reducing the computational time needed to interpolate the ephemerides. Ultimately, node spacing of 400 s was decided upon. With this node spacing, the $\infty-$norm (largest recorded error) of interpolating position with a 3^{rd} order polynomial was 0.87 km and 1.88 km for the LEO and GTO cases, respectively. The corresponding velocity interpolation accuracies were 6.7×10^{-3} and 1.5×10^{-2} $km\ s^{-1}$. If the conjunctions are to be found accurately, the accuracy of position interpolation dictates the range threshold that has to be used to look for conjunctions as in the worst case twice this error could be present when interpolating orbits of the two objects. Hence setting the conjunction threshold at 10 km should guarantee that no very close conjunctions are missed. However, a further refinement of the orbits should be performed around the identified close approaches in order to improve the estimates of the miss distance (separation between centres of mass).

2.2 Conjunction detection

A conjunction is defined as an event where the centres of mass of two objects are within a specified distance from one another. Specifically, the time of the closest approach was chosen as the conjunction epoch. This may not necessarily be the time when the collision probability between the two objects is the greatest if their attitude is accounted for, but this was ignored in this study. This, as well as other assumptions made in this work, will be discussed when analysing the results obtained with the developed tools.

Distance thresholds that are different in different directions (e.g. in-track or cross-track) can also be used for conjunction detection in order to account for the fact that the position uncertainties are generally not the same in every direction [3, 23] and so conjunctions with the same miss distance might have different collision probabilities. However, it was decided to account for this by setting the conjunction threshold distance high and accepting that certain conjunction geometries may result in very low collision probabilities with such a miss distance. Furthermore, conjunctions between more than two objects were treated as multiple conjunctions between pairs of objects.

Even with such a simple formulation of a conjunction, the computational time required to identify them between all the objects in the public catalogue (14 917 objects had been observed in the 30 days preceding 23 Oct 2013 and their orbits were published via Space-Track [135]) is significant (order of hours for finding conjunctions one day ahead [1]). This raises the need to implement a number of pre-filters that discard pairs of objects that cannot have a conjunction, based on simple and fast to evaluate flight dynamics principles, before the more computationally-intensive range-based detection is executed.

The entire simulation period is split into time intervals of duration ΔT, in which all the object pair combinations are analysed. The Cartesian position, velocity, and orbital elements of the objects at the beginning of every interval are used to pre-filter the objects. If all the pre-filters are passed, the minimum distance between the given pair of objects in this time interval is found together with the corresponding time of the closest approach. If the objects pass within the threshold distance, the collision probabilities are computed and the conjunction recorded. The entire process is repeated in the following intervals until the end of the simulation is reached. Then, the same process is repeated for the remaining object pairs.

The entire process of identifying conjunctions is described based on finding conjunctions between a pair of objects because this is how it was implemented.

2.2.1 Pre-filtering stage

A number of pre-filters have been developed to date, starting with the method by Hoots et al. [47] that is still being used, as well as alternative approaches adopted by Khutorovsky et al. [60], Healy [45] and Alarcon Rodriguez et al. [1]. New approaches are being developed, e.g. by Budianto-Ho et al. [18], but the objective of this work was not to contribute towards the development of such tools, hence a set of algorithms deemed traditional and reliable [156] was decided upon.

An overview of pre-filtering methods together with their advantages, disadvantages and relevance to the application described herein is given in this section. The choice of the algorithm, based on the investigations given in detail in section A.2, is be discussed last.

2.2.1.1 Available pre-filters

Typically, one of the objects in a pair for which the conjunctions are to be found is referred to as the primary, i.e. the object for which the conjunctions are sought, and the other as the secondary, i.e. one of the objects that is believed to potentially have close approaches with the primary. However, in this work no such distinction can be made because all objects are equally important. Therefore, ‘primaries’ and ‘secondaries’ are chosen arbitrarily.

Perigee/apogee filter This pre-filter rules out all the objects that do not cross each other’s altitude bands and hence can never collide [47].

The rates of change of the perigee and apogee radii of both objects can further be used to determine whether they will cross each other's altitude bands over the duration of the interval of interest [47, 156]. However, these quantities are not always known depending on the source of the ephemerides. Furthermore, short-period perturbations can cause false negatives, i.e. the objects can cross their altitude bands when examining their osculating radii even if they were initially rejected by this filter [156]. This effect is expected to be increasingly profound as the time interval, at which the pre-filters are evaluated, is extended.

A pad, i.e. a contingency added to the conjunction threshold distance that should cover the short-period variations and evolution of the orbits during the interval of interest, can be added to reduce the number of false negatives. This approach has been investigated in-depth by Woodburn et al. [156], who examined the frequency of altitude filtering and the magnitude of the pad necessary not to miss any conjunctions. Even without pads, this pre-filter is considered safe, i.e. does not produce false negatives [1].

The orbit path filter This filter is sometimes referred to as the "geometric pre-filter" and it is supposed to eliminate the objects whose orbits never get within a specific distance threshold, irrespective of where on their orbits the objects actually are [47, 156]. This problem cannot be solved simply and hence an iterative scheme is necessary [47, 142, 156]. Furthermore, this pre-filter cannot be applied to coplanar orbits as the problem becomes ill-defined [156], so in such cases this filter should be automatically passed. This causes more objects to reach another pre-filtering stage and increases the computational time [1]. This filter works similarly to finding the minimum orbit intersection distance (MOID), which is often computed in the area of identifying close approaches between Earth and asteroids [11].

It was recommended by Hoots et al. [47] to apply this filter at the midpoint of the analysis interval and to compute the secular rate of change of the distance due to Earth oblateness [47, 156]. This rate can be used to project the orbit-to-orbit ("path-to-path") distance to the beginning and end epochs of the current time interval. Those projected values can be used together with the actually sampled orbit-to-orbit distances to see if the two objects get within a specified threshold from one another [47, 156]. This approach, however, cannot be easily performed if the rates of change are not known, which is the case with ephemerides different than TLEs.

It is also difficult to choose a large enough pad for this filter to cope with the path-to-path distance oscillations as they experience short- and long-term variations. It is possible to overcome this by applying complex logic that observes the trends in the path-to-path distance to decide whether a conjunction might take place i.e. whether the path-to-path distance might get within the threshold. However, this requires considerable computational effort and can hence outweigh the savings provided by the filter [156]. Therefore, Woodburn et al. [156] have recommended not to use the orbit path filter due to its low robustness (many false negatives) and little computational time savings.

A modification of this filter has been devised by Alfano [6], where the distance is computed w.r.t. to a torus centred on the primary's orbit. This implementation of the path filter enables it to be used with coplanar orbits but it still requires pads to be empirically set, which introduces potential false rejections caused by inappropriate pad settings.

The time filter The time filter is conceptually similar to the orbit path filter and computes the minimum distance between the objects but accounting for the position of the objects on their orbits [47]. The metric that is actually computed is the distance of the secondary object to the orbital plane of the primary, which is always greater than or equal to the actual distance between the objects [156]. Perhaps the biggest advantage of this pre-filter is that it finds the epoch intervals when the objects may conjunct, thus greatly reducing the computational time required to find the closest approaches [22, 156].

However, this filter suffers from similar disadvantages as the orbit path filter; primarily it assumes that the two orbits are not coplanar [47, 156]. Furthermore, successful application of this filter requires knowledge of variations of the relative nodal period. This period was traditionally computed using the TLE data [47, 156], but the developed conjunction detection algorithm was designed to accept any format of the ephemerides.

The robustness of this filter may be improved by implementing complex control logic that relies on computation of osculating relative nodal periods. This requires more computational time but enables the filter to be applied with fewer false rejections and still provides net computational time savings [156]. Therefore, Woodburn et al. [156] have concluded that this filter is as robust as the perigee/apogee filter,

X, Y, Z sieve Another pre-filter, the X, Y, Z sieve was developed by Healy [45] and also implemented by Alarcon Rodriguez et al. [1]. This sieve is only concerned with the components of the Cartesian positions of the objects at any given time and makes no assumptions as to the trajectories of the objects of interest. It uses an observation that if any Cartesian coordinate pair of the two objects at the beginning of a given time interval varies by more than a certain screening threshold, c, there is no chance that they could have a conjunction. For example, a potential conjunction between a pair of

objects, i and j, will be rejected using the z coordinate if

$$|z_i - z_j| > c. \tag{2.9}$$

"Smart sieve" The "smart sieve" is a set of conditions that the given pair of objects has to meet in order to potentially have a conjunction closer than some distance threshold. This set of filters was developed by Alarcon Rodriguez et al. [1]. The process of applying it is conceptually similar to using several other pre-filters in sequence but the underlying assumptions make it more robust because they make no reference to the types of orbits the objects are in.

The first two stages of the "smart sieve" are the perigee/apogee and the X, Y, Z sieves. The subsequent steps use the simplifications enabled e.g. by the observation that no Earth satellites can move with respect to each other faster than twice the surface escape velocity. The details of all the steps of this pre-filter are not included here for brevity, but they are given in section A.2.1 and in the original paper by Alarcon Rodriguez et al. [1].

2.2.1.2 Choice of the pre-filter combination

The orbit path and time filters cannot be applied to coplanar orbits. If the orbital planes of two orbits are similar, both of these filters should be passed in order not to produce false negatives. This essentially renders the filters surplus for such cases because they do not reject objects that will not have a conjunction. This can be remedied by modifying the orbit path filter [6] but doing so requires a relatively computationally expensive iterative procedure to find if the orbits of the two objects get close together.

Furthermore, these two filters perform best when rates of change of the relative nodal period and orbit-to-orbit distance can be computed, which is best achieved using the rate of change of the mean motion that is provided in TLEs [48]. As mentioned before, the exact source of ephemerides for this study was not *a priori* known, which made these two filters unattractive.

Ultimately, it has been recommended not to use the orbit path filter [156], therefore it was not implemented here. Woodburn et al. [156] also recommended modifying the classical time filter algorithm by Hoots et al. [47] in order to improve its robustness. If such modifications were made this could potentially make the filter useful for the purpose of this work. However, it would still be inapplicable to coplanar orbits and ideally require the ephemerides to be provided in TLE format. It was, therefore, decided not to include it, especially that another pre-filter set, of comparable performance, was available [1].

The "smart sieve", originally devised by Alarcon Rodriguez et al. [1], was decided upon because it makes no assumptions as to the types of orbits the objects are in. This makes the filter robust, i.e. it produces few false negatives compared with the classical pre-filters by Hoots et al. [47] ("smart sieve" performance in quantified in section A.2.3). It does not need ephemerides to be provided in a specific format and does not require special treatment for e.g. coplanar orbits. Moreover, it still offers computational time savings whilst being straightforward to implement. Therefore, this pre-filter set was investigated further to finalise the details of its implementation. The details of the investigations are described in section A.2 of the Appendix. However, the major findings that influenced the selection of the algorithm details and that could impact the results will be summarised in section 2.2.3 of this chapter.

2.2.2 Range-based detection

If all the pre-filter stages are passed, the time of the closest approach is computed by finding the epoch at which the relative range-rate between the two conjuncting objects is zero.

State vectors of the objects propagated to the endpoints of the analysis intervals, separated by a chosen ΔT, are interpolated using piecewise cubic polynomials expressed in dimensionless time domains in order to avoid singularities. This process was described in more detail in section 2.1.

2.2.2.1 Description of the relative motion

The chosen interpolation scheme, which explicitly gives the interpolating polynomials' coefficients as described in section 2.1.1, was used here to analytically express the relative range, range rate $v(t_k)$, and acceleration $a(t_k)$ between the two objects as 6^{th}, 5^{th}, and 4^{th} order polynomials, respectively.

Let the inertial Cartesian positions of the two objects that potentially have a conjunction, $r_1(t)$ and $r_2(t)$, be denoted as:

$$\begin{aligned} r_1(t) &= X_1(t)\,\hat{i} + Y_1(t)\,\hat{j} + Z_1(t)\,\hat{k}, \\ r_2(t) &= X_2(t)\,\hat{i} + Y_2(t)\,\hat{j} + Z_2(t)\,\hat{k}. \end{aligned} \tag{2.10}$$

In Eq. 2.10, $X(t)$, $Y(t)$ and $Z(t)$ are the Cartesian positions of both objects along the unit vectors of the chosen reference frame (e.g. Earth-centred, Earth-inertial) $\hat{i}$, $\hat{j}$ and $\hat{k}$. Using this notation, the relative position, $r(t)$, of the two objects can be written as:

$$\overrightarrow{r(t)} = \overrightarrow{r_2(t)} - \overrightarrow{r_1(t)} = [X_2(t) - X_1(t)]\,\hat{i} + [Y_2(t) - Y_1(t)]\,\hat{j} + [Z_2(t) - Z_1(t)]\,\hat{k}. \tag{2.11}$$

Hence the relative range can thus be computed as:

$$\overrightarrow{|r(t)|} = \left\{ [X_2(t) - X_1(t)]^2 + [Y_2(t) - Y_1(t)]^2 + [Z_2(t) - Z_1(t)]^2 \right\}^{\frac{1}{2}}. \tag{2.12}$$

The Cartesian position components of both objects are interpolated. The three polynomials interpolating the $\hat{i}$, $\hat{j}$ and $\hat{k}$ dimensions will have the same form and therefore, for the sake of brevity and clarity, the following discussion will only use the $\hat{i}$ dimension as an example. It has been decided to perform the interpolation using piecewise 3^{rd} order polynomials, but in principle any polynomial could be used. An example of how every Cartesian position component, say X, of the two objects, 1 and 2, is interpolated using a 3^{rd} order polynomial, with coefficients $A_{j,x1}$ (j is the exponent of the free parameter corresponding to a given coefficient), is given in Eq. 2.13.

$$\begin{aligned} X_1(t) &= A_{3,x1}t^3 + A_{2,x1}t^2 + A_{1,x1}t + A_{0,x1}, \\ X_2(t) &= A_{3,x2}t^3 + A_{2,x2}t^2 + A_{1,x2}t + A_{0,x2}. \end{aligned} \tag{2.13}$$

Equation 2.13 enables the relative $\hat{i}$ position from Eq. 2.11 to be written as:

$$\begin{aligned} &X_2(t) - X_1(t) = \\ &= A_{3,x2}t^3 + A_{2,x2}t^2 + A_{1,x2}t + A_{0,x2} - A_{3,x1}t^3 - A_{2,x1}t^2 - A_{1,x1}t - A_{0,x1} \equiv \\ &\equiv A_{3,x}t^3 + A_{2,x}t^2 + A_{1,x}t + A_{0,x}, \end{aligned} \tag{2.14}$$

where $A_{3,x}$, $A_{2,x}$, $A_{1,x}$, and $A_{0,x}$ have been defined as the relative interpolating coefficients that are simply equal to the difference of interpolating coefficients of the two objects.

The $\hat{i}$-component of the relative distance from Eq. 2.11 is:

$$[X_2(t) - X_1(t)]^2 = m_{x6}t^6 + m_{x5}t^5 + m_{x4}t^4 + m_{x3}t^3 + m_{x2}t^2 + m_{x1}t + m_{x0}. \tag{2.15}$$

The m coefficients in Eq. 2.15 are given by:

$$\begin{aligned} m_{x6} &= A_{3,x}^2, \\ m_{x5} &= 2A_{3,x}A_{2,x}, \\ m_{x4} &= A_{2,x}^2 + 2A_{3,x}A_{1,x}, \\ m_{x3} &= 2A_{x,3}A_{0,x}2A_{3,x}A_{1,x}, \\ m_{x2} &= A_{1,x}^2 + 2A_{2,x}A_{1,x}, \\ m_{x1} &= 2A_{1,x}A_{0,x}, \\ m_{x0} &= A_{0,x}^2. \end{aligned} \tag{2.16}$$

Equations 2.12, 2.14 and 2.16 can be combined together for all three dimensions of space. This enables a generalised relative range function to be written using the coefficients of the polynomials that interpolate positions of the objects.

Furthermore, the rate of change of the range, i.e. the relative range rate (and its first derivative, i.e. the relative acceleration), can also be written analytically using the interpolating polynomials' coefficients. In order to increase the speed of computation, squares of the relative range, range rate and acceleration were used here thus removing the need to repeatedly compute a square root of a number [156]. The squares of the relative range, $\overrightarrow{|r\left(t\right)|}$, range rate, $v\left(t\right) = \frac{d\overrightarrow{|r(t)|}}{dt}$, and acceleration, $a\left(t\right) = \frac{d^2\overrightarrow{|r(t)|}}{dt^2}$, can be written in terms of combined, 3-dimensional $\hat{i}$, $\hat{j}$ and $\hat{k}$ m-coefficients in the following manner:

$$\begin{aligned}
\overrightarrow{|r\left(t\right)|}^2 &= m_6t^6 + m_5t^5 + m_4t^4 + m_3t^3 + m_2t^2 + m_1t + m_0, \\
v\left(t\right)^2 &= \frac{d\overrightarrow{|r\left(t\right)|}^2}{dt} = 6m_6t^5 + 5m_5t^4 + 4m_4t^3 + 3m_3t^2 + 3m_2t + m_1, \\
a\left(t\right)^2 &= \frac{d^2\overrightarrow{|r\left(t\right)|}^2}{dt^2} = 30m_6t^4 + 20m_5t^3 + 12m_4t^2 + 6m_3t + 3m_2.
\end{aligned} \tag{2.17}$$

2.2.2.2 Finding the time of the closest approach

Analytical formulation of the relative range, range rate and acceleration enables the epoch of the closest approach to be found using a Newton-Raphson search [123] to find the point where the relative range rate is zero. The search is initialised in the middle of the interpolation interval and performed in the following manner [1]:

$$t_{k+1} = t_k - \frac{v(t_k)}{a(t_k)}. \tag{2.18}$$

In equation 2.18, k is the index of the current iteration in finding the root of the relative range rate. The number of iterations is limited to 1000 and the TCA convergence to 1×10^{-8} of the time step (which corresponds to 4×10^{-6} seconds for the nominal ΔT of 400 seconds). The root finding is, as conventionally adopted, terminated when the desired accuracy is reached or when the maximum number of iterations has elapsed [123].

When the relative range rate is zero, a check on the second derivative, i.e. the relative acceleration, should be performed to ensure that a minimum was found rather than a maximum. However, if a maximum were found the relative range at the TCA would be greater than the conjunction threshold distance so a range, rather than acceleration, check can be performed to verify what type of local extreme was found. Normally if roots of the relative range rate are real, which they will be when using the numerical scheme described herein, they will correspond to minima of the relative range [3].

2.2.3 Presentation of the devised conjunction detection algorithm

The "smart sieve" set of pre-filters, which increases the computational speed of conjunction detection, developed by Alarcon Rodriguez et al. [1] was adopted for the reasons given in section 2.2.1.2. However, upon testing described in section A.2.2, it was discovered that certain parts of "smart sieve" produced false negatives. It was possible to remove those with minor changes to the algorithm, namely implementing a contingency factor of 2.0 when computing the threshold radius R_{th}, given in Eq. A.1.

Certain pairs of objects are located in completely different orbital regimes, e.g. LEO and GEO, and they should not have conjunctions unless either object manoeuvres, which was ignored in this work. Therefore, it was decided to filter such pairs of objects out in the beginning of the simulation based on a fixed altitude threshold of 1000 km, which reduced the computational time needed to find the conjunctions between all the objects. It is, in theory, possible for this to have caused some conjunctions to have been erroneously filtered out. However, a situation like this is unlikely due to the large threshold that was used (half of the LEO altitude band [89]). Potentially missing certain conjunctions will be addressed when discussing the results obtained with the conjunction and detection framework.

The final modification to the original "smart sieve", which was made in this work, was adding a contingency to the perigee/apogee sieve step, which is the recommended good practice for conjunction screenings [156].

Finally, the set of prefilters that have been implemented in this work is as follows:

1. Initial perigee/apogee filter - if the perigee and apogee altitudes of the two objects in a pair are different by more than 1000 km, this pair is discarded from all the subsequent analysis steps. This was not implemented in the original "smart sieve".

2. Perigee/apogee filter - it is the most robust of the classical pre-filters developed by Hoots et al. [47] and hence has been implemented in the "smart sieve" scheme as well. In this work, it was modified by adding a pad of 50 km, which is to say that the altitude difference between primary and secondary perigee/apogee altitudes would need to be greater than the conjunction threshold distance plus 50 km for the pair of objects not to be analysed in a given analysis step. This pad setting should guarantee almost no false negatives with a conjunction screening distance of up to 20 km [2].

3. X, Y, Z sieve - this part of the "smart sieve" used the threshold radius R_{th}, given in Eq. A.1, to filter objects by their position coordinates according to Eq. 2.9. If this filter has not been passed, a number of subsequent steps are skipped as per Eq. A.2.

4. r^2 sieve - the object pairs with the square of the separation distance at the beginning of the time interval greater than the "smart sieve" threshold radius are not analysed further in a given interval.

5. Minimum distance (MD) sieve - this pre-filter rejects the secondary from further analysis in the current time interval if the square of the minimum separation distance between the two objects in a given interval is greater than the acceleration radius from the "smart sieve".

6. Fine r^2 sieve - this pre-filter is similar to the r^2 sieve but uses the actual relative velocity between the objects rather than the surface escape velocity, as well as the acceleration radius instead of the threshold radius, thus accounting for the fact that the relative motion of the objects is not rectilinear.

All the ephemerides are interpolated using piecewise cubic polynomials with interpolation nodes spaced by $\Delta T = 400\,\text{s}$ for all the objects. As described in section A.1, the accuracy of the chosen interpolation with this ΔT was 0.87 km and 1.88 km for near-circular LEO and GTO orbits, respectively. These errors are in the same order of magnitude as the errors that one would experience in orbit determination process when fitting a TLE to a truth orbit, therefore they were considered acceptable [112]. Even though the interpolation was devised such that it could work with any ephemeris type, TLE accuracy was considered a good benchmark of the accuracy of the publicly available ephemerides.

The interpolation time step is coupled to the time step at which conjunction detection is performed to simplify the software architecture. The selected time step value of 400 s is close to the optimum in terms of computational time and number of false negatives as described in section A.2.3.

Coupling both the interpolation and conjunction detection time steps is not expected to cause any difference to the results because no false negatives were observed during testing. However, this increased the computational speed of the conjunction detection framework, which is beneficial because it allows more studies to be run in less time.

2.3 Collision probability estimation

This section describes the methods available to estimate the probability of collision between two objects when their exact state vectors (positions and velocities, which define a unique orbit) are uncertain.

Other metrics can be used for conjunction risk assessment instead of the collision probability, e.g. the separation distance between the centres of mass of the objects. However, collision probability provides a workable number that can be inherently understood by anyone and accounts for the uncertainty in the state estimation and propagation as opposed to the minimum separation distance measure [4]. Therefore, it is an important metric to be used in conjunction analysis [15]. Collision probability is also often used to select targets for active debris removal as summarised in section 1.4.

The impact of individual conjunctions was of interest. Thus, only methods that apply to pairs of satellites were examined. Others P_C estimation algorithms, which give global collision probability trends or use statistical spatial densities of objects instead of having single-conjunction resolution, were discarded [60].

Once a conjunction has been identified between two objects, their state uncertainties are propagated to the time of the closest approach. Then a number of different algorithms can be applied to compute the probability that they will collide, given uncertainty in the forecasts of their states.

However, state uncertainty grows quickly under the influence of orbital mechanics [147]. This causes the true collision probabilities, $P_C|^{TRUE}$, that we can forecast to decrease the longer the prediction [4, 5]. This can be overcome by scaling and rotating the state vector uncertainty to obtain the maximum collision probability, $P_C|^{MAX}$, that a given conjunction could result in if the forecast is made closer to the TCA [4, 15]. Both $P_C|^{TRUE}$ and $P_C|^{MAX}$ were of potential interest in this study, therefore a method was sought that was able to compute the two metrics.

The algorithms that can be used to compute collision probabilities are briefly presented first. Then, the implementation and testing of one of them is described in detail.

2.3.1 Available collision probability estimation algorithms

This section describes methods that can be utilised to compute the probability of collision between two objects given the uncertainties in their positions and velocities. Three general groups of such methods have been identified and are described in turn. Those are Monte Carlo (MC), semi-analytical and fully-analytical ones.

2.3.1.1 Monte Carlo methods

Given some bounds on the uncertainty of positions and velocities, a large number of possible encounters can be generated in a computer simulation using random numbers. Then a simple collision criterion can be applied to those (if two objects' centres of mass are within a fixed distance from one another a collision takes place) to determine the fraction of the seeded conjunctions in which a collision occurred. This number can be regarded as the collision probability [106].

The main disadvantage of such a method is the computational time required to estimate the collision probability for every encounter. Even if Markov Chains are used to increase the computational speed of the Monte Carlo methods, the computational time required per conjunction remains in the order of 0.1 s per conjunction at best [106]. This rendered such an approach unfeasible in the scope of this project given the potential number of encounters to be evaluated.

This drawback is, however, partially offset by the capability of this method to cope with uncertainty on any of the input parameters (not only states but also object sizes, encounter geometries etc.). Another advantage of Monte Carlo methods is the ability to perform statistical analysis of the results, thus enabling fast assessment of the possible P_C estimation error in the form of variance of the MC sample. Finally, semi- and fully-analytical P_C estimation methods, which are presented next, make a number of simplifying assumptions. The Monte Carlo methods can be completely free of those [106].

All this makes the Monte Carlo methods ideal for the purpose of verifying other developed algorithms but impossible to apply to the large-scale simulations performed here.

2.3.1.2 Fully-analytical method

A completely analytical P_C estimation approach has been devised by Bai et al. [13]. However, this method is only accurate with respect to others presented here to within an order of magnitude.

Moreover, it requires alterations in the algorithm implementation based on the eccentricity of the objects' orbits and thus requires additional computation and conditional checks to be performed. These computational speed offsets were not expected to be significant, but an algorithm was sought that could confidently represent differences in collision probabilities of different conjunctions. Therefore, a more accurate, established and validated method was preferred.

2.3.1.3 Semi-analytical methods

Given the importance of assessing the probability of collisions between objects in orbit, several approaches have been devised that are considerably faster than direct Monte Carlo simulations yet do not suffer from very low accuracy. All these have been classified as "semi-analytical methods" here.

In semi-analytical methods, the collision probability is computed by evaluating a multivariate integral of the probability density function of the relative position of the two objects over the volume swept out by their combined hard-body area. Different methods of evaluating this integral exist, but they are typically based on projecting the position uncertainties of the two objects, in the form of a probability density function (PDF), onto the B-plane (a plane normal to the relative velocity vector at the closest approach). This PDF is then integrated inside a circle with radius equal to the sum of the radii of the two objects (collision radius). This yields the probability that the objects will be within this circle during the closest approach i.e. whether a collision will take place. In order to make the computation even faster, this integral can be approximated by a one-dimensional contour integral [119], or expressed as an infinite series of completely analytical terms [21], which makes the entire method fully analytical. [5, 15]

A different sub-set of semi-analytical methods exist that compute the overall probability based on a sum of intermediate probabilities. Those are obtained by propagating nominal and error-affected orbits of the primary and secondary vehicles and numerically integrating the probability density functions for every case [61]. This approach has not been found to yield any accuracy improvements relative to others discussed herein and is not anticipated to reduce the computational effort significantly [61]. Also, a method that can work with ephemeris tables generated with third-party tools was sought in order to enable identification of conjunctions between objects propagated with accurate numerical propagators. This meant that propagation should be excluded from P_C estimation, if possible. This set of P_C semi-analytical methods was therefore not investigated any further.

2.3.2 Algorithm choice

Two classical approaches, one fully and one semi-analytical, in which every conjunction is analysed in a B-plane frame of reference centred on the primary (arbitrarily chosen because both objects are equally important in this study) were adopted [5, 15, 21].

This makes the predictions made herein only approximate relative to the highest-fidelity methods and limits the applicability of the adopted collision probability estimation algorithms to several days [147]. However, the chosen method provides *exemplar* collision probabilities, which depend on the size of the objects, the miss distance, and the uncertainty of the states in the same fashion as when using higher-fidelity algorithms.

Therefore, the chosen algorithms return plausible collision probabilities, while reducing the computational time required for the analyses. Reducing the computational time was of prime concern in the algorithm selection, because this process was by far the most computationally intensive part of the conjunction detection and assessment. What is more, the implemented methods are widely used, and therefore verification data for them were readily available.

It was not possible to use higher-fidelity Monte Carlo methods, similar to those by e.g. Morselli et al. [106], because of the computational time they require. Finding conjunctions for one of the test objects from Table 2.1 over one year took approximately 5663 seconds, which included computing the collision probabilities using the chosen semi-analytical method. If a Monte Carlo method had been used to compute the collision probabilities for the 103 799 conjunctions, the computational time would have more than doubled (at least order of 0.1 s are needed per conjunction [106]). It was not *a priori* known how many conjunctions would be found in the debris environment and how the necessary computational time would compare to the limits imposed by the supercomputer queuing system. However, in hindsight, it would not have been possible to conduct the work described herein had a different, more computationally expensive, collision probability estimation method been chosen.

2.3.3 Method details

The used algorithm can be subdivided into several consecutive steps, each of which is briefly described in the same order as they are performed in the algorithm. All the assumptions that are made are mentioned when describing the corresponding steps, and their influence on the results is described at the end of this section.

2.3.3.1 The relative frame of reference at the conjunction epoch

The conjunctions are analysed in a B-plane, also referred to as the "encounter" or "collision" plane. This is a plane normal to the relative velocity between the two objects involved in the conjunction and centred on the primary. This is visualised in Fig. 2.1.

Any matrix C and vector A can be rotated into the B-plane given a rotation matrix R as per Eq. 2.19. These transformations are given by e.g. Berend [15].

$$\begin{aligned} C' &= RCR^T, \\ A' &= RA. \end{aligned} \tag{2.19}$$

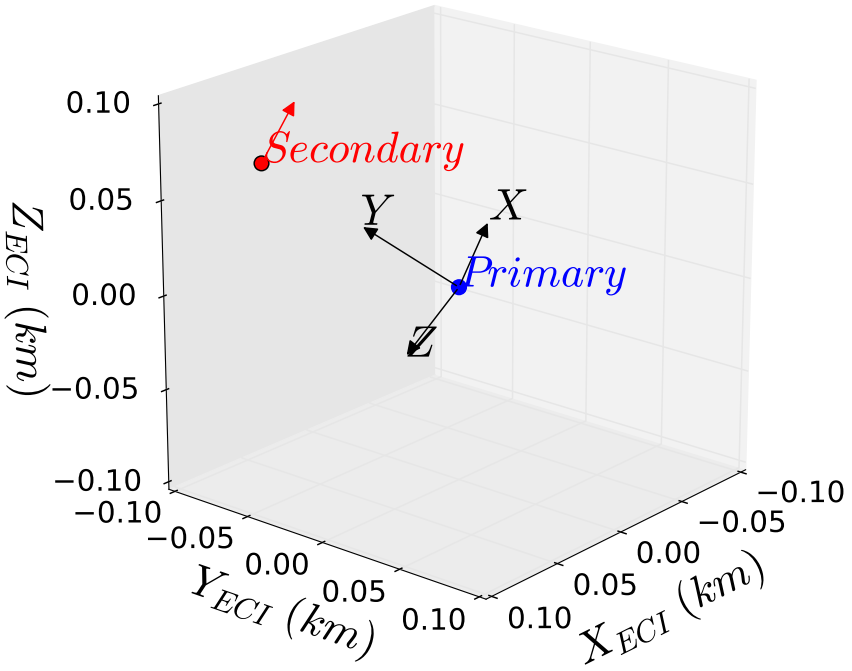

Figure 2.1: Orientation of the B-plane (y, z plane) in an inertial frame $X_{ECI}, Y_{ECI}, Z_{ECI}$. The B-plane is normal to the relative velocity of the two objects (marked with a red arrow) and centred on the primary.

The rotation matrix R, which accounts for rotation from the inertial frame (e.g. Earth-centred, Earth-inertial) to the B-plane, can be computed by taking a dot product of the unit vectors of both reference frames. An example rotation matrix that transforms between one coordinate frame, with unit vectors $[i_1\ j_1\ k_1]$, and another, with unit vectors $[i_2\ j_2\ k_2]$, is given in Eq. 2.20 [151, 155].

$$R_{1to2} = \begin{bmatrix} i_2 \cdot i_1 & i_2 \cdot j_1 & i_2 \cdot k_1 \\ j_2 \cdot i_1 & j_2 \cdot j_1 & j_2 \cdot k_1 \\ k_2 \cdot i_1 & k_2 \cdot j_1 & k_2 \cdot k_1 \end{bmatrix}. \tag{2.20}$$

Whenever a conjunction is identified, the state uncertainties of both objects, in the form of covariance matrices, are rotated to a common inertial reference frame from the ones in which they are known (typically radial, in-track, cross-track, or RIC, frame). They are subsequently rotated into the B-plane reference frame according to Eq. 2.19. This assumes zero-mean normal distribution of the position uncertainty so that it can be described by a covariance matrix.

By assuming that the uncertainties on the states of both objects are uncorrelated, they can be added to yield a covariance matrix of the relative position [5, 15, 21, 106]. This is not necessarily always true but it is highly unlikely that the same set of sensors was used in similar conditions to perform observations of the two objects and so that the errors are correlated. It is therefore a common assumption to make in all semi-analytical P_C estimation algorithms [5].

Next, rectilinear relative motion and time-invariant position uncertainties are assumed in the vicinity of the time of the closest approach (TCA), thus allowing the covariance matrix to be projected onto the B-plane and reduce the number of dimensions of the problem from three to two [15, 21]. The rectilinear relative motion assumption is not always true - it breaks down when the relative velocity between the objects is low. However, analyses by McKinley [96] showed that even for relative velocities as low as $0.013\,km\ s^{-1}$, the rectilinear relative motion assumption resulted in collision probability estimates to be in the same order of magnitude as when this assumption was relieved. Frigm and Rohrbaugh [38] found that rectilinear relative motion assumption held in over 99% cases for both LEO and GEO satellites that they analysed. Thus, this assumption did not affect most of the conjunctions analysed here.

The above P_C estimation method makes a number of simplifying assumptions to reduce its computational time. However, it was used to investigate the impact of individual conjunctions on the final accumulated collision probability. Therefore, such assumptions were acceptable because they would not change the fact that certain events would have much higher P_C than others, and such events would be as rare when using the adopted algorithms as when using the highest-fidelity methods. This is because the state uncertainty had to be small, the miss distance low and the objects large for the P_C to be high.

2.3.3.2 Formulation of the collision probability

Having projected the relative position's covariance matrix, C, onto the B-plane a probability density function of the relative position can be formulated. This is achieved by ignoring the velocity covariance because it has been found not to affect the collision probability significantly [15]. It was also confirmed by Monte Carlo analyses of several exemplar conjunctions conducted while devising the algorithms described here. The probability density function of relative position for an exemplar conjunction is shown in Fig. 2.2.

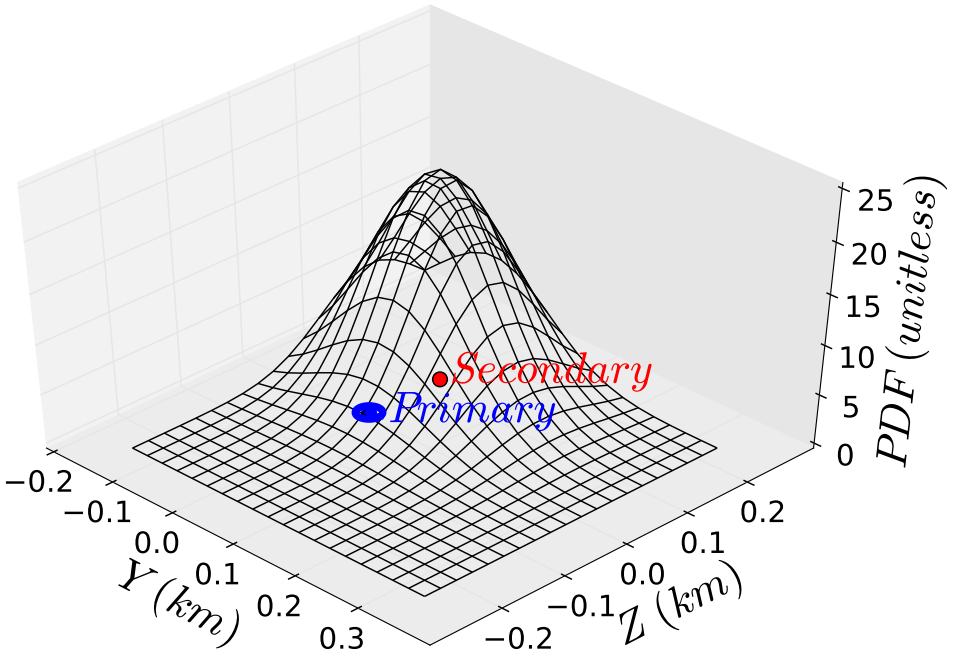

Figure 2.2: Probability density function (PDF) of the relative position centred on the secondary, plotted in the B-plane (y, z plane). The PDF is integrated over the circle with radius equal to the combined radii of both objects (collision radius r) centred on the primary to compute P_C.

The PDF of the relative position, here expressed in Cartesian coordinates in the B-plane (y, z), can be integrated inside a circle with radius equal to the combined radii of the two objects (collision radius r) and centred on the primary as given in [15, 21]:

$$P_C = \int_{-r}^{+r} \int_{-\sqrt{(r^2+z^2)}}^{+\sqrt{(r^2+z^2)}} \frac{2\pi}{\det(C)} e^{\frac{-1}{2} D^T C^{-1} D} \, dydz. \tag{2.21}$$

In equation 2.21 det denotes the determinant of the matrix and D is the discrepancy vector defined as:

$$D = \begin{bmatrix} y \\ z \end{bmatrix} - p_{mean}, \tag{2.22}$$

where y and z are instantaneous values of the Cartesian in-plane relative position and p_{mean} is the mean value of the relative position at the TCA projected onto the B-plane.

Integrating Eq. 2.21 yields the probability that the objects' centres of mass will be within the collision radius at the TCA, i.e. the probability that they will collide. This definition of collision probability ignores the attitude of the objects - they are assumed to be spherical and therefore the collision radius is not a function of attitude. This is, of course, inaccurate. It does not, however, change the fact that the collision probabilities found for every object scale with other significant parameters, e.g. the miss distance, and thus a large spread in the collision probabilities was expected.

2.3.3.3 Computing the collision probability

There exist multiple ways of integrating Eq. 2.21 to yield the P_C. Those are well presented in [106], but they all are conceptually similar and make almost the same assumptions; therefore only two were investigated here for simplicity since they should all provide the same result, i.e. the integral from Eq. 2.21.

Direct numerical integration Direct numerical integration of Eq. 2.21 can be performed to yield collision probability. This technique will be hereafter referred to as "direct integration".

The numerical integration is performed here by using a two-dimensional Simpson's rule [123] in the y, z Cartesian coordinates of the B-plane. This involves computing integrals along the y-direction by using evaluations of the relative position probability density function, PDF_i, spaced by h_y, as per Eq. 2.23.

$$Y = \frac{1}{3}h_y[PDF_0 + 4\left(PDF_1 + PDF_3 + \ldots + PDF_{2n-1}\right) + \\ + 2\left(PDF_2 + PDF_4 + \ldots + PDF_{2n-2}\right) + PDF_{2n}] + T_y. \quad (2.23)$$

The Y integrals, obtained via Simpson's rule, are themselves embedded in a Simpson's rule that integrates along the z-direction to yield the collision probability P_C, as shown in Eq. 2.24.

$$P_C = \frac{1}{3}h_z\left[Y_0 + 4\left(Y_1 + Y_3 + \ldots + Y_{2n-1}\right) + 2\left(Y_2 + Y_4 + \ldots + Y_{2n-2}\right) + Y_2 n\right] + T_z. \quad (2.24)$$

The same number of function evaluations, $2n$, is used when performing both integrations. This means that the step h_z is constant but h_y has to be recomputed every time a new Y is evaluated. The truncation errors, T_y and T_z accumulate, but the number of function evaluations can be increased to reduce them.

Series expansion of the integral The integral in Eq. 2.21 has been approximated as a line integral by Alfano [5] and an infinite series of fully analytical terms by Chan [21]. Both approaches are expected to yield the same accuracy and require similar computational time. The latter one was decided upon because, even if the infinite series is truncated after the first term, it has been shown to be accurate to within 1% [21]. This was desirable because truncating the infinite series after so few terms could reduce the net computational time. The following algorithm was adopted from work by Chan [21].

In order to express the PDF in Eq. 2.21 as a series of terms, the covariance matrix C, with components from Eq. 2.25, which has been projected onto the B-plane, has to be rotated into its principal axes. This is done to remove the correlation coefficient ρ_{yz} and produce a diagonalised covariance matrix C' with standard deviations of position, σ'_{yy} and σ'_{zz} on the diagonal as per Eq. 2.26.

$$C = \begin{bmatrix} \sigma_{yy}^2 & \rho_{yz} \\ \rho_{yz} & \sigma_{zz}^2 \end{bmatrix}, \tag{2.25}$$

$$C' = \begin{bmatrix} \sigma_{yy}'^2 & 0 \\ 0 & \sigma_{zz}'^2 \end{bmatrix}. \tag{2.26}$$

After diagonalisation of the covariance matrix into the form from Eq. 2.26, the relative in-plane position of the two objects has to be rotated into the principal axes as well. This can be done by rotating it by an angle θ that can be computed according to Eq. 2.27. The relative position expressed in the principal axes has the form $p'_{mean} = \left[Y'_p,\ Z'_p\right]^T$.

$$\theta = tan^{-1}\left(\frac{2\rho_{yz}\sigma_{yy}\sigma_{zz}}{\sigma_{yy}^2 - \sigma_{zz}^2}\right). \tag{2.27}$$

All the above transformations enable two dimensionless variables, u and v given in Eq. 2.28, to be introduced,

$$\begin{aligned} u =& \frac{r^2}{\sigma'_{yy}\sigma'_{zz}}, \\ v =& |p_{mean}|^2 \frac{1 + \left(\frac{\sigma_{zz}'^2}{\sigma'_{yy}} - 1\right)\left(\frac{Y_p'^2}{Y_p'^2 + Z_p'^2}\right)}{\sigma_{zz}'^2}. \end{aligned} \tag{2.28}$$

Using Eq. 2.28, the collision probability from Eq. 2.21 can thus be rewritten as:

$$P_C = e^{\frac{-v}{2}} \sum_{m=0}^{N} \left[\frac{v^m}{2^m m!}\left(1 - e^{\frac{-u}{2}} \sum_{k=0}^{m} \frac{u^k}{2^k k!}\right)\right] + T_N, \tag{2.29}$$

where T_N is the truncation error corresponding to truncating the infinite sum after the first N terms.

2.3.3.4 Computing the maximum collision probability

The maximum collision probability is found by scaling the covariance matrix C by a scaling factor, k. The latter can be found analytically as in Eq. 2.30 by assuming that the collision probability takes its peak value when the relative position's probability density function does (as given by e.g. Berend [15]),

$$k = \sqrt{\frac{p_{mean}^T C^{-1} p_{mean}}{2}}. \tag{2.30}$$

The covariance is scaled by multiplying it by k^2 as per Eq. 2.31.

$$C_{P_C|^{MAX}} = k^2 C. \tag{2.31}$$

Once the covariance has been scaled, any method can be used to calculate the associated maximum collision probability.

The uncertainty ellipsoids can also be rotated to provide absolute maximum collision probability for a given conjunction [4], but in this work maximum collision probability was only used to remove the time dependence from the problem. The maximum collision probability is largely time-invariant as it is not affected by the growth of the covariance. The maximum probability is a means to highlight the events that are likely to have a high P_C if the predictions are conducted with more certain state information, that is to say if the predictions are made with ephemerides obtained closer to the TCA.

2.3.4 Final algorithm presentation

The direct numerical integration and series expansion P_C estimation algorithms were tested and verified as described in section A.3. Six test cases, which investigate the extreme shapes of the covariance matrices projected on the B-plane, were chosen. This guaranteed that any conjunction would result in an intermediate geometry bound by two of the test cases.

It was found in section A.3.2 that $2n = 5000$ integration intervals gave the most accurate results for all the tested geometries compared to the Monte Carlo P_C estimation. Thus, this value was used in the direct numerical integration of the PDF of relative position in Equations 2.23 and 2.24. Furthermore, it was discovered in section A.3.3 that 50 terms in Eq. 2.29 correctly modelled the dependence of the collision probability on the conjunction details but only for collision probabilities less than 1.0. It was not possible to increase the number of terms further to improve the precision of the algorithm for

P_C close to 1.0 due to floating point accuracy. It was therefore decided to use a mixed approach, where the series expansion algorithm with 50 terms is used for conjunctions where the combined radius of the objects is less than 80% of the miss distance, and direct numerical integration with $2n = 5000$ elsewhere. Such a mixed approach was not proposed by Chan [21], and therefore is novel.

During the verification process, which compared the collision probabilities obtained using direct numerical integration and series expansion approaches to Monte Carlo estimates, it was verified that both developed approaches agreed to within 1% for most cases. Discrepancies were only present for collision probabilities less than 1×10^{-4} where the truncation error in the series approach caused the estimated collision probability to be up to two orders of magnitude higher than the Monte Carlo and direct integration results. This could cause the importance of the high P_C conjunctions to be underestimated, but conjunctions with low miss distances, and thus high P_C, will be evaluated using direct numerical integration, i.e. the more accurate method. Therefore, the collision probability estimation algorithms were deemed verified.

Finding the maximum collision probability was also investigated. It was decided to employ a golden ratio search [123] to refine the analytical estimate of the covariance scaling factor, which yields the maximum collision probability, from Eq. 2.30. This is because this analytical estimate could lead to the importance of particular events with extremely high $P_C|^{MAX}$ being underestimated ($P_C|^{MAX} = 1.0$ cannot be reached with it). This investigation is described in more detail in section A.3.5.

The final collision probability estimation algorithm and its main assumptions are:

1. Covariance matrices of both objects involved in a conjunction are propagated to the time of the closest approach. This assumes that the uncertainty of both objects is a zero-mean, normal distribution and hence can be described by a covariance matrix.

2. Covariance matrices are rotated into the B-plane of the conjunction and projected onto it. This assumes rectilinear relative motion and constant uncertainty throughout the conjunction.

3. The covariance matrices are added and a probability density function of the relative position is formulated from them. This assumes that the state uncertainties of both objects are uncorrelated and ignores the velocity uncertainty.

4. If the combined collision radius r is less than 80% of the miss distance (computed by assuming rectilinear relative motion), a series expansion algorithm with 50 terms is used to integrate the PDF inside a circle with collision radius; otherwise a double Simpson's rule with 5000 evaluations is used. This ignores the attitude of the objects.

5. Maximum collision probability is computed by scaling the combined covariance matrix to yield the highest collision probability. This assumes that the highest collision probability will take place at the TCA, which ignores the attitude of the objects. Also, the covariance matrices are not rotated to yield even higher $P_C|^{MAX}$ because the scaling is only performed to remove the growth of the uncertainties over time. If $r < 80\%$ of the miss distance, an analytical estimate of k from Eq. 2.30 is used. Elsewhere, the estimate is refined by a golden ratio search to enable $P_C|^{MAX}$ to reach 1.0.

2.3.5 Combining collision probabilities from multiple conjunctions

Multiple conjunctions are expected to occur for Earth-orbiting objects throughout their orbital lifetimes. This raises the need to combine the collision probability from multiple encounters to produce an overall figure for the total collision probability that has been accumulated over time.

The task of combining individual collision probabilities is not trivial because all the computed collision probabilities are located in their own sample spaces (the probability of a single collision and no collision sums to 1.0) [25]. In order for these to be combined into a meaningful figure, which can be analysed using standard statistical methods, the accumulated probability of any collision and its complement (resulting probability of no collision) should also be equal to 1.0 as required by the second axiom of probability [25].

An analogy to a simple situation of making repeated tosses of a "fair coin" was identified. A tree diagram illustrating this series of events and their probabilities is shown in Fig. 2.3. By assuming that the outcome of every toss is independent of the others, the probabilities of every potential outcome of the series of tosses can be computed by multiplying the individual probabilities of each toss' outcome by using the multiplication rule (which, in this case is 50% because a fair coin is assumed) [25].

The above reasoning can be applied to a series of conjunctions with the only difference being that once a collision has occurred, no further conjunctions may take place (catastrophic collisions only are assumed). This simplifies the tree diagram because any node has only one branch that is not terminated. This does not change the fact that the conjunctions are statistically independent, which is to say that the collision probability and the outcome of one do not affect others. If the objects do collide any subsequent conjunctions cannot take place, but this was accounted for when formulating the problem. If a collision does not take place, subsequent conjunctions may have higher collision probability because, for example, the objects might be getting closer. This is caused by astrodynamics and not the statistical treatment of the problem, however. An illustration of a series of such events is shown in Fig. 2.4.

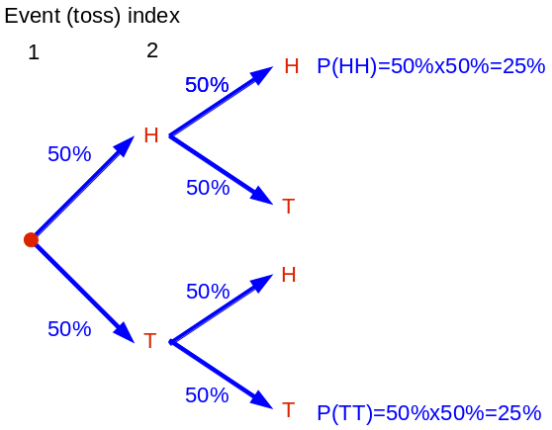

Figure 2.3: Tree diagram showing the probability of obtaining two heads (H) or two tails (T) in two tosses of a fair coin.

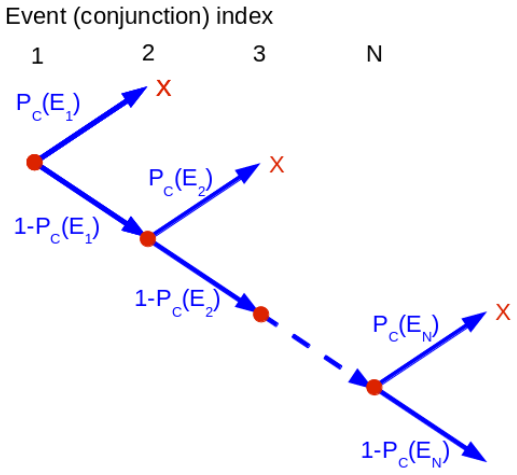

Figure 2.4: Tree diagram analogous to that from Fig. 2.3 used to derive the formula to compute the probability of any out of a number of conjunctions resulting in a collision. All collisions are assumed to be catastrophic - whenever a collision takes place, the tree branch terminates.

By the multiplication rule [25], the cumulative collision probability for N conjunctions E_i, each with collision probability $P_C(E_i)$, was computed as the complement of the probability that no collision will occur as stated in Eq. 2.32.

$$P_C(\text{any out of N}) = 1 - P_C\left(\bigcap_{i=1}^{N} \neg E_i\right) = 1 - \prod_{i=1}^{N}(1 - P_C(E_i)). \tag{2.32}$$

2.4 Public catalogue covariance estimation and propagation

Computing the collision probability for every conjunction requires the uncertainties of the ephemerides of both objects to be known at the time of the closest approach. Given the type of ephemerides used in this study, it was not possible to compute the actual collision probabilities of all the conjunctions because TLEs are not supplied with uncertainty information. Nonetheless, it was considered insightful to compute a figure that would be representative of the true collision probability to investigate the impact of the reducing orbit prediction accuracy the further ahead these predictions are made.

The lack of TLE covariance can be overcome e.g. by computing the collision probabilities using objects' spatial densities [27] or estimating TLE uncertainty [36]. However, only estimating TLE uncertainty allowed individual conjunctions to be resolved. Moreover, such an approach enabled realistic aspect ratios of the uncertainty ellipsoids to be used [15], meaning that the impact of the alignment of the ellipsoids, dictated by the conjunction geometry, would be similar to what would be obtained using other ephemerides. Therefore, this approach was adopted here.

A method to estimate the covariance of a TLE based on previous TLEs for the same object was developed by Osweiler [114] and implemented in this work. All the historical TLEs of a given object, spanning the period of 14 days from the epoch of the TLE used for conjunction detection, are gathered and the position residuals are computed with respect to that most-recent TLE for every object. The covariance matrix is then computed from these residuals by treating them as state observations and assigning all of them equal weight [114]. If fewer than five TLEs are available for a given object, it is discarded from the analysis entirely as covariance estimated with so few observations would be contrived.

Moreover, certain TLEs have to be ignored in case they are erroneous or a manoeuvre was conducted by the spacecraft in the 14-day time window. In order to do this, specific orbital energies of all the TLEs from the two-week window for a given object are analysed and the TLEs whose energies are more than three standard deviations above the average are rejected [121].

Such derivation of the TLE covariance can be used readily to propagate the covariance to any epoch - it suffices to propagate all the TLEs for the given object to the specified epoch and re-compute the covariance. This allows collision probability to be computed using this covariance at the TCA, which reflects the capability to predict a given collision with TLEs. This covariance propagation does not account for uncertainty in modelling of the

atmospheric drag or solar radiation pressure. Including these uncertainties would require a computationally-intensive process of propagating the covariance [30], which would make the large-scale simulations envisioned here unfeasible in therms of computational time. The effect of neglecting such uncertainties is covered by discussion related to incorrectly calculating the collision probabilities for individual conjunctions.

Given that the covariances are only estimates of the actual state uncertainty at the TCA, the P_C computed with them cannot be referred to as the actual collision probability and its sole purpose is to examine the evolution of the data accuracy with time. It is, however, henceforth referred to as the true collision probability because it expresses the collision probability that can be forecast using the adopted set of assumptions. Maximum collision probability can also by computed from these estimated covariances by scaling the matrices according to Eq. 2.31.

The implemented TLE covariance estimation algorithm was verified, which is presented in section A.4 of the Appendix and the work by Lidtke et al. [83]. It was shown that the implementation of the TLE covariance estimation agrees, at worst, to within an order of magnitude with the original work by Osweiler [114]. Such poor precision was caused by the fact that no complete TLE set and corresponding covariance is given by Osweiler [114] to enable comparison. The implemented algorithms were also compared to TLE uncertainties estimated by Krag et al. [63] for 18 objects spanning the eccentricity-inclination-perigee altitude space. Those reference data were obtained by performing orbit determination on TLEs, numerically propagating the fitted orbit, and comparing the TLEs to this numerical propagation; this process is detailed in the work by Flohrer et al. [36]. Typically, the standard deviations of position estimated here were in the same order of magnitude as those obtained by Flohrer et al. [36], except for the in-track direction. This is because the TLEs, from which the covariance was estimated, are dispersed in this direction due to Keplerian dynamics [148, 149] and the simplifications made when modelling atmospheric drag in the SGP4 theory [29, 57]. The uncertainties obtained by Flohrer et al. [36] quantified the difference between TLEs and reality, while this work focused on the variability between the TLE sets themselves and evolution of the position uncertainty with time. Thus, an agreement to within an order of magnitude was deemed sufficient, especially that the behaviour exhibited by the estimated TLE covariances agrees with the expected qualitative behaviour. This is to say the position uncertainty depends on the altitude of the object, eccentricity of its orbit, position along the orbit etc. Estimated covariances for the mentioned 18 test cases are presented in Table 2.3.

Table 2.3: Estimated TLE position standard deviations in kilometres for the used test cases from Flohrer et al. [36]. Components of the matrices are computed in the radial, in-track, cross-track (RIC) reference frame.

$e \leq 0.1$

	$\mathbf{h_P \leq 800\,km}$			$\mathbf{800 < h_P \leq 25000\,km}$			$\mathbf{25000\,km < h_P}$		
	$i \leq 30°$	$30° < i \leq 60°$	$60° < i$	$i \leq 30°$	$30° < i \leq 60°$	$60° < i$	$i \leq 30°$	$30° < i \leq 60°$	$60° < i$
R	2.0E-1	1.3E0	2.8E-1	8.4E-2	3.3E-1	1.4E-1	7.9E-1	7.9E-1	7.9E-1
I	6.0E-1	1.2E+2	2.2E0	1.9E0	1.0E+1	2.7E0	2.7E0	2.7E0	2.7E0
C	4.7E-1	1.6E0	5.2E-1	7.3E-1	1.1E0	1.1E-1	3.3E-1	3.3E-1	3.3E-1

$0.1 < e$

	$\mathbf{h_P \leq 800\,km}$			$\mathbf{800 < h_P \leq 25000\,km}$			$\mathbf{25000\,km < h_P}$		
	$i \leq 30°$	$30° < i \leq 60°$	$60° < i$	$i \leq 30°$	$30° < i \leq 60°$	$60° < i$	$i \leq 30°$	$30° < i \leq 60°$	$60° < i$
R	1.8E0	1.4E+1	7.8E0	8.1E0	3.0E0	7.1E+1	3.1E0	3.1E0	3.1E0
I	3.7E+1	3.3E+1	2.0E+1	1.0E+1	5.1E0	7.7E+1	4.3E+1	4.3E+1	4.3E+1
C	3.6E-1	2.5E0	1.3E0	1.1E0	2.2E0	7.7E0	4.2E-1	4.2E-1	4.2E-1

2.5 Final conjunction detection and assessment algorithm

The algorithm that was eventually implemented to find conjunctions between objects in orbit and compute their collision probabilities is briefly described and verified in this section.

2.5.1 Presentation of the algorithm

The algorithm that identifies conjunctions between objects in orbit was implemented in C++ in order to allow many studies to be performed in a relatively short time. The simulation framework was kept cross-platform to allow the simulations to be performed on machines running Windows as well as Linux operating systems, most importantly the Iridis 4 High-Performance Computing cluster at the University of Southampton. The C++ code is wrapped in Python, which handles distributed memory parallelisation implemented in Open MPI. Whenever conjunctions are to be found for a given set of TLEs between two epochs, the simulation period is split into a user-specified number of sub-periods that are analysed in parallel.

A block diagram of the implemented simulation functional flow is shown in Fig. 2.5. The objects are propagated using two-line element sets and a freeware implementation of the SGP4 propagator [56]. The ephemerides are interpolated according to the algorithm laid out in section 2.1, and the conjunctions between the objects are found using a Newton-Raphson root finding method to identify times when the relative range rate between a given pair objects is zero. This is repeated for all the possible object pairs in order to find all the conjunctions taking place between a given set of objects. The computational time required for finding conjunctions is reduced by using the modified "smart sieve" pre-filter set. Section 2.2 gives details regarding this process.

When objects' centres of mass are within a given threshold distance, the collision probability is computed using the algorithms described in section 2.3. In order to compute the collision probability, uncertainty of the position has to be known at the time of the closest approach. The ephemerides used in this study are not supplied with such information, therefore orbit uncertainty for every object has to be estimated at the TCA epoch following the algorithm summarised in section 2.4.

The final step is to record all the information about the conjunctions that have been found. Objects that re-entered Earth's atmosphere and their possible erroneous conjunctions, which took place after the decay epoch, are filtered out during post-processing.

2.5.2 Verification

The final implementation of the conjunction detection and assessment algorithm was verified by comparing the conjunctions for the two test cases from Table 2.1 to the same data obtained using the algorithm by Patera [120] implemented in the Conjunction Analysis Tools (CAT) that is a part of AGI's STK. Several other algorithms implemented in STK CAT were tested but they all share similar fundamental assumptions and produced essentially identical results. The absolute difference between the P_C of any conjunction found using the approach by Patera [120] and other STK CAT algorithms was at most 10^{-7}% and 10^{-18}% for Envisat and Delta 1 R/B test cases, respectively.

In order to enable this comparison, fixed covariance matrices had to be used for all the objects because STK does not implement any algorithm that could be used to estimate uncertainty of the TLEs. Moreover, one year long simulations were decided upon in order to provide a large set of conjunction geometries. True uncertainty of the orbit would increase by many orders of magnitude over such a period, thus making it impossible to record collision probabilities as double precision floating point numbers. Specifically, time-invariant 1.0 km position standard deviations in the RIC reference frame were decided upon. This is because STK computes maximum collision probability by rotating the covariance matrices, which is different than the approach adopted herein;

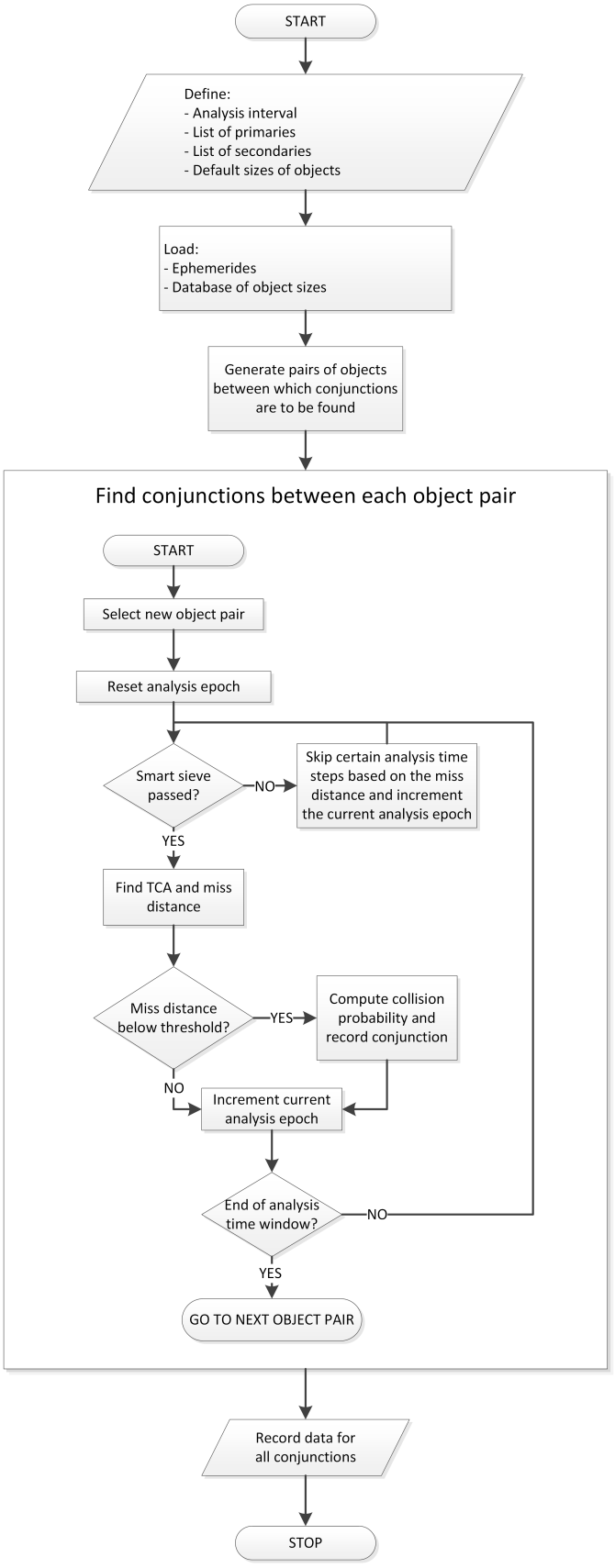

Figure 2.5: Block diagram of the developed conjunction detection and assessment framework.

only a unity aspect ratio of the uncertainty ellipsoids makes the two $P_C|^{MAX}$ estimation approaches produce the same results. A database of physical radii of objects, supplied with STK, was used to compute the collision radii for the conjunctions. If an object was not present in the database, it was assumed to have a radius of 5 m, which is the default value in STK CAT.

Maximum and true (computed using the unscaled covariance matrices) collision probabilities accumulated by Envisat, resulting from conjunctions closer than 20 km it experienced between 23 Oct 2013 (epoch of its TLE) and 23 Oct 2014 against the entire public TLE catalogue [135], are shown in Fig. 2.6a and 2.6b, respectively. The same data obtained in the same time interval but for the Delta 1 R/B are shown in Fig. 2.7a and 2.7b for $P_C|^{MAX}$ and $P_C|^{TRUE}$, respectively. Collision probabilities obtained using both direct numerical integration of Eq. 2.21 as well as using the series expansion of the integral are presented in all cases.

Totals of 19 311 and 38 conjunctions were recorded for Envisat and Delta 1, respectively. The corresponding errors in the final accumulated collision probability, relative to STK, in computing $P_C|^{MAX}$ with direct numerical integration were 4.6% and 28.3%. The relative errors for $P_C|^{TRUE}$ were 4.9% and 43.5%. Similar errors were observed for the series expansion algorithm where the errors relative to STK in the final $P_C|^{MAX}$ were 5.3% and 30.6%, and 4.8% and 47.8% for $P_C|^{TRUE}$ of Envisat and Delta 1, respectively.

The biggest contribution to these differences were different state vectors returned by the SGP4 propagator implemented in STK and in this work with the same TLEs at the same epochs. Different state vectors resulted in different conjunction geometries and hence also collision probabilities. This is particularly visible for Delta 1 because it experienced fewer conjunctions than Envisat and hence discrepancies in estimating P_C of individual conjunctions had more influence on the final accumulated collision probability. Because STK's source code is proprietary, it was impossible to investigate the exact origin of these differences. Even though this would be an issue from an operations point of view, it sufficed for the purposes of this work because all of the objects were studied using the same propagator.

The different collision probabilities of individual events, caused by different miss distances, are evident in Fig. 2.6a when noting that the algorithms used here found several conjunctions with high $P_C|^{MAX}$ for Envisat that were not present in STK and *vice versa*. These high collision probability events correspond to large instantaneous changes in the accumulated $P_C|^{MAX}$, e.g. in mid February and end of April in the STK dataset.

It was attempted to refine the conjunction details, mainly the miss distance, by performing interpolation with higher precision around the originally found time of the closest approach. When a conjunction was detected, additional points were seeded around the TCA that was found in the initial coarse search, spaced by one tenth of the original interpolation interval, i.e. 40 seconds for a 400 s time step. This changed the final collision probability accumulated by Envisat by 1.1% while the computational time increased by 0.8%. It was decided not to include the refinement algorithm in the final code because the discrepancies were caused by differences in the implementations of the SGP4 itself, not the conjunction detection or P_C estimation algorithms.

Despite the differences w.r.t. STK, the developed conjunction detection and assessment framework can be regarded as verified. Both STK CAT and the framework developed here make similar simplifying assumptions, which could be relieved to increase accuracy [106]. This was discussed when choosing the P_C estimation algorithm, however, and it was argued that higher-fidelity algorithms would require unfeasible amounts of computational time. Also, the adopted P_C estimation algorithms were compared to a Monte Carlo method in section A.3 and agreement to within 1% was found in most cases. Therefore, the developed conjunction detection and assessment framework was deemed sufficiently accurate because the collision probabilities it identified were in the same order of magnitude as the reference data, which is regarded sufficient for P_C estimates [13].

The collision probability of the conjunctions computed here scaled with the miss distance, object size, and magnitude and orientation of the uncertainties on the objects' states. The higher the P_C, the fewer conjunctions would be able to reach it when using the developed framework, which would also be the case for the highest-fidelity methods. Therefore, conjunctions with extremely high P_C were as infrequent when using the adopted method as when using higher-fidelity algorithms. The identified collision probabilities or even entire conjunctions may not have been exactly the same as those that could be found using the highest accuracy data and algorithms for the same time period. However, the found sets of collision probabilities were examples of what *could* take place.

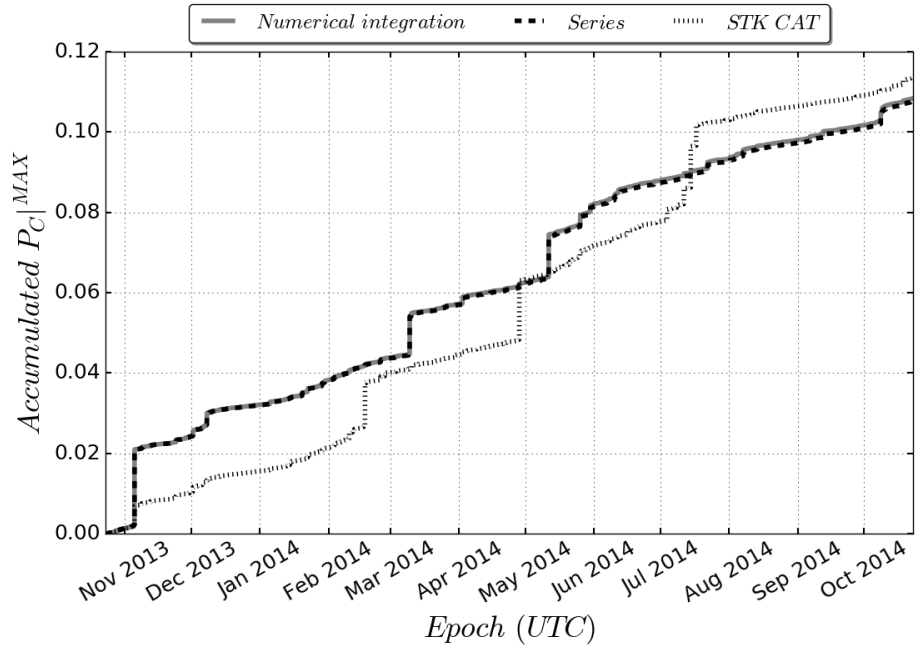

(a) $P_C|^{MAX}$

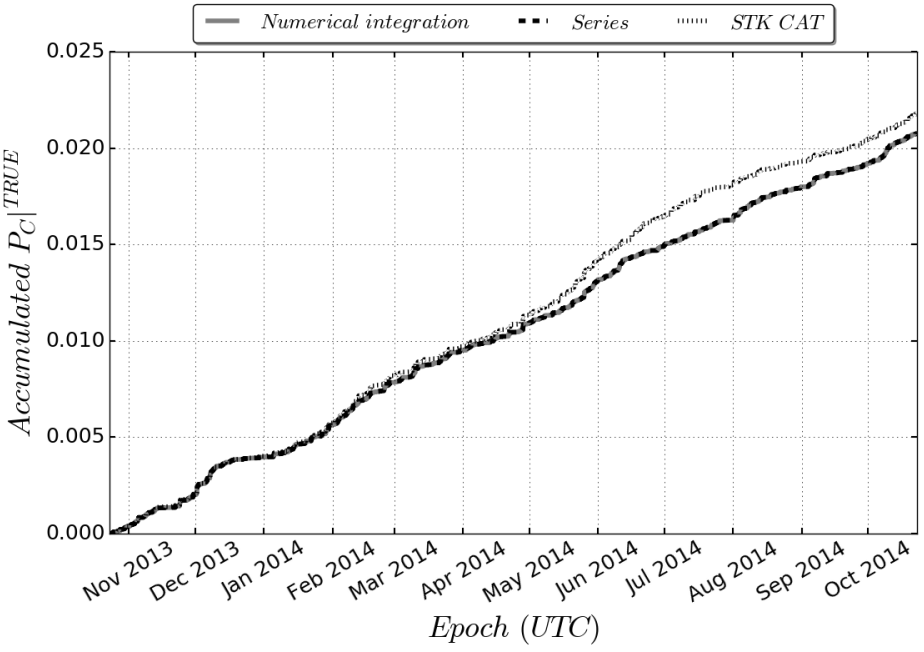

(b) $P_C|^{TRUE}$

Figure 2.6: Accumulated maximum and true collision probabilities of Envisat test case from Table 2.1 computed using series expansion and numerical integration of equation 2.21, together with reference results generated with STK CAT. Using time-invariant, 1 km position standard deviations for the entire duration of the simulation to enable comparison between the two algorithms. 5.0 m radius assumed for the objects not present in the radii database. Conjunctions closer than 20.0 km found using the public TLE catalogue snapshot from 23 Oct 2013 over one year.

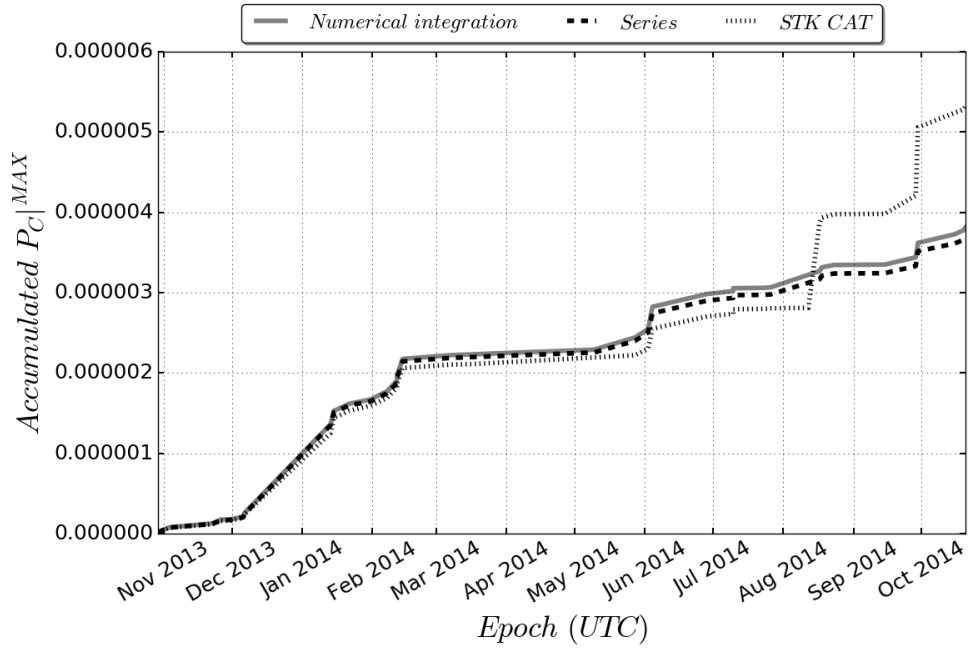

(a) $P_C|^{MAX}$

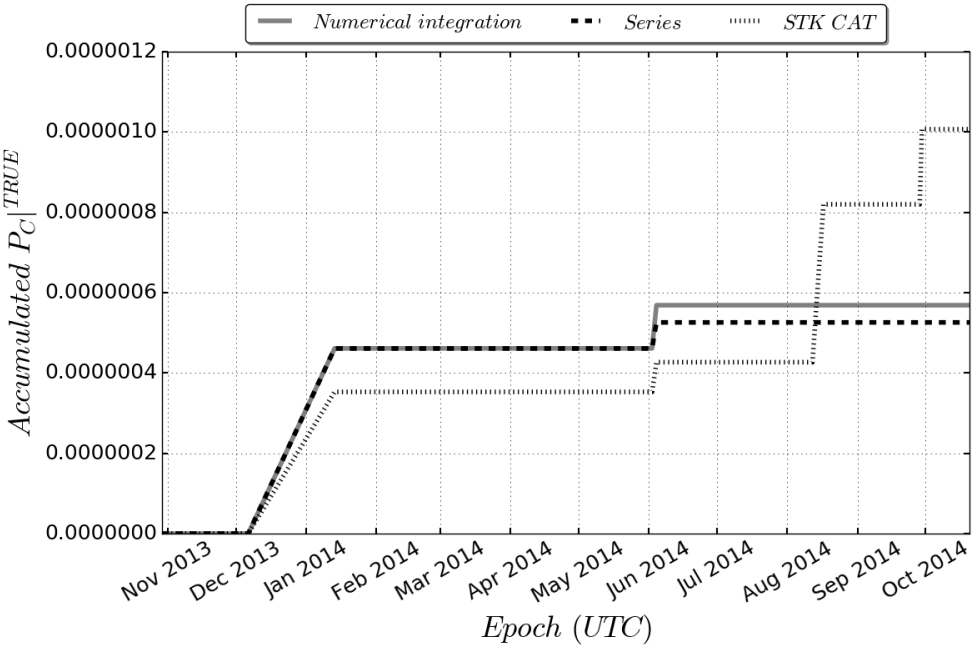

(b) $P_C|^{TRUE}$

Figure 2.7: Accumulated maximum and true collision probabilities of Delta 1 R/B (SSC 00862) test case from Table 2.1 computed using series expansion and numerical integration of equation 2.21 together with reference results generated with STK CAT. Using time-invariant, 1 km position standard deviations for the entire duration of the simulation to enable comparison between the two algorithms. 5.0 m radius assumed for the objects not present in the radii database. Conjunctions closer than 20.0 km found using the public TLE catalogue snapshot from 23 Oct 2013 over one year.

Chapter 3

Impact of Individual Conjunctions

This chapter fulfils research objectives number 1, 2, 3 and 4 from section 1.6.

First, addressing objectives 1, 2 and 3 is described. To this end, the conjunction detection and assessment algorithms, described in Chapter 2, were used to analyse the impact of particular conjunctions with high collision probabilities on the collision probability accumulated by individual objects, relative to all other events. The impact of such conjunctions on the probability of any collision occurring in the entire debris environment was also examined. The aim of this particular study was to investigate why "statistical ADR target selection" described in section 1.4, or removal of objects that are likely to be involved in collisions with high severity, might not prevent sufficiently many collisions to halt the increase of the number of objects in the debris environment.

Next, fulfilling the research objective number 4 is described. This was addressed by analysing results from DAMAGE to show that close approaches with high collision probabilities take place in evolutionary debris models, e.g. DAMAGE introduced in section 1.3.1, and hence can lead to incorrect objects being selected for active debris removal. Furthermore, the hypothesis that high-P_C close approaches cause more collisions than other events was verified.

3.1 Fine spatial and temporal resolutions investigation

3.1.1 Study description

The set of algorithms that identify conjunctions between objects in orbit and compute the collision probabilities for them, which was described in Chapter 2, was used on a number of snapshots of the public catalogue of two-line element sets. Each snapshot contained all the objects whose ephemerides were made available to the public through Space-Track [135] that had been observed 30 days preceding the date when the snapshot was taken.

Conjunctions closer than 20 km were recorded. This was twice as high as the threshold that should be used to identify all conjunctions, as reported in section A.1. This threshold distance meant that the centres of mass of the objects were separated by 0.2 to 237.7 position standard deviations presented in Table 2.3. The relatively high conjunction threshold distance guaranteed that many conjunctions with relatively low collision probabilities were recorded and ensured that a large spectrum of collision probabilities was seen. This ensured that the importance of the high-P_C events was not overestimated, because many low-P_C conjunctions could constitute a large fraction of the collision probability accumulated by every object.

For every object, the accumulated true ($P_C|^{TRUE}$) and maximum ($P_C|^{MAX}$) collision probabilities, which are the probabilities that *any* of the conjunctions involving this object would result in a collision, were computed at all the epochs when the given object was involved in a conjunction. These cumulative collision probabilities were computed according to Eq. 2.32.

The accumulated collision probabilities were also multiplied by the objects' respective masses. Doing so allowed the examination of the criticality of every conjunction from the debris environment point of view [91, 128, 145, 158] because such a figure can be thought of as the risk of increasing the number of objects in the environment posed by a given conjunction. Mass is deemed as the second most influential parameter governing the consequences of a breakup of an object, just after the altitude where the fragmentation occurs [128].

Risk is often computed by multiplying the probability of an event by the severity of its consequences [78, 125, 145], which in this case is roughly proportional to mass because fragmentations of large-mass objects are likely to produce many new debris [51]. Here, "criticality" ζ is defined as collision probability P_C multiplied by the mass of the object m, as per Eq. 3.1. Maximum criticality, $\zeta|^{MAX}$, will refer to cases where the maximum probability was used to compute this index. Similarly, the term true criticality will also be used when $P_C|^{TRUE}$ was utilised.

$$\zeta = P_C \times m. \tag{3.1}$$

Ultimately, it is the increase in the risk of collisions in orbit caused by fragmentation of objects [91] that is of concern from the point of view of long-term debris environment evolution [125] and space operations. However, computing this figure for every conjunction requires use of a breakup model to simulate how many new debris and of what sizes would be generated if the objects did collide in a given conjunction. Simulating such consequences of collisions requires assuming a threshold of kinetic energy that leads to catastrophic breakups [51]. Also, different implementations of the breakup model produce different results [68] with standard deviations of the numbers of collision fragments in the same order as the average [129]. Once the distribution of possible collision fragments is known, the change in the probability of a collision occurring in orbit can be computed. This can be done using algorithms that are based on spatial density of objects and so are faster to evaluate than the framework developed here. However, fragmentations of the same type of object are never going to produce identical clouds of debris [51], therefore a sensitivity analysis should be performed for every conjunction, thus increasing the computational time required to assess the criticality of every conjunction. This increase in computational time is further amplified by having to investigate the sensitivity of the results to the catastrophic collision energy threshold or breakup model implementation details.

Therefore, due to computational time of one to two days per one day of simulation time needed for the analyses conducted here, a simple metric using mass directly was used as a proxy of criticality. This metric is consistent with all the commonly used approaches described in section 1.4.

A database of the masses of objects in the public TLE catalogue, relating the space surveillance catalog number (SSC) to mass of a given object, m, was kindly provided by Dr Darren McKnight and used in this study. It was compiled by working with the manufacturers and hence estimating the dry mass of the objects. If mass of an object was not present in the database, this object was excluded from all the analyses that needed m to be known. All such objects were included in the samples that only used probability metrics, however. No other database of masses was available to reduce the number of objects rejected from the analyses that relied on m. Statistical analysis of the MASTER 2009 (Meteoroid and Space Debris Terrestrial Environment Reference) reference population was attempted to find typical masses of different classes of objects, e.g. rocket bodies or spacecraft. However, objects with masses different by orders of magnitude are present in every class of objects. Thus, assuming the mass of an object, if it was not known, would cause ζ of such objects to be contrived, and so mass was not assumed. Still, 8656 objects of known mass were present in the sample, which was considered a reliable sample size. Moreover, the behaviours of P_C as well as ζ were analysed to ensure that they experienced similar contributions of particular events.

In order to compute the collision probability of a conjunction, the size of the objects that are involved has to be known. The used value could potentially have a significant effect on the results because it will change the contribution of individual conjunctions to the P_C and ζ accumulated by every object. Mass will affect the absolute value of criticality of an object, but the contributions of individual conjunctions to the final accumulated value are driven by P_C. The state uncertainty of every object also affects P_C, and the estimation of this was described in section 2.4. The choice of the object size is detailed next.

3.1.1.1 Object physical size

TLEs come with no information as to the size of the associated objects. In order to compute the collision probability, the collision radius r in Eq. 2.21 has to be known. A database containing the physical radii of objects launched before 2003 (up to catalogue number 28057), originally compiled by The Aerospace Corporation, was used to allow the collision radius to be computed for some conjunctions. It is the same database that is distributed with AGI's STK and that was used in the verification process of the conjunction detection and assessment framework, but it was also kindly provided by Dr T.S. Kelso for the purpose of this research. For the remainder of the catalogue, statistical data from the MASTER reference population of 1 May 2009, which is the reference population used e.g. in the IADC studies, were used. This population comprises 19 630 objects larger than 10 cm, and associates each object with a hard body radius and a type, i.e. classifies it as a rocket body (R/B), payload (P/L), mission-related object (MRO), or debris (DEB). An average radius was computed for all the objects of a given type present in the MASTER reference population. The standard deviation of every group was also found and the results are shown in Table 3.1.

Some of the MASTER object types can be directly linked to TLEs through three-line element sets that contain information about the type of certain objects in their common name fields. Because the three-line element sets do not distinguish mission-related objects, the data for this type of object were not directly utilised. Moreover, the three-line element set database contains many objects that are not classified as payloads, rocket bodies or debris. For these objects, the average size of the entire MASTER 2009 (all four types of objects) population was used.

The standard deviation for mission-related objects and debris is greater than the mean. This is also the case if all the four types of objects are analysed. This is because there are many relatively small objects in those groups, which means the average size is low. But there are objects with radii much higher than the mean in all of them, which increases the standard deviation. This signifies that using an average radius for every group of

Table 3.1: Radii of the objects according to the their types (rocket bodies (R/B), payloads (P/L), mission-related objects (MRO), and debris (DEB)) as present in MASTER reference population of 1 May 2009 and discerned in Space-Track's three-line element sets.

Object type	**R/B**	**P/L**	**MRO**	**DEB**	**Other**
MASTER Object ID	1	2	3	4	$1, 2, 3, and\ 4$
Average radius (m)	1.769	1.035	0.539	0.156	0.347
Standard deviation (m)	0.815	0.782	0.722	0.555	0.780

objects is a simplification. It was, however, necessary to perform the analysis described herein. The effect of assuming a radius for many of the objects was investigated by finding all the conjunctions with the public TLE catalogue, closer than 20.0 km, over one year for the two test cases (Envisat and Delta 1) located in different orbital regimes (LEO and GTO) and first introduced in section 2.1.2.

When the default radius of the objects was varied by $\pm 1\sigma$ (standard deviation) around the MASTER 2009 average, the collision probabilities accumulated by Delta 1 and Envisat changed by no more than $+23.9\%$ and -3.2% as presented in Fig. 3.1. The more conjunctions that take place for which the radius has to be assumed, the greater the effect of assuming the radius will be. This is particularly evident for Delta 1 because it had two conjunctions (mid-January and beginning of June) with high collision probabilities where the object size had to be assumed.

In the absence of a complete database of object sizes that could associate every space surveillance catalog number with a particular object size, the statistical values from Table 3.1 were assumed whenever an object's size was not available in the database. This allowed all the objects to be kept in the analysis, thus ensuring that the number of conjunctions in the simulation was similar to what takes place in reality. Rejecting objects of unknown size, as was done with the unknown mass, would reduce the size of the sample to 7806 objects. Also, it would make it impossible to compare the contributions of individual conjunctions on the final accumulated criticality and P_C for two different sample sizes. Moreover, using the database of the estimated sizes meant that objects larger than the average object of their type experienced higher collision probabilities and *vice versa*, as they would in reality. Therefore, this assumption was considered acceptable given its advantages.

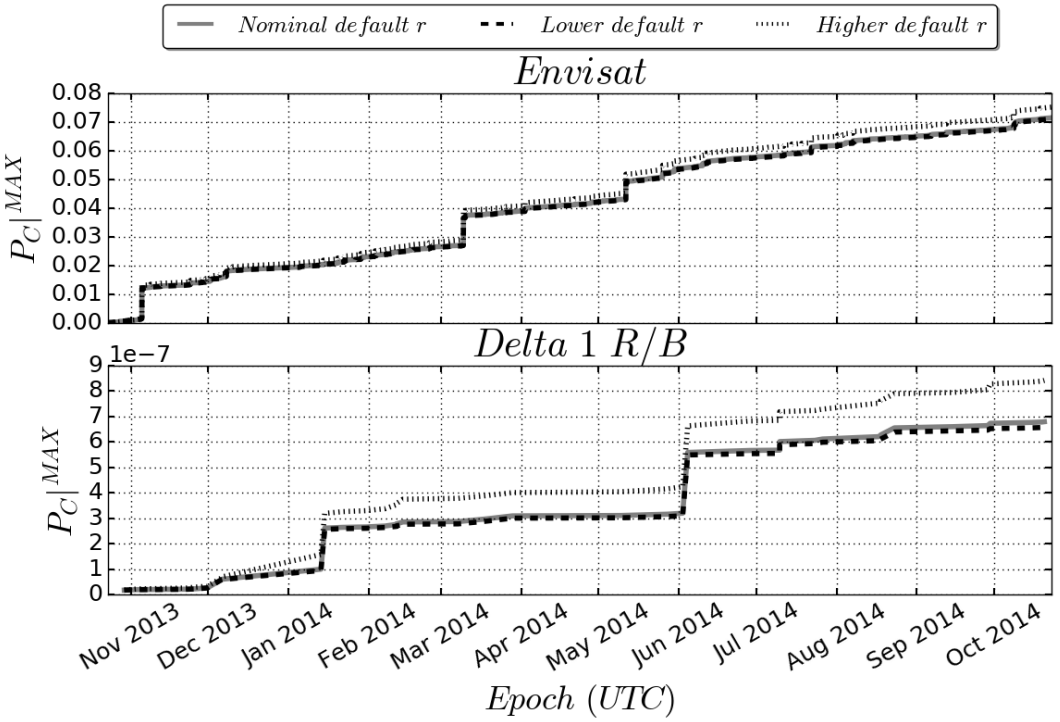

Figure 3.1: Accumulated maximum collision probabilities of the Envisat and Delta 1 R/B test cases when assuming average or $\pm 1\sigma$ MASTER 2009-derived radii for the objects not present in the database. Conjunctions closer than 20.0 km found using the TLEs from 23 Oct 2013 over one year.

3.1.2 Importance of particular conjunctions

3.1.2.1 Study description and results

Conjunctions were found for the public TLE catalogue snapshot from 7 Nov 2013 containing 14 920 objects. After 1903 objects with fewer than five historical TLEs were discarded, the population size decreased to 13 017. Another subset of objects, which had non-zero mass present in the database, was selected and totalled 8656 objects. The International Space Station (ISS, catalogue number 25544) was also removed from this dataset because it has mass at least an order of magnitude higher than other high-mass satellites and was therefore found to be always present in the list of several highest-criticality objects. Due to its special nature, ISS performs routine collision avoidance and therefore is believed to have little probability to be involved in a catastrophic collision. Moreover, its low altitude means that, should it fragment, its debris will decay from orbit relatively quickly without contributing to future collision activity in orbit or hindering space operations for long.

The analysis was performed for a period of 30 days; in this period, $P_C|^{TRUE}$ of individual events decreased close to the smallest number that can be represented as a double floating point precision number. When $P_C|^{MAX}$ is used, the collision probability of individual events is not time-dependent. However, the more conjunctions are included, the closer the accumulated collision probability will be to 1.0. Eventually, when sufficiently many conjunctions have taken place, P_C will be within double floating point precision from 1.0. This will mark the longest possible interval over which analyses based on collision probability remain insightful. Also, when P_C has reached 1.0, or "saturated", any further conjunctions, even with extremely high collision probabilities, will not change the final accumulated P_C and so their contributions will be zero. This is a limitation of using collision probability as a metric, however, not the methods used here and for operational collision avoidance. For this reason, Radtke et al. [125] used the flux of the objects, rather than P_C found with long-term evolutionary debris models, to identify the objects most likely to be involved in a collision. The investigation of how long it takes for P_C to saturate will be performed when analysing the results of evolutionary debris models in section 3.2 (in the scope of the entire debris environment this is in the order two to three decades).

A total of 3 252 201 conjunctions closer than 20 km were found in the 30 day time interval. All the objects in the sample were ranked based on the collision probabilities and criticalities they accumulated over the one month time window. The catalogue numbers and common names of the 20 objects that were found to have the highest final $P_C|^{MAX}$, $P_C|^{TRUE}$, and $\zeta|^{MAX}$ are shown in Table 3.2. Only 20 objects are presented because they serve as a good example of various types of behaviour that were identified. Table 3.2 will be referred to as a "target list" because the objects that are located in it could be targeted by debris remediation to reduce the collision probability in orbit in the analysed time window.

First observation that can be made while examining Table 3.2 is that including mass in the criticality metric enables the discussion to focus on objects that may drive the growth of the number of objects in the environment [98]. Objects with lower mass that are not likely to generate many fragments when they break up themselves, e.g. the BRITE-U Unibrite small satellite or pieces of debris, are not present in the criticality-based list. That said, the lighter objects should still be kept in the analysis as they could potentially cause breakups of the large derelicts if the collision energies are high enough [51]. Collisions have to involve more than one object. However, in this analysis, criticality was computed based on the masses of individual objects, not masses of all the objects involved in a given conjunction, to identify the *objects*, not *conjunctions*, that pose the risk of increasing the number of debris in orbit.

Table 3.2: Catalogue numbers and common names of the 20 objects with the highest $P_C|^{MAX}$, $P_C|^{TRUE}$, and maximum criticality, $\zeta|^{MAX}$, at the end of the simulation. Conjunctions closer than 20 km recorded amongst the object in the public TLE catalogue from 7 Nov 2013 over 30 days.

Index	$\mathbf{P_C}\|^{\mathbf{MAX}}$	$\mathbf{P_C}\|^{\mathbf{TRUE}}$	$\zeta\|^{\mathbf{MAX}}$
1	24949 IRIDIUM 30	25285 IRIDIUM 62	27386 ENVISAT
2	25285 IRIDIUM 62	24949 IRIDIUM 30	24949 IRIDIUM 30
3	13149 SL-8 R/B	27386 ENVISAT	25285 IRIDIUM 62
4	34858 COSMOS 2251 DEB	36916 METEOR 2-5 DEB	13149 SL-8 R/B
5	20436 SPOT 2	10514 METEOR 2-3	20436 SPOT 2
6	23007 SL-8 DEB	28057 CBERS 2	24277 ADEOS
7	25940 CBERS 1	14452 METEOR 2-10	13718 METEOR 2-9
8	27386 ENVISAT	27450 IRIDIUM 97	25634 ARGOS
9	25432 IRIDIUM 76	24971 IRS 1D	25940 CBERS 1
10	13718 METEOR 2-9	25468 IRIDIUM 81	23705 SL-16 R/B
11	25979 ARIANE 40 R/B	25528 IRIDIUM 86	22803 SL-16 R/B
12	24277 ADEOS	24945 IRIDIUM 32	25979 ARIANE 40 R/B
13	24944 IRIDIUM 29	25171 IRIDIUM 54	18187 COSMOS 1867
14	25634 ARGOS	39092 BRITE-U UNIBRITE	26070 SL-16 R/B
15	23606 CERISE	25577 IRIDIUM 20	17369 COSMOS 1818
16	18096 SL-8 R/B	39091 BRITE-A TUGSAT-1	27006 SL-16 R/B
17	34086 IRIDIUM 33 DEB	24795 IRIDIUM 5	21574 ERS 1
18	25528 IRIDIUM 86	25041 IRIDIUM 40	18096 SL-8 R/B
19	18187 COSMOS 1867	25042 IRIDIUM 39	25861 SL-16 R/B
20	24945 IRIDIUM 32	24905 IRIDIUM 46	22823 SPOT 3

Another observation that can be made is that the three target lists are different. Out of 20 possible objects, only Iridium 30, Iridium 62 and Envisat appear on all the lists, although in different positions. Eleven objects are present in two lists, namely SL-8 R/B (13149 and 18096), Spot 2, Cbers 1, Meteor 2-9 (13718), Ariane 40 R/B (25979), Adeos, Argos, Iridium 86 and 32, and Cosmos 1867 (18187), but in different positions as well. A total of 60 unique objects could be present on the three target lists in Table 3.2; but due to repetitions, only 43 objects (71.7%) are unique.

3.1.2.2 Investigating differences in target lists

To better understand why the target lists from Table 3.2 differ in composition, the histories of the collision probabilities and criticalities accumulated by each of the top 20 objects were analysed. These histories for the top six objects, which represent different types of observed behaviour, are shown in Fig. 3.3 and Fig. 3.4 for collision probabilities and criticalities, respectively.

Particular conjunctions with extremely high individual maximum collision probabilities and maximum criticalities significantly contributed towards the final accumulated values for most objects. These events are visible as instantaneous and large changes in the accumulated collision probabilities or criticalities.

Similar behaviour can also be observed for $P_C|^{TRUE}$ and $\zeta|^{TRUE}$ but only within approximately the first week of the analysis. Beyond approx. 7 days, the uncertainty in position of the objects becomes large enough for $P_C|^{TRUE}$ of individual conjunctions to be sufficiently low not to affect the accumulated true collision probability of the object. This is only different for Iridium 32 and Iridium 60 that had many close conjunctions between 2 and 5 Dec, which resulted in a gradual build-up of $P_C|^{TRUE}$ in that period.

Table 3.4 shows how much the event with the highest recorded $P_C|^{MAX}$, $P_C|^{TRUE}$ or $\zeta|^{MAX}$ contributed to the final accumulated value for the 20 objects from the target lists from Table 3.2. The same data are shown in Fig. 3.2. This contribution, ϵ, is computed as a ratio of the highest P_C (or criticality ζ) a given object encountered during its conjunctions ($max\left(P_C(E_i)\right)$) to the final collision probability accumulated by it during N conjunctions ($P_C(E_N)$), as per Eq. 3.2.

$$\epsilon = \frac{max\left(P_C(E_i)\right)}{P_C(E_N)}. \tag{3.2}$$

Due to probability dilution, the contribution of particular events is lower for true collision probability than the maximum probability. The largest contribution of a single event to the accumulated $P_C|^{TRUE}$ (46.96%) was observed for Iridium 86 (25528). The reason for this was that this conjunction took place on 10 Nov 2013 20:10:28, i.e. just three days after the beginning of the analysis. This meant that the covariances of this object and its secondary, SL-14 R/B (13272), had not grown sufficiently to dilute the collision probability of this event, compared with later events.

Specific events largely define P_C of the objects and effectively place them in their locations in the target lists that use $P_C|^{MAX}$. Thus, small changes in the conjunction details, e.g. the miss distance, can impact the position of the object in the list. Maximum collision probability does not undergo dilution and hence enables the identification of events that could evolve to have high collision probabilities when the predictions are made closer to the conjunction epoch. It can, therefore, be used instead of performing regular conjunction screenings with consecutive TLE catalogue snapshots over a period of time. $P_C|^{MAX}$ should not be viewed as an artificial metric, even though it is not directly linked to the state uncertainty at the TCA. $P_C|^{MAX}$ is shown not to affect the conclusions of the following studies in section 3.1.5. Therefore, small changes to conjunction details will change what objects are the most likely to be involved in a collision even if higher probability algorithms and ephemerides are used in an operational settings instead of $P_C|^{MAX}$.

3.1.2.3 Investigating importance of individual events for all the objects

Examining the behaviour of several objects with the highest final accumulated collision probabilities and criticalities suggests that particular conjunctions, with high individual P_C, contribute more to the final value accumulated by a given object than many other events and effectively define the composition of the target lists. It was therefore investigated whether this trend is exhibited by all the objects. Furthermore, it was studied how much of the collision probability and criticality in the entire debris environment can be attributed to these particular events.

The contribution of the event with the highest individual $\zeta|^{MAX}$ to the final accumulated value was computed for all the objects in the sample using Eq. 3.2. These contributions are defined by $P_C|^{MAX}$ of every object because the mass of every object is identical in all the conjunctions it takes part in. A histogram, showing how big this contribution was for a given fraction of the sample, is shown in Fig. 3.5. The top 20 objects analysed in section 3.1.2.2 are also presented to investigate whether the position of the object in the

Table 3.4: Contributions of particular events with the highest individual $P_C|^{MAX}$, $P_C|^{TRUE}$, and maximum criticality, $\zeta|^{MAX}$, to the final values accumulated at the end of the simulation by the objects from Table 3.2. Contribution computed using Eq. 3.2.

Index	$\mathbf{P_C}\|^{\mathbf{MAX}}$	$\mathbf{P_C}\|^{\mathbf{TRUE}}$	$\zeta\|^{\mathbf{MAX}}$
1	60.53%	1.44%	27.31%
2	60.56%	1.45%	60.53%
3	99.23%	8.56%	60.56%
4	99.98%	19.43%	99.23%
5	93.80%	5.49%	93.80%
6	99.92%	3.29%	61.16%
7	80.68%	2.50%	66.78%
8	27.31%	1.59%	93.05%
9	96.08%	5.60%	80.68%
10	66.78%	5.93%	43.29%
11	75.57%	46.96%	29.11%
12	61.16%	10.26%	75.57%
13	78.35%	7.82%	8.13%
14	93.05%	7.86%	7.95%
15	99.40%	12.17%	6.77%
16	94.09%	8.88%	20.00%
17	99.33%	6.79%	14.11%
18	75.30%	10.22%	94.09%
19	8.13%	3.87%	73.50%
20	33.90%	6.93%	78.43%

target lists impacts the importance of the particular events. Only maximum criticality was used to avoid having to repeat the analysis with more snapshots of the public TLE catalogue, which reduced the computational time required, and to focus the discussion on objects that could generate many new debris. The impacts of this simplification are shown to not affect the conclusions of this work in section 3.1.5.

An initial drop of 45% in the contribution of the highest $P_C|^{MAX}$ events can be observed. This corresponds to 4629 objects that did not have any conjunctions, and thus the contribution of a particular event from Eq. 3.2 to their final accumulated criticality was zero. For 20% of the objects, the event with highest $P_C|^{MAX}$ accounted for 35% of the final accumulated criticality. For 10% of the objects this contribution was 58%.

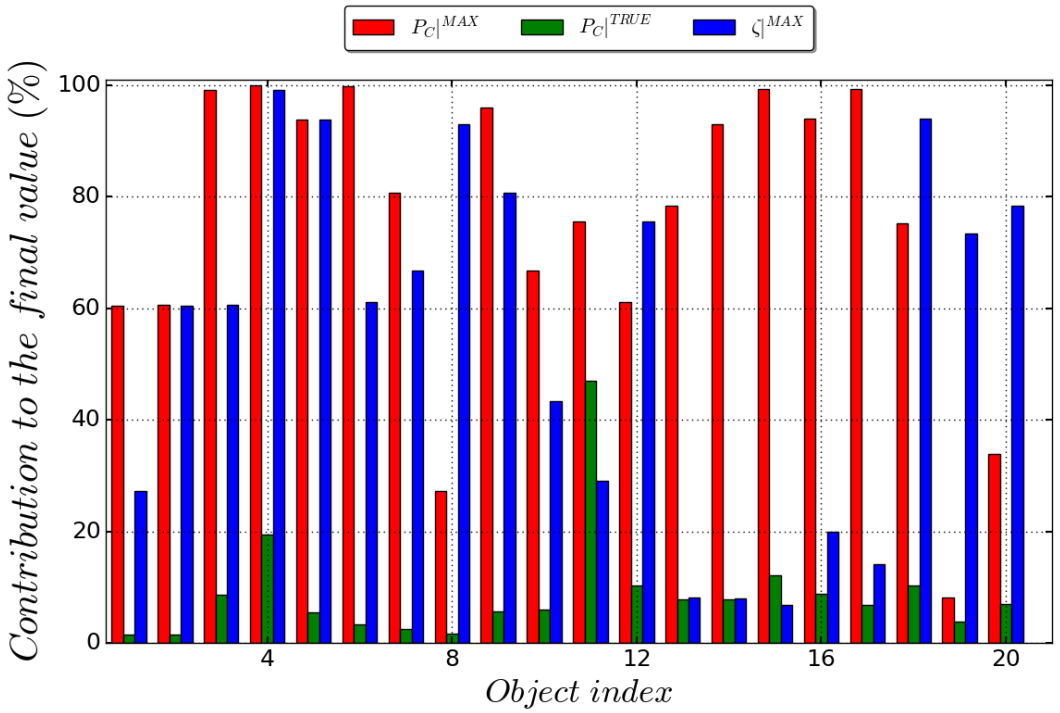

Figure 3.2: Contributions of particular events with the highest individual $P_C|^{MAX}$, $P_C|^{TRUE}$, and maximum criticality ($\zeta|^{MAX}$) to the final values accumulated at the end of the simulation by the objects from Table 3.2.

It appears that a given contribution of the particular events is more prominent for the top 20 objects than the entire sample; i.e. a higher fraction of the sample experienced a conjunction that affected the final criticality of the object by a given amount when the sample had 20 rather than 8656 objects. However, when the objects that experienced no conjunctions were filtered out from the sample with respect to which the fraction of the population was computed, little difference was observed between the top 20 objects and the entire population. Quantitatively, particular events contributed 14.5% to the final maximum criticality for 81% of the objects that had a conjunction and 80% of the top 20 objects (16 objects).

3.1.2.4 Investigating importance of individual events in the scope of the collision risk in the entire environment

If the criticalities of individual objects are largely defined by relatively few particular conjunctions, how much of the total collision probability in orbit comes from such events? If it is indeed few events, how few exactly and could they be remedied, thus significantly lowering the probability of seeing any collisions in orbit?

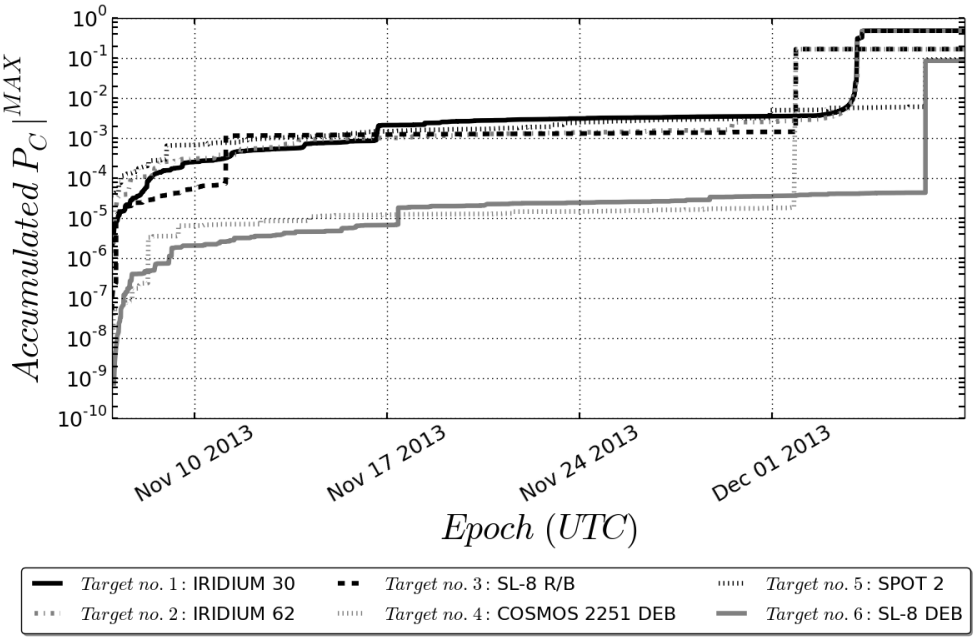

(a) Maximum collision probability

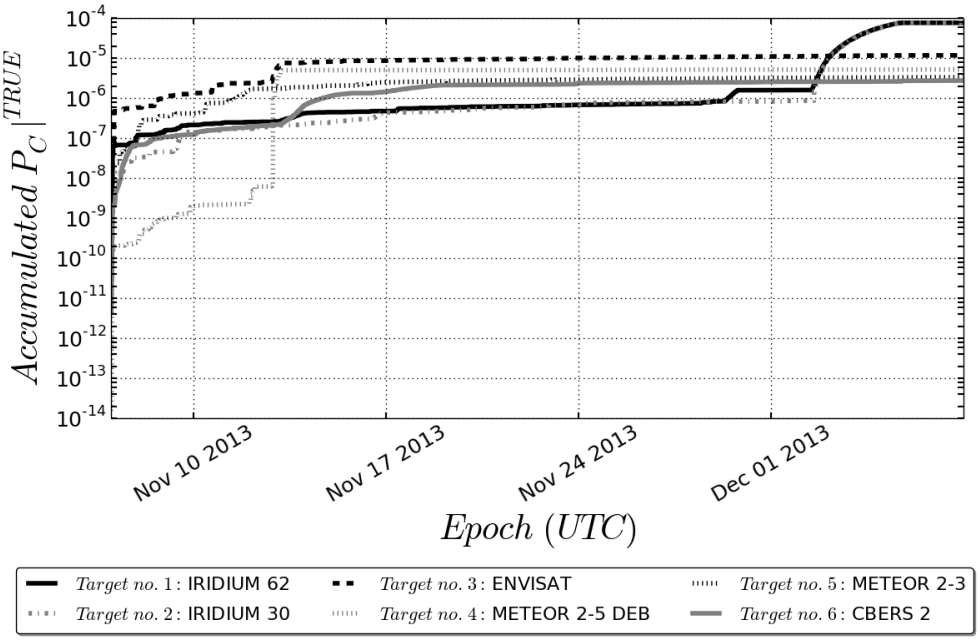

(b) True collision probability

Figure 3.3: Maximum and true collision probabilities accumulated by the top six objects from Table 3.2.

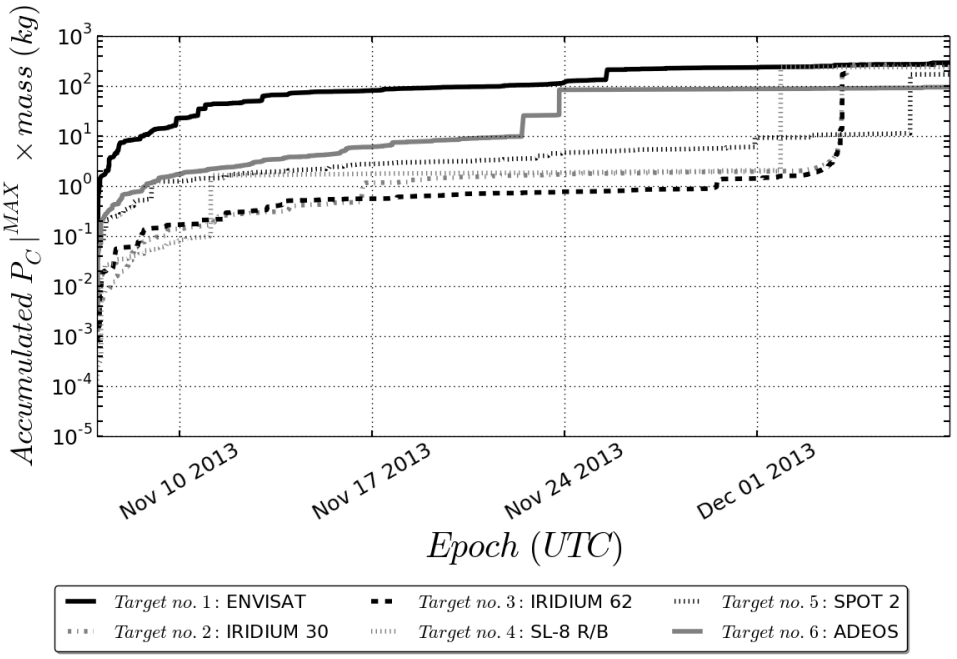

(a) Maximum criticality

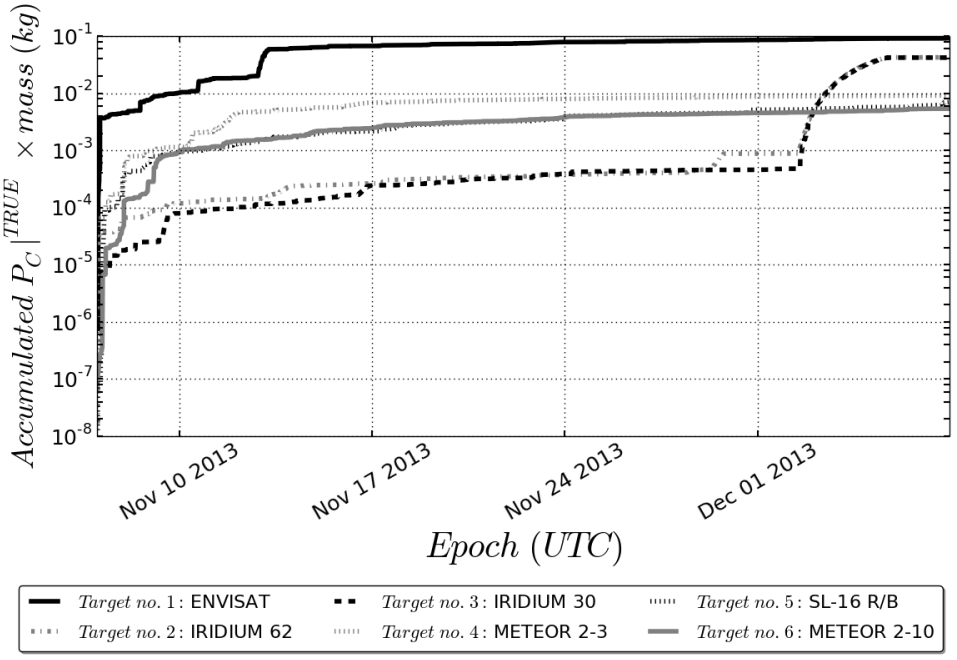

(b) True criticality

Figure 3.4: Maximum and true criticalities (collision probability multiplied by the object's mass) accumulated by the top six objects from Table 3.2.

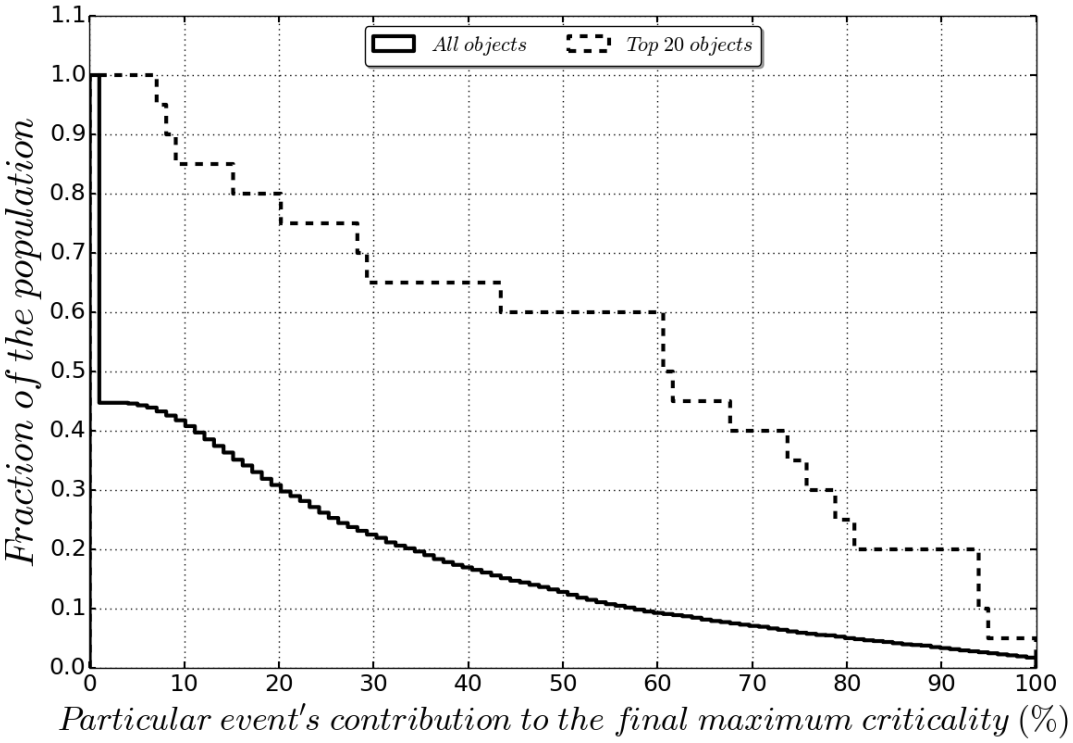

Figure 3.5: Histogram of the contribution of the conjunction with the highest maximum criticality to the final value accumulated by each object. Contribution computed using Eq. 3.2. Conjunctions closer than 20 km recorded amongst the objects in the public TLE catalogue from 7 Nov 2013 over 30 days.

In order to answer these questions, the probability of any collision taking place between any pair of objects was computed according to Eq. 2.32. The conjunctions were sorted in ascending P_C order to examine the impact of the events with the highest individual collision probabilities. In order to enable the discussion to focus on events that could, potentially, generate many new debris, criticality was examined instead of the collision probability. Masses of both objects involved in a conjunction were used when computing this criticality because both objects could potentially break up and generate fragments. This is different to the case of computing the criticality of specific objects where only the mass of that object was used. The contribution, ϵ_{env}, of every conjunction with collision probability P_C to the criticality in the environment accumulated when using the first i conjunctions $P_{C,i,ACC}$, was computed using Eq. 3.3.

$$\epsilon_{env} = \frac{P_C}{P_{C,i,ACC}}. \tag{3.3}$$

The evolution of the criticality accumulated in the debris environment with the number of conjunctions is shown in Fig. 3.6.

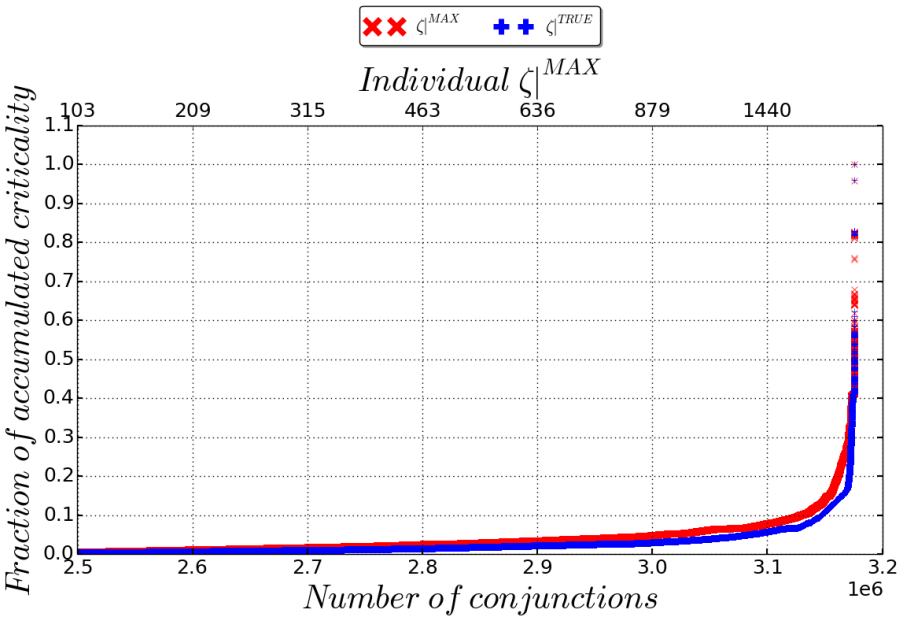

Figure 3.6: Dependence of the criticality in the entire debris environment on the number of conjunctions. Conjunctions closer than 20 km recorded amongst the objects in the public TLE catalogue from 7 Nov 2013 over 30 days. Conjunctions were sorted in ascending criticality order and fraction of accumulated criticality computed using using Eq. 3.3. Also showing the maximum criticality of individual events ($\zeta|^{MAX}$) corresponding to the given number of conjunctions.

Out of 3 193 196 conjunctions that involved objects with non-zero mass, only several events with relatively high individual collision probabilities contributed the most to the total criticality in the entire environment. This is visible as a sharp increase in the accumulated criticality that takes place when the criticality introduced by approx. 40 000 events with the highest P_C is accounted for. Conjunctions with individual maximum criticalities of less than 1440 did not contribute more than 7.8% to the final criticality accumulated in orbit. 50% of the final accumulated criticality can be attributed to 234 (0.007%) events with individual criticalities between 9174 and 18 364. Two conjunctions between Iridium 30 and 62 gave rise to 15.9% of the total criticality.

This means that if 234 conjunctions could have been avoided, the total risk would have been halved. These events may not have been prevented by removing statistically important objects through active debris removal, unless all the objects are removed from the orbit. However, section 3.1.3 and section 3.1.4 test whether the lists of the most risky objects in a given period of time are dependent on the epoch, when the list is compiled, and on solar activity, which cannot be accurately forecast far in advance. If they do, we may never be able to predict which objects are going to collide and thus should be removed from orbit.

3.1.3 Sensitivity to the prediction epoch

A snapshot of the public TLE catalogue taken exactly one year after the one investigated in section 3.1.2, i.e. 7 Nov 2014, was screened for conjunctions over 30 days. This was done to investigate the variability of the highest risk objects in a given time window depending on the start epoch of this window.

Conjunction screening epoch is expected to affect the collision probabilities of the objects because the relative motion of their orbits will cause certain objects to have many close approaches in a given time interval and few at other times; it will also change the conjunction details. Therefore, depending on when the forecast is made, different objects could be found to have the highest collision probabilities or criticalities. Analysis identical to that from section 3.1.2 was repeated but with the different TLE catalogue snapshot.

The 20 objects with the highest collision probabilities or maximum criticality are presented in Table 3.5. Thirteen satellites appear on the lists obtained both in November 2013 and November 2014, namely:

1. Iridium 62, 29 and 81
2. Spot 2
3. Envisat
4. Meteor 2-3 (13718), 2-9 (13718) and 2-10 (14452)
5. Cosmos 1818 (17369) and 1867 (13718)
6. BRITE-A TUGSAT-1
7. SL-16 R/B (23705 and 17369)

They do, however, appear in different locations and on lists using different metrics for predictions made in 2013 and 2014. The 2013 lists contain 43 unique satellites whereas 44 unique objects made it to the 2014 lists. Out of these 87 unique objects in both sets, 74 (85%) are completely unique i.e. appear once on the target lists from either 2013 or 2014. This proves that the epoch of conjunction screening will largely redefine the objects that will be the most risky in a given time window.

Even though the 20 most-risky objects identified in the month following 7 Nov 2013 were found to be largely different to those being the most risky a year later, the impact of particular conjunctions was evident in both cases. Figure 3.7, which is analogous to Fig. 3.5, shows that these very close conjunctions with relatively high collision probabilities significantly contributed to the final accumulated criticalities of individual objects.

Table 3.5: Catalogue numbers and common names of the 20 objects with the highest $P_C|^{MAX}$, $P_C|^{TRUE}$, and maximum criticality, $\zeta|^{MAX}$, at the end of the simulation. Conjunctions closer than 20 km recorded amongst the objects in the public TLE catalogue from 7 Nov 2014 over 30 days.

Index	$\mathbf{P_C}\|^{\mathbf{MAX}}$	$\mathbf{P_C}\|^{\mathbf{TRUE}}$	$\zeta\|^{\mathbf{MAX}}$
1	40092 HAIYANG 2A DEB	24794 IRIDIUM 6	25407 SL-16 R/B
2	30115 FENGYUN 1C DEB	25262 IRIDIUM 51	18187 COSMOS 1867
3	35201 FENGYUN 1C DEB	13718 METEOR 2-9	24794 IRIDIUM 6
4	24794 IRIDIUM 6	25468 IRIDIUM 81	25262 IRIDIUM 51
5	25262 IRIDIUM 51	24792 IRIDIUM 8	17369 COSMOS 1818
6	18187 COSMOS 1867	24904 IRIDIUM 25	19120 SL-16 R/B
7	12458 NOVA 1	39089 NEOSSAT	12644 SL-8 R/B
8	18362 OSCAR 29	26536 NOAA 16	24944 IRIDIUM 29
9	24944 IRIDIUM 29	39088 SAPPHIRE	22285 SL-16 R/B
10	25468 IRIDIUM 81	20436 SPOT 2	25468 IRIDIUM 81
11	24792 IRIDIUM 8	35423 METEOR 2-2 DEB	24792 IRIDIUM 8
12	25039 IRIDIUM 43	23657 SICH 1	25039 IRIDIUM 43
13	25407 SL-16 R/B	14452 METEOR 2-10	25400 SL-16 R/B
14	30630 FENGYUN 1C DEB	25285 IRIDIUM 62	27386 ENVISAT
15	12644 SL-8 R/B	25530 IRIDIUM 84	16953 SL-8 R/B
16	13761 COSMOS 1429	39091 BRITE-A TUGSAT-1	13718 METEOR 2-9
17	39645 COSMOS 1867 COOLANT	24950 IRIDIUM 31	27006 SL-16 R/B
18	25077 IRIDIUM 42	10514 METEOR 2-3	12443 SL-8 R/B
19	17369 COSMOS 1818	24944 IRIDIUM 29	19650 SL-16 R/B
20	39672 COSMOS 1867 COOLANT	25263 IRIDIUM 61	23705 SL-16 R/B

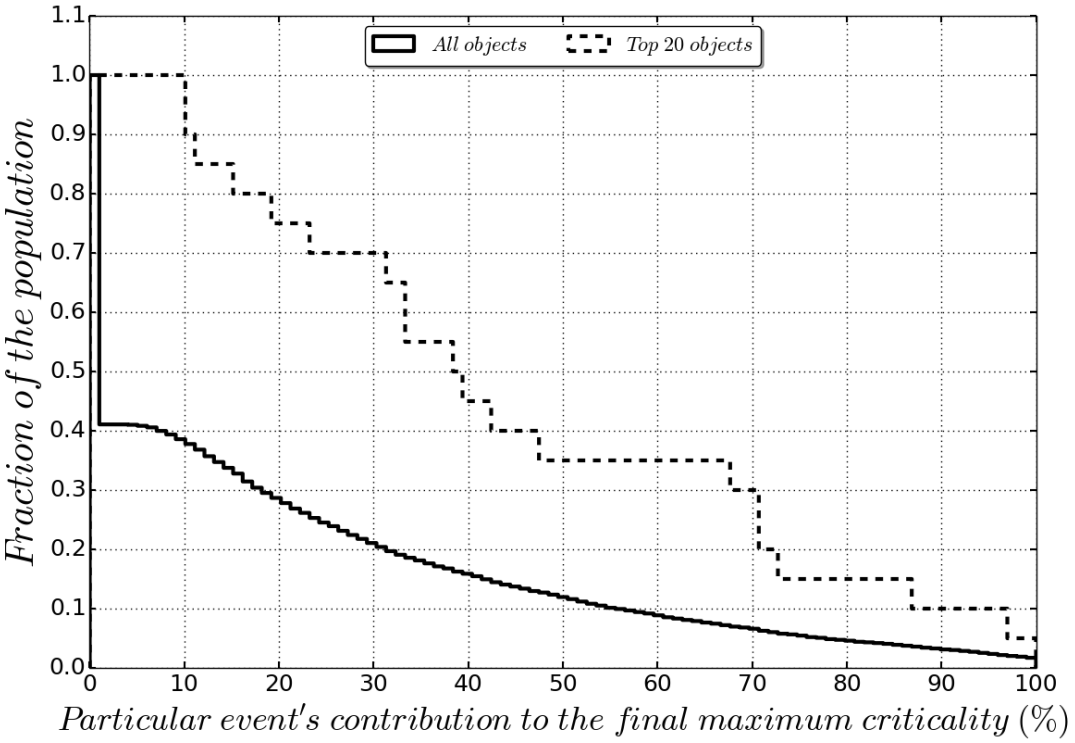

Figure 3.7: Histogram of the contribution of the conjunction with the highest maximum criticality to the final value accumulated by each object. Conjunctions closer than 20 km recorded amongst the objects in the public TLE catalogue from 7 Nov 2014 over 30 days.

In 2014, 5283 objects (42% of the population), rather than 4629 a year earlier, saw no conjunctions in the analysis time window. Other than that, similar contributions of particular conjunctions to the final criticalities accumulated by individual objects were observed for the investigated prediction epochs. For 20% of the objects, the event with the highest $P_C|^{MAX}$ accounted for 32% (c.f. 35% in 2013) of the final accumulated criticality. For 10% of the objects this contribution was 56%, while in 2013 it was 58%.

Moreover, Fig. 3.8 shows that, just as in the period starting on 7 Nov 2013, relatively few particular conjunctions gave rise to most of the total criticality in the debris environment. Specifically, 405 conjunctions contributed 50% to the total criticality in the environment in 2014. This is almost twice as many conjunctions as the ones that contributed the same amount to the total criticality in 2013 (234), but it remains a small fraction of the total number of conjunctions recorded in this analysis interval (0.014%). Note that $P_C|^{MAX}$ in the entire environment saturated whereas $P_C|^{TRUE}$ did not. Beyond the saturation of $P_C|^{MAX}$, increases in $\zeta|^{MAX}$ were only caused by conjunctions involving large-mass objects. Still, in both cases only a small fraction (0.014% and 0.019% for $\zeta|^{MAX}$ and $\zeta|^{TRUE}$, respectively) of conjunctions gave rise to most of the criticality accumulated in orbit.

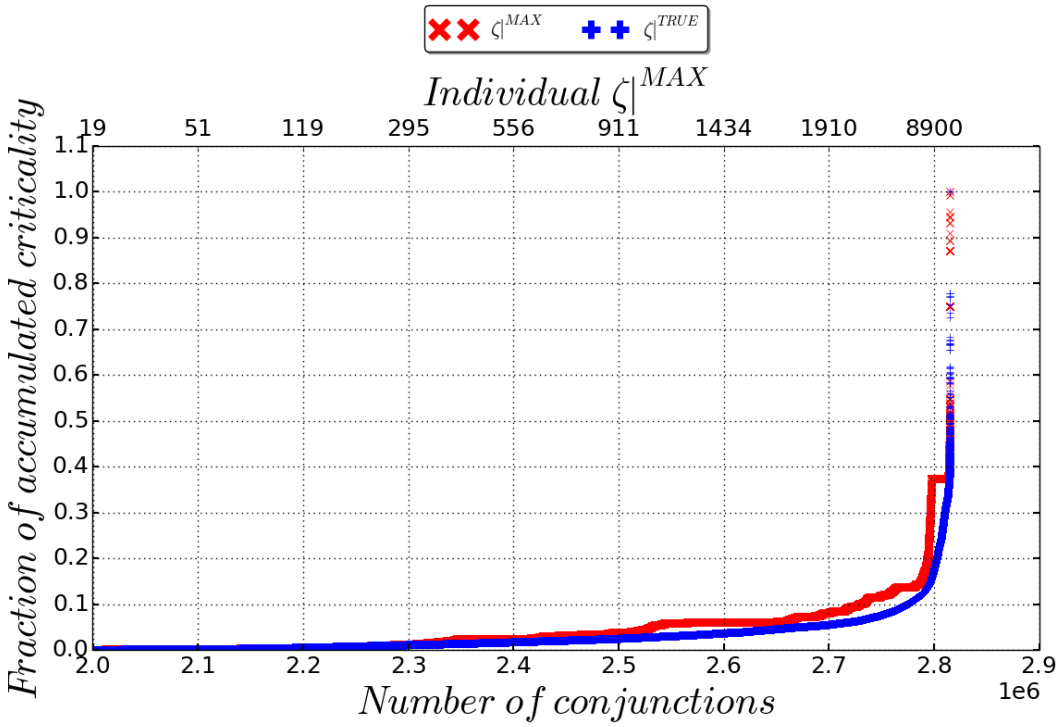

Figure 3.8: Dependence of the criticality in the entire debris environment on the number of conjunctions. Conjunctions closer than 20 km recorded amongst the objects in the public TLE catalogue from 7 Nov 2014 over 30 days. Conjunctions sorted in ascending criticality order and fraction of accumulated criticality computed using using Eq. 3.3. Also showing the maximum criticality of individual events ($\zeta|^{MAX}$) corresponding to the given number of conjunctions.

There are three partial conclusions that can be drawn based on the above observations. Firstly, the most risky objects vary depending on the prediction epoch. This means that care should be taken when selecting ephemerides and algorithms to find objects that are likely to collide with others, i.e. ADR targets. Otherwise only some of these "risky objects" may be found.

Related to this sensitivity of the most risky objects to the prediction epoch is the fact that the objects that are likely to be involved in a collision are not necessarily the ones that will do so - there were 74 unique objects in the top 20 lists in 2013 and 2014. If all the objects from Table 3.2 (all the targets from 2013 according to any metric) were removed from the environment, 31 unique objects (70%) from the 2014 list would still be in orbit. This is because high-P_C conjunctions define the objects that are the most risky in a given time window. Ultimately, any object can take part in conjunctions with high collision probabilities and thus be involved in a collision, even though it may not appear likely to do so in the long term.

However, 13 objects were found in both target lists and therefore could be found to be the most risky if a prediction was made at a different epoch. These objects had close, high-risk conjunctions in both analyses, so this subset does not undermine the importance of the particular conjunctions. This could mean, however, that the subset of objects that often have such dangerous conjunctions, and thus contribute the most to the cumulative collision risk in the debris environment, is relatively small (15% of the top 20 objects in 2013 and 2014 analyses). Removing those could lower the probability of a collision occurring in orbit more than removal of any other 13 objects. If these 13 objects had been removed, the maximum collision probability in the debris environment in Nov 2013 would have been reduced from 8.80×10^{-1} to 8.55×10^{-1} and 11 057 conjunctions would have been avoided. This shows that ADR is an effective means of reducing the collision probability in orbit. However, if only the 13 objects were removed, most of the collision probability would not have been mitigated and collisions could occur despite ADR.

3.1.4 Sensitivity to the atmospheric density

Sensitivity of the accumulated collision probabilities and criticalities to the solar activity, which results in varying atmospheric density, was examined. This sensitivity study was considered insightful because daily variations in solar activity cannot be predicted far in advance and, therefore, could potentially lead to unpredictable conjunctions and collisions.

The SGP4 propagator does not explicitly accept any parameters that are used to describe solar activity; it only uses two-line element sets as inputs. However, TLEs do have a term that accounts for the atmospheric drag an object with surface area A, mass m and drag coefficient C_D flying through a fluid of density ρ_0 experiences, namely the B^* coefficient given in Eq. 3.4 [148].

$$B^* = \frac{C_D A}{m} \frac{\rho_0}{2}. \tag{3.4}$$

Varying B^* is equivalent to changing the atmospheric density, when assuming that the spacecraft properties remain unchanged, because it is proportional to ρ_0. Even though all the objects reside at different altitudes, and therefore experience different atmospheric densities, the objects that have conjunctions have to cross the same altitude regimes at the conjunction epochs. According to Fig. 3.9, 59% of the objects from the 7 Nov 2013 TLE snapshot had eccentricities ≤ 0.01. Therefore, most of these objects resided at constant altitudes and thus should experience similar atmospheric densities as the objects they had conjunctions with. Thus, scaling B^* by the same fraction for all the objects was equivalent to scaling the atmospheric density by the same fraction. This scaling enabled investigation of variations in collision probabilities that would result from varying solar activity. However, scaling the atmospheric density by scaling B^* makes it impossible to make a connection between the results of this study and solar activity proxies e.g. the daily $F10.7$ flux.

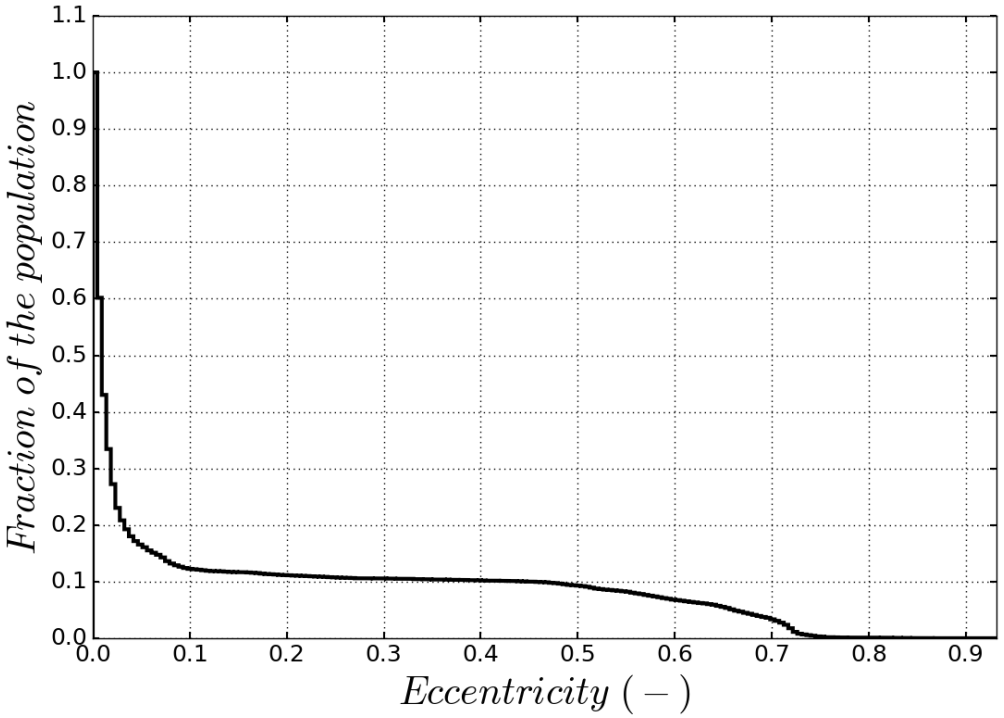

Figure 3.9: Cumulative histogram of the eccentricities of the TLEs from the public TLE catalogue from 7 Nov 2013.

3.1.4.1 Impact on the collision probabilities of individual objects

Firstly, the impact of varying B^* on collision probability accumulated by individual objects was examined for two objects that are often referred to as likely objects to be actively removed from orbit, namely Envisat and a Zenit-2 rocket body (27006) [17, 98, 128]. Conjunctions closer than 20 km with the entire public catalogue from 23 Oct 2013 over one year were found.

The duration of the simulation would reduce the collision probabilities of individual conjunctions beyond double precision floating point numbers if estimated TLE covariances were used. Therefore, fixed 1.0 km standard deviations of positions were used together with a database of object sizes and statistical radii from Table 3.1.

The B^* coefficient of all the objects was reduced and increased by 30% from the nominal value present in the TLEs. This was not aimed at reproducing a scenario that takes place in reality; rather, it served the purpose of testing the sensitivity of the results to B^*, as done, for example, by Dolado-Perez et al. [26]. In reality, increased solar activity would lead to atmospheric density changing by a different fraction at different altitudes. However this approach was sufficient to investigate whether the most risky conjunctions change when the solar activity changes, and the simulated variation in B^* was less than the variation in drag coefficient estimation for spherical satellites [117]. The collision probabilities accumulated by the two test objects for varying B^* are shown in Fig. 3.10.

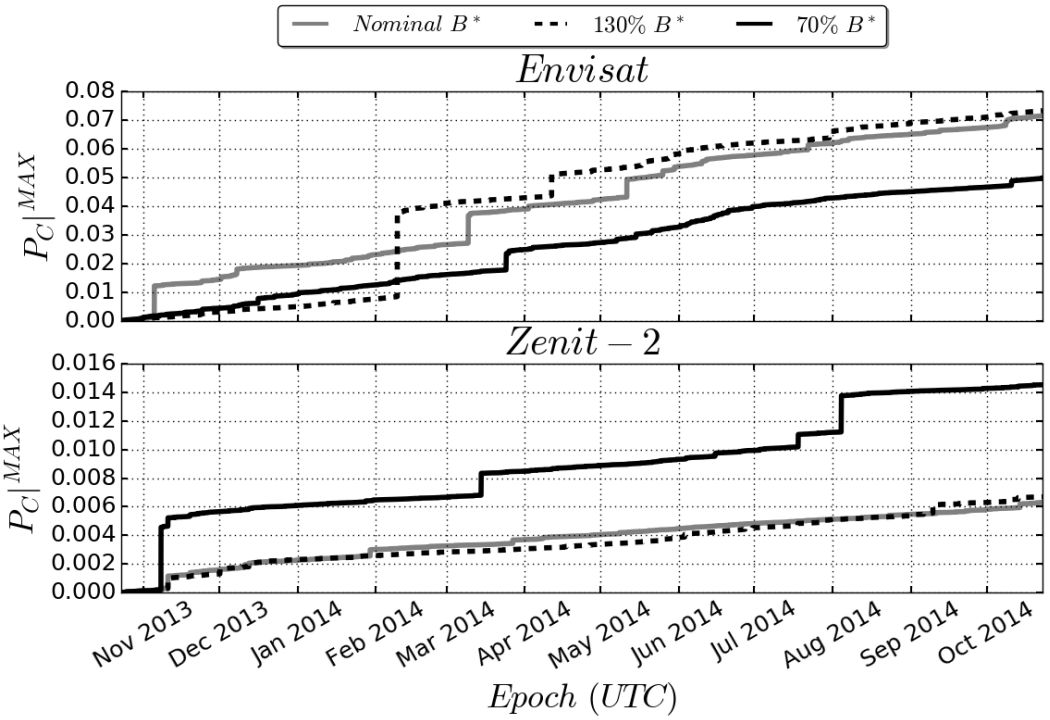

Figure 3.10: Accumulated maximum collision probabilities of the Envisat and Zenit-2 test cases for nominal, 130% and 70% B^* coefficient. Conjunctions closer than 20.0 km found using the TLEs from 23 Oct 2013 over one year. Assuming time-invariant, 1.0 km position standard deviations.

When B^* was lowered, the final accumulated $P_C|^{MAX}$ of Zenit 2 increased by 130.5% with respect to the nominal B^* value. This was caused by several conjunctions that had lower miss distance, and thus higher $P_C|^{MAX}$, when the drag was lowered. This change in miss distance was caused by the fact that the trajectories of the involved objects had been altered when the drag force acting on the objects changed. Those conjunctions can be seen as rapid and large changes in the accumulated collision probability on 8 Nov, 15 May, and 4 Aug.

This signifies that the collision probability of individual objects can change upon variations in atmospheric density that cannot be predicted far in advance. This means that certain objects, which are not considered likely targets for active removal, may experience conjunctions with high collision probabilities that cannot be forecast far in advance.

3.1.4.2 Effect on the lists of most risky objects in a given time window

The effect of varying atmospheric density on the composition of the lists of the most risky objects was investigated by repeating the analysis from section 3.1.2 but with scaling the B^* coefficient of all the objects. In the two investigated scenarios, the B^* coefficient of all the objects was scaled to 70% and 130% of the value present in the TLEs as in section 3.1.4.1. The lists of the six most risky objects for nominal, higher, and lower B^* values are shown in Table 3.7. Only the top six objects, rather than 20 as before, are shown for brevity.

As far as individual target selection metrics are concerned, the $P_C|^{TRUE}$ has the most non-unique objects that appear on the list for higher, lower and nominal B^* values. Specifically, four out of six top objects appear three times, namely Iridium 62 and 30, Envisat, and Meteor 2-5 DEB (36916). This is because the first and second, and the third and fourth objects on those lists had several conjunction with one another during the analysis period regardless of the B^* value. Namely, Meteor 2-5 DEB and Envisat had 25, 29, and 28 conjunctions for 70%, 130%, and 100% B^*, respectively. Iridium 62 and 30 had 47, 76, and 88 conjunctions for the corresponding B^* values.

When the B^* was varied, the number and details of the conjunctions between these object pairs, i.e miss distance, collision probability, importance w.r.t. final accumulated P_C, and epoch, changed as well. But, regardless of the B^* value, these two object pairs always had a conjunction with high enough $P_C|^{TRUE}$ or sufficiently many conjunctions with each other to bring them to the top of the target list. This suggests that these object pairs could be prone to having many close conjunctions because of the natural evolution of their orbits.

Envisat can be seen amongst the top six objects in the list using maximum criticality for every investigated B^* value. However, in all three cases, it had the conjunction with the highest maximum criticality with a different object. For 70%, 130%, and 100% B^* scaling factors, these conjunctions involved Cosmos 1937 (19038), Meteor 2-5 DEB (36916) and Cosmos 2251 DEB (36368), respectively. These three conjunctions had maximum collision probabilities of 1.03×10^{-2}, 6.60×10^{-4} and 1.36×10^{-3}, and contributed 19.4%, 19.9% and 27.3% to the final accumulated $P_C|^{MAX}$ of Envisat, respectively. These particular events did not contribute more to the final accumulated criticality of Envisat than other conjunctions so they were not the reason why it was found amongst the top-six objects for all B^* values. However, due to relatively high mass and many conjunctions that Envisat experienced in all three analyses, it was always close to the top of the list of the most risky objects; albeit in different locations. This suggests that it is a good candidate for active debris removal.

Table 3.7: Catalogue numbers and common names of the six objects with the highest $P_C|^{MAX}$, $P_C|^{TRUE}$, and maximum criticality, $\zeta|^{MAX}$, at the end of the simulation for the two B^* scaling values. Conjunctions closer than 20 km recorded amongst the objects in the public TLE catalogue from 7 Nov 2013 over 30 days.

$100\%B^*$

Index	$\mathbf{P_C}\|^{\mathbf{MAX}}$	$\mathbf{P_C}\|^{\mathbf{TRUE}}$	$\zeta\|^{\mathbf{MAX}}$
1	24949 IRIDIUM 30	25285 IRIDIUM 62	27386 ENVISAT
2	25285 IRIDIUM 62	24949 IRIDIUM 30	24949 IRIDIUM 30
3	13149 SL-8 R/B	27386 ENVISAT	25285 IRIDIUM 62
4	34858 COSMOS 2251 DEB	36916 METEOR 2-5 DEB	13149 SL-8 R/B
5	20436 SPOT 2	10514 METEOR 2-3	20436 SPOT 2
6	23007 SL-8 DEB	28057 CBERS 2	24277 ADEOS

$130\%B^*$

Index	$\mathbf{P_C}\|^{\mathbf{MAX}}$	$\mathbf{P_C}\|^{\mathbf{TRUE}}$	$\zeta\|^{\mathbf{MAX}}$
1	24949 IRIDIUM 30	25285 IRIDIUM 62	24949 IRIDIUM 30
2	25285 IRIDIUM 62	24949 IRIDIUM 30	25285 IRIDIUM 62
3	19650 SL-16 R/B	27386 ENVISAT	19650 SL-16 R/B
4	30241 FENGYUN 1C DEB	36916 METEOR 2-5 DEB	27386 ENVISAT
5	25432 IRIDIUM 76	27450 IRIDIUM 97	23088 SL-16 R/B
6	27386 ENVISAT	24905 IRIDIUM 46	13718 METEOR 2-9

$70\%B^*$

Index	$\mathbf{P_C}\|^{\mathbf{MAX}}$	$\mathbf{P_C}\|^{\mathbf{TRUE}}$	$\zeta\|^{\mathbf{MAX}}$
1	11170 SL-8 R/B	25285 IRIDIUM 62	11170 SL-8 R/B
2	37574 CZ-4B DEB	24949 IRIDIUM 30	22220 SL-16 R/B
3	27376 IRIDIUM 96	27386 ENVISAT	25400 SL-16 R/B
4	25276 IRIDIUM 60	36916 METEOR 2-5 DEB	27386 ENVISAT
5	13718 METEOR 2-9	10514 METEOR 2-3	22803 SL-16 R/B
6	22220 SL-16 R/B	28057 CBERS 2	13718 METEOR 2-9

Despite four objects being often present in the lists of the six most-risky objects, variability in the lists was noted. There were 44, 27 and 37 unique objects in the top 20 of the target lists based on $P_C|^{MAX}$, $P_C|^{TRUE}$ and $\zeta|^{MAX}$, respectively, for the different B^* scaling factors. The maximum number of unique objects for each risk metric was 60 (20 per each B^* scaling factor). This means that, regardless of the target selection criterion, at least 45% of the 20 most risky objects were different for every B^* scaling factor. This can be attributed to the fact that varying atmospheric density changes the details of the conjunctions and can move objects with relatively low P_C (or derived criticality) to the top of the target list.

Changing the B^* did not, however, change the fact that particular conjunctions with high individual P_C values contributed more to the total criticality in the debris environment than many other events. Figure 3.11 shows that particular events contributed a large fraction of the probability of any collision taking place in orbit for 70% and 130% of nominal B^*. For lower B^* only 466 (0.015%) conjunctions contributed 50% of the total criticality in the entire environment. The corresponding value for higher B^* was 268 (0.008%) conjunctions. This is similar to what was found in sections 3.1.2 and 3.1.3 where the same fraction of the total criticality in the environment was attributed to 0.007% and 0.014% of the total numbers of conjunctions, respectively.

3.1.5 Discussion

This section has addressed research objectives number 1, 2, and 3 from section 1.6. The key findings of the presented investigations are:

- Particular events with P_C higher than the rest of the events for a given object contributed large portions of the collision probability or criticality accumulated by that object over 30 days. For 20% of the objects, a single event accounted for 35% of the final accumulated maximum criticality in the analysis starting on 7 Nov 2013. This fulfils the objective no. 1.

- 50% of the collision probability in orbit was attributed to 234 (0.007%) and 405 (0.014%) of conjunctions recorded in 2013 and 2014 analyses, respectively. This fulfils the objective no. 2.

- Changing the prediction epoch affected the lists of the most risky objects in the time window - 14 out of 20 (70%) the most risky objects in 2014, according to $P_C|^{MAX}$, $P_C|^{TRUE}$ or $\zeta|^{MAX}$, were not found the most risky in 2013. This fulfils the objective no. 3.

- Varying B^* by $\pm 30\%$ changed $P_C|^{MAX}$ of Zenit-2 by 130.5% as well as changed at least 45% of 20 the most risky objects for a given B^* scaling factor. This fulfils the objective no. 3.

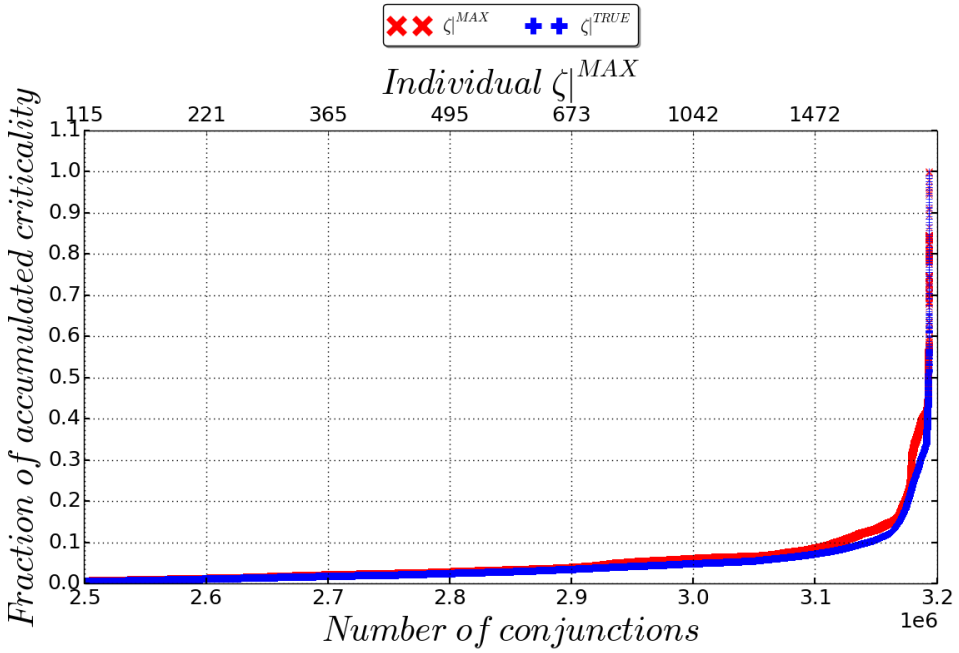

(a) 70%B^*

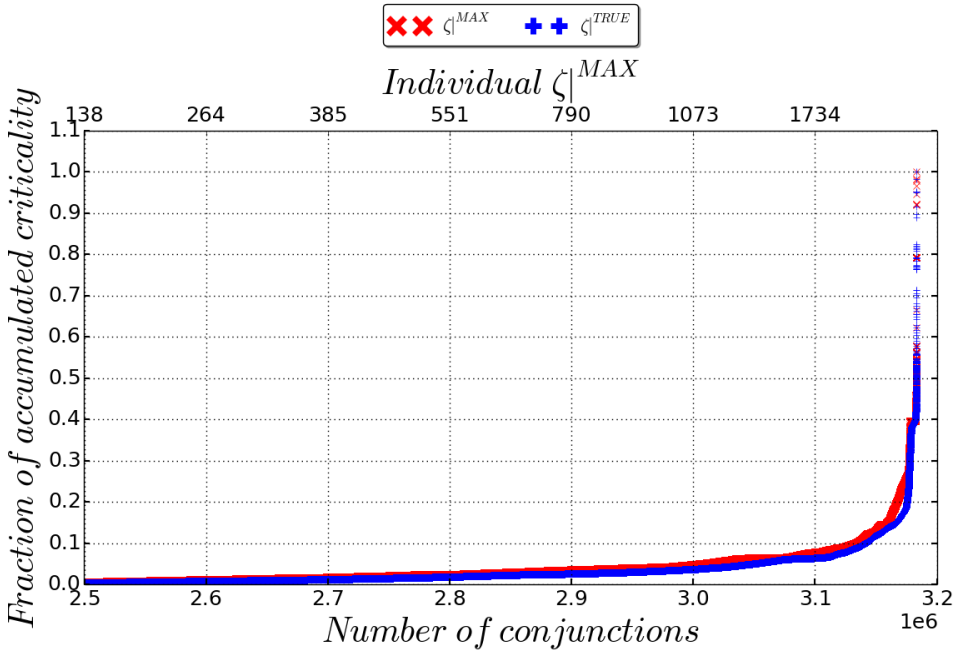

(b) 130%B^*

Figure 3.11: Dependence of the criticality in the entire debris environment on the number of conjunctions. Computed for the nominal B^* coefficient of all the objects decreased and increased by 30%. Conjunctions closer than 20 km recorded amongst the objects in the public TLE catalogue from 7 Nov 2013 over 30 days. Conjunctions sorted in ascending criticality order and fraction of accumulated criticality computed using using Eq. 3.3. Also showing the maximum criticality of individual events ($\zeta|^{MAX}$) corresponding to the given number of conjunctions.

Several simplifications were made when generating the data on which the findings of this section are based. This was done in order to reduce the computational time needed for the analysis and to make it feasible given the computational resources that were available. Even in the current implementation, approximately 1.5 months of CPU time were needed to gather 1 month of conjunction data. Parallelising the code further, and thus requiring more supercomputer nodes and CPUs, would mean that the queue waiting time would be longer, thus increasing the overall time needed for the analyses.

These simplifications included e.g. interpolating the state vectors, using a semi-analytical orbital propagator, estimating sizes of certain objects, ignoring their attitude, estimating uncertainty of the ephemerides, or making several simplifying assumptions when computing the collision probabilities of individual conjunctions. There are several ways in which these could have affected the collision probabilities of the objects.

Missing potentially very close conjunctions or incorrectly computing collision probabilities due to interpolation errors would alter the collision probabilities accumulated by individual objects. Using a physical radius from the database for certain objects but not for the others renders the collision probabilities of the objects with assumed radius different to what they would be when using their actual size. On the other hand, using the database of sizes ensures that the objects much larger than others of the same type, and hence average MASTER 2009 radius, will experience higher collision probabilities as they would in reality. Furthermore, ignoring the attitude of the objects and the simplifying assumptions in the collision probability estimation algorithms mean that different collision probabilities of individual conjunctions could have been found had higher-fidelity algorithms been used.

However, the point of this work was not to examine the conjunctions that took place in reality as accurately as possible. The conjunctions were detected using a set of actual objects to provide a real-life example of a set of the possible events that *could* occur in reality. Despite the assumptions and simplifications that were made, a large spectrum of collision probabilities (from 2.92×10^{-1} to 3.64×10^{-8} for $P_C|^{MAX}$ of Iridium 30 in the 7 Nov 2013 analysis) that were inversely proportional to the miss distance, scaled with size of the objects and ephemeris uncertainty was found for every object. This means that the sets of *exemplar* conjunction geometries found with the TLE catalogue snapshots provided corresponding sets of exemplar collision probabilities and the events with high collision probability were as infrequent as the ones with very low miss distance.

Such high collision probability conjunctions do take place when using higher fidelity ephemerides and algorithms, which leads to collision screening being routinely performed for operational spacecraft [37]. The existence of such events is not an artefact resulting from the simplifications of this study, for example the used ephemerides or the assumed object sizes.

It cannot be guaranteed that all the conjunctions of every object were affected by the simplifications of this study in the same manner. Furthermore, only a part of all the conjunctions were found in this analysis because the size of the objects that can be tracked is limited, and ephemerides of certain objects are classified. When new sensors are commissioned, the minimum size of the objects that can be tracked will decrease [43], effectively increasing the number of debris that we know of. This will cause more orbital conjunctions to be forecast and thus increase the contribution of the many low-probability events to the final accumulated collision probability. All this means that the contributions of the highest-probability events to the final collision probabilities cited here may not be exactly what they would be if using the highest-fidelity input data and algorithms or a more complete set of objects in orbit.

Furthermore, the contribution of the particular events to the final collision probability of every object will depend on the conjunction threshold distance. The lower this distance, the fewer low-probability events are recorded and so the contribution of the high-probability events is reduced. This threshold distance could be scaled with the combined hard body radius or the eigenvalues of the covariance matrix, for example. However, this would not change the fact that some conjunctions would still have P_C orders of magnitude higher than most other events [37] due to, for example, the ratio of the hard body radius to the miss distance and the orientation of the uncertainty regions.

Lastly, the contribution of particular conjunctions could be different when using $P_C|^{TRUE}$ from many TLE snapshots, taken at short intervals of time, as was done for operational conjunction screenings [37], than when using $P_C|^{MAX}$. In order to ensure this is not the case, contributions of the conjunctions with the highest $P_C|^{TRUE}$ found with multiple TLE snapshots were compared to the contributions of $P_C|^{MAX}$ obtained with only one snapshot in Fig. 3.12. The larger the contribution of particular events, the lower the discrepancy between the different metrics. The largest recorded difference between $P_C|^{MAX}$ computed with one and $P_C|^{TRUE}$ obtained with six TLE snapshots taken every five days was 12.7%. This means that using $P_C|^{MAX}$ in the previous analyses did not affect the finding that particular events will contribute more to the final P_C than many others.

All the simplifications and assumptions that have been made do not undermine the finding that the frequency at which conjunctions with extremely high collision probabilities (several orders of magnitude higher than the average) occur is low; for the six objects with the highest $P_C|^{MAX}$ in the Nov 2013 analysis, one in over a thousand of events gave rise to most of the P_C accumulated by the objects. Neither does this change the finding that these relatively infrequent, high-probability events contribute more to the final accumulated collision probability than the remainder of the conjunctions with much lower collision probabilities. Similar behaviour has also been found by McKnight et al. [98].

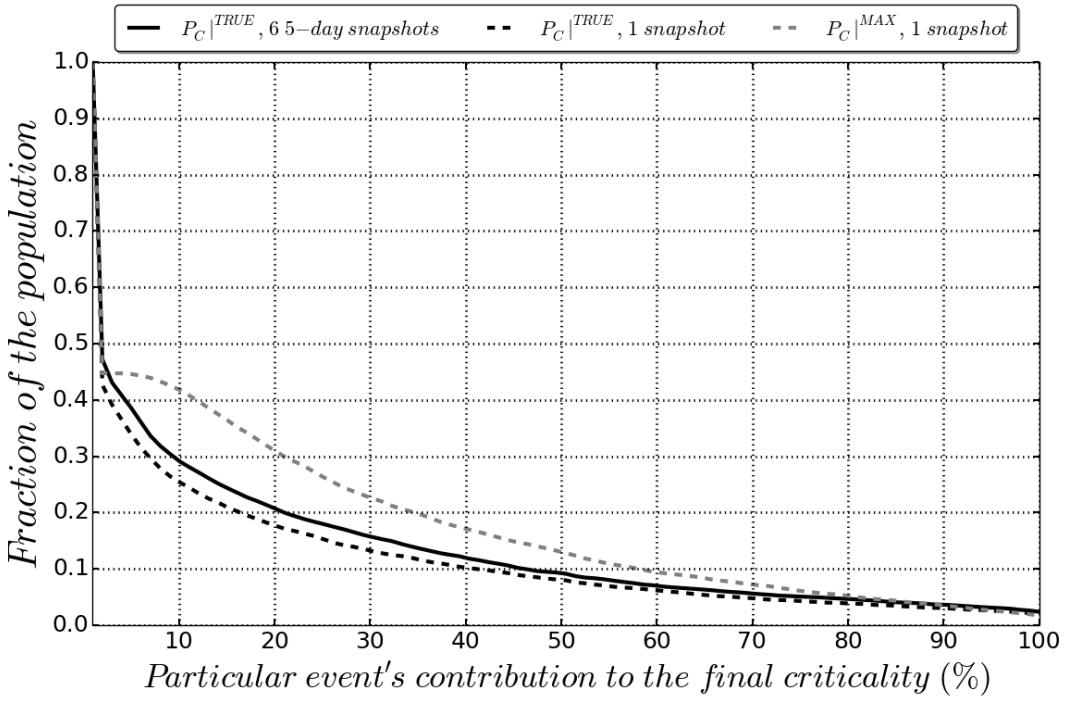

Figure 3.12: Histogram of the contribution of the conjunction with the highest maximum and true collision probability to the final value accumulated by each object. Also showing the same contribution obtained from six TLE snapshots separated by five days. Contribution computed using Eq. 3.2. Conjunctions closer than 20 km recorded amongst the objects in the public TLE catalogue from 7 Nov 2013 over 30 days. More details on using multiple TLE snapshots are given by Lidtke et al. [83].

The simplifications made to obtain the results presented herein mean that the identified objects were not necessarily the ones most likely to be involved in a collision in the analysed time periods. This is especially true because only several events had the largest contribution to the formulation of the target lists and the collision probabilities of these events were affected by the assumptions made. Conjunctions with higher collision probabilities could have taken place and these could not have been identified here and, consequently, objects involved in those could not have been included in the target lists.

Moreover, the fact that the TLE catalogue snapshots obtained at only two epochs were analysed means that the identified high-risk objects may not be the ones with the highest probability of being involved in a collision in the long term. In fact, the most risky objects could not have been present in the analysis if their ephemerides are not part of the "public catalogue" available on Space-Track [135], which is to say they are classified.

Therefore, the exact composition of the lists of objects with the highest collision risk cannot be relied upon. But what remains valid despite the simplifications that were made in this study is the impact of the highest-probability events on the final accumulated collision probabilities of the objects and the collision risk in the entire debris environment.

3.1.6 Conclusions of the fine-resolution investigations

It was shown that particular conjunctions with extremely high collision probabilities often contribute as much as 99% to the collision probability a given object accumulates over a time interval. In two studies conducted here, single, particular events contributed 56% and 58% to the final collision probabilities accumulated by 10% of the objects over 30 days.

This importance of particular conjunctions was also observed for the probability of any collision taking place in the debris environment. It was found that half of this collision probability can be attributed to less than 0.1% of the total number of conjunctions, specifically 0.007%, 0.014%, 0.008% or 0.015% in the four studies that were conducted.

The exact contributions of these particular conjunctions to the final P_C accumulated by the objects will depend on e.g. the conjunction threshold distance. However, it was shown that conjunctions with collision probabilities orders of magnitude higher than the rest will take place, often involving objects that do not have a high collision probability in the long term.

Relatively small changes in atmospheric density were shown to affect details of conjunctions between the objects, most prominently their collision probabilities. Such changes can be caused by, for example, variations in the solar activity that are unpredictable far in advance. This will result in certain objects being involved in conjunctions with high collision probabilities, as in case of Zenit 2 R/B in section 3.1.4.1. Those high-P_C events will cause the objects to experience orders of magnitude higher collision probability than what could be predicted over long periods of time. It was shown that such changes in collision probability can change the objects that are the most risky in a given time window.

Predicting the objects that will be involved in the conjunctions with very high P_C would require methods with fidelity higher than the ones used here. However, even with the highest-accuracy ephemerides, propagators, force models etc., it is not expected that conjunctions could be forecast for more than several days or at most a few weeks ahead. If those were to be prevented, a system capable of addressing potential collisions at short notice, when the conjunctions can still be predicted accurately, would be required.

A debris remediation architecture that operated with such short lead times would differ from what is currently being proposed in the field of space debris remediation. Perhaps even a ground-based laser [95] or an air-launched "nudger" [99] system would suffice to prevent the most-dangerous conjunctions. This can be achieved by exerting a force on the involved objects and increasing their miss distance, and thus reducing the probability of collision between uncontrolled objects.

Certainly the longer the period over which the collisions can be forecast accurately, the easier it would be to implement a mission to prevent them. This can only be achieved if improvements in space surveillance and tracking (SST) systems, propagators and force models are made. Nonetheless, extremely rapid deployments of such debris remediation missions (order of days) will need to take place if such an approach to debris remediation is to be followed.

Of course, all debris remediation strategies that do not remove the collision risk entirely, by removal of all the objects, might not prevent all the collisions. But, unlike a statistical target selection approach, a collision prevention method could use the most accurate collision forecasts and hence could potentially address the most likely collisions that cannot be reliably forecast far in advance. Evolution of the collision probability, encounter geometry, object details, and potential impact of a collision could also be taken into consideration.

Furthermore, an approach that addresses individual conjunctions, rather than objects likely to be involved in a collision in the long term, allows an accepted risk threshold to be set. This enables the residual risk, due to some of the conjunctions being ignored, to be quantified. Being able to set such a threshold enables the benefit of reducing the residual risk to be traded off against the cost of preventing more collisions.

However, whilst investigating the variability of the target lists to atmospheric density, several pairs of objects were noticed to have dangerous conjunctions regardless of what the atmospheric density was. This suggests that certain object pairs are prone to have conjunctions with one another. Also, certain objects with large cross sectional area and mass that are located in densely populated orbital regimes are bound to take part in many conjunctions and thus accumulate collision risk faster than other objects. An example of such a spacecraft is Envisat, which was found close to the top of the target lists in all the studies performed in this chapter. This means that such spacecraft could be good candidates for active removal because they will take part in many conjunctions over time and reducing the collision probability of those events could be less cost effective than removing the object entirely.

It is hence recommended that a discussion about the fundamental approach to space debris remediation be initiated and an *ad hoc* architecture, which prevents the collisions when they can be forecast accurately [99], be evaluated alongside popular approaches that remove mass from the environment using statistical target selection schemes described in section 1.4. This is primarily because, if not all or most of the derelict objects are removed, collisions may still occur despite the efforts to prevent them by removal of statistically important objects.

3.2 Analysis of evolutionary debris model results

It was shown in section 3.1 that particular conjunctions, with high collision probabilities, dominate others as far as the P_C of individual objects accumulated over one month is concerned. These particular events were also shown to be the source of most of the collision risk in the entire debris environment. In order to verify that presence and importance of such events is not an artefact originating from the method developed in Chapter 2 the results of DAMAGE, the previously used evolutionary debris model, were analysed. This investigation also addressed the research objective number 4 from section 1.6, which was aimed at demonstrating that more future collisions are expected to be caused by high-P_C close approaches.

The collision probabilities of close approaches found in DAMAGE represent the probability of two objects colliding over an interval of time, here 5 days, which is fundamentally different to collision probabilities of individual conjunctions found in section 3.1. In fact, the quantity actually used in DAMAGE is the collision rate computed using the algorithms outlined in section 1.3.1, which can even exceed 1.0. However, the term "collision probability" will be used when referring to the collision rates found with DAMAGE because they are typically in the range $[0, 1]$ and span several orders of magnitude. Thus, these "collision probabilities" are similar to what was computed in section 3.1 and events with extremely high P_C are relatively rare in both cases. Therefore, similar analyses will be performed on both sets of data, i.e. DAMAGE conjunctions will be assumed to be proxies of actual conjunctions. This assumption will be acknowledged when drawing conclusions based on the following investigations, however.

3.2.1 Events with high collision probability in DAMAGE

Close approach and collision events from 100 Monte Carlo runs of DAMAGE were analysed. These were obtained in the "mitigation only" scenario from Table 1.1. Close approaches were all the conjunctions recorded between the objects in the simulation, while collisions were the subset of conjunctions in which the objects collided. It was deemed insightful to analyse the collision probabilities of events that resulted in collisions to better understand what types of conjunctions might lead to increasing the number of objects in the debris environment. Histograms in Fig. 3.13 show how the collision probabilities of close approaches and collisions, from all the Monte Carlo runs, were distributed.

Figure 3.13a shows that the minimum collision probability, which resulted in a collision, is approximately four orders of magnitude higher than the lowest P_C recorded in the simulation (1.00×10^{-7} and 4.58×10^{-11}, respectively). The collision probability of 36.2% of close approaches in Fig. 3.13b was in the range from 1×10^{-5} to 1×10^{-4}. 62.8% of close approaches, which resulted in a collision, had P_C in the same range. There is a clear shift towards high-P_C events amongst collisions relative to close approaches. This is particularly visible on Fig. 3.13b, when noting that 83.3% close approaches had $P_C \leq 1 \times 10^{-3}$, whereas such collision probabilities resulted in a collision in only 11.8% cases

Not all conjunctions with $P_C \in \left[1 \times 10^{-1},\ 1 \times 10^{-0}\right]$ resulted in a collision. This stresses the point that even events with very high probability of occurring may not take place, and *vice versa*.

It can be concluded that particular conjunctions, with collision probabilities orders of magnitude higher than most of the events, also take place in the simulations performed using evolutionary debris models like DAMAGE. They are not an artefact created by the method developed in Chapter 2 and used to obtain the results from section 3.1. Such conjunctions with collision probability several orders of magnitude higher than most others do occasionally occur in reality, regardless of the algorithms used to estimate the collision probabilities [37]. Therefore, observing such a trend in the data presented in this section increases confidence in the results of this work.

More importantly, it appears likely that the conjunctions with relatively high P_C are responsible for causing more orbital collisions than the numerous conjunctions with very low collision probabilities. This is to be expected because collisions in DAMAGE are simulated by drawing random numbers and comparing them to the P_C of every close approach. Similar results are obtained when using a random number generator to produce "collision probabilities" and comparing them to another set of random numbers, which decide whether a collision has taken place. However, this finding confirms the hypothesis behind the research objective number 4 from section 1.6.

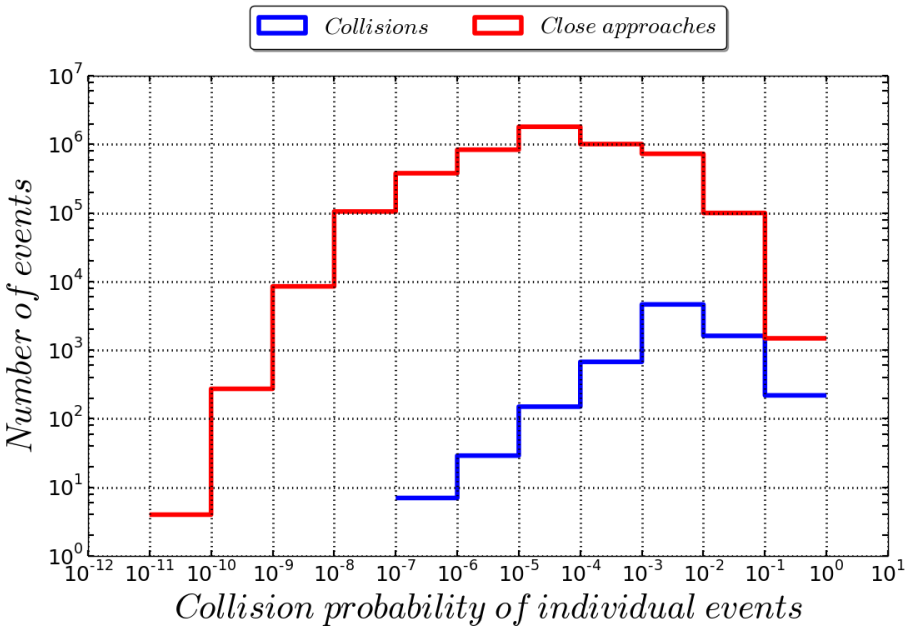

(a) Actual distributions

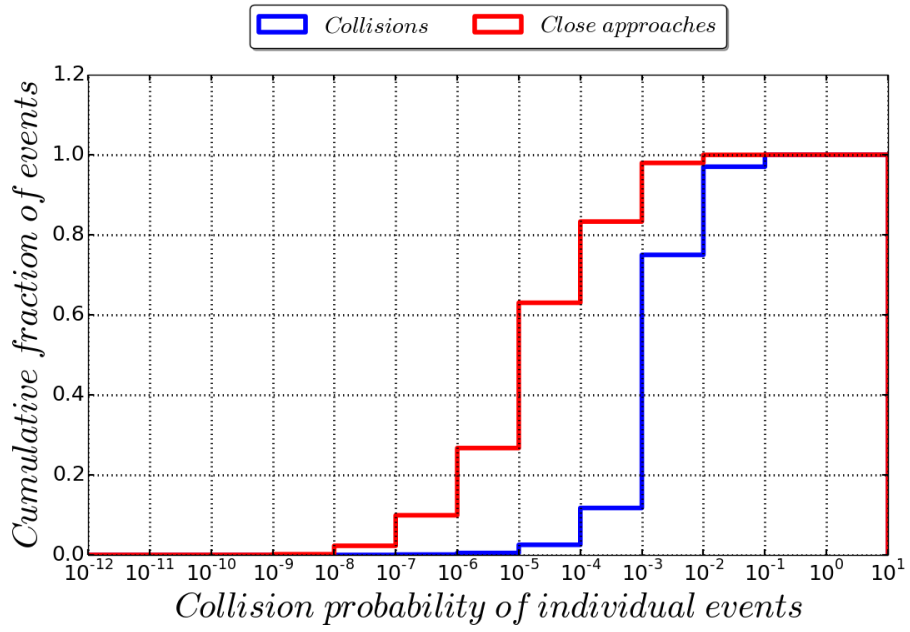

(b) Fractions of the total number of events

Figure 3.13: Histograms of the collision probabilities of close approaches, which did not result in a collision, and collisions. Showing absolute numbers of events as well as fractions of events that had a particular collision probability. Data from 100 runs of the "mitigation only" scenario from Table 1.1. Data provided by Dr Hugh G. Lewis.

Lastly, such rare, high-P_C "conjunctions" found using evolutionary debris models might impact ADR target selection. If an object takes part in one or several high-P_C "conjunctions" in DAMAGE, it could be brought close to the top of the potential ADR target list if P_C is used as a selection metric. However, these events might not represent what will happen in reality and, therefore, the collision probability accumulated by the hypothetical object could be several orders of magnitude higher than what could be found when performing daily conjunction screenings. If this ADR target list is then used for actual active debris removal, the hypothetical object could be unnecessarily removed from orbit.

3.2.2 Importance of particular conjunctions in DAMAGE

The importance of single, particular events in the individual Monte Carlo runs was analysed. Figure 3.14 shows the evolution of the accumulated P_C with the number of events in every Monte Carlo run. It can noted that particular events lead to sudden and large changes in the accumulated P_C. This effect is particularly evident for collisions because much fewer events allow discerning the effect of those particular conjunctions more clearly.

The contribution of the event with the highest collision probability to the final accumulated P_C in a given Monte Carlo run was computed and is presented in in Fig. 3.15. The particular events with relatively high P_C can contribute as much as 99.86% to the collision probability accumulated in the entire debris environment in a given Monte Carlo run. For half of the MC runs, the collision with the highest P_C in a given Monte Carlo run contributed 37% to the final collision probability in that MC run. The corresponding contribution for close approaches was 46%. This signifies that particular events, with relatively high collision probabilities, can dominate many other close approaches with lower P_C. This observation agrees with what was observed in section 3.1 that used completely different algorithms. However, in the present data, the accumulated collision probability of close approaches saturates. Such behaviour was also observed amongst the likelihood of collisions, but only in two Monte Carlo runs. This was investigated in more details in Chapter B of the Appendix and it was found that the P_C accumulated in the investigated 100 MC runs reached 99.99% after 8 to 32 years. Beyond this point, assuming that collision rates from DAMAGE are similar to collision probabilities becomes invalid. This is why fluxes of objects at a target are often used to rank the targets according to their long-term collision probabilities, e.g. by Radtke et al. [124].

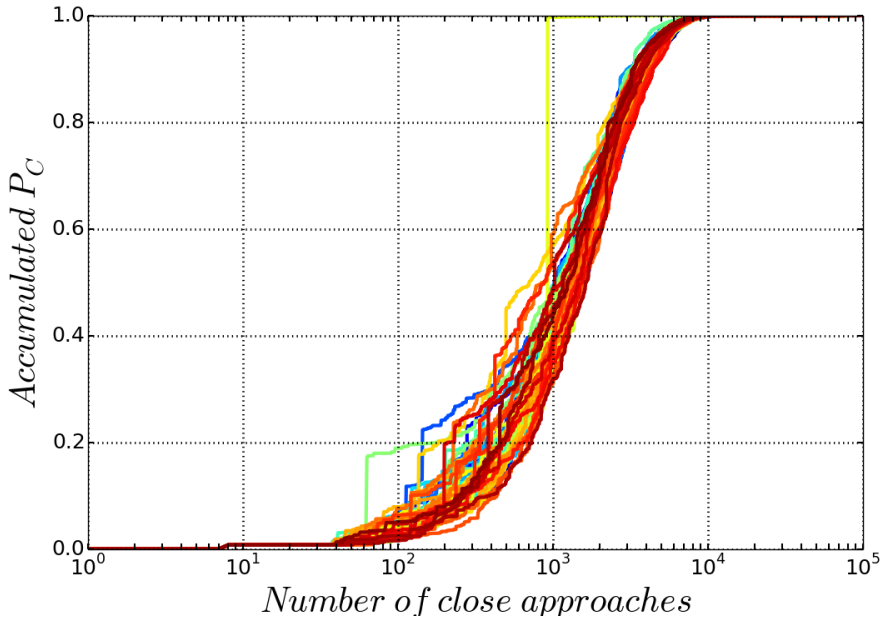

(a) Close approaches

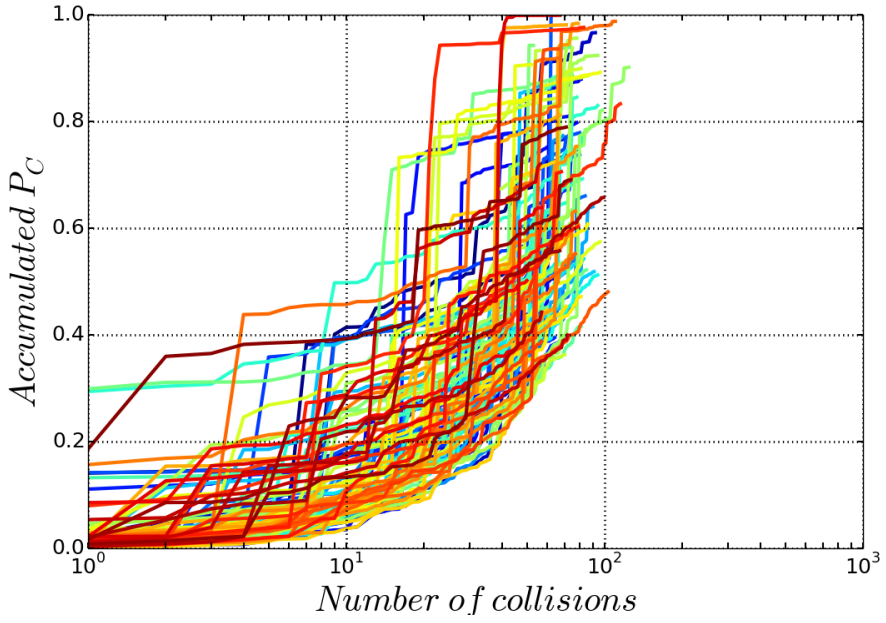

(b) Collisions

Figure 3.14: Evolutions of the accumulated collision probabilities in the entire debris environment with the number of events in every Monte Carlo run. Examining close approaches, which did not result in a collision, and collisions separately. Data from 100 runs of the "mitigation only" scenario from Table 1.1. Data provided by Dr Hugh G. Lewis.

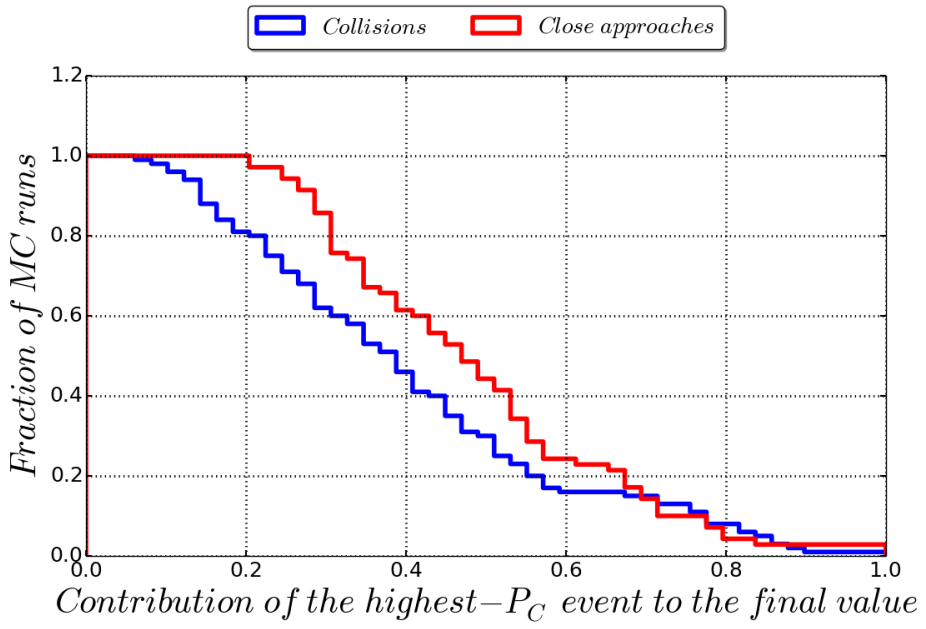

Figure 3.15: Cumulative histogram of the contribution of the event with the highest collision probability in a given Monte Carlo run to the final value accumulated in the entire debris environment. Data from 100 runs of the "mitigation only" scenario from Table 1.1. Data provided by Dr Hugh G. Lewis.

3.2.3 Discussion

A total of 7 027 475 close approaches were recorded in the 100 Monte Carlo runs that were analysed. Out of these, 24 close approaches with collision probabilities greater than 1.0 were recorded. Such values are inconsistent with the second axiom of probability [25]. This is a manifestation of the fact that collision probabilities computed in DAMAGE represent a fundamentally different quantity than the probabilities analysed in section 3.1. As such, these values should not be compared directly. Collision probabilities in DAMAGE are computed using the algorithms outlined in section 1.3.1 and represent the probability that two objects will collide over a period of time.

However, the collision rates in DAMAGE span several orders of magnitude and events, which have an extremely high collision rate relative to others, are extremely rare. Thus, observing that such particular events dominate others, as far as the accumulated collision probability is concerned, can be used to verify the findings from section 1.3.1.

Also, analysing the close approaches from DAMAGE is useful to understand why active debris removal, simulated within DAMAGE, does not always prevent the growth of the number of space debris, as was reported in section 1.3.2.2. Not all of the evolutionary debris models use the same algorithms, and not all of them identify conjunctions between objects, for example DELTA [14]. However, even if a different stochastic debris model was used, collisions would still be simulated using random numbers. Thus, the objects that were ranked the most risky and were removed via ADR are not necessarily the ones that were involved in collisions.

3.2.4 Conclusions

It was found that close approaches with high collision probabilities cause more collisions than other events in DAMAGE simulations. This is the reason why ADR is unsuccessful in some Monte Carlo runs, as exhibited by the tail above the mean visible in Fig. 1.9b and Fig. 1.7a. This is because different objects are removed in those runs than are involved in collisions. ADR is simulated by removing five objects (in the "ADR 5 per year" scenario) that are forecast to have the highest target selection metric, e.g. $P_C \times m$, for the upcoming year. However, these forecasts do not represent the close approaches, which actually take place in the MC runs and based on which the collisions are simulated. This is analogous to a situation where the objects that have high collision probability in the long term are not always the ones that are going to be involved in high-P_C conjunctions. Thus, preventing collisions on an *ad hoc* basis, when they can be forecast, should be analysed as a possible means to space debris remediation.

Chapter 4

Assessing the prevention of collisions between derelicts

It was shown in Chapter 3 that particular conjunctions with relatively high collision probabilities might sometimes involve objects that are not large in mass and cross sectional area, and are not located in densely populated orbital regimes. Therefore, these particular conjunctions, and the resulting collisions, may occur despite active debris removal. Thus, if not all objects in orbit can be removed, which would prevent all collisions, these particular conjunctions need to be prevented in order to limit the growth of the number of object in orbit. This effect of the particular conjunctions was the hypothesis behind the investigations carried out in Chapter 3, as shown in Fig. 1.10. The following chapter studies whether such conjunctions can be prevented in an *ad hoc* manner and thus reduce the growth rate of the number of debris, which is the following block in Fig. 1.10.

Section 4.1 briefly reviews the work of other authors which introduces the concept of *ad hoc* derelict collision prevention, also referred to as "just in-time collision avoidance" (JCA) [99]. A JCA simulation framework is then developed and applied to test, using DAMAGE to enable direct comparison to other space debris remediation and mitigation means, the viability of JCA. The key factors, which are associated with the requirements set for a JCA system, are identified and their likely ranges established. Permutations of different values of these factors are then combined into JCA scenarios. These scenarios are then used in a sensitivity study, which shows how the predicted population of objects in orbit varies depending on the requirements set for JCA. The conjunction detection and assessment framework described in Chapter 2 is also used to estimate the rate of JCA false alarms, which will drive the cost [99] of JCA, for the same scenarios. The effects and false alarm rates of various JCA scenarios are then compared to enable development of a cost-effective JCA system, which could complement active debris removal and space debris mitigation measures. The way in which these topics are discussed throughout this chapter, as well as the use of the developed simulation tools, is shown in Fig. 4.1.

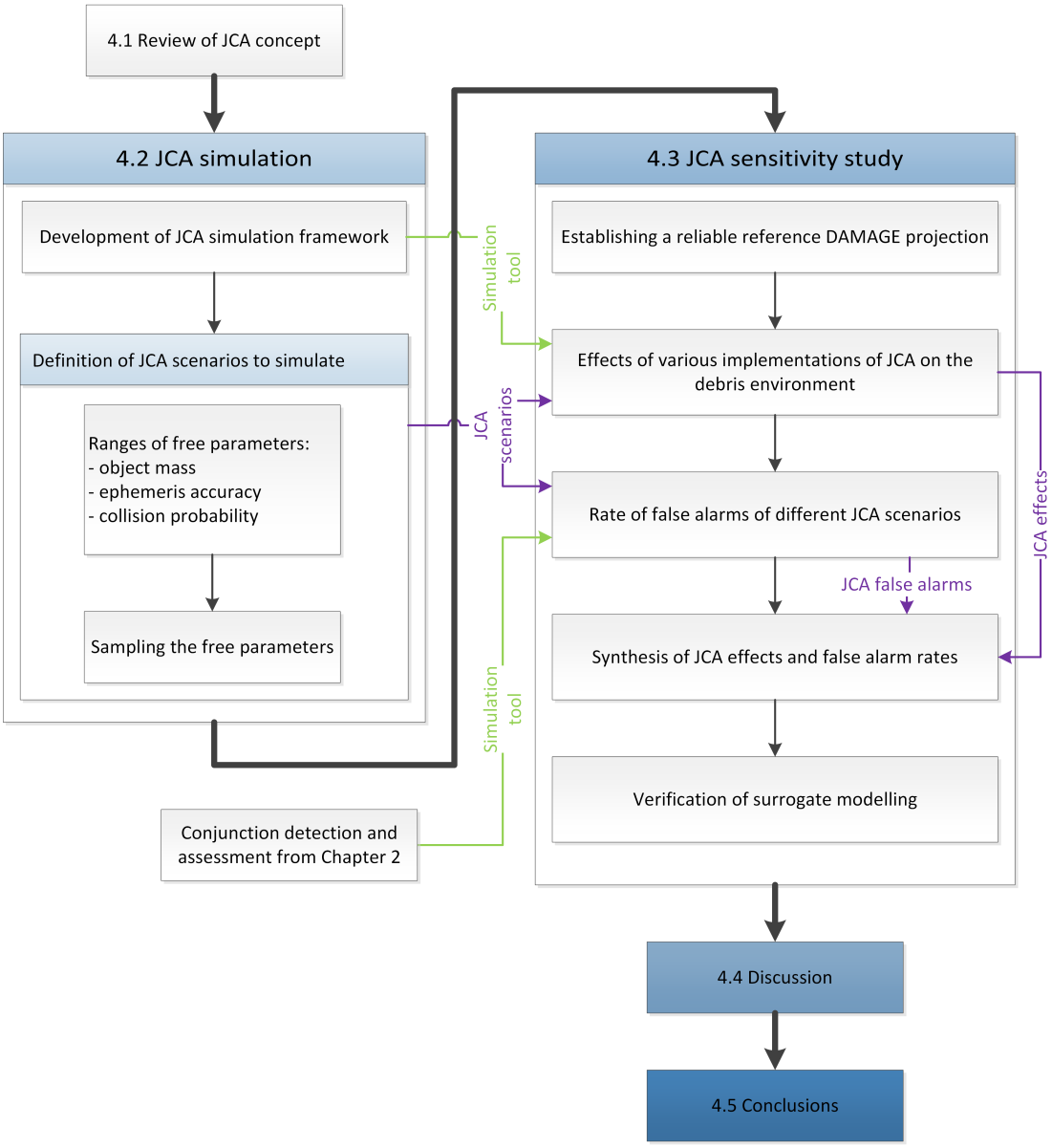

Figure 4.1: The flow of the topics covered in this chapter, including the development and use of existing simulation tools. Grey arrows indicate the chronological order, in which the indicated topics are discussed. Green arrows indicate utilisation of the simulation tools developed in this work, whereas purple arrows show where the generated data are used.

4.1 Review of the JCA concept

It has been suggested that photon pressure from medium-power (5 to 10 kW, continuous wave) ground-based lasers could be used to conduct collision avoidance between relatively small objects incapable of manoeuvring themselves [136]. In order to implement such an orbital collision prevention scheme, comprehensive collision forecasting, treating all the catalogued objects as primaries rather than secondaries as done currently, would need to be carried out on a daily basis. If a conjunction with collision probability higher than some threshold, $P_{C,TH}$, is predicted, laser stations would illuminate the two involved objects. Alternatively, only the object with higher area-to-mass ratio would be illuminated because it will experience larger momentum change for the same illumination time and laser power [95]. Such laser illumination will deliver an along-track ΔV, which will make the objects phase with respect to each other, thus rendering the collision less probable (the event's P_C will be lowered until it is deemed sufficiently low) [95]. In order to achieve a low P_C, the objects have to be moved far enough apart so that the uncertainty regions, where the objects might be present at the time of the closest approach, no longer significantly overlap (the displacement has to be in the same order of magnitude as the orbit uncertainty, ideally twice as large [95, 97]).

However, commercially-available, non-military grade laser systems were found capable of moving an object with mass of at most 100 kg by 100 m in 48 hours of illumination time [95]. In order to extend the idea of preventing orbital collisions to higher-mass derelicts, it has been suggested to affect their trajectories by dispersing clouds of gas along the derelicts' orbits [99]. When the two objects traverse the gas clouds, they will exchange momentum with gas particles, which will deliver an along-track ΔV to the objects. The gas clouds would be delivered into orbit on board air-launched ballistic missiles, which would lower the cost of preventing a single derelict-on-derelict collision c.f. orbital launches. The intervention would be planned hours to days before the time of the closest approach in order to increase confidence that a collision is going to take place if no action is taken [99]. Reducing the number of interventions as much as possible will lower the total cost of JCA.

To limit the number of false alarms, or prevention actions that were unnecessary because a collision would not have taken place anyway, the accuracy of the ephemerides used to forecast conjunctions has to be high [95, 97]. Fewer false alarms would reduce the total cost of derelict-on-derelict collision prevention, thus making it more likely to be implemented [130]. The number of JCA actions can be reduced further by only reacting to collisions involving large objects [99], or ones that are likely to have a severe impact on the debris environment should they fragment (will involve large-mass objects located in densely populated orbital regimes etc. [95]).

The cost of every JCA action would also be reduced by improvement of the ephemeris accuracy because the objects would need to be displaced less to ensure that the collision will not take place. This equates to fewer laser stations with lower-power lasers [95] or lower-mass ballistic missiles [99] that would need to be used.

Preventing the collisions between derelicts has been suggested as a possible means to reduce the growth rate of the number of objects in orbit by two groups of authors [95, 99]. However, the effects of such an initiative on the debris environment have not been studied using evolutionary debris models, despite the recommendations made by Mason et al. [95]. The JCA action thresholds, namely the minimum size (or mass) of the potentially colliding objects as well as the collision probability ($P_{C,TH}$), have to be tuned to lower the cost of JCA to an economically feasible level. At the same time, these parameters will affect the number of collisions prevented and so also the impact that JCA will have on the debris environment. These parameters have to be studied together with the ephemeris accuracy of the space object catalogue being used to perform collision forecasts. This is because varying accuracy levels will result in different P_C that can be predicted for the collisions, and so will affect which events fall above $P_{C,TH}$. This ephemeris accuracy will also affect the necessary displacement of the objects. The remainder of this chapter focuses on analysing derelict collision prevention and identifying which collisions should be prevented to achieve a given result on the debris environment. A JCA simulation framework is developed first. It is then applied to simulate different JCA architectures in a sensitivity study of the free parameters, i.e. ephemeris accuracy, $P_{C,TH}$, and mass threshold of the objects.

4.2 JCA simulation

As described in section 1.3.1, the spatial and temporal resolutions at which evolutionary debris models, including DAMAGE, find actual close approaches between objects in orbit is low, relative to the framework developed in Chapter 2 and operational conjunction screenings. What is more, when a collision takes place in DAMAGE, the separation distance between the objects might be in the order of tens of kilometres, depending on the user-defined conjunction threshold distance. This can be discerned from the histogram of distances between objects at the epochs when they collided (blue curve in Fig. 4.2a). DAMAGE finds more distant than close conjunctions, regardless of whether the close approach ends up being a collision (blue curve) or not (red curve) when compared to the high-resolution code developed in Chapter 2 (green curve). Also, the collision probabilities found with DAMAGE do not correlate to the found miss distances, because they do not depend on the position uncertainty. Instead, an algorithm similar to that by Liou and Johnson [88] is used to find the collision probabilities. The miss distances obtained using both approaches may have come from the same underlying distribution, as shown by the high correlation ($R = 0.9723$) on the quantile-quantile plot in Fig. 4.3a.

Therefore, the DAMAGE close approach detection algorithm is representative of reality, but the collision miss distances it identifies are often larger than the physical size of the objects. Consequently, if collision probability was computed for DAMAGE close approaches using realistic ephemeris accuracy and P_C estimation algorithms used operationally (reviewed in section 2.3), the resulting P_C would, in most cases, be smaller than a double floating point precision number.

Collision rates computed by DAMAGE could be utilised to simulate JCA, however those do not use realistic ephemeris uncertainties, as described in section 1.3.1. Also, as can be seen in histograms and the quantile-quantile plot in Fig. 4.2b and Fig. 4.3b, the collision rates computed by DAMAGE follow different distributions that what can be expected when using higher-fidelity conjunction detection and assessment algorithms. This means that it is impossible to map from DAMAGE collision rates to a realistic P_C. Therefore, in order to simulate JCA using realistic ephemeris uncertainty and conjunction assessment algorithms, an approach that does not use DAMAGE collision rates or miss distances had to be developed. This JCA simulation tool is described in section 4.2.1. The ranges of free JCA parameters, which were used in the sensitivity study, are then reviewed in section 4.2.2.

4.2.1 JCA simulation methodology

It was shown in Fig. 4.2a that the miss distances, which correspond to collisions simulated in DAMAGE, are orders of magnitude larger than the physical size of the involved objects. This is because evolutionary debris models, like DAMAGE, typically have coarse spatial and temporal resolutions to enable analyses to be conducted on the timescale of decades to centuries. Therefore, one "close approach" in DAMAGE is a proxy of a number of close approaches that the two objects might experience over a period of time. This conjunction is not necessarily the one with the lowest miss distance that resulted in the collision. Such large collision miss distances do not compromise the results of the debris models as such. However, they make it impossible to link the results of DAMAGE to the conjunction forecast that would be obtained operationally, because the collision probabilities of such distant conjunctions would be vanishingly small.

If a collision takes place, the two involved objects have to physically interact. If their attitude is ignored, this criterion reduces to the centres of mass of the objects being closer than the collision radius r from one another (reviewed in more detail in section 2.3). To recover the geometry of the close approach, which resulted in the collision, the collision miss distances from DAMAGE are scaled to r. Here, this geometry is used with the P_C estimation algorithms developed in section 2.3. Due to the fact that such simulated miss distance will be comparable to r, direct numerical integration of Eq. 2.21 is employed. This follows the analyses presented in section A.3.2. The collision radius r is used as

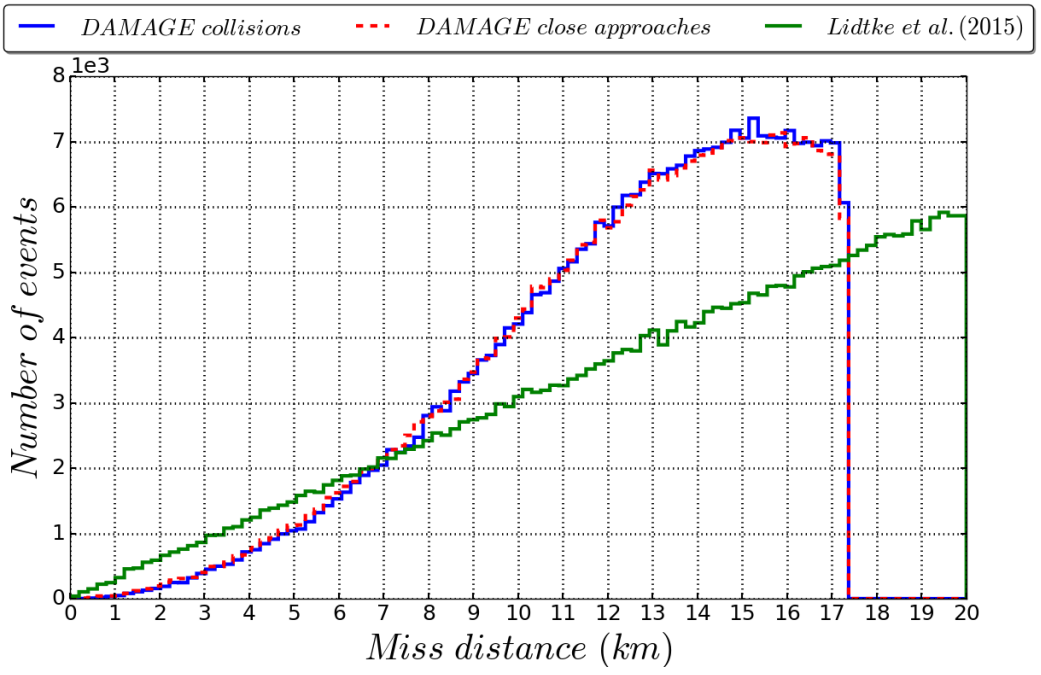

(a) Miss distance

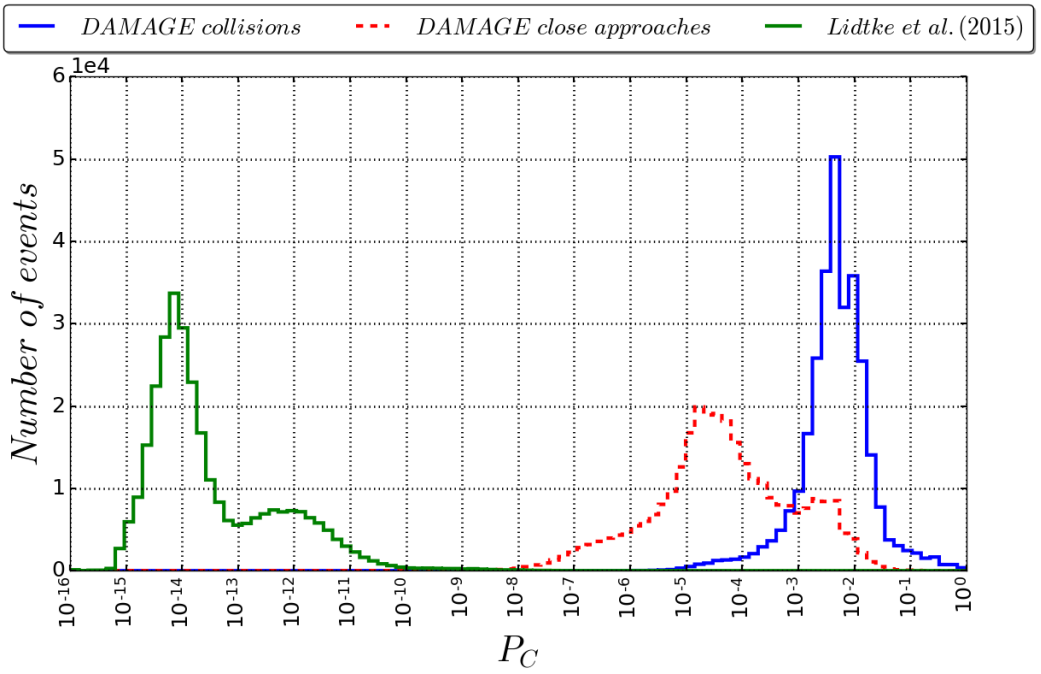

(b) Collision probability

Figure 4.2: Histograms of miss distances and collision probabilities obtained with DAMAGE and the conjunction detection and assessment framework developed in Chapter 2. 300 000 conjunctions from work by Lidtke et al. [83], and close approaches and collisions obtained with DAMAGE using the "mitigation only" scenario from Table 1.1.

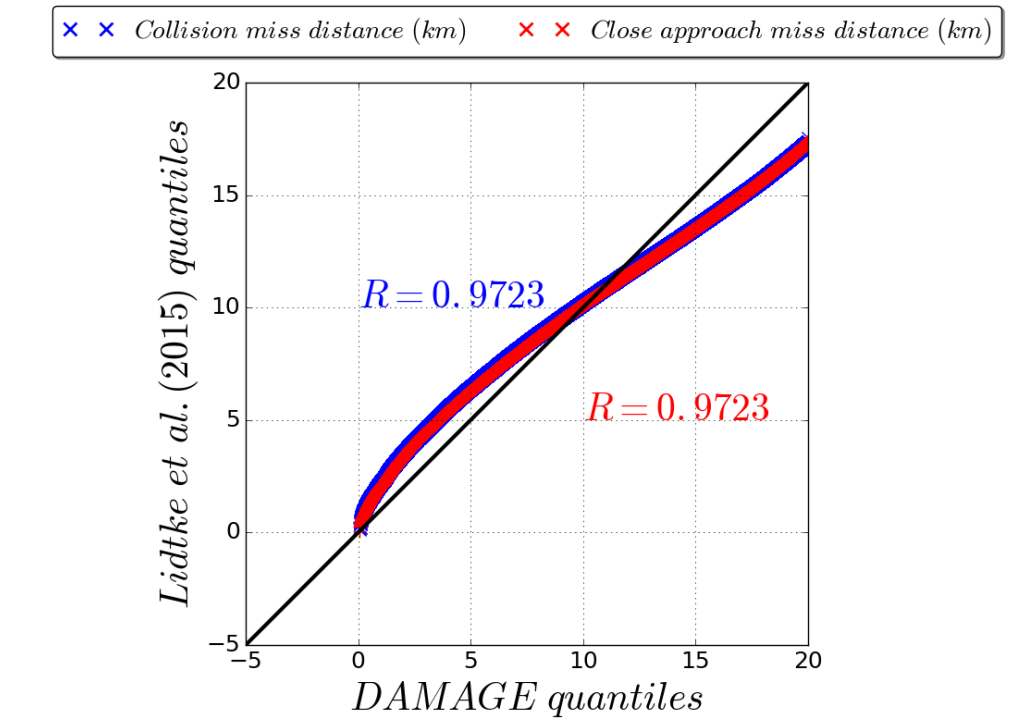

(a) Miss distance

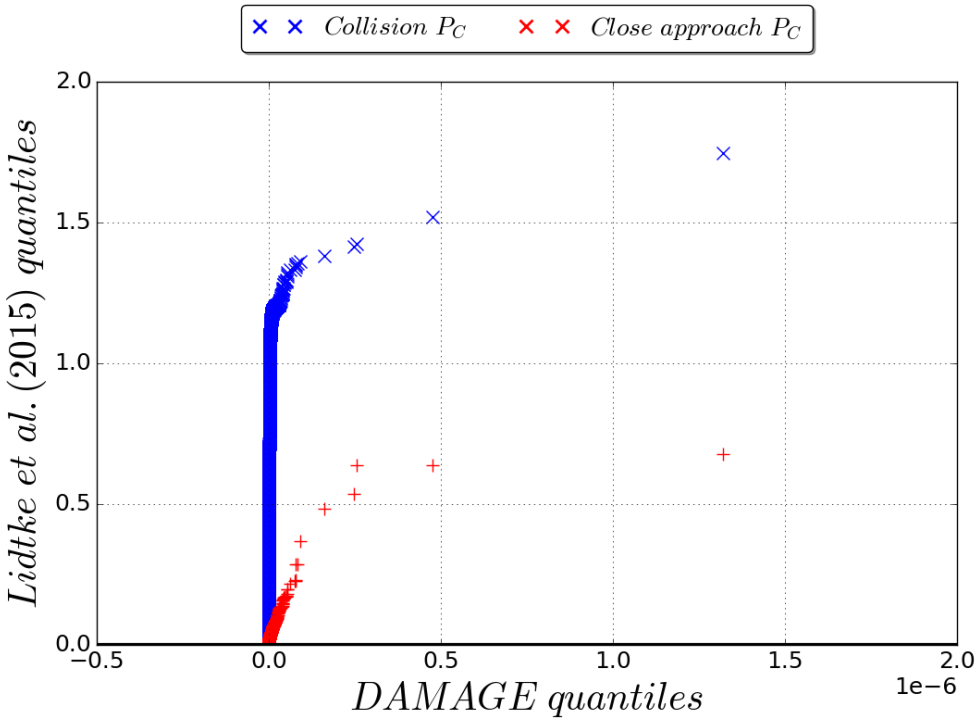

(b) Collision probability

Figure 4.3: Quantile-quantile plots of miss distances and collision probabilities obtained with DAMAGE and the conjunction detection and assessment framework developed in Chapter 2. 300 000 conjunctions from work by Lidtke et al. [83], and close approaches and collisions obtained with DAMAGE using the "mitigation only" scenario from Table 1.1.

the simulated separation between centres of mass, instead of e.g. zero separation, in order to yield *the lowest* P_C that could be forecast for the collision (lower separation will result in higher P_C). This means that if JCA is performed on all conjunctions with P_C higher than the $P_{C,TH}$ recommended here, the resulting change in the number of objects in orbit will be at least as much as the one predicted here (to within space debris model accuracy, reviewed in section 1.3.2). However, the miss distance for certain collisions could be forecast to be greater than it will be in reality due to propagation inaccuracies. This will lead to these collisions not being prevented by JCA because they will be below the collision probability action threshold. In order to deal with such propagation inaccuracies, details of the most dangerous conjunctions would need to be refined before the TCA through dedicated tracking, as is done for operational spacecraft [37].

In the process of changing the conjunction geometry, the primary object's position is kept fixed, whereas the other object (secondary) is moved inside the B-plane (plane normal to the relative velocity vector) to within r of the primary. This is because it is the miss distance in the B-plane that is used to compute the P_C, and so moving the secondary in the inertial frame could result in a miss distance different from the intended one. Thus, to enable P_C computation, the secondary is moved along the relative position vector in the B-plane. The inertial velocities of the two objects are kept constant throughout the process. This assumes that the location of the close approach along the orbits of the two objects, and so also the relative velocity at the TCA found with DAMAGE, is identical to the one during the actual collision. This is an approximation, which assumes that the two orbits' relative orientation does not vary significantly over the duration of one time step of DAMAGE, which was used to find the close approaches. This may not be the case, if the orbits of the collided objects have different nodal precession rates, for example. However, if *sufficiently many* collisions are analysed and the time step of DAMAGE is small enough, this approximation allows all the typical conjunction geometries, which result in collisions, to be included in the sample, on which the conclusions are drawn. The validity of this assumption is also investigated in section 4.4. An example conjunction geometry that resulted in a collision in DAMAGE, together with the simulated position of the secondary, is shown in Fig. 4.4.

Once the simulated collision geometry is recovered, a number of metrics are checked against associated thresholds to see if JCA would be performed for this conjunction. These thresholds correspond to JCA requirements and are aimed to reduce the number of JCA missions, and thus the overall cost of the JCA initiative, while preventing collisions that might have severe consequences. The quantities that should be evaluated for every conjunction are associated with the likelihood and severity of the possible collision and are [95, 99]:

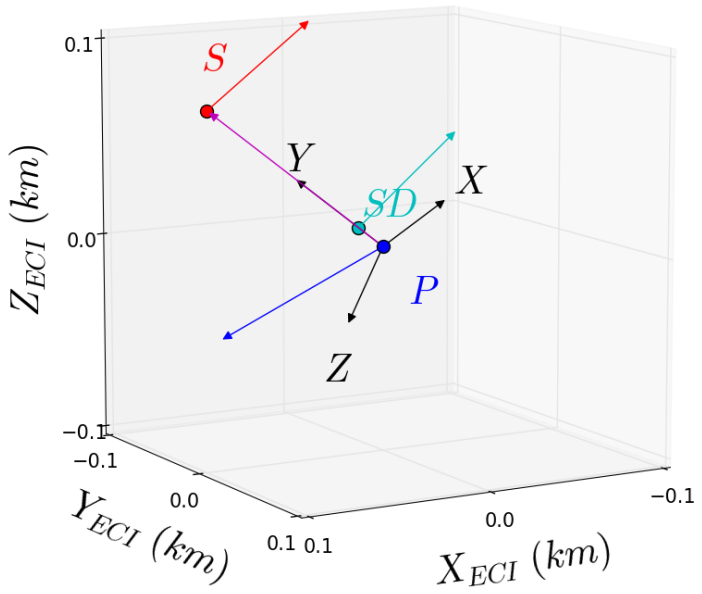

Figure 4.4: Scaling the miss distance of a DAMAGE close approach to simulate the conjunction that resulted in a collision. The secondary object (red S) is moved to position SD, i.e. to a collision radius from the primary (blue P) to simulate a collision. The secondary is moved along the relative position vector at the TCA (shown with a magenta arrow). The inertial velocities of the primary and secondary are shown with blue and red arrows, respectively. X_{ECI}, Y_{ECI}, and Z_{ECI} are the axes of an inertial frame, while black arrows show the orientation of the B-plane.

- collision probability P_C - operationally used metric for collision avoidance that enables the conjunctions, which are likely to result in collisions, to be identified [37, 70],
- mass of the involved objects m - if the objects involved in a conjunction are small, they should not produce many fragments even if they collide [68], so the event should not significantly affect the debris environment and can be ignored,
- conjunction altitude h - it is a constraint stemming from the fact that not every altitude can be reached with short advance warning times, which are expected for JCA [99].

One final aspect of JCA, which should be considered, is the ephemeris accuracy. Even though not part of the JCA system *per se*, ephemeris accuracy was considered in this study because it can affect the number of JCA actions and the number of prevented collisions [95, 99]. All these parameters are described in more detail in section 4.2.2. The ranges for them, which were simulated in the sensitivity study, are also given in section 4.2.2.

If a given conjunction exceeded all the set thresholds with the simulated ephemeris accuracy, the JCA action was simulated by assuming that the collision was prevented from taking place. In order to do so, all the objects that resulted from the collision at hand were removed from the population of objects at the epoch of interest (the final population in 2213 was used). Note that this also includes fragments of collisions that took place between this collision's fragments and other objects, i.e follow-on or "feedback" collisions. However, it ignores all the collisions that the objects *could have* taken part in had they remained in the DAMAGE simulation. This assumes that such potential collisions would also be prevented via JCA or, if the objects kept being involved in dangerous conjunctions, they would be removed from orbit altogether.

If the collision prevented via JCA was catastrophic and two objects were completely destroyed in the process, two objects were added into the population snapshot because, if JCA was successful, these objects would not be destroyed during this collision. The block diagram of the JCA simulation framework is shown in Fig. 4.5.

4.2.2 Range of the free JCA parameters

This section describes how the parameter ranges for the JCA sensitivity study were chosen. They were set to provide data on which the requirements for the JCA chain, from ephemerides accuracy to JCA action thresholds, can be compared and traded-off.

4.2.2.1 Object mass

Mass of the colliding objects is an important JCA criterion because the number of fragments a collision will generate is proportional to object mass [51, 68]. A breakup model is used in DAMAGE to determine how many fragments every collision will produce; the same logic can be applied to conjunctions to identify the ones with the potential to generate many fragments, and thus decide whether they should be prevented if this number is higher than a chosen threshold [95]. Mass can also be used to estimate the size of the objects; Fig. 4.6 shows the relationship between the radius of the resident space objects and their mass, together with the correlation coefficient between the two ($R = 0.4202$). Figure 4.7 presents the distribution of the dry masses used to generate Fig. 4.6. In Fig. 4.7, 26.6% of objects had mass of 100 kg or greater. Several sharp decreases in the

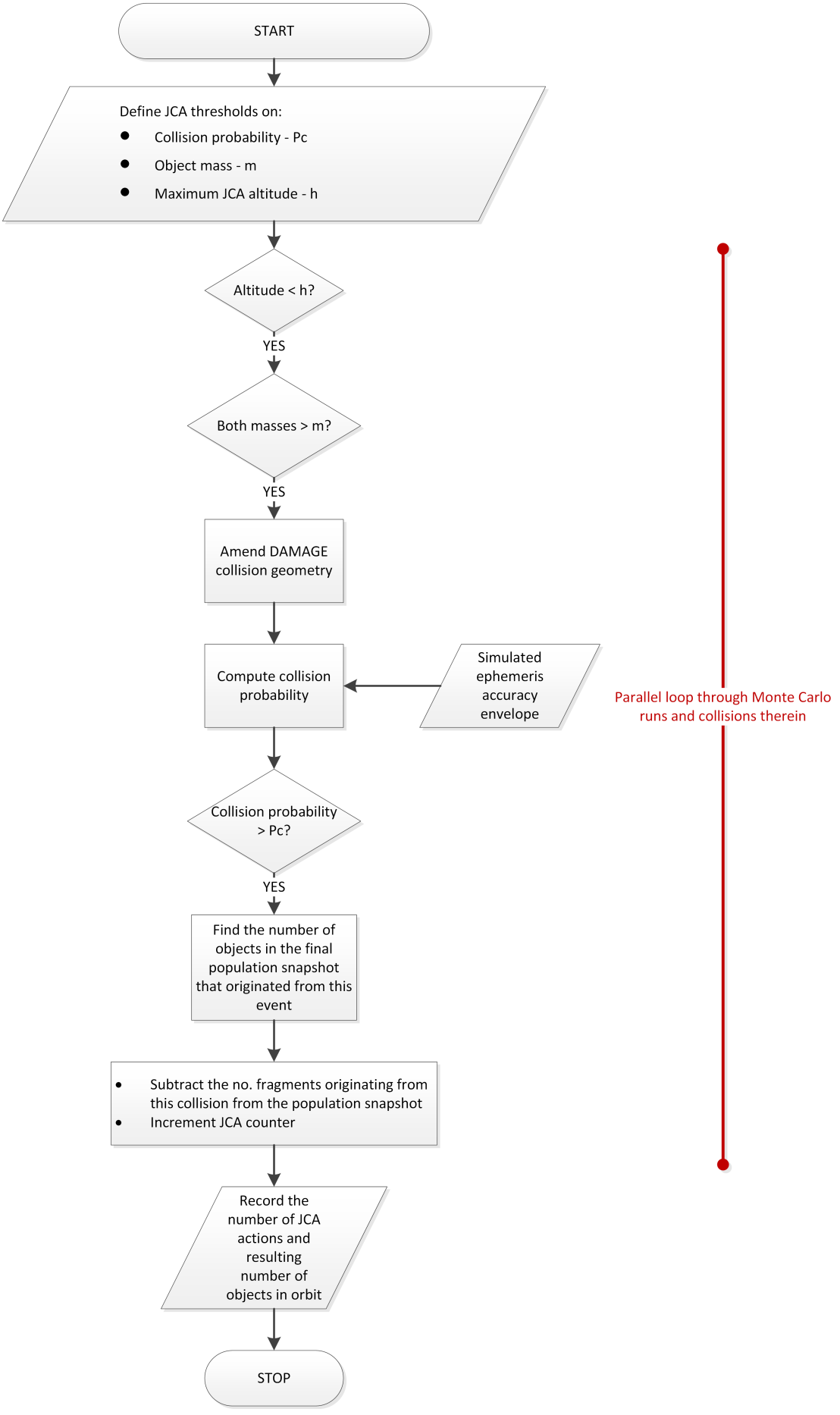

Figure 4.5: Block diagram of the developed just in-time collision avoidance (JCA) simulation framework.

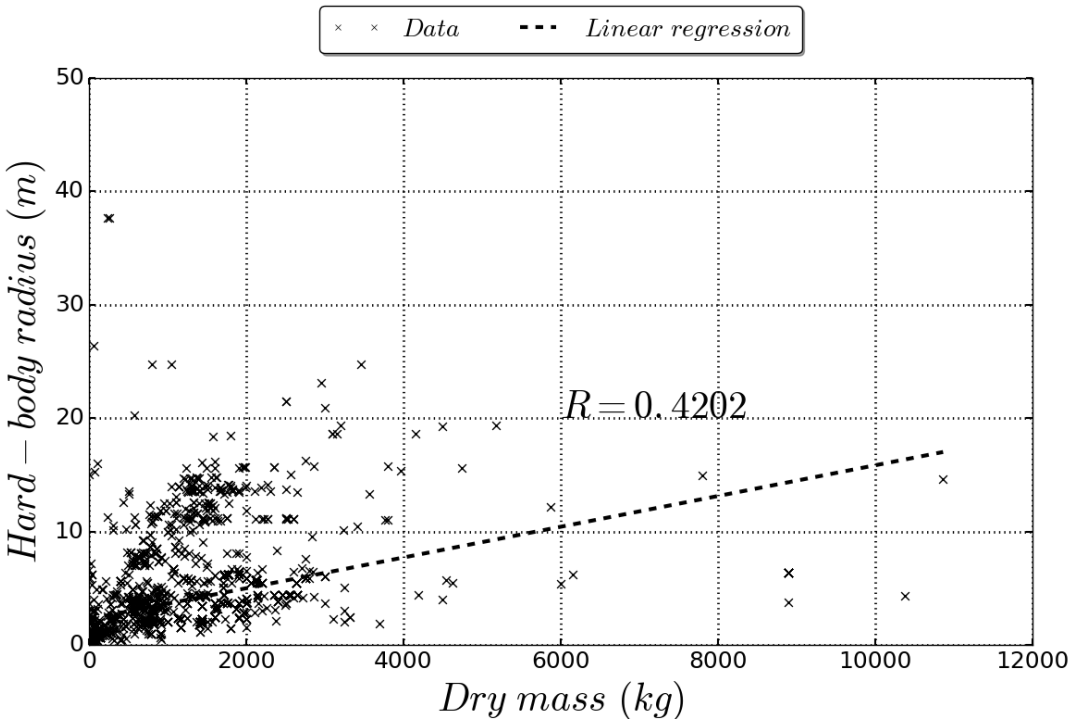

Figure 4.6: Hard body radius as a function of object's dry mass. Data from the radii and masses' databases first introduced in section 3.1 with the International Space Station and already decayed objects filtered out.

fraction of the population above a given mass can be observed in Fig. 4.7 around 1400, 2400, and 4585 kg. The maximum dry mass was 11 800 kg. The International Space Station, which has mass of 20 700 kg in the analysed database, was not included in the sample because it is deemed unlikely to take part in catastrophic collisions due to its special character and routine collision avoidance it performs.

Masses involved in collisions in the DAMAGE simulations performed as part of the IADC comparison study described in section 1.2 were analysed. Histograms showing the distributions of the masses of the larger-mass objects (targets) and the lower-mass objects (projectiles) as well as the sum of the two are shown in Fig. 4.8. All the collisions took place between relatively large-mass objects (minimum target mass was 6693.5 kg) and low-mass ones (maximum projectile mass was 78.0 kg). According to the regression line on Fig. 4.6, this corresponds to collisions between objects with hard-body radii of 2.39 and 11.36 m, i.e. objects whose sizes differ by a factor of 4.75. For all other collisions, this disparity will be even greater (the largest projectile and the smallest target were analysed here).

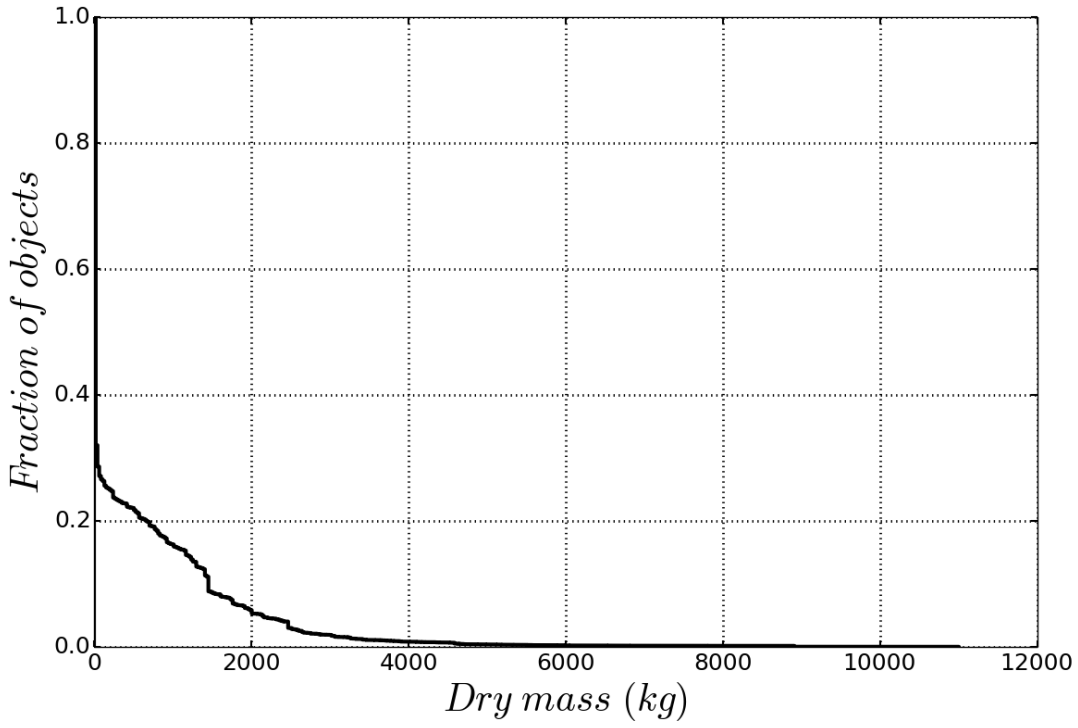

Figure 4.7: Cumulative histogram showing the fraction of the objects in the database of masses, first introduced in section 3.1, that have mass above a given value. The International Space Station and already decayed objects were filtered out.

The breakup model implemented in DAMAGE, and in fact most evolutionary space debris models [86], uses the work by Johnson et al. [51]. This is to say that it ignores the impact of the details of the collision geometry and the involved objects on the number of generated fragments; only the ratio of the relative kinetic energy of the projectile to the mass of the target is used to determine whether the collision caused both objects to completely fragment in the process or not [51]. Zaccariotto et al. [159] have shown using simulations, and before them McKnight et al. [100] using experiments, that the number of fragments resulting from a collision is dependent on the relative size of the two objects, their structural details and the location where the projectile impacts the target. A good discussion of this topic is presented by Nock et al. [109], with the conclusion being that collisions involving low-mass objects with large areas (low areal density) are unlikely to cause catastrophic breakups.

The goal of this work presented in this section was to determine the range of the possible mass thresholds, m_{TH}, that two objects involved in a conjunction should exceed in order for the event to be considered for JCA action. According to Fig. 4.8b, 93.7% of collisions in DAMAGE involved an object with mass lower than 10 kg. The relationship between the masses of the collided objects and the number of fragments they correspond to in the final population is investigated in more detail in section 4.4. However, based

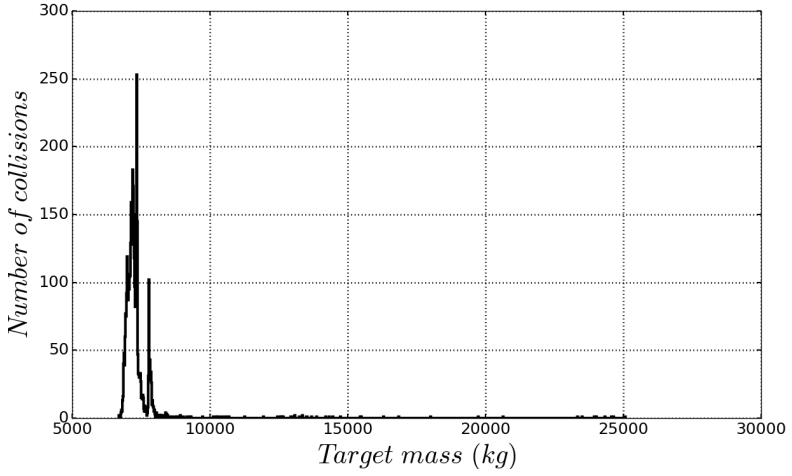

(a) Targets

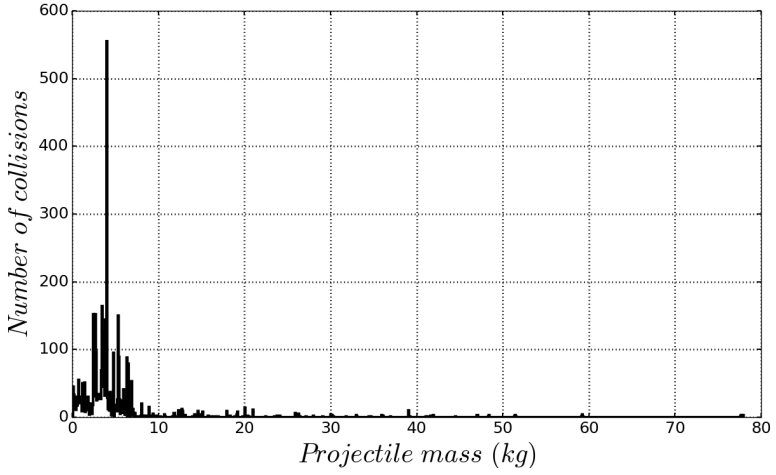

(b) Projectiles

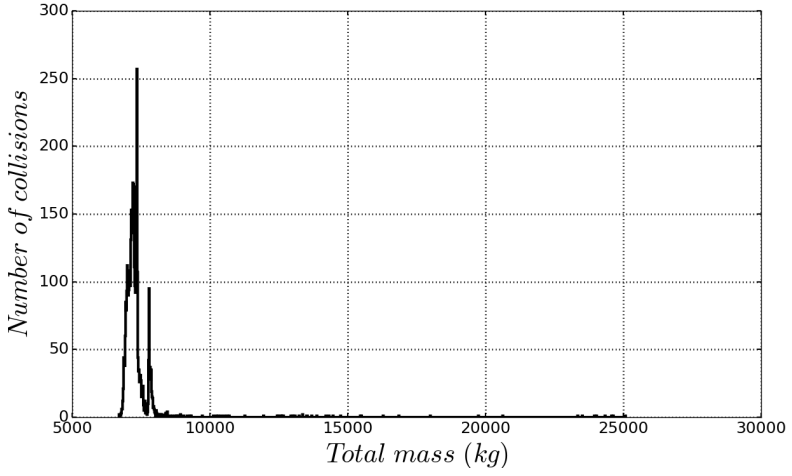

(c) Sum

Figure 4.8: Histograms of masses that were involved in collisions in a DAMAGE simulation. Targets are the larger-mass objects, and projectiles are the lower-mass objects. Data from 100 runs of the "mitigation only" scenario from Table 1.1 provided by Dr Hugh G. Lewis.

on the results from Fig. 4.8, objects with masses as low as 10 kg could be responsible for most of the future collisions and, consequently, the increase in the number of the objects on orbit reported in section 1.2.1. Therefore, JCA systems should be designed to prevent conjunctions involving even such low-mass objects. Based on the breakdown shown in Fig. 4.7, it is expected that many actual conjunctions will involve such low-mass objects - 32.6% of objects in the database of masses have mass above 10 kg, therefore JCA should potentially target a third of the population of the resident space objects, not only a handful of the largest-mass objects. The m_{TH} range, which was used here, was established on the likely range of values that would be seen in DAMAGE simulations. However, when updated, higher-fidelity breakup models become available, the m_{TH} range should be re-evaluated. As for the results of this work, the effects of JCA depending on the m_{TH} value should be interpreted in a relative sense. This is to say that the results of this sensitivity study can be used to conclude whether JCA should target all the objects in orbit, the ones with the largest mass, or any objects in between. Also, the distribution of the projectile masses shown in Fig. 4.8b does not closely follow the actual distribution of the masses of objects in orbit shown in Fig 4.7. For example, more collisions involved projectiles with mass of 5 kg than 1 kg, even though the larger the object's mass the fewer such objects are present in orbit and thus fewer collisions are expected. This suggests that the distributions of projectile and target masses in Fig. 4.8 may not have been captured reliably due to undersampling. This phenomenon could have also been caused by the fact that larger-mass objects also have larger cross-sectional area and so higher P_C as shown in Fig. 4.6. They will, therefore, take place in more collisions. However, the subsequent analyses in this work only used the extreme values of such distributions, and thus are not reliant on reliably capturing the distributions presented in Fig. 4.8.

Ultimately, it was decided to investigate m_{TH} values between 1 and 4585 kg, which included 33.8% of the objects on orbit, including the largest-mass ones, and 92.1% of the objects that were involved in the DAMAGE simulations that formed part of the IADC comparison study from section 1.2. Both objects individually should be above m_{TH} for JCA to be considered. This criterion was imposed to simulate prevention of only those collisions that involve objects of similar sizes, which have similar aerial densities and thus their collisions are likely to be catastrophic [109]. Even though objects with mass larger than 4585 kg are present in orbit, using this m_{TH} range enabled probing scenarios where JCA was performed only on a handful of objects or almost all of them (178 objects in the analysed database had mass larger than 4585 kg).

4.2.2.2 Ephemeris accuracy

Ephemeris accuracy at the TCA affects the collision probability that can be forecast for a given conjunction. If the position uncertainty is too large, even very close conjunctions will have a relatively low P_C, which is referred to as "probability dilution" [4]. If the ephemeris knowledge of the space catalogue, which is used to support JCA decisions, is poor enough, then most collisions will occur in the probability dilution regime. In such a scenario, the JCA P_C action threshold, $P_{C,TH}$, has to be set low to prevent any collision. If the ephemeris accuracy is perfect, on the other hand, $P_{C,TH}$ can be set to 1.0 because every collision can be forecast with absolute certainty. An example of the behaviour of P_C when the covariance of the two conjuncting objects, C, is scaled by a factor k^2, such that $C' = k^2C$, for differnent ratios of the hard body radius to miss distance is given in Fig. 4.9. The same behaviour for more conjunction geometries is demonstrated in section A.3.2. When the collision radius is equal to the miss distance, which corresponds to a collision, and there is no position uncertainty (covariance scaling factor $k^2 = 0$), $P_C = 1.0$. However, when the state is uncertain ($k^2 > 0$), collision cannot be forecast with absolute certainty and $P_{C,TH}$ has to be increasingly lower the larger the state uncertainty (the larger k^2). This shows that ephemeris accuracy is an important factor from JCA's point of view, and hence was included in this sensitivity study.

The ephemeris uncertainty, which is used for P_C calculations, is the uncertainty of the state at the orbit determination epoch propagated to the time of the closest approach [37, 70]. Thus, this ephemeris accuracy is a function of the method, which is used to propagate the uncertainty from the state vector's epoch to the TCA, as well as the frequency at which the state vectors in the catalogue get updated (uncertainty grows as it is being propagated [28]). Lidtke et al. [81] have shown that this update frequency for TLEs is, in general, different from object to object and may vary over time, and different uncertainty propagation methods may give different results [149]. Therefore, including uncertainty propagation in the JCA simulation framework would require a study investigating the sensitivity of the results to the assumed state vector update frequency and uncertainty propagation method. It was decided to avoid such a study, thus reducing the computational time required, by varying the state vector uncertainty at the TCA directly. This enabled definition of an ephemeris accuracy envelope, which is never to be exceeded, that would enable JCA to achieve a given result with the recommended m_{TH} and $P_{C,TH}$.

Levit and Marshall [72] have suggested that two-line element sets could be sufficient to support laser-based JCA, if their accuracy is improved by fitting numerically propagated orbits to the TLEs. However, to make the results of this analysis readily usable, the currently achievable accuracy of the ephemerides was analysed to ensure that this JCA study reflects the present space object catalogue accuracy. Vector Covariance Messages

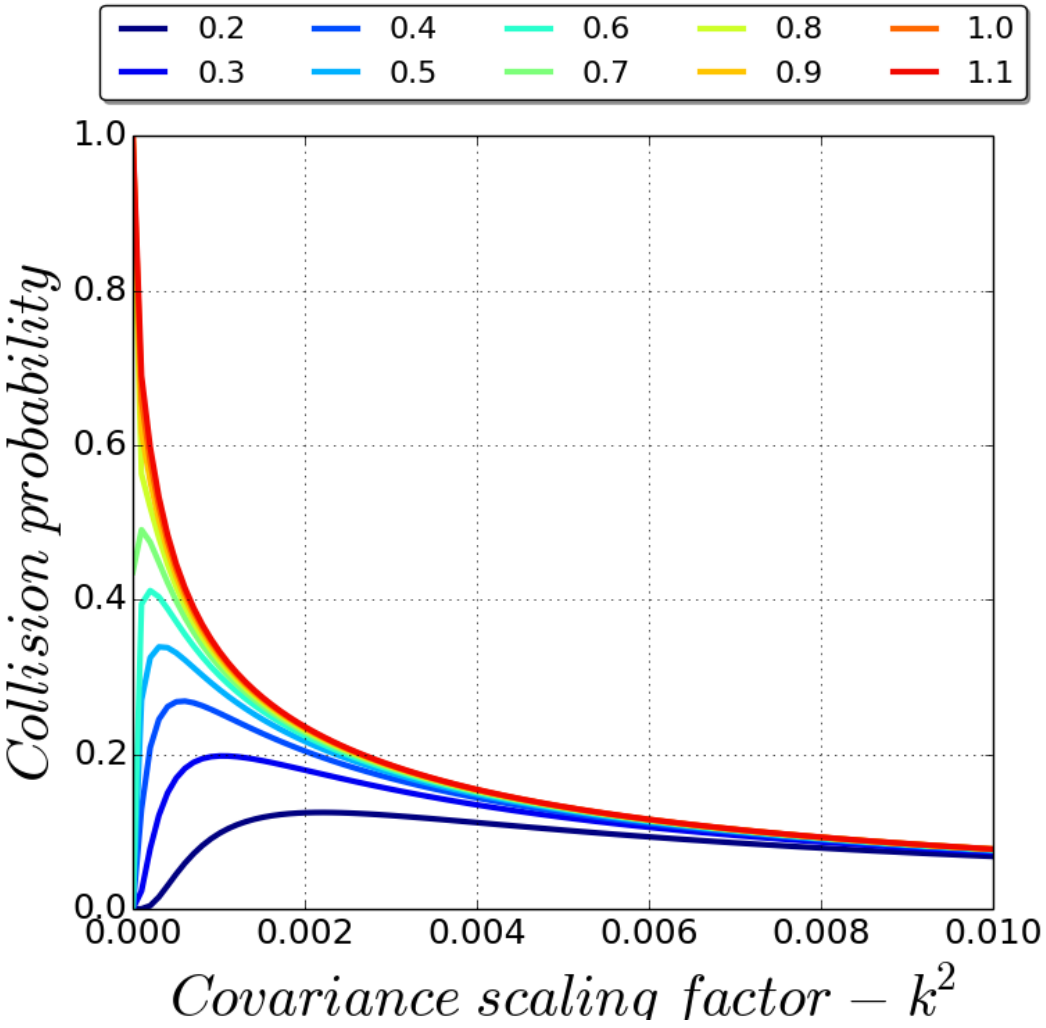

Figure 4.9: Collision probability as a function of the covariance scaling factor for various ratios of the collision radius to the miss distance. "Left-to-right" conjunction geometry from Fig. A.9d.

(VCM) for the entire public catalogue, spanning the month of December 2014, were provided by the Joint Space Operations Center (JSpOC). VCM format is shown in Fig. 4.10; lines 25 and 26 contain standard deviations of the state vector, i.e. position and velocity, in the radial, in-track, cross-track (RIC) frame of reference at the state vector epoch.

Median standard deviations of position in the RIC frame were computed for every object. Using median of the position uncertainty in every direction ensured that any outlying data points, e.g. with unusually large or small position uncertainty, were filtered out. Figure 4.11 shows the variation of this median position uncertainty with object's mass (correlates with it size, $R = 0.4202$) and its perigee altitude, h_P; both of these factors affect the accuracy of the object's tracking data and thus also of the ephemerides [31, 36, 46, 53].

```
 1 <> SP VECTOR/COVARIANCE MESSAGE - V2.0
 2 <>
 3 <> MESSAGE TIME (UTC):                                    CENTER:
 4 <> SATELLITE NUMBER:     5                    INT. DES.: 1958-002B
 5 <> COMMON NAME: VANGUARD 1
 6 <> EPOCH TIME (UTC): 2013 336 (02 DEC) 04:01:32.274  EPOCH REV: 94590
 7 <> J2K POS (KM):      4182.85661723    5327.31383408    1975.71259599
 8 <> J2K VEL (KM/S):  -6.426755648471   3.196693759190   3.908474611282
 9 <> ECI POS (KM):      4163.54380568    5340.37985192    1981.22397634
10 <> ECI VEL (KM/S):  -6.442024042506   3.176817979228   3.899534165111
11 <> EFG POS (KM):      1235.21828193   -6658.00193606    1981.22397634
12 <> EFG VEL (KM/S):   6.164703708150   2.624058908291   3.899534165111
13 <> GEOPOTENTIAL: EGM-96 36Z,36T  DRAG: JAC70/MSIS90  LUNAR/SOLAR:  ON
14 <> SOLAR RAD PRESS:  ON  SOLID EARTH TIDES:  ON  IN-TRACK THRUST: OFF
15 <> BALLISTIC COEF (M2/KG):  0.206683E-01 BDOT (M2/KG-S): 0.000000E+00
16 <> SOLAR RAD PRESS COEFF (M2/KG):  0.258457E-01  EDR(W/KG):  0.45E-04
17 <> THRUST ACCEL (M/S2):  0.000000E+00  C.M. OFFSET (M):  0.000000E+00
18 <> SOLAR FLUX: F10: 176  AVERAGE F10: 152  AVERAGE AP:  10.0
19 <> TAI-UTC (S): 35  UT1-UTC (S): -0.06148  UT1 RATE (MS/DAY): -1.100
20 <> POLAR MOT X,Y (ARCSEC):  0.0532  0.2905 IAU 1980 NUTAT:   4 TERMS
21 <> TIME CONST LEAP SECOND TIME (UTC): 2049 365 (31 DEC) 23:59:59.999
22 <> INTEGRATOR MODE: ASW          COORD SYS: J2000  PARTIALS: FAST NUM
23 <> STEP MODE: AUTO  FIXED STEP: OFF  STEP SIZE SELECTION: MANUAL
24 <> INITIAL STEP SIZE (S):   20.000  ERROR CONTROL: 0.100E-13
25 <> VECTOR U,V,W SIGMAS (KM):           0.0124     0.0530     0.0109
26 <> VECTOR UD,VD,WD SIGMAS (KM/S):      0.0001     0.0000     0.0000
27 <> COVARIANCE MATRIX (EQUINOCTIAL ELS): ( 9x 9) WTD RMS:  0.11031E+01
28 <>  0.42255E-11  0.41132E-12  0.76041E-12 -0.99354E-11 -0.89253E-12
29 <>  0.40469E-10 -0.71798E-13 -0.33776E-14  0.30115E-12  0.27939E-14
30 <>  0.12358E-11  0.22524E-12 -0.14392E-11 -0.12571E-13  0.23944E-11
31 <>  0.36651E-13 -0.15150E-12 -0.13586E-12  0.40621E-14  0.59381E-12
32 <>  0.59100E-12 -0.62234E-07  0.35086E-08  0.22947E-06  0.22472E-08
33 <> -0.11983E-07  0.16224E-08  0.22216E-02  0.00000E+00  0.00000E+00
34 <>  0.00000E+00  0.00000E+00  0.00000E+00  0.00000E+00  0.00000E+00
35 <>  0.00000E+00  0.22312E-06 -0.26106E-07 -0.55914E-06 -0.53576E-08
36 <>  0.46806E-07 -0.61319E-08 -0.53200E-02  0.00000E+00  0.20231E-01
```

Figure 4.10: Example of an ephemeris in the Vector Covariance Message (VCM) format. Also showing line numbers, which are not part of the actual messages.

The larger the perigee altitude and the lower the mass of the object, the more uncertain its position is. The in-track uncertainty is typically the largest; this is because all the observations on which the orbit determination is performed are spread the most along this direction due to the influence of drag [29] and Keplerian dynamics [149]. Not all objects follow this trend and there are outliers in the data, which have lower ephemeris accuracy than other objects in a similar mass and perigee altitude regime, or larger radial than in-track uncertainty. Such outliers with poor orbit knowledge would be important if they were involved in a conjunction for which JCA was being considered;

Table 4.1: Results of the statistical analysis of the radial, in-track, and cross-track position standard deviation of the VCMs with perigee altitudes between 500 and 2000 km. Also showing the data for a subset of objects with masses larger than 459.4 kg, which is used in Chapter 5.

Direction	**Min.** (m)	**Max.** (m)	**Percentile** (m)			$\mathbf{m_{TH} \geq 459.4}$ **kg**,
			$\mathbf{5^{th}}$	$\mathbf{50^{th}}$	$\mathbf{95^{th}}$	$\mathbf{50^{th}}$ (m)
Radial	1.6	469.8	3.9	6.8	33.7	6.7
In-track	5.4	348.7	10.6	16.7	68.1	16.3
Cross-track	1.7	186.2	3.2	6.6	29.1	6.4

the knowledge about their orbits would need to be refined in such cases, as is done for operational satellites [37, 70]. However, such outliers may not serve as a good example of *typical* position uncertainty. A statistical analysis of the VCM position uncertainty in different orbital regimes was undertaken to understand what the distribution of the state vector uncertainty is and how common outliers are.

Figure 4.12 shows the distributions of the components of the position uncertainty in several perigee altitude (h_P) bins. The position uncertainty is initially large for objects with perigee altitudes of up to approximately 500 km, and then decreases. This confirms that the atmospheric drag, which is more profound the lower the altitude, affects the orbit knowledge uncertainty [117]. The distributions of position uncertainties remain approximately constant up to h_P of 1500 km, and then the orbit knowledge deteriorates.

Most future collisions are expected to take place at altitudes between 800 and 1000 km [89]. Therefore, it was decided to focus the analysis of the position uncertainty on objects with h_P between 500 and 2000 km, because most new collision fragments will be produced in this altitude regime and thus this is where JCA actions should focus to prevent the growth of the number of objects in orbit. In this regime, the radial position standard deviation varies between 1.6 and 469.8 m, whereas in-track and cross-track between 5.4 and 348.7 m, and 1.7 and 186.2 m, respectively. To remove the effect of the largest outliers and generate *typical* position uncertainty ranges in this perigee altitude regime, the 5^{th} and 95^{th} percentiles of the data were investigated [25] and are shown in Table 4.1.

It was decided to use the 5^{th} percentiles of the RIC position standard deviations as the lowest achievable state vector uncertainty at the TCA. For the largest possible uncertainty, the 95^{th} percentiles were considered. If the state of a LEO satellite, with initial RIC position standard deviations of 1.7, 5.7, and 0.3 m, i.e. 56, 46, and 91% smaller than the 5^{th} percentiles, is propagated for one day, the standard deviations grow to 3.9, 41.9, and 4.6 m [28]. In other words, the RIC standard deviations increase by factors of 2.3, 7.7, and 18.8, respectively, when propagated for one day. Here, the RIC 95^{th} and 5^{th} percentiles differ by factors of 8.6, 6.4 and 9.0, respectively. This means that using the 95^{th} percentiles as the largest state vector uncertainties could also account for the the growth of the uncertainty with time, if all the objects are catalogued with the accuracy at the 5^{th} percentile level and the state vectors are updated once a day.

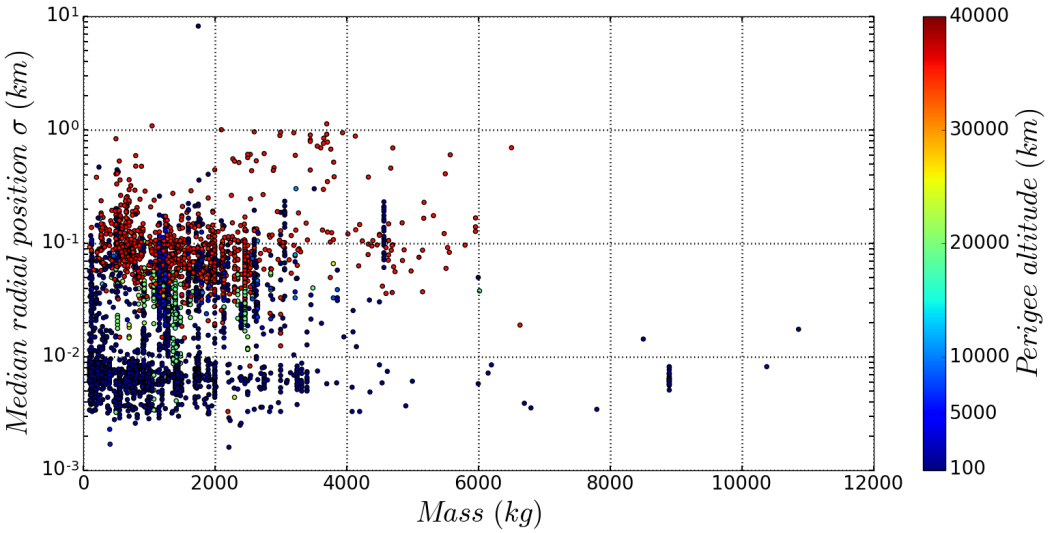

(a) Radial (σ_R)

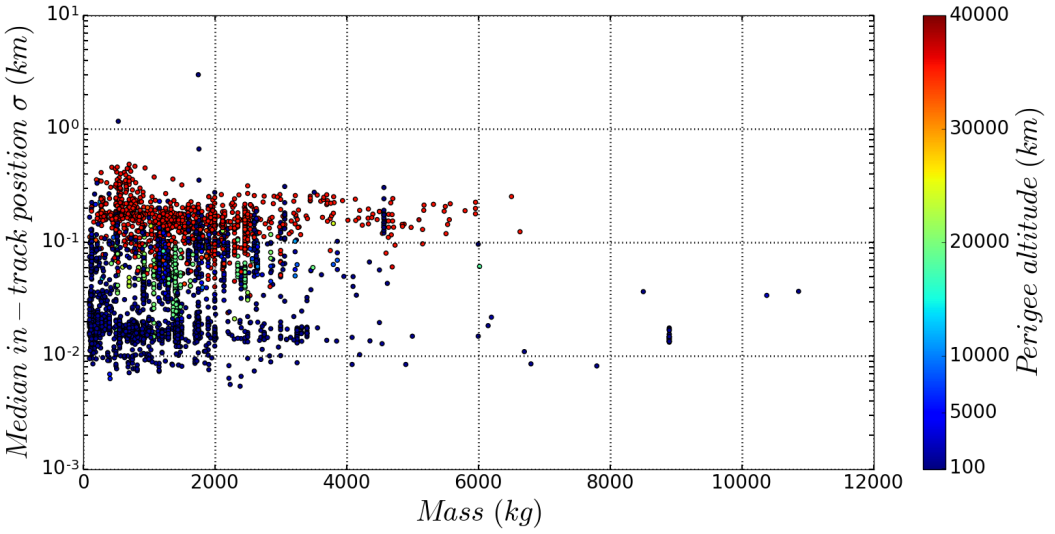

(b) In-track (σ_I)

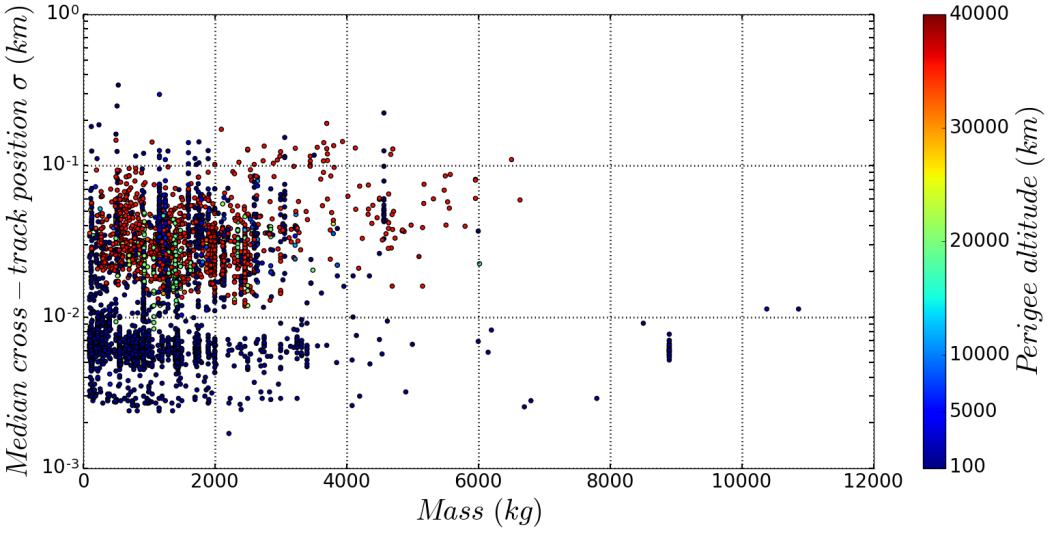

(c) Cross-track (σ_C)

Figure 4.11: RIC position standard deviations for the public catalogue from the Vector Covariance Messages spanning December 2014; median per object.

Table 4.2: Investigated ranges of the radial, in-track, and cross-track position standard deviations.

Direction	**Standard deviation (m)**	
	Minimum	**Maximum**
Radial	3.9	337.0
In-track	10.6	681.0
Cross-track	3.2	219.0

However, it was decided to use position standard deviations an order of magnitude larger than the 95^{th} percentiles from Table 4.1 as the largest possible state vector uncertainty. This was done in order not to over constrain the search space of the JCA parameters. Finally, the RIC position uncertainty bounds, which will be investigated in the sensitivity study, are presented in Table 4.2.

4.2.2.3 Collision probability

It was shown in Chapter 3 that 50% of the probability of any collision taking place in orbit can be attributed to at most 0.015% of conjunctions closer than 20 km in the analysed periods of one month. The same analysis as in section 3.1 was repeated but with more TLE catalogue snapshots propagated for shorter periods of time, and using only the "true" collision probability. This made the analysis rely data more similar to what would be used in operational collision avoidance, and the same trend was observed [83].

Conjunctions with high P_C are relatively rare - most events have relatively low collision probabilities. However, any conjunction could result in a collision. Therefore, when the collision probability is only mitigated for conjunctions that exceed a certain $P_{C,TH}$, certain probability is left unaltered and so is accepted. This leads to a trade off between the ignored and avoided collision probabilities, where the design variable is the $P_{C,TH}$ [37]. To illustrate this trade off, the ignored and avoided collision probabilities, for the entire month of conjunctions from the work by Lidtke et al. [83], are presented in Fig. 4.13a. The corresponding number of conjunctions that exceed the $P_{C,TH}$ threshold is shown in Fig. 4.13b.

The higher the collision probability of individual conjunctions one is willing to accept, the fewer JCA actions need to be performed and so the lower the cost of JCA. This is accompanied by ignoring more and avoiding less collision probability. This gives rise to including $P_{C,TH}$ in this sensitivity study. For operational LEO satellites, the better the ephemeris accuracy of the catalogue, the higher the collision probability threshold for which the ignored P_C exceeds the avoided P_C [34]. This not only shows that both of these parameters should be studied concurrently, but that the $P_{C,TH}$ values from Fig. 4.13a should not be used to devise the settings for this JCA parameter study directly. This is because the state vector accuracies obtained in section 4.2.2.2 are different to the ones used to obtain the results for Fig. 4.13a.

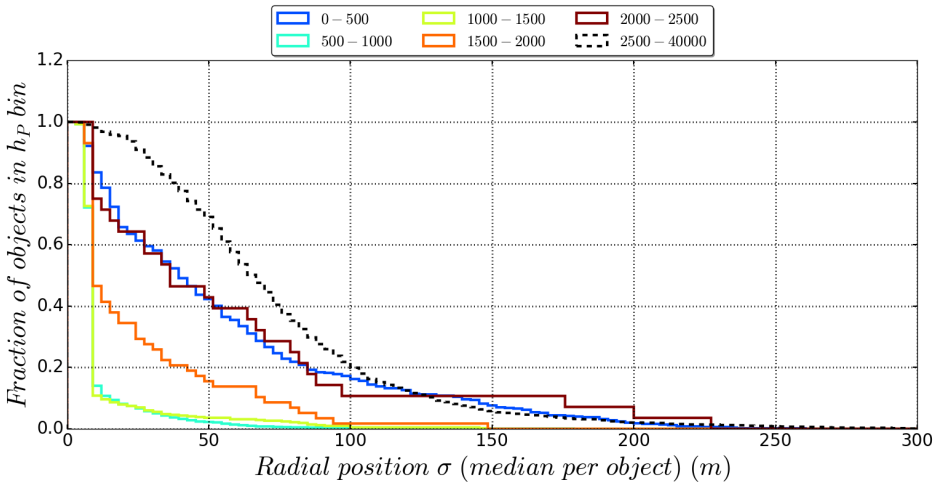

(a) σ_R

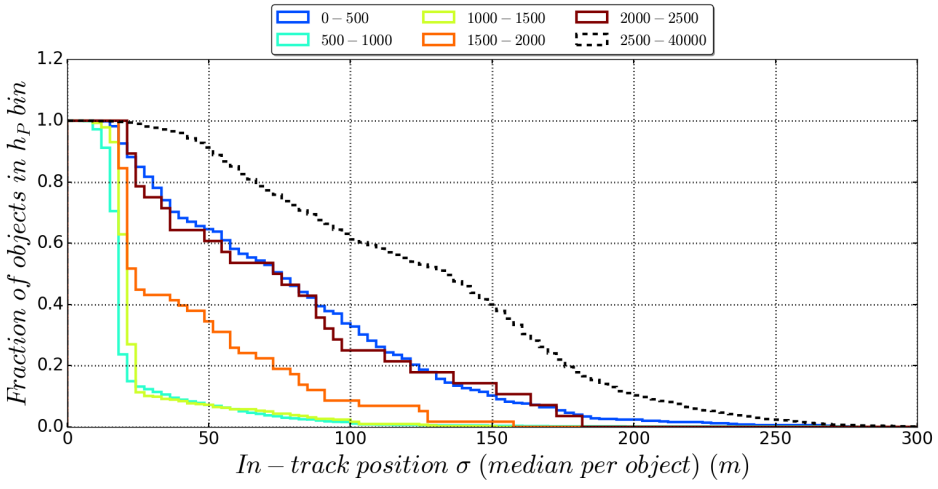

(b) σ_I

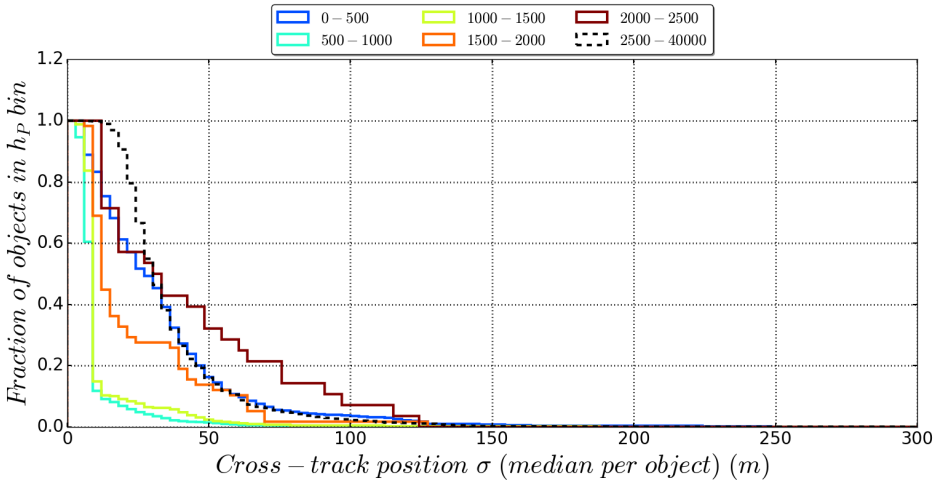

(c) σ_C

Figure 4.12: Cumulative histograms of the RIC position uncertainties of the public catalogue in different perigee altitude (h_P) regimes in km. The data are medians per object, obtained from the Vector Covariance Messages spanning the December 2014.

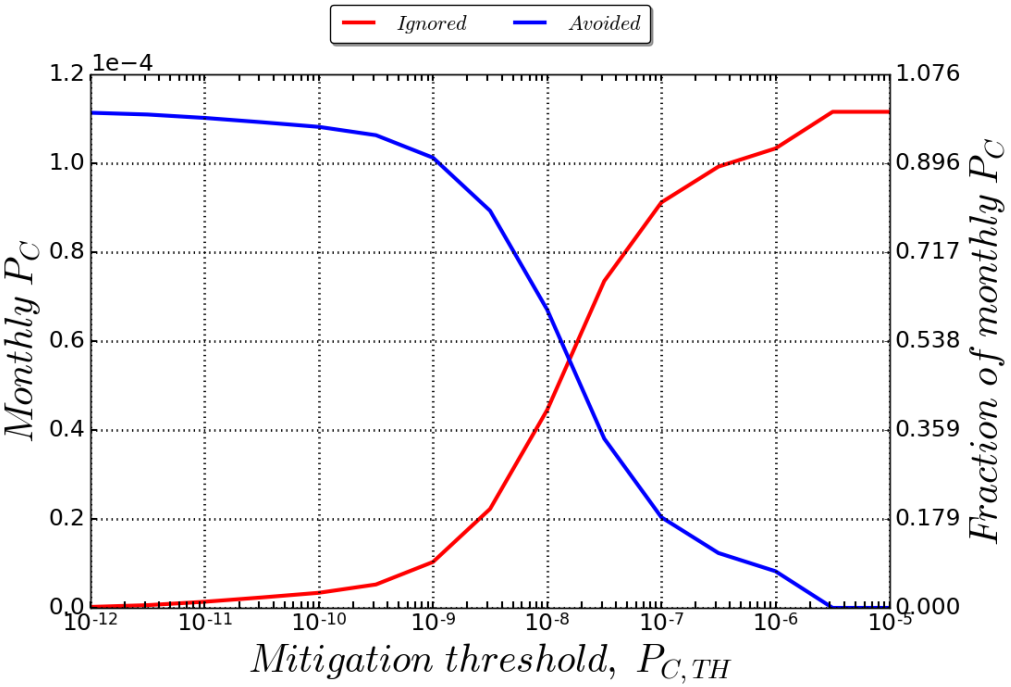

(a) Ignored and avoided collision probabilities

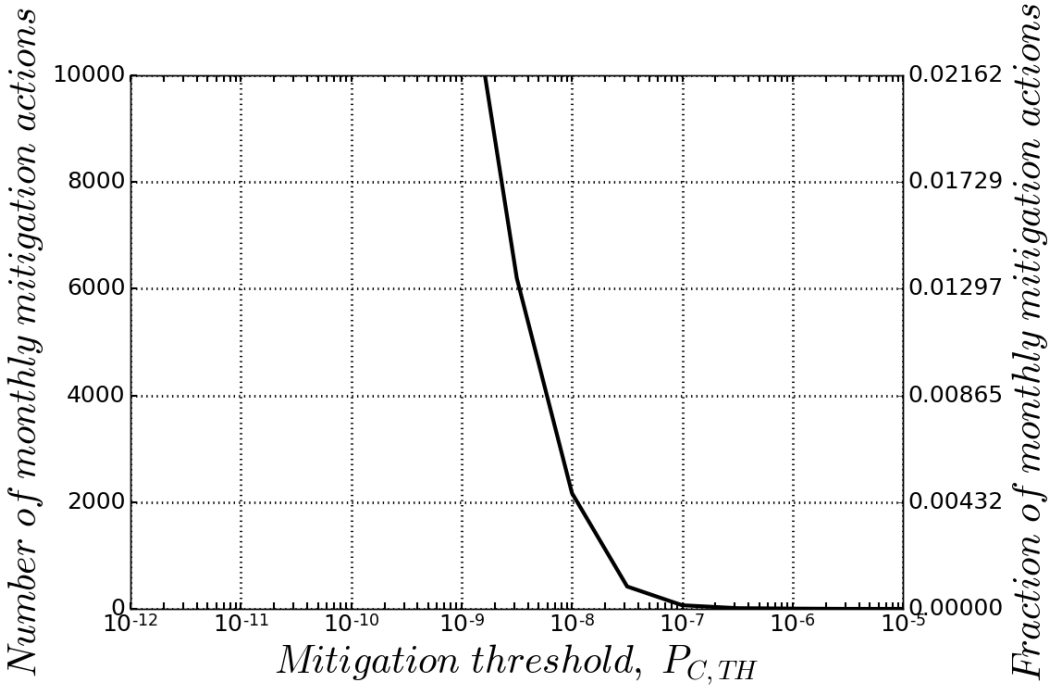

(b) No. corresponding JCA actions

Figure 4.13: Evolution of the collision probabilities that are ignored and avoided over one month depending on how high a P_C of individual conjunctions is accepted and not mitigated. Also showing the corresponding number of JCA actions. Data from the work by Lidtke et al. [83]. Assuming that mitigating the collision probability of a conjunction removes that probability entirely.

The European Space Agency analyses a conjunction involving one of their operational satellites in detail if the event's P_C exceeds 1.0×10^{-4}; typically improving the orbit knowledge is sufficient to lower the collision probability below accepted levels [34]. If the collision probability is still above 5.0×10^{-3}, an avoidance manoeuvre is performed [34]. It was decided that examining $P_{C,TH}$ as low as 1.0×10^{-6} would help understand whether JCA could realistically prevent all the collisions in orbit. The maximum action threshold, which was used in the sensitivity study, is 1.0. If $P_{C,TH}$ is set to 1.0, no JCA will ever be performed because no conjunction can ever be predicted with 100% certainty, and so P_C can never reach 1.0. However, it was considered insightful to analyse the effects of JCA when preventing only the conjunctions with collision probabilities in the order of several percent.

4.2.2.4 Sampling the different scenarios

The parameters that affect the performance of just in-time collision avoidance were described above and the ranges, which should be investigated for each of them, were identified. In order to study the outcomes of JCA for various permutations of these parameters, a DAMAGE Monte Carlo study was employed. Evaluating every permutation with a Monte Carlo sample sufficiently large to correctly capture the likely future number of objects in orbit, as well as the associated uncertainty, required several days per permutation. In order to limit the number of permutations to be evaluated, without under-sampling the results space, rigorous design of experiment and surrogate modelling methods were employed [54].

Let $\vec{x}$ be the vector of all the inputs to the model, here the JCA parameters m_{TH}, $P_{C,TH}$ and ephemeris accuracy σ. Every evaluation of the Monte Carlo debris model yields the distributions of the number of objects in orbit and the number of JCA actions in all the MC runs. All of these outputs can be concatenated into a vector of results, $\vec{y}$, and are a function of the model inputs as per Eq. 4.1:

$$\vec{y} = f(\vec{x}) = f\begin{pmatrix} m_{TH} \\ P_{C,TH} \\ \sigma \end{pmatrix}. \tag{4.1}$$

The modelled response of the debris environment to implementing JCA, $\vec{y} = f(\vec{x})$, is unknown and has to be sampled with as few points, i.e. different $\vec{x}$ vectors, as possible to reduce the computational time. In order to find a suitable set of $\vec{x}$, the possible ranges of the components of $\vec{x}$ were scaled to a unit interval, $[0, 1]$ [54]. Then, a set of 50 points was seeded to span the dimensionless parameter space. The effects of selecting such a sample size are discussed in section 4.3.2.3. In order not to potentially leave important regions of the parameter space unsampled, those points were not made equidistant in every

dimension of $\vec{x}$ [54]. Instead, an initial randomised latin hypercube was generated and further optimised using simulated annealing to increase the "space fillingness" metric developed by Morris and Mitchell [105]. This metric ensures that the distances between the sample points are maximised whilst minimising the number of points that have similar distances to one another [105]. The optimised dimensionless points, which sample the JCA parameter space, are shown in Fig. 4.14. All the components of the RIC position standard deviation were scaled uniformly to reduce the number of dimensions of the problem, and $P_{C,TH}$ was sampled in the logarithmic space. In order to evaluate the function $f(\vec{x})$ at the sample points, they have to be dimensionalised. The distribution of the points from Fig. 4.14, but with m_{TH}, $P_{C,TH}$ and σ scaled to the used values, is shown in Fig. 4.15. The corresponding values are reported in Table 4.3.

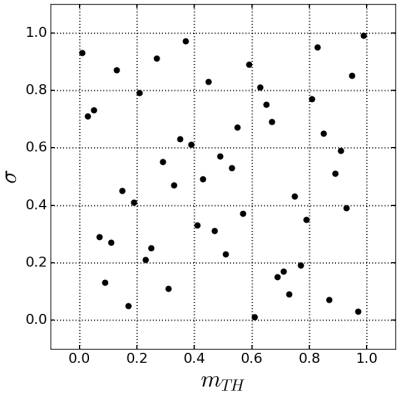

(a) σ VS m_{TH}

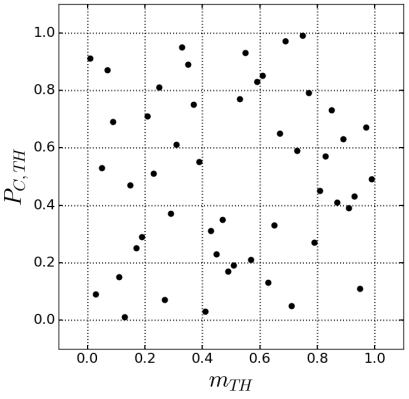

(b) $P_{C,TH}$ VS m_{TH}

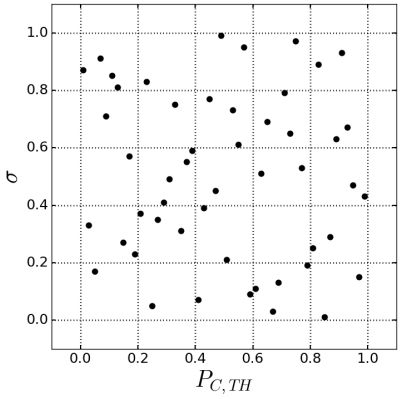

(c) σ VS $P_{C,TH}$

Figure 4.14: The investigated permutations of dimensionless JCA parameters from Table 4.3. All components of the RIC standard deviation are scaled by the same factor σ.

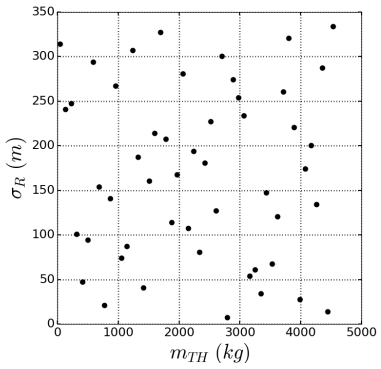

(a) σ_R VS m_{TH}

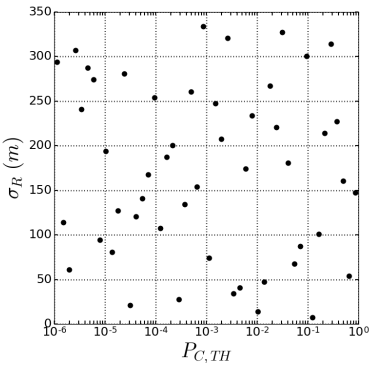

(b) σ_R VS $P_{C,TH}$

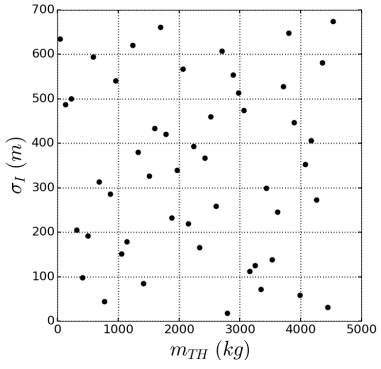

(c) σ_I VS m_{TH}

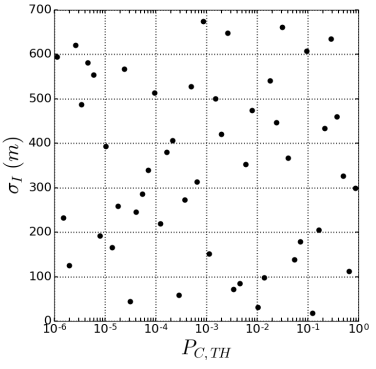

(d) σ_I VS $P_{C,TH}$

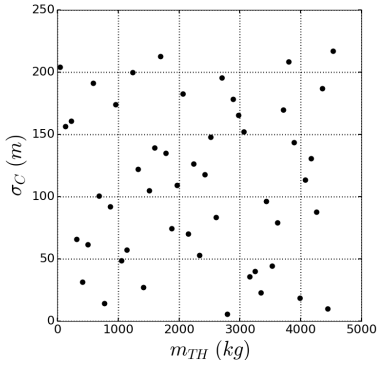

(e) σ_C VS m_{TH}

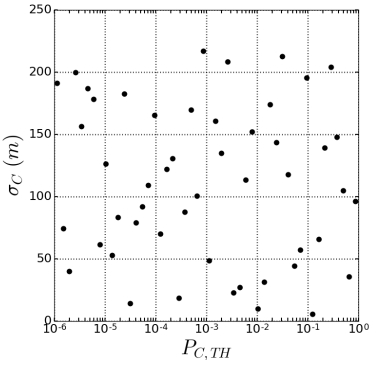

(f) σ_C VS $P_{C,TH}$

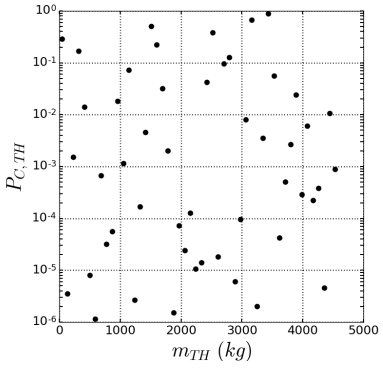

(g) $P_{C,TH}$ VS m_{TH}

Figure 4.15: The investigated permutations of dimensional JCA parameters from Table 4.3. Distinguishing different components of the RIC standard deviation, i.e. σ_R, σ_I and σ_C, respectively.

Table 4.3: Distribution of the dimensional points used to sample the space of JCA's free parameters together with the Monte Carlo run identifiers. Distinguishing different components of the RIC standard deviation, i.e. σ_R, σ_I and σ_C, respectively. Also showing the extents of the intervals for every sampled variable.

Point	$\mathbf{m_{TH}}$ **(kg)**	$\mathbf{P_{C,TH}}$	**Position standard deviation (m)**		
			$\sigma_\mathbf{R}$	$\sigma_\mathbf{I}$	$\sigma_\mathbf{C}$
1	3164	6.61e-01	53.87	111.16	35.57
2	47	2.88e-01	313.68	634.07	203.89
3	1514	5.01e-01	160.46	325.69	104.63
4	2339	1.38e-05	80.51	164.79	52.83
5	2431	4.17e-02	180.44	365.91	117.57
6	2522	3.80e-01	227.08	459.77	147.79
7	3806	2.63e-03	320.34	647.48	208.21
8	2889	6.03e-06	273.71	553.62	178.00
9	872	5.50e-05	140.47	285.46	91.68
10	1697	3.16e-02	327.01	660.89	212.53
11	1239	2.63e-06	307.02	620.66	199.58
12	1605	2.19e-01	213.75	432.95	139.15
13	4264	3.80e-04	133.81	272.06	87.36
14	414	1.38e-02	47.20	97.75	31.25
15	505	7.94e-06	93.84	191.61	61.47
16	3622	4.17e-05	120.48	245.24	78.73
17	1330	1.66e-04	187.11	379.32	121.89
18	3897	2.40e-02	220.42	446.36	143.47
19	2614	1.82e-05	127.15	258.65	83.05
20	3989	2.88e-04	27.22	57.53	18.31
21	2706	9.55e-02	300.36	607.26	195.26
22	139	3.47e-06	240.40	486.58	156.42
23	3256	2.00e-06	60.53	124.57	39.89
24	4356	4.57e-06	287.03	580.44	186.63
25	2155	1.26e-04	107.16	218.42	70.10
26	2247	1.05e-05	193.77	392.73	126.21
27	1422	4.57e-03	40.54	84.34	26.94
28	780	3.16e-05	20.55	44.12	13.99
29	689	6.61e-04	153.80	312.28	100.31
30	3714	5.01e-04	260.39	526.81	169.37
31	2981	9.55e-05	253.73	513.40	165.05
32	3347	3.47e-03	33.88	70.94	22.62
33	597	1.15e-06	293.70	593.85	190.95
34	3439	8.71e-01	147.13	298.87	95.99
35	4539	8.71e-04	333.67	674.30	216.84
36	322	1.66e-01	100.50	205.02	65.78
37	1972	7.24e-05	167.12	339.10	108.94
38	2797	1.26e-01	7.23	17.30	5.36
39	230	1.51e-03	247.06	499.99	160.73
40	1055	1.15e-03	73.85	151.38	48.52
41	1789	2.00e-03	207.09	419.54	134.84
42	3531	5.50e-02	67.19	137.98	44.20
43	1147	7.24e-02	87.18	178.20	57.15
44	1880	1.51e-06	113.82	231.83	74.41
45	4172	2.19e-04	200.43	406.14	130.52
46	3072	7.94e-03	233.74	473.18	152.10
47	4447	1.05e-02	13.89	30.71	9.67
48	964	1.82e-02	267.05	540.22	173.68
49	4081	6.03e-03	173.78	352.50	113.26
50	2064	2.40e-05	280.37	567.03	182.31
Interval	$[1, 4585]$	$[1.0E-6, 1.0E+00]$	$[3.9, 337.0]$	$[10.6, 681.0]$	$[3.2, 219.0]$

4.3 JCA sensitivity study

This section describes studying the results of implementing different JCA systems, as represented by various permutations of the free parameters. The development of the JCA simulation framework was described in section 4.2.1. Definition of the ranges of the free JCA parameters and their permutations, which represent different sets of requirements for a JCA system, was described in section 4.2.2.4. As shown in Fig. 4.1, this simulation tool and JCA scenarios, together with the conjunction detection and assessment algorithms from Chapter 2, represent all the external inputs into the work described in this section.

The JCA simulation framework required an existing Monte Carlo projection obtained with DAMAGE, in order to simulate different JCA architectures. This reference scenario is described in section 4.3.1. Next, the impact of implementing different JCA architectures on the debris environment is discussed in section 4.3.2.1. Section 4.3.2.2 discusses the corresponding number of false alarms that is expected for every studied JCA architecture. These two sets of results are combined in section 4.3.2.3 to test the hypothesis behind this work: JCA can stop the growth of the number of debris in orbit. The number of false alarms and the corresponding effect on the debris have to be studied concurrently to test this thesis. This is because performing few JCA actions could be economically feasible but might have a negligible effect on the evolution of the debris population. Conversely, if the collision probability of every conjunction is mitigated via JCA, no collisions will take place in orbit. However, performing many JCA actions could not be feasible from an economic point of view. The effects of JCA had to be studied using an evolutionary debris model to test the long-term impact of every JCA scenario. The number of false alarms, however, had to be studied using the tool from Chapter 2 to be able to incorporate the uncertainties in the state vectors of the objects.

4.3.1 Reference scenario

The “mitigation only” scenario, settings of which are summarised in Table 1.1, was used as the reference because it shows the possible future of the debris environment if good compliance with the debris mitigation guidelines is achieved. Unless debris mitigation is widely implemented, investing in debris remediation could be unreasonable, given that every act of non-compliance, e.g. not deorbiting the satellites or rocket bodies at the end of life, will negate the the benefits of remediation [78].

Collision avoidance was added to the previously used “mitigation only” scenario for the purpose of the work shown in this chapter. Collision avoidance was simulated by only allowing satellites to take part in collisions after 8 years since their launch, i.e. after the end of their operational life. This reduced the mean number of objects at the end of the projection by 6.5% in the study by Lewis et al. [80] relative to a scenario

with other mitigation measures being implemented. If derelict collision avoidance is implemented, it could also be used to protect active satellites capable of manoeuvring [95]. However, it is in the interest of spacecraft operators to protect their assets, therefore if a collision involving an active satellite is forecast it is reasonable to expect that it will be avoided. This assumption only adds to the additional assumptions that make the reference scenario used in this work optimistic relative to "business as usual" or "no mitigation" scenarios, for example. These assumptions are:

- No future explosions,
- High post-mission disposal compliance rate (90%),
- No increase in launch traffic,
- 100% efficiency of collision avoidance,
- Only considering a population of objects ≥ 10 cm in size.

These assumptions mean that the reference scenario used here cannot be regarded as a prediction of the future. However, it is not intended to forecast the future number of debris. In fact, depending on the future solar activity or launch traffic that cannot be forecast due to unpredictable nature of the sun or human factor, the future number of debris in orbit can vary by an order of magnitude [152]. This means that the future evolution of the number of objects is, at present, impossible to forecast accurately. However, the *relative* effects of various mitigation measures can still be investigated and assessed, as in the work by Lewis et al. [78], for example. The remainder of this work will focus on such relative analysis, where different implementations of JCA will be compared to each other and a reference scenario, where no JCA is implemented. This will enable assessing whether JCA can have a beneficial effect on the debris environment.

A Monte Carlo sample of 25 000 runs was used to project the "mitigation only" scenario from Table 1.1, with the addition of collision avoidance, for 200 years. The evolution of the number of objects in different percentiles of the sample is shown in Fig. 4.16. The mean number of objects in 2213 in Fig. 4.16 is 20262, whereas the mean for the same scenario projected shown in Fig. 1.9b is 24846 objects, i.e. they differ by 23%. Part of this difference can be attributed to simulating collision avoidance in Fig. 4.16. Also that the MC sample in Fig. 1.9b contained only 140 runs. Therefore, it likely would have changed if more MC runs had been added to it, which is discussed in the remainder of this section.

Varying numbers of MC runs were randomly selected and the variability of parameters describing the shape of the distribution was investigated to verify convergence. This was identical to the bootstrap technique by Liou [90] but investigated more shape parameters of the distribution, not only the MC mean. The analysed parameters describing the shape of the distribution were the arithmetic mean, variance, skewness, kurtosis, and

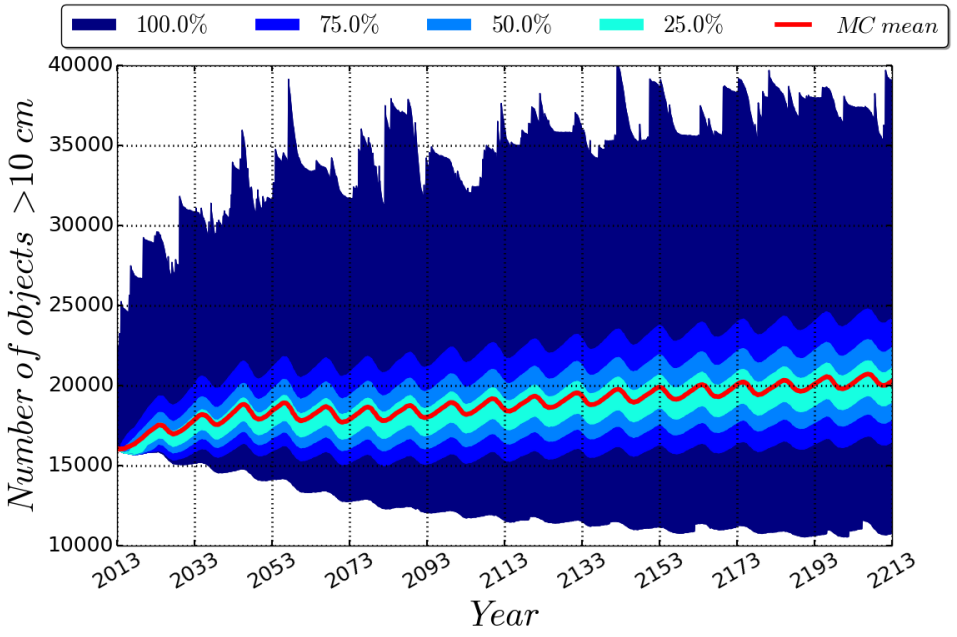

Figure 4.16: Evolution of the number of objects larger than 10 cm in the Monte Carlo sample of the "mitigation only" scenario from Table 1.1, including collision avoidance, projected using 25 000 MC runs. Showing the number of objects in a given fraction of the Monte Carlo runs, centred on the median. Also showing the mean of the sample.

median. These are the first four moments of the distribution that can be used to describe its shape, as well as the value that divides the probability space in two halves [25]. Here, the value of the kurtosis of the normal distribution was zero, i.e. Fisher kurtosis was computed [140]. The tested MC sample sizes ranged between 10 and 25 000 with increments of 50. For each MC sample size, the individual MC runs were randomly selected from the pool of 25 000 and the mentioned statistical parameters of the distribution were recomputed. This random selection was repeated 2000 times, thus giving distributions of the shape parameters for every sample size. Percentiles of these distributions were computed, the MC sample size was incremented and the process repeated until all desired sample sizes were investigated. The hypothesis behind this investigation is that when sufficiently many MC runs are present in the sample, the individual runs do not significantly affect the distribution parameters. The evolution of the mean number of objects with the number of Monte Carlo runs in the sample is shown in Fig. 4.17. The variations of the median and variance are given in Fig. 4.18, whereas Fig. 4.19 shows how the skewness and kurtosis of the distribution depend on the size of the sample.

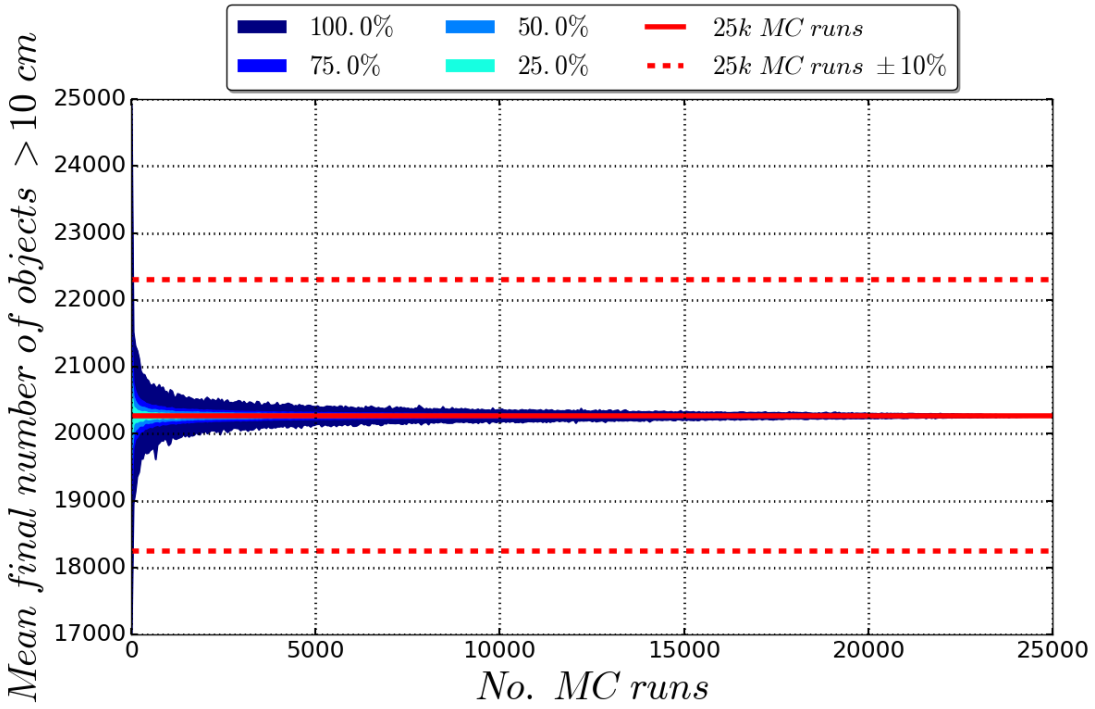

Figure 4.17: Variation of the arithmetic mean of the number of objects ≥ 10 cm in the MC sample of the "mitigation only" projection from Fig. 4.16 at the end of the projection (2213) with the sample size. Monte Carlo runs corresponding to the given sample size were randomly selected 2000 times, and the indicated percentiles of the distribution computed for every sample size. Also showing the value obtained with 25 000 MC runs, ±10%.

Fewer than 60 MC runs were needed to achieve a mean and median that were within 10% of the values obtained with 25 000 MC runs, i.e. to within 2027 objects. This accuracy threshold was achieved with 90% confidence using 10 to 40 runs in the study by Liou and Johnson [87]. However, when higher precision is desired, more Monte Carlo runs may be needed. More importantly, estimation of the variance, skewness and kurtosis, i.e. higher order moments, of the final distribution required more MC runs than estimating the mean or the median. Overall, these moments were within 10% of the value obtained with 25 000 MC runs with sample sizes of 3560, 16060 and 23960 for variance, skewness and kurtosis, respectively.

Using a smaller sample, which is faster to evaluate, allows more JCA system permutations to be analysed and cost-effective solutions to be identified. Therefore, it was decided to use a Monte Carlo sample of 15 000 runs. Based on the presented analysis, this sample was large enough for the mean, median and variance to have converged to within 10% of the value obtained with 25 000 MC runs but produces considerable time savings. The skewness and kurtosis converged to within 15 and 54%, respectively. This is to say that the chosen sample size was large enough to precisely estimate the first two moments of the distribution, associated with the expected number of objects in orbit

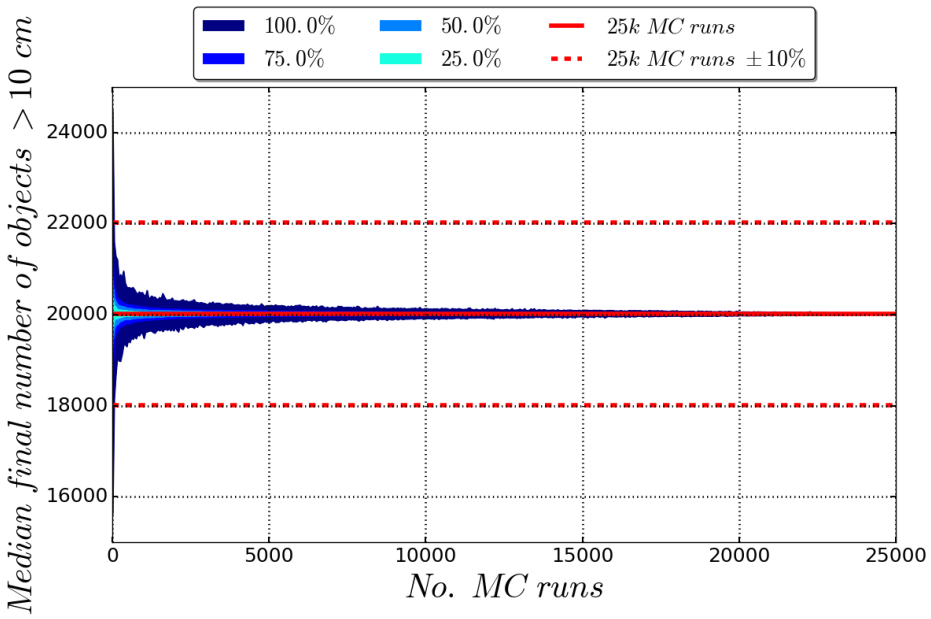

(a) Median

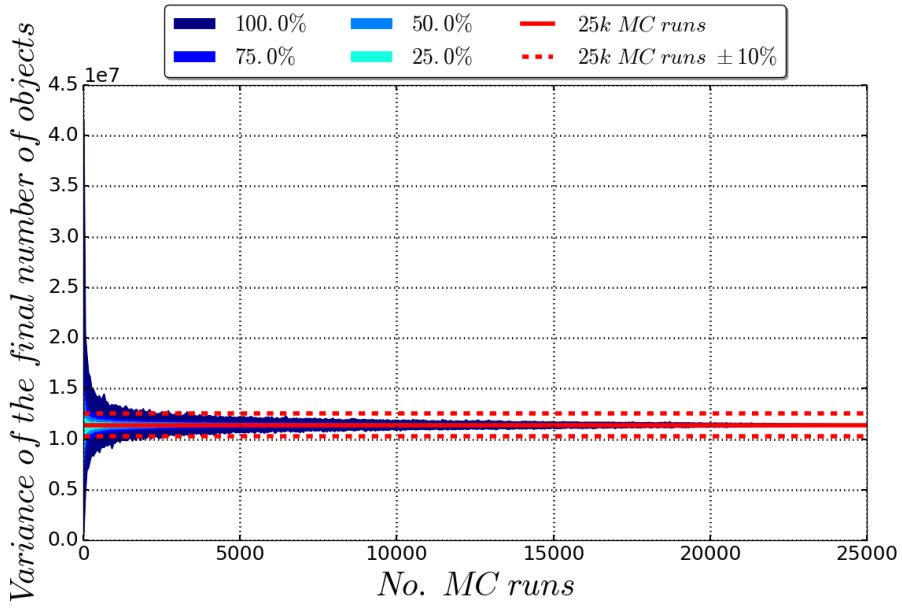

(b) Variance

Figure 4.18: Variation of the median and variance of the number of objects $\geq$ 10 cm in the MC sample of the "mitigation only" projection from Fig. 4.16 at the end of the projection (2213) with the sample size. Monte Carlo runs corresponding to the given sample size were randomly selected 2000 times, and the indicated percentiles of the distribution computed for every sample size. Also showing the value obtained with 25 000 MC runs, ±10%.

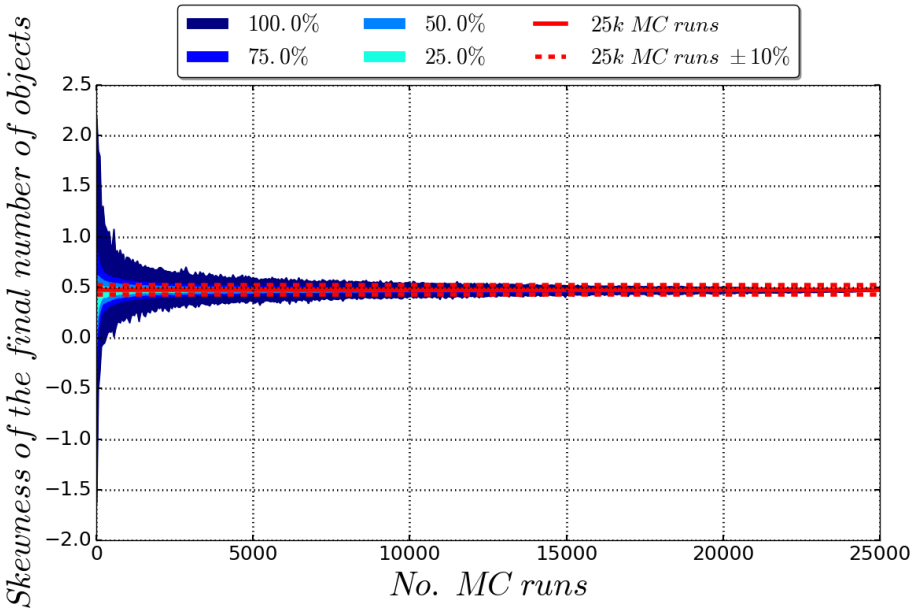

(a) Skewness

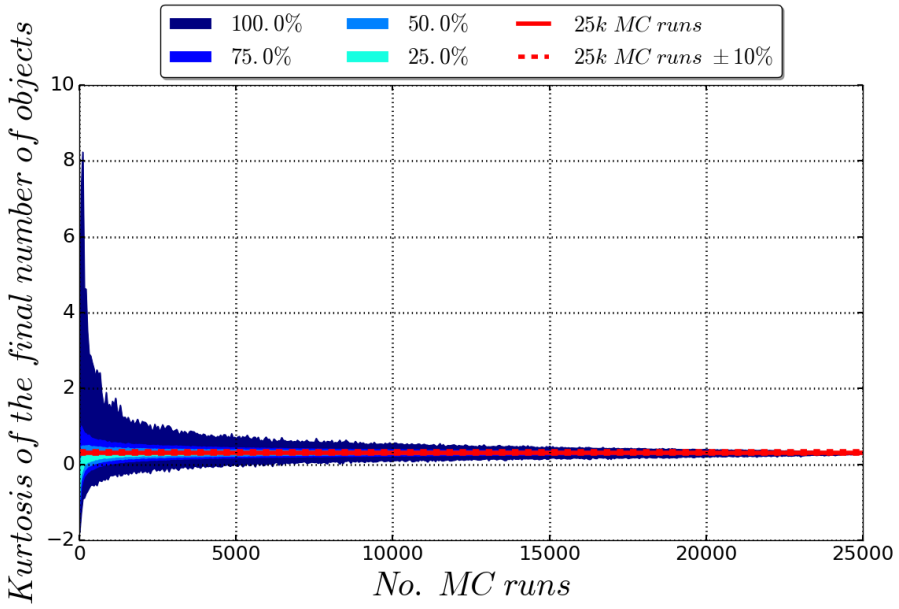

(b) Kurtosis

Figure 4.19: Variation of the skewness and kurtosis of the number of objects ≥ 10 cm in the MC sample of the "mitigation only" projection from Fig. 4.16 at the end of the projection (2213) with the sample size. Monte Carlo runs corresponding to the given sample size were randomly selected 2000 times, and the indicated percentiles of the distribution computed for every sample size. Also showing the value obtained with 25 000 MC runs, ±10%.

as well as its variability. The higher orders, associated with how profound the tail of the distribution is [25], were still estimated with precision of at worst 54%. However, the convergence of individual JCA simulations was verified to ensure that the sample of 15 000 MC runs was sufficiently large not to cause variability in the moments of the obtained distributions. This is covered in section 4.4.

It was shown in Chapter 3 that orbital collisions could involve objects that are not likely to be removed via ADR, whereas section 1.3.2.2 showed that the number of debris could still increase in spite of ADR. It was supposed that performing JCA on a small subset of objects could be used to reduce the tail of the distribution, i.e. prevent a substantial increase in the number of objects in orbit despite mitigation. If such targeted action was possible, JCA could be used as a complement to ADR that would ensure that debris remediation efforts will not be thwarted by unpredictable collisions. In order to test this hypothesis, the tail of the distribution had to be captured reliably. Thus, higher orders of the distribution of the number of objects, i.e. skewness and kurtosis, had to be estimated accurately in the reference scenario.

4.3.2 Results

4.3.2.1 Debris environment

The JCA simulation framework described in section 4.2.2.4 was used with all the free parameter permutations from Table 4.3, every permutation being a different $\vec{x}$ in Eq. 4.1. The final distribution of the number of objects in the Monte Carlo sample (at the end of year 2213) was analysed and statistical metrics were computed for it for every $\vec{x}$ (denoting the vector of the statistical metrics as $\vec{y} = f(\vec{x})$). The investigated metrics were median, variance, skewness and kurtosis, which are associated with the expected value of the number of objects in orbit and its uncertainty, as described in section 4.3.1. The effects of the JCA on the number of objects in orbit, not the number of collisions prevented i.e. no. JCA actions, were investigated because every collision produces a different number of fragments. Identifying whether preventing only the collisions of large-mass objects would have a positive effect on the debris environment was of interest. Therefore, a figure of merit that depends on the mass of the collided objects had to be chosen.

The evaluated values of $\vec{y}$ were regressed using a Gaussian radial basis function (RBF) kernel [54], implemented in scikit-learn [133], to provide estimates of $f(\vec{x})$ at more locations. These estimates, also referred to as a 'surrogate model', were denoted as $\vec{y}_{REG}$ and the corresponding points, where they were obtained, as $\vec{x}_{REG}$. Whenever a variable was regressed, the RBF kernel was first trained on the evaluated points by minimising the error on those points while varying the extents of influence of the evaluated points as well as smoothing of the regression. The error was never reduced to zero, however,

because the evaluated points were obtained using Monte Carlo simulations and so their results could change. Note that the RBF regression was only used to indicate regions of the $\vec{x}$ space where different components of $\vec{y}$ were low or high. Thus, imperfections of the RBF regression were acceptable. The errors of the RBF regression are investigated in detail in section 4.3.2.3.

The individual components of the response of the debris environment ($\vec{y}$) to implementing various JCA architectures ($\vec{x}$) are shown in Fig. 4.20 and Fig. 4.21. The figures also show surfaces, along which the given component of $\vec{y}_{REG}$ is constant (isosurfaces). These surfaces can be used to identify the regions of the $\vec{x}$ space where the components of $\vec{y}$ have similar range of values and the direction, in which $\vec{y}$ changes (gradient of every i component of $\vec{y}$, ∇y_i is normal to the isosurfaces).

For m_{TH} and $P_{C,TH}$ lower than approximately 0.5 (2293 kg and 10^{-3}, respectively), isosurfaces in Fig. 4.20 and Fig. 4.21 "curve" around the $m_{TH} = P_{C,TH} = 0$ line for all values of σ. However, while the median and the variance reduced for m_{TH} and $P_{C,TH}$ lower than 0.5, the skewness and kurtosis increased. This means that the expected value and the uncertainty on the number of objects reduced, but the tail of the distribution became more profound for $m_{TH} < 0.5 \wedge P_{C,TH} < 0.5$.

The insensitivity of $\vec{y}$ to σ was investigated in more detail, which is shown in Fig. 4.22 - the same median number of objects was achieved with higher $P_{C,TH}$ when the ephemeris accuracy improved, i.e. σ was lower. This can be discerned by observing where the lines of constant median cross the Y-axis in different subplots in Fig. 4.22. Variability in m_{TH} can also be observed in Fig. 4.22 when σ is changed, which is unphysical. This was likely caused by the fact that the regression was less accurate at the edges of the $\vec{x}$ domain. The accuracy of regression was quantitatively analysed, as reported in section 4.3.2.3.

The variation of $\vec{y}$ with every component of $\vec{x}$ was investigated in detail. Fig. 4.23, Fig. 4.24, and Fig. 4.25 show how the median, variance, and skewness of the number of objects vary with m_{TH}, $P_{C,TH}$, and σ, respectively. Kurtosis is not shown for brevity, because its behaviour was identical to that of skewness, and because skewness was estimated more accurately with the chosen size of the MC sample. The values of $\vec{y}_{REG}$ are also shown for a uniform grid of $\vec{x}_{REG}$ with five linearly spaced points per dimension of $\vec{x}$. A number of JCA parameter permutations, which investigated the entire range of $\vec{x}$ as well as $\vec{y}$, were selected for further investigation. The histograms of the final distribution of the number of objects for these parameter permutations are shown in Fig. 4.27. These selected permutations are marked with red crosses on Fig. 4.23, Fig. 4.24, and Fig. 4.25.

No trend in $\vec{y}$ can be observed for σ in Fig. 4.25 because σ affects the m_{TH} and $P_{C,TH}$ needed to achieve a given effect on the debris environment. σ itself will not increase the number of prevented collisions if the corresponding JCA action thresholds are too high, as was shown in Fig. 4.22. Note that all the dimensions of $\vec{x}$ were being perturbed when generating the sampling points (black dots). The outlier points in Fig. 4.25 were

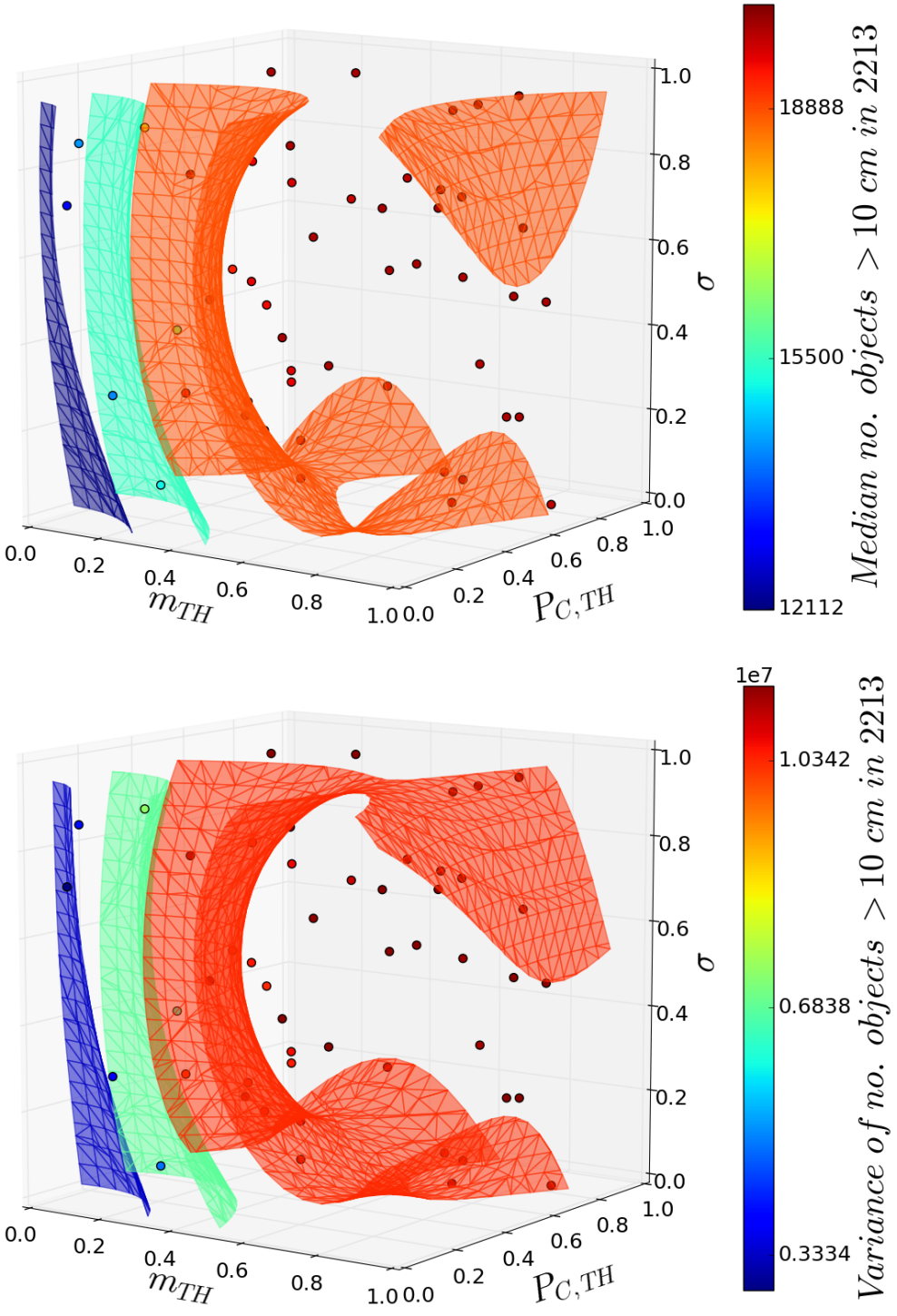

Figure 4.20: Median and variance of the distribution of the number of objects $\geq$ 10 cm in orbit at the end of the projection (2213) as a function of the ephemeris accuracy, probability threshold $P_{C,TH}$, and the mass threshold m_{TH}. Showing all the permutations from Table 4.3 as dots. Also showing isosurfaces of $\vec{y}_{REG}$ (obtained using RBF regression) at levels indicated on the colourbar.

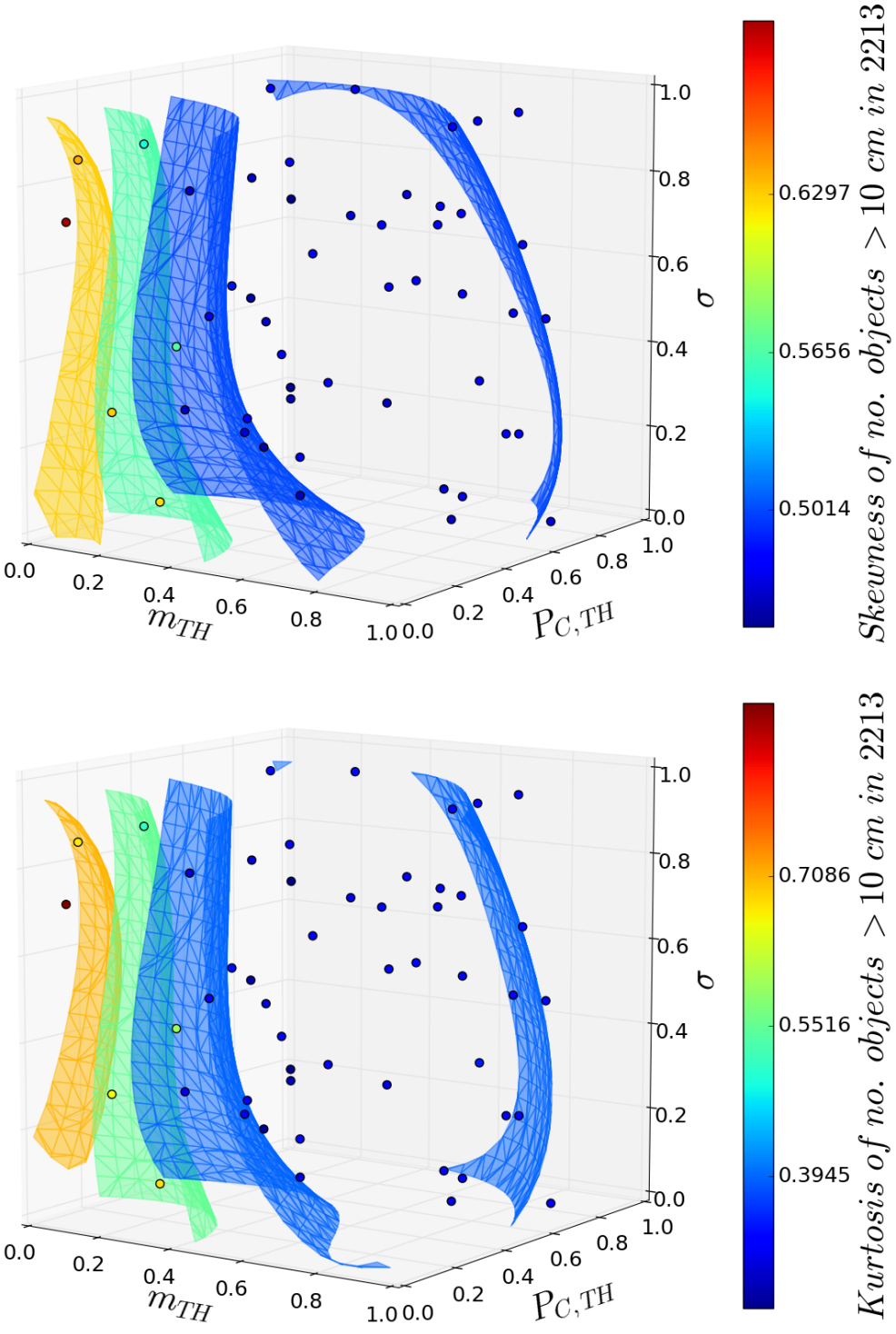

Figure 4.21: Skewness and kurtosis of the distribution of the number of objects ≥ 10 cm in orbit at the end of the projection (2213) as a function of the ephemeris accuracy, probability threshold $P_{C,TH}$, and the mass threshold m_{TH}. Showing all the permutations from Table 4.3 as dots. Also showing isosurfaces of $\vec{y}_{REG}$ (obtained using RBF regression) at levels indicated on the colourbar.

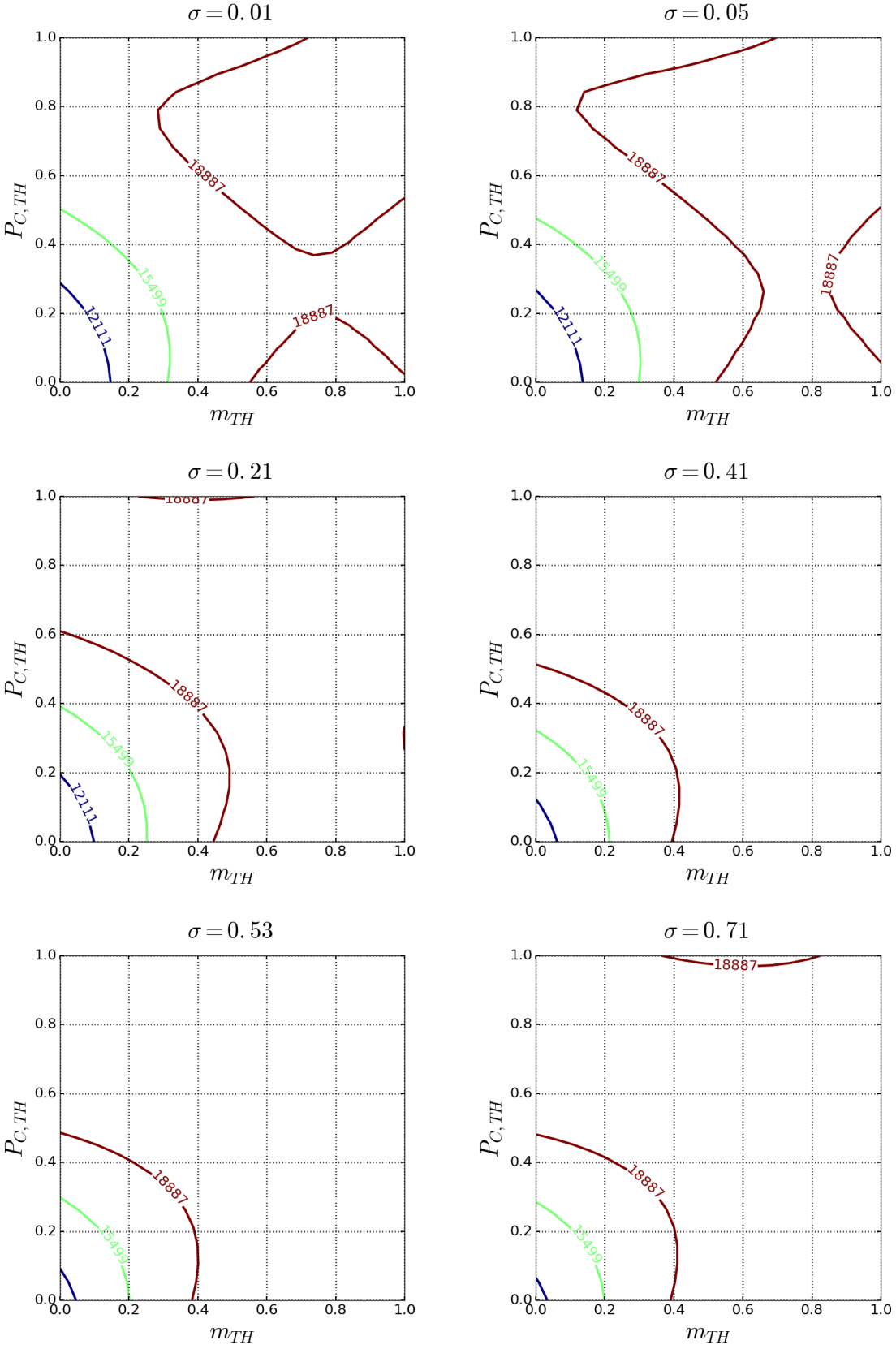

Figure 4.22: Projection of median number of objects $\geq$ 10 cm in 2213 onto the $P_{C,TH}$, m_{TH} plane for different levels of σ. Showing lines of constant median computed with RBF regression ($\vec{y}_{REG}$) also shown as isosurfaces in Fig. 4.20.

created by different permutations of m_{TH} and $P_{C,TH}$, not varying σ. This can be further ascertained by noting that, according to the regression, almost any value of median, variance, and skewness was possible for any value of σ, depending on the values of m_{TH} and $P_{C,TH}$. Still, the minimum number of objects that could be reached with a given σ according to the RBF regression in Fig. 4.25 (the lowest value of y_{REG}) reduced with improved ephemeris accuracy. This is because σ did not directly define how many collisions were prevented; it only defined how many collisions had P_C above a given $P_{C,TH}$. When $P_{C,TH}$ was set too high for the given σ, the corresponding number of objects in orbit did not change. When $P_{C,TH}$ was lower while σ was kept constant, the number of objects in orbit reduced. Similarly, if $P_{C,TH}$ was kept constant and σ was reduced, more conjunctions had P_C above $P_{C,TH}$. This has direct implications for potential JCA implementation because it shows that certain level of ephemeris accuracy has to be met for JCA, operating at a given $P_{C,TH}$, to limit the future number of collisions. This behaviour was explained in more detail in section 4.2.2.2 and it was argued that, if σ is too high, all collisions will occur in the "probability dilution" regime and it will be impossible to forecast them. This also shows the importance of choosing the correct $P_{C,TH}$ for the achievable σ to reduce the ignored collision probability, as described in section 4.2.2.3; ignoring too much collision probability will cause too few collisions to be avoided and JCA to have little positive impact on the debris environment.

The space debris environment responded similarly to varying both m_{TH} and $P_{C,TH}$. For high values of these two JCA parameters, the final distribution of the number of objects did not change because few JCA actions were being performed. When m_{TH} was lowered to the order of 2000 kg and $P_{C,TH}$ to $o\left(10^{-3}\right)$, collisions began to exceed these thresholds, JCA actions started to be performed, and the final population of objects began to vary (median and variance reduced, whereas the skewness and kurtosis increased). This can be seen when examining the mean number of JCA actions in the MC sample as a function of various components of $\vec{x}$ shown in Fig. 4.26. For $m_{TH} > 2000.0$ kg and $P_{C,TH} > 10^{-3}$, at most four JCA actions were performed in 200 years in a single Monte Carlo run. On average, less than one JCA took place in this parameter regime in the entire MC sample. When m_{TH} and $P_{C,TH}$ were reduced, more JCA actions began to take place.

It was impossible to lower the skewness of the distribution (reduce the tail above the median [25]) without affecting the median or the variance. This means that the number of objects could not be reduced *only* in the MC runs where many collisions have taken place and where the number of debris was high relative to the median. In order for JCA to have a measurable, guaranteed effect on the long-term evolution of the debris environment, its action thresholds had to be lowered sufficiently for many JCA interventions to be performed. However, in circumstances like this, many false alarms would take place and so the JCA cost would be high, which is discussed in more detail in section 4.3.2.2. This finding means that JCA cannot be used as a selective alternative to active debris removal, whereby the aim is to ensure that the number of debris in orbit does not grow significantly above the median. As the JCA thresholds were being reduced, the peaks

of the distributions of the numbers of objects in Fig. 4.27 shifted, rather than only the tails disappearing. The "Kessler syndrome" would manifest itself by the appearance of such tails above the median, i.e. as MC runs where many collisions took place and the debris population increased more than in most of the runs. Even though the collision cascade may not have taken place in any of the samples in Fig. 4.27, the outlying MC runs with relatively high numbers of objects serve as an example of such tails. The fact that median and variance of the number of objects had to be decreased to reduce the skewness means that JCA cannot be used only to reduce the probability that the "Kessler syndrome" will start or continue, if it has started already [88]. If it could, only the tails in Fig. 4.27 would disappear without shifting the entire distributions.

4.3.2.2 Number of false alarms

It was shown in the analysis presented in section 4.3.2.1 that the ephemeris accuracy σ does not directly affect the distribution of the number of objects in orbit in 2213. However, σ affects how many conjunctions exceed $P_{C,TH}$, and so it will drive the false alarm rate (number of conjunctions that exceed $P_{C,TH}$ without resulting in collisions). This rate will, in turn, affect the cost of JCA [95, 99].

The expected cost of a single JCA action using suborbital rockets depends strongly on the launch costs and is expected to be between $\$1 - 2M$, however no cost estimates of the JCA payload were made by McKnight [103] or other authors. The cost of preparing a complete laser for JCA operations was estimated to be $\$3 - 6M$ by Mason et al. [95], however the cost of the entire JCA laser station has not been estimated. What is also missing from the mentioned analyses is the running cost of maintaining an object catalogue and performing collision screenings [130]. Overall, a thorough cost analysis of the complete JCA system should be conducted [95]. However, because the cost of developing JCA will depend on the corporate structure of the entity building such a system, amongst other factors, this work will not attempt to associate monetary value with the JCA system permutations from Table 4.3 due to lack of agreement on how JCA should be developed or by whom. Instead, this study will provide an estimate of the number of false alarms and the corresponding effects on the environment, which can be traded-off when JCA implementation is being considered.

In order to assess the number of JCA actions that would take place per unit time, the conjunction detection and assessment algorithm developed in Chapter 2 was used. Three public TLE catalogue snapshots, listed in Table 4.4, were screened for conjunctions closer than 1 km with eight σ values ($\sigma \in \{0.01, 0.05, 0.21, 0.41, 0.53, 0.71, 0.87, 0.99\}$) and 25 linearly spaced m_{TH} and $P_{C,TH}$ values (25 m_{TH} and $P_{C,TH}$ pairs per one σ value). The interpolation and conjunction detection time step was reduced to 100 seconds to improve the accuracy of miss distance and P_C estimation. This value was arrived at by comparing the P_C accumulated by the test objects from section 2.5.2 computed using

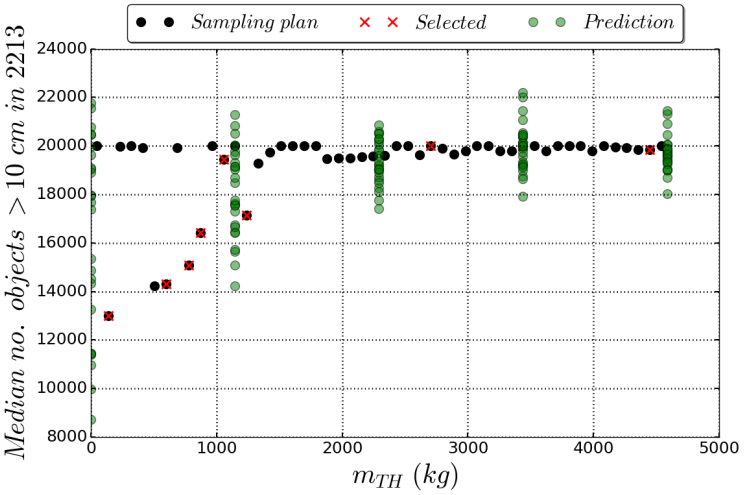

(a) Median

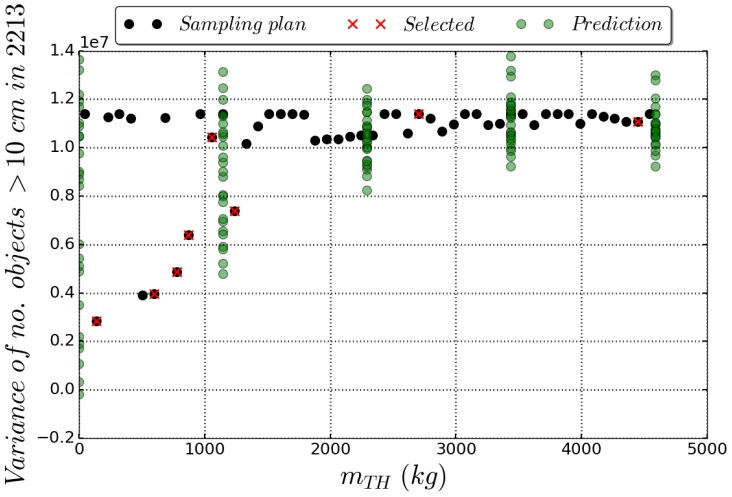

(b) Variance

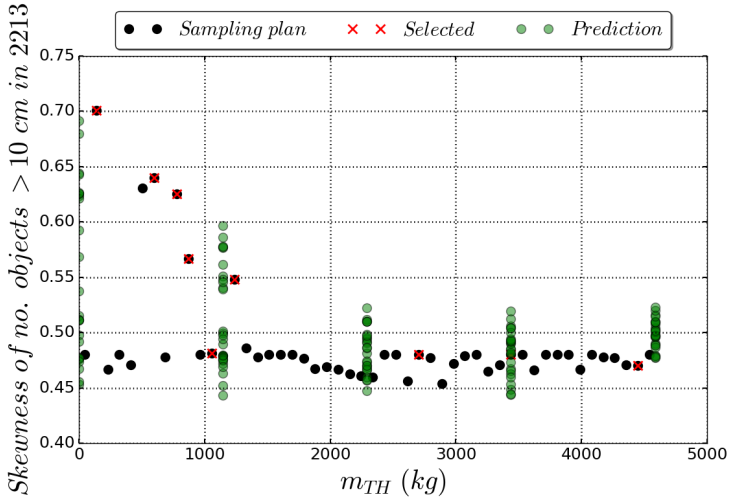

(c) Skewness

Figure 4.23: Shape parameters of the distribution of the number of objects $\geq$ 10 cm in orbit at the end of the projection (2213) as a function of the mass threshold m_{TH}. Showing all the permutations from Table 4.3 (black dots), the values predicted using RBF regression ($\vec{y}_{REG}$, green dots), and the permutations selected for further investigation (red crosses).

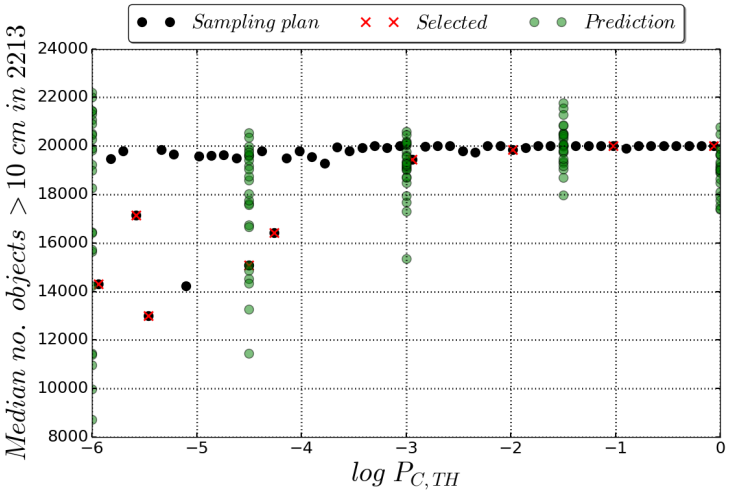

(a) Median

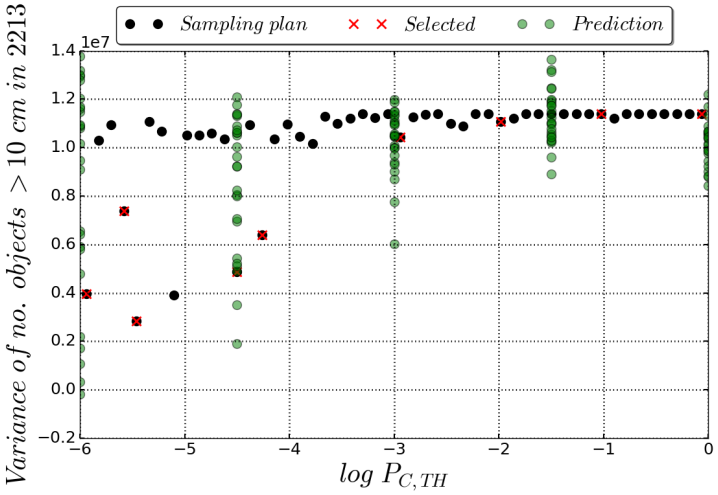

(b) Variance

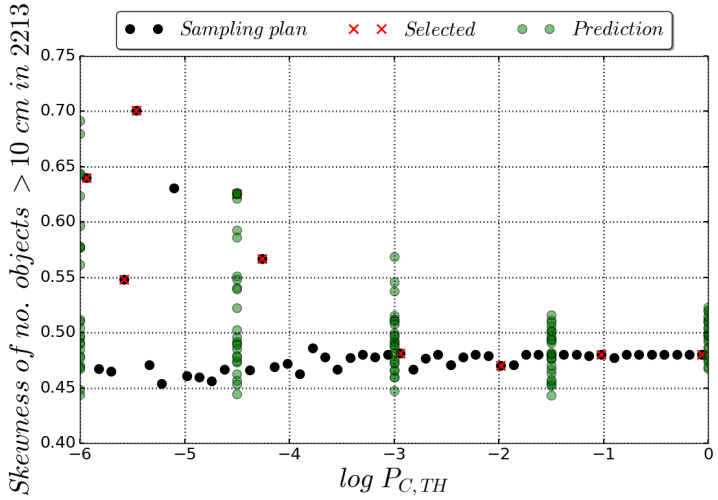

(c) Skewness

Figure 4.24: Shape parameters of the distribution of the number of objects $\geq$ 10 cm in orbit at the end of the projection (2213) as a function of the collision probability threshold $P_{C,TH}$. Showing all the permutations from Table 4.3 (black dots), the values predicted using RBF regression ($\vec{y}_{REG}$, green dots), and the permutations selected for further investigation (red crosses).

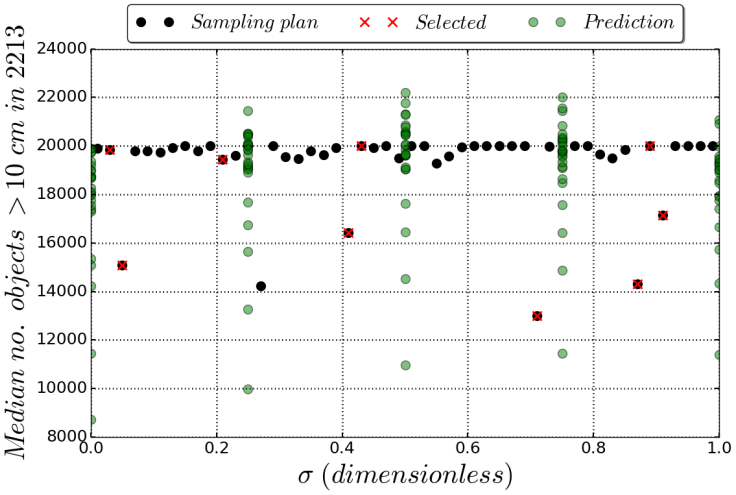

(a) Median

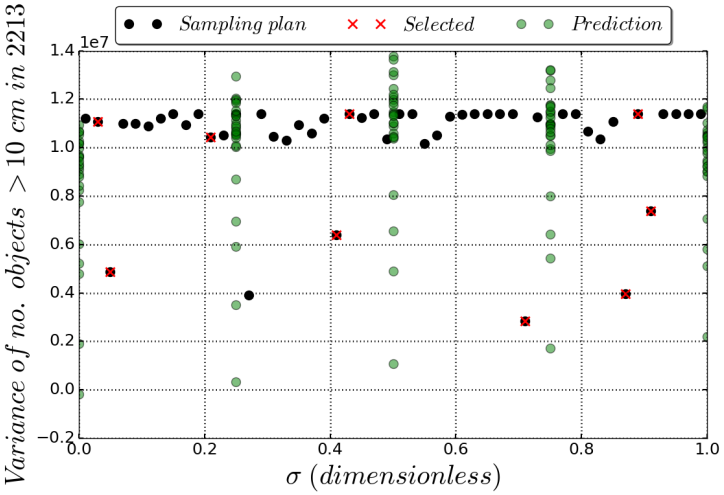

(b) Variance

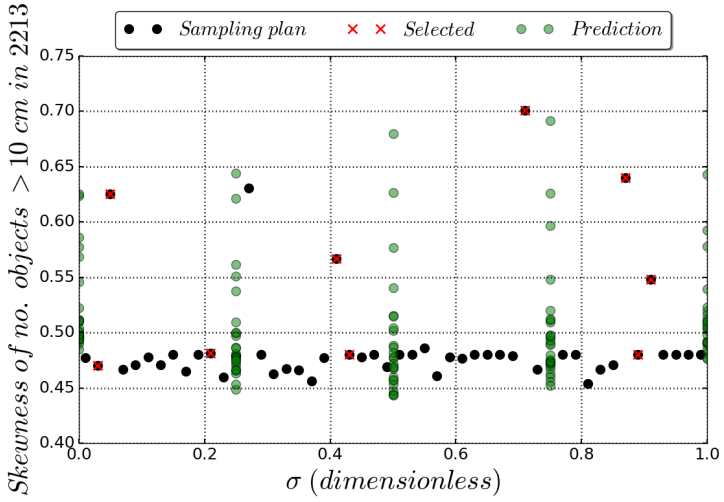

(c) Skewness

Figure 4.25: Shape parameters of the distribution of the number of objects $\geq$ 10 cm in orbit at the end of the projection (2213) as a function of the ephemeris accuracy. Showing all the permutations from Table 4.3 (black dots), the values predicted using RBF regression ($\vec{y}_{REG}$, green dots), and the permutations selected for further investigation (red crosses).

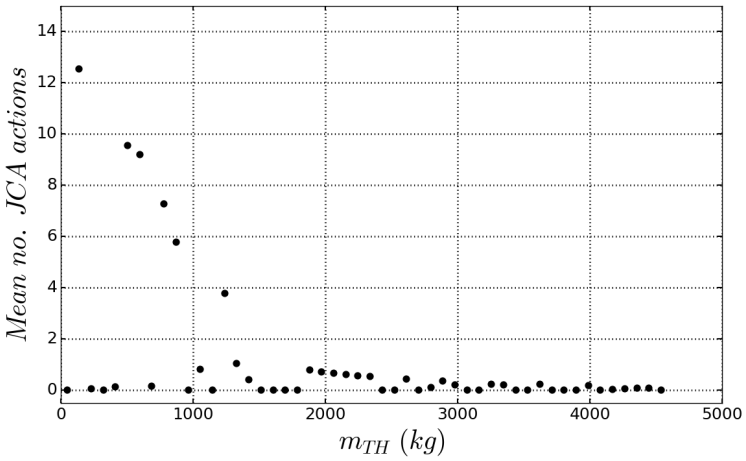

(a) m_{TH}

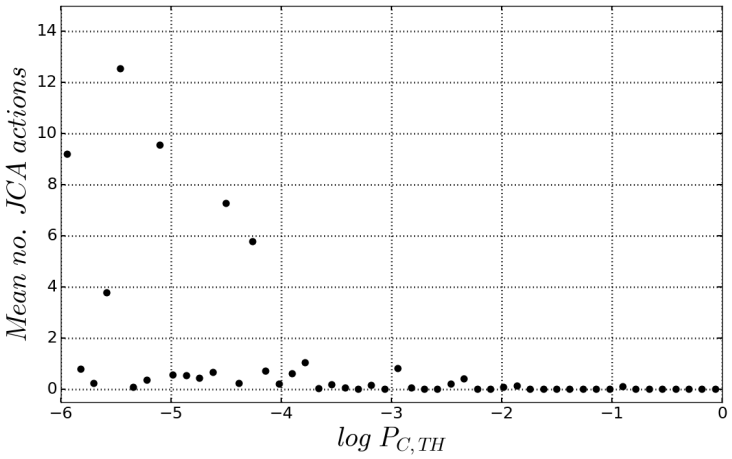

(b) $P_{C,TH}$

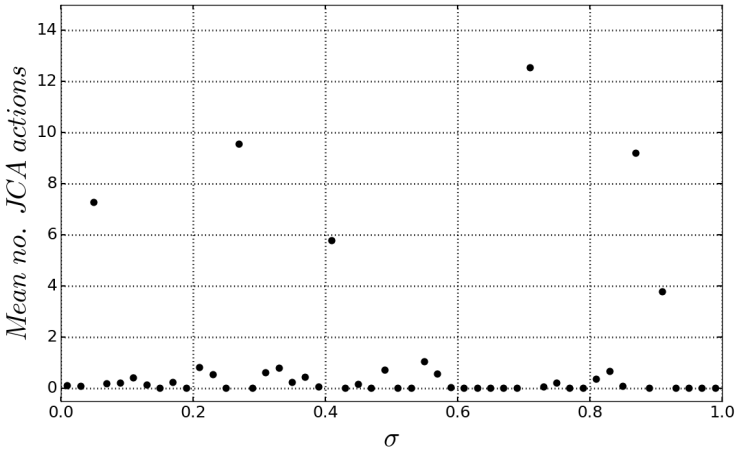

(c) σ

Figure 4.26: Mean number of JCA actions in the Monte Carlo sample as a function of the JCA action thresholds.

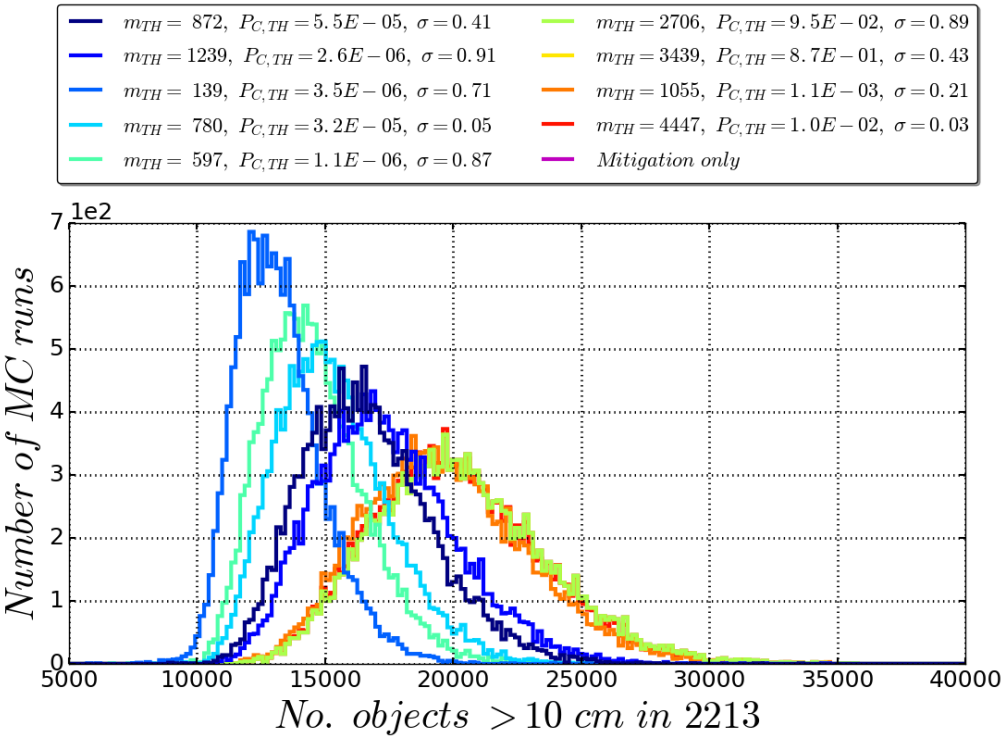

Figure 4.27: Distributions of the number of objects $\geq$ 10 cm in orbit at the end of the projection (2213) in the Monte Carlo samples for the selected just in-time collision avoidance parameter permutations. Showing permutations of JCA parameters number 9, 11, 21, 22, 28, 33, 34, 40, 47 from Table 4.3 together with the reference data for the "mitigation only"scenario.

Table 4.4: Public two-line element set catalogue snapshots analysed to assess the expected number of JCA actions depending on the free parameters of the system. The simulations started and ended at UTC midnight on the indicated day.

Snapshot date	**Start epoch**	**End epoch**	**Duration (days)**	**No. objects**
23 Oct 2013	23 Oct 2013	07 Nov 13	15	14 917
07 Nov 2013	07 Nov 2013	21 Nov 13	14	14 920
07 Nov 2013	07 Nov 2013	21 Nov 13	14	15 099

different time steps with position standard deviations of 100 m. The details of this study are not shown here for brevity but are given in section C.2 of the appendix. Radial basis function regression was created from the evaluated points, and the expected number of false alarms was evaluated on the $\vec{x}$ points from the sampling plan in Table 4.3, as shown in Fig. 4.28. This was done because evaluating one σ value took over three years of CPU time, therefore directly evaluating all 50 permutations from Table 4.3 would be prohibitively expensive. This RBF regression was also used to evaluate the number of false alarms at every $\vec{x}_{REG}$ from section 4.3.2.1. Because no collision was reported in the analysed periods, every conjunction found in them was a false alarm.

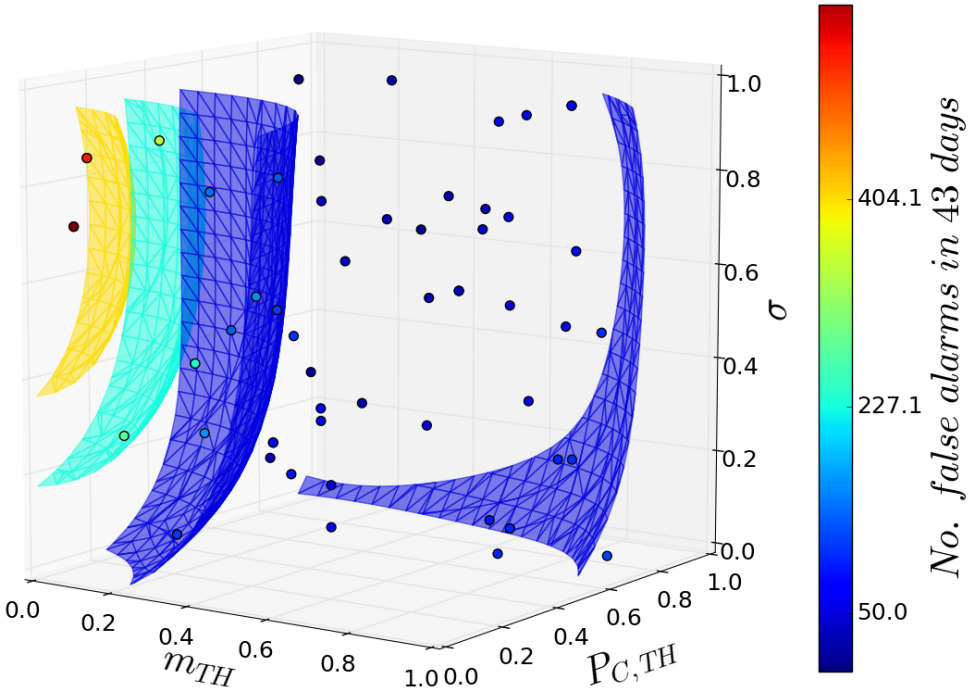

Figure 4.28: Number of JCA false alarms as a function of the ephemeris accuracy, probability threshold $P_{C,TH}$, and the mass threshold m_{TH}. In order to reduce the computational time, eight points, which spanned the dimension of σ, were evaluated together with a rectangular grid of $P_{C,TH}$ and m_{TH} (200 points in total). The evaluated numbers of JCA false alarms were then regressed onto all points from Table 4.3 (shown as dots) using radial basis functions. Also showing isosurfaces, obtained using radial basis function regression, at levels indicated on the colourbar.

Apart from analysing the results from Fig. 4.28, it is insightful to understand the distributions of the collision probabilities, which will be seen for the orbital conjunctions depending on the σ value. These distributions are presented in Fig. 4.29a. For the best ephemeris accuracies (lowest σ), a broad spectrum of P_C can be observed for all the conjunctions. For $\sigma = 0.01$ (corresponding to RIC position standard deviations of $\sigma_R = 7.23$, $\sigma_I = 17.30$, $\sigma_C = 5.36$ metres, respectively), P_C values between less than a double floating point precision number and 21.1% were observed. For 76.8% of conjunctions (13 780 out of 17 932), P_C was virtually 0.0 and hence the peak of the distribution shown with the darkest blue line could not be represented on a logarithmic scale. Consequently, conjunctions with P_C of up to 1×10^{-4} could be ignored without increasing the collision risk in orbit (Fig. 4.29b shows the ignored and avoided collision probabilities of any collision taking place depending on $P_{C,TH}$). When ephemeris accuracy decreased (σ increased), more conjunctions had $P_C >= 1 \times 10^{-4}$, i.e. could cause operator concerns [34]. This is because higher miss-distance can give rise to a high P_C when the ephemeris accuracy is low. However, as the ephemeris accuracy reduced, even the very close conjunctions began to have low P_C, due to "probability dilution" [4]. This

was reflected in the number of conjunctions that exceeded a given $P_{C,TH}$ for the given ephemeris accuracy, which is shown in Fig. 4.29c. For $\sigma > 0.21$ and $P_{C,TH} > 1 \times 10^{-2}$, no conjunction had $P_C \geq P_{C,TH}$ and all the collision risk in orbit was ignored. This analysis shows that, with the currently achievable ephemeris accuracies, comprehensive all-on-all conjunction screenings could be performed without operating in the "probability dilution" regime or having to perform many JCA actions. Thus, JCA could be economically feasible because $P_{C,TH}$ could be set at 1×10^{-4} without ignoring any risk in orbit. However, position standard deviations close to the 5^{th} percentile level should be achieved for all the objects to facilitate this.

Including m_{TH} as a JCA action criterion reduced the number of false alarms from at most 17 932 to at most 571, which can be observed when comparing Fig. 4.29c to Fig. 4.28 (Fig. 4.29c uses a logarithmic scale to represent the number of false alarms while the scale in Fig. 4.28 extends up to 571). Recall from section 4.3.2.1 that reducing m_{TH} reduced the future number of objects in orbit. However, when m_{TH} was lowered from 1.0 to 0.0 (4585 to 1 kg), the number of false alarms increased from 0 to 571 in 43 days as shown in Fig. 4.28. The same holds true for $P_{C,TH}$. This confirms that reducing the number of false alarms (lowering the cost) and reducing the number of objects in orbit are conflicting requirements for the JCA system, and therefore should be studied concurrently.

4.3.2.3 Synthesis of JCA false alarms and debris remediation effects

The number of false alarms that took place over the 43 days analysed in section 4.3.2.2 was plotted against the median number of objects found in section 4.3.2.1 for all $\vec{x}$ from Table 4.3. The values regressed on a rectangular grid of 20 points per dimension, $\vec{y}_{REG}$, were also included in the plot, which is shown in Fig. 4.30. For 70.7% of the $\vec{y}_{REG}$ points (5656 out of 8000), the median was above 19 000; these points were filtered out so as not to obscure the evaluated $\vec{x}$ points. This signifies that most of the investigated JCA implementations are clustered around the median of the reference scenario and zero JCA false alarms (corresponding to no JCA actions). A small fraction of the $\vec{y}_{REG}$ points had relatively few false alarms (such JCA would be relatively inexpensive) and reduced the median of the number of objects (JCA would be effective). For only 255 out of 8000 $\vec{y}_{REG}$ points, the number of false alarms was fewer than 200 in 43 days (fewer than 1699 in a year) and the median number of objects was lower than 16 000.

Two $\vec{y}_{REG}$ points from Fig. 4.30 were chosen; one with a median number of objects of approximately 13 000 and the lowest predicted number of false alarms with such a median, and one with median of approx. 12 500 and more false alarms. These points do not represent any specific optima and were chosen to test the accuracy of the surrogate modelling around the predicted location of the most cost-effective JCA systems (the points with fewest false alarms for a given median [54]). These two points

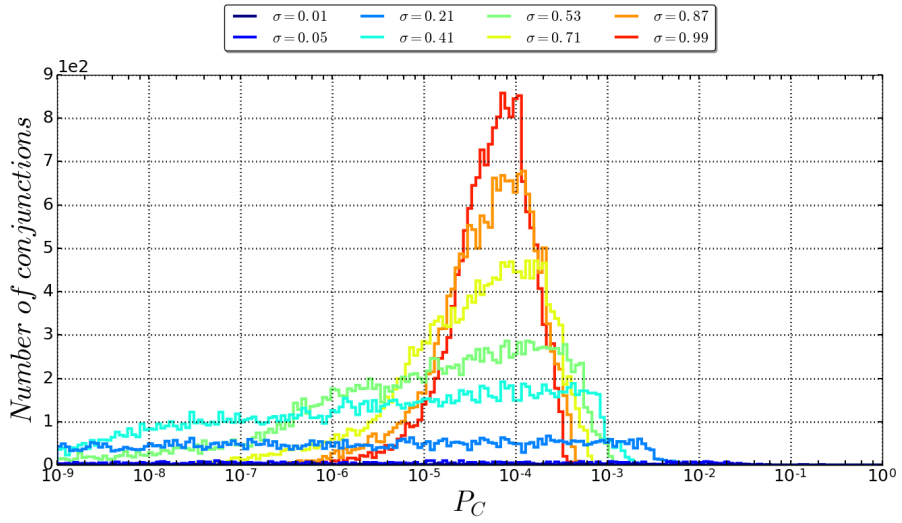

(a) P_C histogram

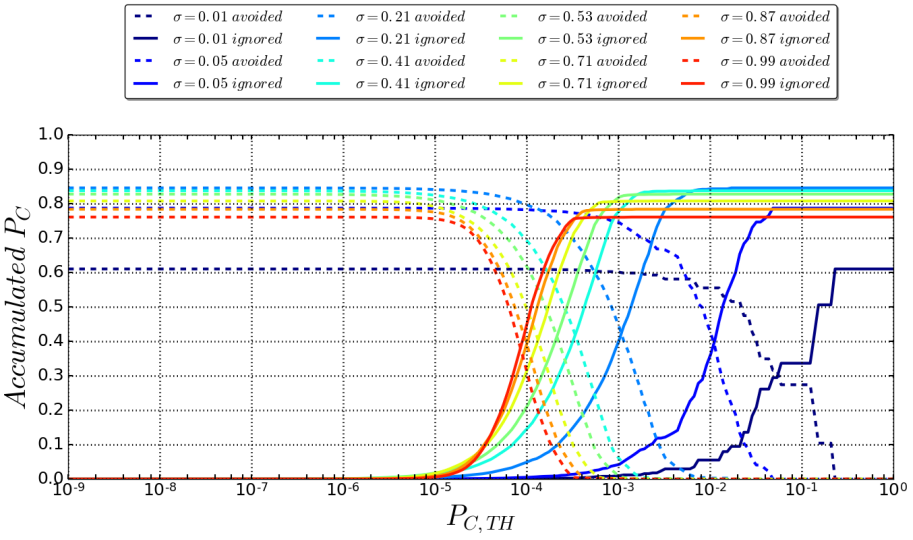

(b) Ignored VS avoided risk

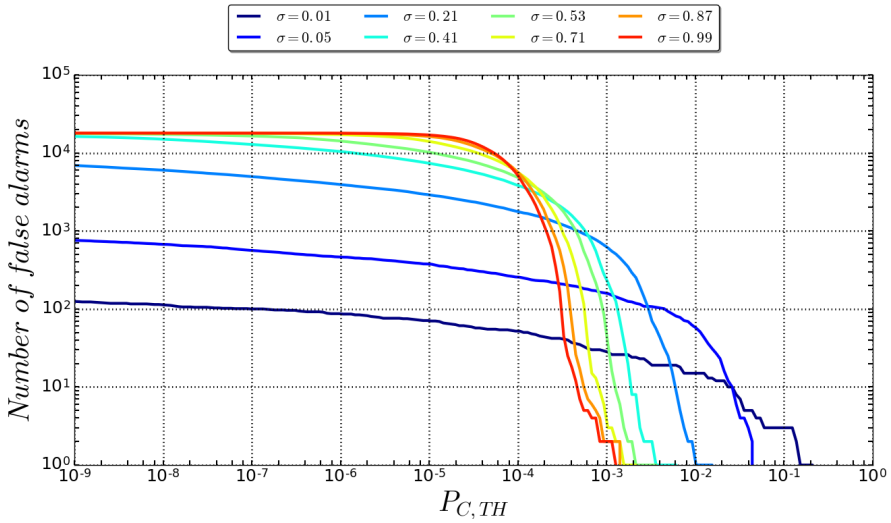

(c) Number of false alarms in 43 days

Figure 4.29: Effects of varying dimensionless ephemeris accuracy σ and JCA action threshold $P_{C,TH}$ on the number of JCA false alarms. m_{TH} is not taken into account. 43 days of conjunctions closer than 1 km.

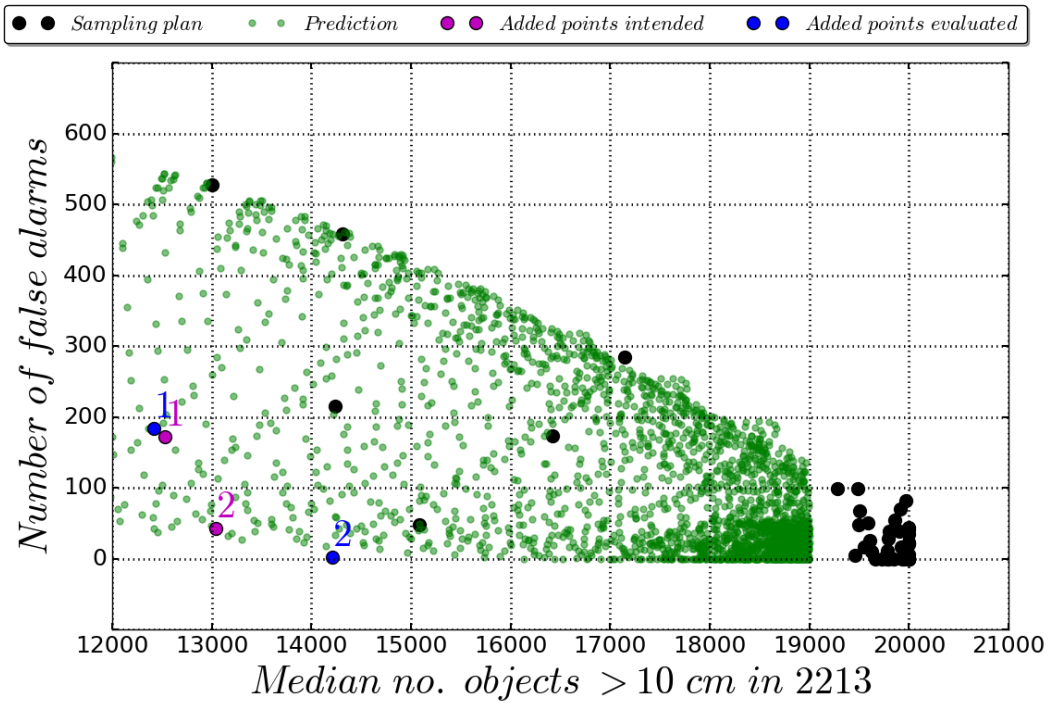

Figure 4.30: The number of false alarms and the expected median number of objects in 2213 for all the investigated JCA parameter permutations from Table 4.3 (black) and additional points obtained using RBF surrogate modelling (green). The additional points were obtained by evaluating the surrogate models at a rectangular grid of 20 points per dimension of $\vec{x}$ and filtering out medians larger than 19 000. Two points added to the sample, in their intended locations derived using the surrogate models (magenta), and the locations obtained by evaluating the JCA model (blue), are also shown.

were evaluated using the JCA simulation tool from section 4.2.1, and by finding all the conjunctions between the TLE snapshots from section 4.3.2.2. The intended locations of the points, obtained from the surrogate models, i.e. RBF regressions, are shown in Fig. 4.30 as magenta dots, while the results of evaluating these points directly are shown as blue dots. Table 4.5 provides a summary of the results for these two points. Point number 2 was less accurate than point 1: in the less accurate case, the number of false alarms was overestimated by an order of magnitude and the median by 8.24%. The origin of the inaccuracy was investigated and the distances between the added points and the 50 in the original sample were computed; the location of the added points with respect the original sampling plan is shown in Fig. 4.31. Both points are located outside of the initial sampling plan points, however the less accurate added point 2 is 3.8% further from the bulk of the sampling plan points than added point 1 (two-norms of the dimensionless distance to all the sampling plan points were 5.97 and 5.75, respectively).

Table 4.5: Points added to the original sampling plan from Table 4.3 to investigate the possible set of JCA outcomes and to verify the predictions. Medians and numbers of false alarms predicted by the surrogate models denoted as 'Pred.' and the values evaluated directly as 'Eval.'.

Point	Dimensionless			Dimensional (kg and m)				
	$\mathbf{m_{TH}}$	$\mathbf{P_{C,TH}}$	σ	$\mathbf{m_{TH}}$	$\mathbf{P_{C,TH}}$	$\sigma_\mathbf{R}$	$\sigma_\mathbf{I}$	$\sigma_\mathbf{C}$
1	0.01	0.215	0.2	46.8	1.95×10^{-5}	70.52	144.7	46.36
2	0.1	0.25	0.01	459.4	3.16×10^{-5}	7.23	17.3	5.36
Point	**Median**			**No. false alarms**				
	Pred.	**Eval.**	**% err.**	**Pred.**	**Eval.**	**% err.**		
1	12 525	12 419	0.85%	172	184	−6.52%		
2	13 037	14 208	−8.24%	43	2	2050.0%		

In order to assess the accuracy of the RBF surrogate models, the predictions by them at all the evaluated points were plotted against the actual evaluated values and are shown in Fig. 4.32. Recall that the number of false alarms was directly evaluated for only eight $\vec{x}$ points due to computational time constraints, and the rest of the $\vec{x}$ points were evaluated using RBF regression.

If the surrogate models were perfect, they would always predict the response of the space debris system exactly. Therefore, all the points in Fig. 4.32 would follow a straight line with slope of 1.0. Errors in the magnitudes of both the number of false alarms and the median number of objects in orbit were incurred by the surrogate models. However, they approximated the behaviours of the perfect models with $R = 0.9600$ and $R = 0.9893$ for median and number of false alarms, respectively. This shows that the trends that the surrogate models exhibited were identical to the actual response of the space debris system, however the exact value of the response varied, as was seen for the added point number 2 from Table 4.5. Therefore, the predicted values in Fig. 4.30 may be inaccurate, especially close to the lowest numbers of false alarms per given median, as in the case of the added point 2. However, the location of the most cost-effective JCA systems in the parameter space of $\vec{x}$ is correct.

Out of all the 52 evaluated JCA parameter permutations (50 in the original sampling plan in Table 4.3 plus two added from Table 4.5), the added point number 2 was the most cost-effective. The large positive impact of this JCA system on the debris environment was brought by relatively low m_{TH} and $P_{C,TH}$ action thresholds (459.4 kg and 3.16×10^{-5}, respectively), which ensured that many collisions were prevented. Such low action thresholds could mean that the number of false alarms of this JCA system would make it financially unfeasible. However, if the ephemeris accuracy is improved to the order of several metres (for this point, the RIC position standard deviations were $\sigma_R = 7.23$, $\sigma_I = 17.30$, $\sigma_C = 5.36$ metres, respectively), the number of false alarms will be low. For this point, only two false alarms were observed in the analysed 43 day interval, which corresponds to 17 false alarms in a year.

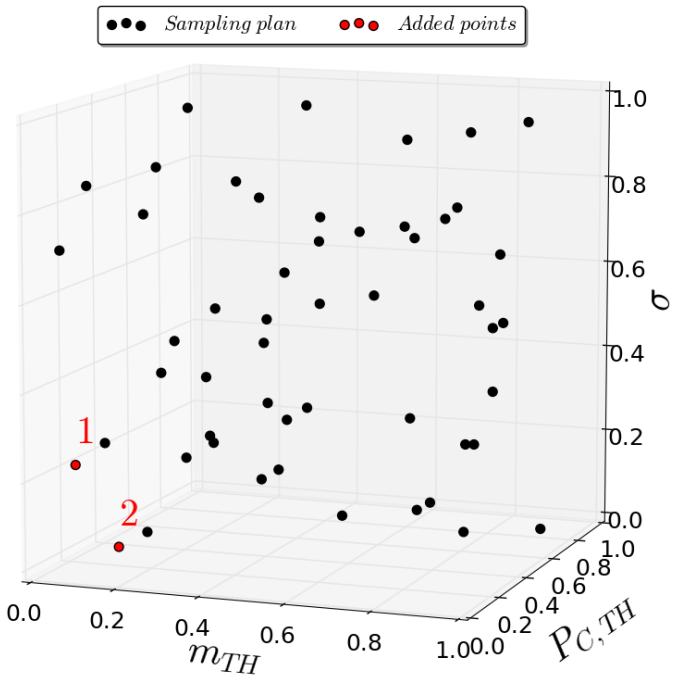

Figure 4.31: Points added to the original sampling plan from Table 4.3, which is shown with black dots.

4.4 Discussion

The work presented in this chapter used several simplifications and made a number of assumptions; they were necessary to reduce the computational time needed for the analyses to make them feasible. Many of these simplifications were associated with the JCA simulation framework developed in section 4.2.1. Firstly, it was assumed that the nominal positions of objects at the time of the closest approach were separated by the collision radius, and the collision probability was computed based on these state vectors. In the presence of propagation errors, even if the objects do collide, their predicted miss distance might be large. This will lead to low collision probabilities that could fall below $P_{C,TH}$. The same holds true for all the collision probability calculation assumptions that this work has made, e.g. Gaussian, zero-mean position uncertainty, rectilinear relative motion of the objects etc. Propagation accuracy has to be addressed together with how the state vector uncertainty is represented and propagated [50], as well as how P_C is computed hence [106], in order to make sure that few actual collisions are not predicted. This is crucial for JCA to work, however these issues are being addressed by other authors (Morselli et al. [106] and Horwood and Aristoff [50], for example), therefore they were not investigated as part of this work. The way in which JCA was simulated here was the best case scenario (ideal propagation accuracy) of currently used P_C estimation algorithms (section 2.3).

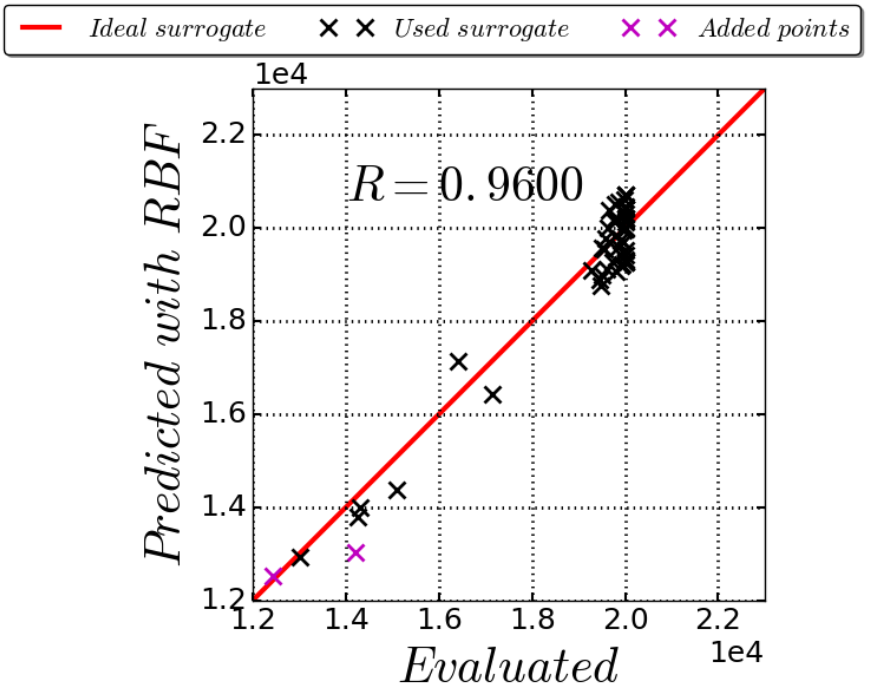

(a) Median

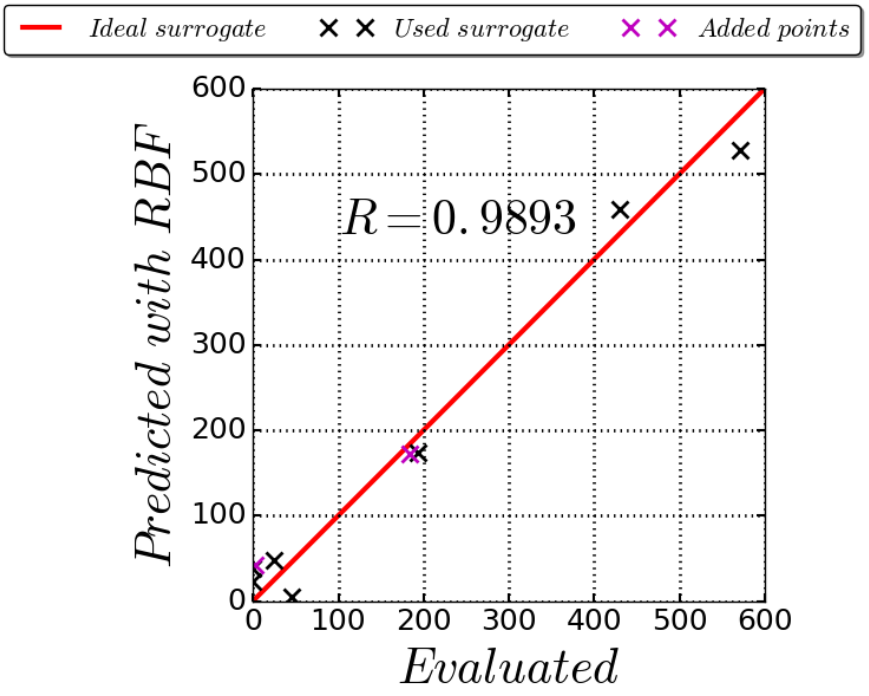

(b) Number of false alarms in 43 days

Figure 4.32: Assessing the accuracy of the surrogate models by comparing the predicted values to the ones obtained by directly evaluating the chosen permutations of JCA free parameters. An ideal surrogate model would always predict the same value as the actual one, i.e. the points would follow a straight line with gradient of 1.0. Showing the median number of object in orbit in 2213 and the number of false alarms, obtained in section 4.3.2.1 and section 4.3.2.2, respectively.

When simulating JCA it was also assumed that all objects have the same position uncertainty, and every component of the RIC covariance matrix was scaled by the same factor (aspect ratio of uncertainty ellipsoids was kept constant). It was shown in section 4.2.2.2 that this is not the case in the catalogue used operationally. However, this approach resulted in an ephemeris accuracy envelope that the SST system should be designed to deliver for JCA to be feasible. Moreover, the results of this work could still be applied to real conjunctions by comparing the real covariance matrices at the TCA and the P_C obtained with them to the $P_{C,TH}$ and σ used here.

It was assumed that JCA works in all cases, i.e. that once a conjunction exceeds the m_{TH} and $P_{C,TH}$ thresholds it is prevented. This would likely not be the case if a JCA system is deployed; even if efforts are made to mitigate the probability of a collision, it might still occur, leading to an increase in the number of objects. What is more, collisions not previously forecast might occur because the trajectory of either object is altered. Modelling of the interaction of laser light [95] and gas particles [103] with derelicts needs to be addressed in order to enable screening JCA targets for collisions before their trajectories are altered. Improving the reliability of JCA as well as improving force modelling of the derelicts are issues that should be addressed by the entities developing JCA systems, however. This work has shown that if JCA is 100% reliable and does not cause any collisions itself, positive impact on the debris environment can be achieved.

While simulating JCA, the inertial velocities of the two objects were kept constant while their positions were changed so that the objects were within a collision radius from one another. This could have affected the conjunction geometries and changed the relative orientation of the uncertainty ellipsoids. This would have made the spectrum of P_C seen in the JCA simulation different to what would be seen operationally. In order to ascertain that the the spectrum of conjunction geometries in the JCA simulation was realistic, azimuth and elevation were computed for 15 000 conjunctions from section 4.3.2.2 and collisions found with DAMAGE in section 4.3.2.1 (the positions of the secondaries in DAMAGE were altered according to the algorithm described in section 4.2.1 before plotting). The two distributions are presented in Fig. 4.33. Both distributions were similar; in the respective cases 94.9% and 93.3% events have elevation between 170 and 190 degrees (relative velocity was in the transverse-cross-track plane), and 22.2% and 28.8% events had azimuth between 135 and 225 degrees (head-on conjunctions). Thus, the simulated spectrum of uncertainty ellipsoid alignments was comparable to what would be observed in reality.

Convergence of the Monte Carlo sample of the reference scenario was successfully verified in section 4.3.1. Convergence of the individual just in-time collision avoidance simulations was also verified in the same manner, which is to say by conducting a bootstrap study of statistical parameters of the final distribution of the number of objects. However, the MC runs were randomly selected from a sample of 15 000, unlike in section 4.3.1. The bootstrap was conducted for a number of JCA parameter permutations

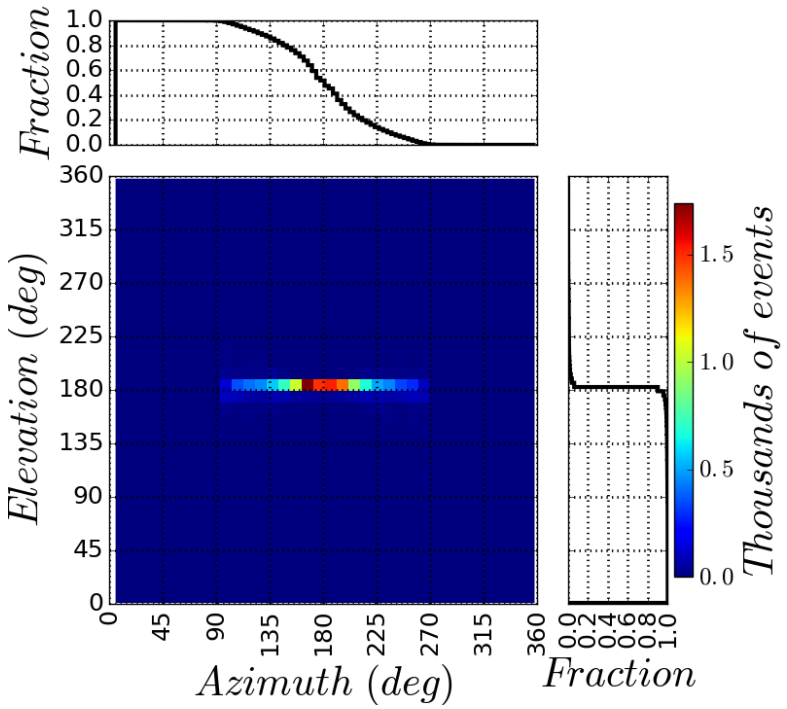

(a) DAMAGE

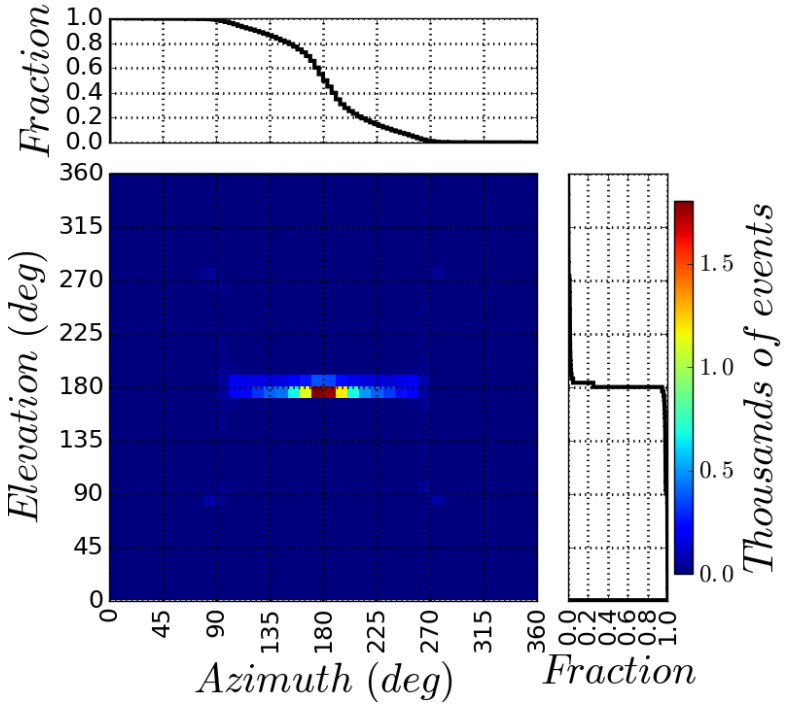

(b) Algorithm developed in Chapter 2

Figure 4.33: Comparison of the distributions of azimuth and elevation found with DAMAGE, and the conjunction detection framework developed in Chapter 2. 15 000 DAMAGE collisions, and 15 000 conjunctions closer than 1 km obtained using the TLE snapshots from Table 4.4. Azimuth and elevation are defined in Fig. 4.34.

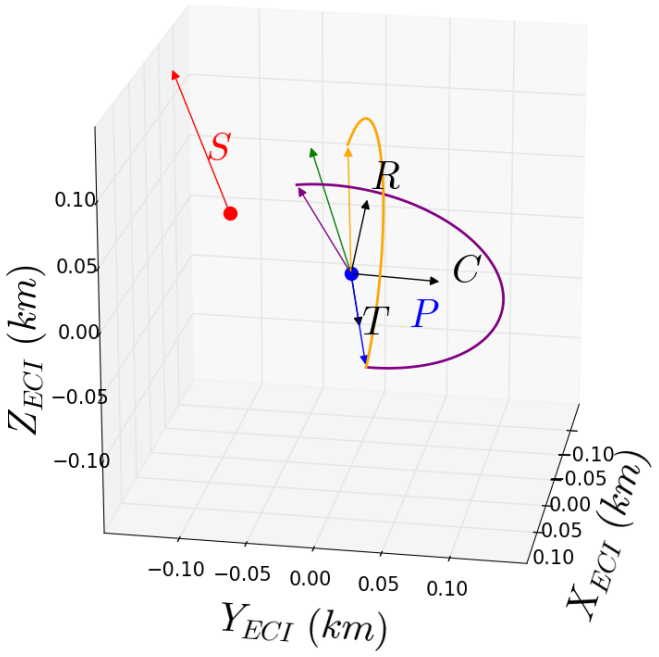

Figure 4.34: Definition of the azimuth (purple) and elevation (orange) angles. Azimuth is defined as the angle between the relative velocity at the TCA projected onto the transverse-cross-track plane (purple arrow) and the transverse unit vector. Elevation is defined as the angle between the relative velocity at the TCA projected onto the radial-transverse plane (orange arrow) and the transverse unit vector. The mentioned RTC unit vectors and planes correspond to the RTC system of the primary defined at the TCA (black). The positions and velocities of the primary and secondary are shown in blue and red, respectively. The relative velocity is shown in green. X_{ECI}, Y_{ECI} and Z_{ECI} are the axes of the inertial reference frame.

from Table 4.3. An example convergence plot is shown in Fig. 4.35, whereas the remainder of the investigated permutations are described in section C.1 of the Appendix. With 10 000 MC runs in the sample, the maximum difference between any of the 2000 random means and medians was less than 1% w.r.t. the value obtained with 15 000 MC runs. The corresponding precisions for variance, skewness and kurtosis were 2.89, 11.06 and 44.57%, respectively. Therefore, it is expected that the sample was large enough to estimate the first three moments of the distribution. Kurtosis was reported to vary by a similar fraction in section 4.3.1, because occasionally large outliers may be added into the sample and thus increase the kurtosis. Arbitrarily large outliers may be present in certain MC runs, therefore the kurtosis could require more than 25 000 MC runs to converge further. This was not carried out due to computational time constraints and because the analysis focused on other, already converged, moments of the distribution.

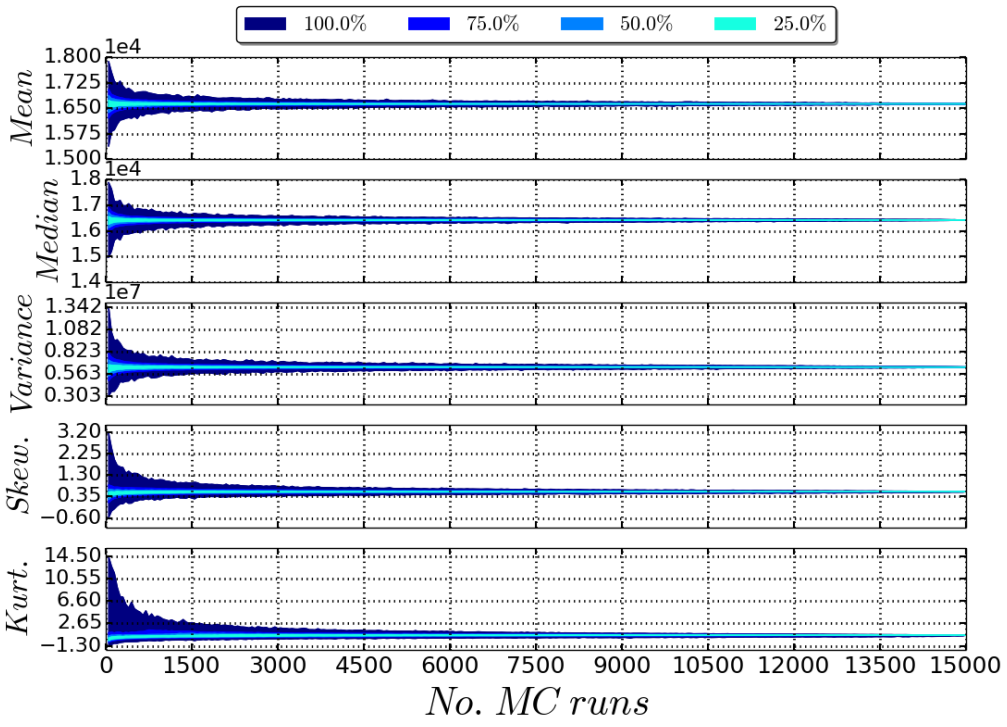

Figure 4.35: Bootstrap of the statistical parameters of the distribution of the number of objects ≥ 10 cm at the end of the projection (2213) in the MC sample of the JCA settings number 47 from Table 4.3. Details of the process given in section 4.3.1.

Only a limited number of JCA parameter permutations was investigated to reduce the computational time. For a large part of these sampling points, JCA did not have any effect on the environment because no remediation actions were carried out. However, the parameter values, where JCA began to have an effect, were approximately in the middle of the sampling domain. This means that the sampling ranges were suitably chosen because the response of the debris environment to implementing JCA was not known *a priori*. Also, the errors of the surrogate models were compared to the actual physics-based modelling results in section 4.3.2.3, and it was demonstrated that the same behaviour was observed. Even though the actual Pareto front of the JCA effects on the environment and the number of false alarms was not reached, the subspace of $\vec{x}$ where the most cost-effective solutions are located was identified correctly. Moreover, several JCA systems located close to the optimum were evaluated directly, and the performance found for those was not dependent on the surrogate models.

The effects of JCA at only the final projection epoch were analysed because this work was concerned with long-term evolution of the environment. Evaluating the effects of JCA on more population snapshots would require more computational time and, therefore, fewer JCA scenarios could be analysed in the timeframe of this project. This would likely result in the response of the debris environment to implementing JCA not being

as thoroughly investigated and understood. Individual MC runs and single collisions therein have a large impact on the analysed distribution parameters [124]; a large MC sample that was analysed here (relative to most IADC studies, for example [86]) reduced this impact. Moreover, most of the analyses performed in this work were based on the median rather than the mean, which is more robust to outliers in the sample [25]. Therefore, analysing the population at only one epoch did not affect the robustness of the results of this work, and was considered acceptable given the advantage of being able to analyse more JCA scenarios it provided.

Finally, a relatively low median number of objects in 2213 was reached with $P_{C,TH}$ of 3.16×10^{-5} for the added point number 2 from Table 4.5, which was close to the lowest investigated values of $P_{C,TH}$. This seems to contradict the finding from Chapter 3, where the high-P_C conjunctions were found to give rise to the majority of the collision probability in orbit. It also negates the effect of σ on increasing the P_C of the likely collisions. In order to verify this behaviour, another point was added into the sample with $\vec{x} = [0.1, 0.5, 0.01]$, i.e. with $m_{TH} = 459.4$ kg, $P_{C,TH} = 1.0 \times 10^{-3}$, and $\sigma_R = 7.23$, $\sigma_I = 17.3$, and $\sigma_C = 5.36$ metres. The predicted median number of objects for this point was 16 270 and the evaluated median was 14 208 (14.5% relative error), i.e. identical to the median evaluated for the added point number 2 from Table 4.5. The higher collision probability threshold reduced the number of false alarms from 2 to 1 (1 false alarm was predicted with the surrogate model). This shows that the accuracy of the surrogate model regressing the median number of objects would need to be improved if the most cost-effective JCA systems, located on the Pareto front, were to be found. However, the expense of the computational time needed to evaluate more points closer to the expected location of the front is unjustified because the Pareto front would be affected by the assumptions of the debris modelling and so would not be directly usable operationally.

The figures of merit of the JCA systems that have been identified here (no. false alarms and the effect on the debris environment) are based on a number of assumptions. Firstly, the number of false alarms was extrapolated from 43 days which assumes that the number of false alarms per unit time is constant, as well that the used space object is complete. Also, the cited response of the debris environment assumes that the "mitigation only" scenario represents the future evolution of the number of objects in orbit. Neither of these figures of merit can be forecast confidently and so any Pareto front that could be found is not going to represent reality exactly. It is impossible to predict how many conjunctions exceeding given $P_{C,TH}$ and m_{TH} will take place more than several weeks ahead. Similarly, it is impossible to confidently predict solar activity, launch traffic, the number of explosions, and post-mission disposal compliance rates. Consequently, the evolution of the space debris environment cannot be accurately forecast. Nonetheless,

this work has shown that cost-efficient JCA systems could be implemented and that reducing the number of false alarms conflicts with increasing the positive impact on the debris environment. The location of such systems in the parameter space has also been identified, even though the exact values of the figures of merit cannot be relied upon in an absolute sense due to the mentioned unpredictability of the future.

4.5 Conclusions of the derelict collision avoidance study

It was shown that JCA systems, which would reduce the median number of objects to 14 208 (mean of 14 407), could be deployed. Such systems would experience approximately 8 false alarms annually if ephemeris accuracy close to the best currently achievable by JSpOC can be reached and when including the object mass action threshold. Methodology, which enabled the number of false alarms to be traded off against the expected number of objects in orbit, was presented; this can readily be applied when defining the operational JCA action thresholds.

It was found that the ephemeris accuracy reduced the number of collision false alarms by several orders of magnitude. There were 17 932 conjunctions that exceeded $P_{C,TH} = 1.0 \times 10^{-9}$ in the investigated 43 days with $\sigma = 0.99$. With $\sigma = 0.01$, this number reduced to 125. Including the mass of the objects as an action threshold for JCA reduced the number of false alarms by two further orders of magnitude, i.e. to only 1 in 43 days. Such a low number of false alarms will reduce the cost of JCA and thus increase the probability that it will be implemented [130]. What is more, in the long-term, JCA could be used to reduce the collision risk to the operational assets [95], which could lower the fuel consumption of active spacecraft and increase their utilisation by reducing the number of collision avoidance manoeuvres they perform. This would give the operators a financial incentive to support JCA development, which is mostly absent in the case of ADR - no direct positive returns will be observed when ADR is successful because few or no orbital collisions will take place [130].

It is thus recommended to conduct development of JCA technologies in parallel to ADR. It was shown here that JCA offers a viable means of controlling the long-term evolution of the number of objects in orbit. Even though it may be more cost-effective to remove certain derelicts from orbit entirely via ADR rather than repeatedly preventing their collisions, it was shown in Chapter 3 that not all collisions can be prevented via ADR. JCA offers a means to prevent such collisions [102] as long as the involved objects can be tracked. Depending on how the two are performed, JCA may also be more suitable for certain types of objects than ADR (e.g. derelicts that are difficult to grapple) [99]. In

order to prevent as many collisions as possible, improvements in space surveillance and tracking systems will need to be made to improve ephemeris accuracy to be close to the current 5^{th} percentile level and catalogue as many objects in orbit as possible. However, such improvements are being carried out independently [43], and so JCA could exploit those.

Space-based lasers could be used to conduct JCA, and these could be involved in collisions [132]. However, other JCA concepts do not significantly increase the collision risk in orbit themselves because they are launched on ballistic trajectories [101] or use ground-based lasers [95]. This means that the debris from the breakup of the sub-orbital JCA payloads would re-enter the atmosphere. However, JCA could cause orbital collisions by altering the trajectories of the derelicts. In order to avoid such situations, modelling of the forces that JCA will impart on the objects should be improved to enable post-JCA conjunction screenings before the objects are intercepted.

Chapter 5

Discussion

This work was based on the hypothesis, that most of the collision probability in orbit originates from relatively rare, particular conjunctions with high, relative to other events, collision probabilities. Consequently, a thesis was formulated: mitigating the collision probability of such particular conjunctions will prevent collisions and thus stop the growth of the number of debris in orbit. Testing this hypothesis and corroborating the thesis was split into the following research objectives, first given in section 1.6:

1. Test whether particular conjunctions with high collision probability are experienced by all objects in orbit or only a subset.

2. Determine whether these particular conjunctions give rise to a large portion of probability of any collision taking place in orbit.

3. Test whether variations in external conditions, e.g. solar activity, which cannot be forecast far in advance change the objects that have the highest collision probability in a given period of time by introducing new conjunctions with relatively high collision probabilities.

4. Demonstrate that such conjunctions with extremely high collision probabilities also take place in evolutionary debris models and result in more collisions than other close approaches with lower collision probabilities.

5. Correctly capture the underlying distribution of the future number of objects in a DAMAGE projection to provide a reliable reference scenario, on which the effects of preventing only excessive growth of the number of debris (tail of the distribution) can be tested.

6. Corroborate the thesis that preventing collisions between objects on an *ad hoc* basis is a viable means of reducing the growth rate of the number of debris.

7. Determine the number of conjunctions that need to be prevented annually to achieve a given result on the debris environment, to enable financial viability of an *ad hoc* collision prevention framework to be assessed.

8. Identify characteristics of the objects, collisions of which should be prevented to stop the number of debris from increasing.

Objectives 1 2, and 3 were addressed in section 3.1. It was shown that 50% of the collision probability accumulated by the entire debris environment over the analysed periods of 30 days originated from fewer than 0.01% of all the recorded collisions (Fig. 3.6., objective 2). For 10% of the objects, a single, high-P_C conjunction gave rise to 56% and 58% of the collision probability accumulated by the given object in the analysed time windows (Fig. 3.5, objective 1). Objective 3 was addressed by varying B^* coefficient of all the objects and observing how the ones with the highest criticality vary in the investigated scenarios (Table 3.7).

In order to reduce the required computational time to make the corresponding studies feasible, certain assumptions and simplifications had to be made when generating these results. The effects of those assumptions and simplifications were discussed in detail in section 3.1.5. It was explained that the cited contributions of the particular, high-P_C conjunctions to the final values accumulated by individual objects and the debris environment could change if the highest-fidelity data and algorithms were used. However, the occurrence of conjunctions with P_C orders of magnitude higher than most others was not an artefact introduced in this study because such events are regularly monitored by spacecraft operators and sometimes even actively avoided via dedicated manoeuvres [35]. What is more, significant contribution of particular conjunctions to the collision probability accumulated by individual objects was also observed by McKnight et al. [98] and in DAMAGE results, which corroborates this finding. The presence and impact of such events mean that long-term collision probability assessments of objects may not reflect the collision probability that will be found for them during operational conjunction screenings. Objects that are found to have a high collision probability, i.e. are large in size and located in densely populated orbital regimes, were found amongst the ones with the highest collision probability in section 3.1. However, section 3.1 also showed that the rare, high-P_C conjunctions change depending on the epoch of the conjunction screening and the atmospheric density, which is affected by unpredictable variations in solar activity. Consequently, such events and the involved objects can only be predicted at a relatively short notice when their attitude, solar activity and atmospheric density can be forecast accurately. This means that objects selected for ADR based on long-term collision probability estimates may not be the only objects involved in high-P_C conjunctions and collisions. This importance of the particular conjunctions in the scope of ADR target selection and the variability of the "target lists" with varying atmospheric density are some of the key novel contributions of this work. These findings are important in the scope of space debris remediation because they demonstrate that ADR alone

is likely to be insufficient to halt the growth of the number of debris in orbit. Moreover, these findings confirm the thesis set here, and also by McKnight et al. [98], that a combined approach to space debris remediation, i.e. preventing likely collisions and removing objects from orbit to reduce the cost of collision prevention, has the highest chance of constraining the number of objects in orbit.

It is impossible to quantify how long in advance collisions can be forecast based on the results of this study, however. This is mainly due the fact that it used a semi-analytical propagator and estimated ephemeris uncertainties. State uncertainty increases when it is propagated, regardless of the propagator details [107, 147]. Thus, even the highest-fidelity state vectors and algorithms can only be used to forecast collisions with confidence with a finite advance warning. This has implications on how the unpredictable, high-P_C conjunctions can be addressed because rapid deployments are likely to be necessary, unlike in the case of ADR as suggested by e.g. McKnight et al. [99].

The finding about the impact of high-P_C conjunctions is only relevant to space debris remediation if the choice of the ADR targets is necessary, i.e. not every object can be removed. Otherwise choosing objects to be removed from orbit is not important because every satellite, rocket body or piece of debris could be de-orbited when it is no longer needed. However, a situation where all the derelicts are removed from orbit is unlikely due to the expected cost of ADR as well as political constraints associated with e.g. interfering with classified or military satellites [130, 134]. Similarly, it is unlikely that perfect ephemeris and propagation accuracies will ever be reached and thus it is unlikely that it will be possible to forecast collisions far in advance.

High-P_C close approaches were also identified in DAMAGE results in section 3.2.2, which fulfilled the research objective number 4 (Fig. 3.15). Evolutionary debris models vary and not all of them identify conjunctions to compute the P_C of the objects [86]. One such model, currently used by the IADC, is DELTA [14]. Thus, not all of the models will be affected by the occurrence of high-P_C close approaches. However, if objects are ranked according to their collision probabilities estimated using the models that use the CUBE or the derived Kernel algorithms, e.g. DAMAGE or LEGEND, this ranking will be affected by the close approaches that took place in the simulations. Thus, if the same models are used to rank the objects again, a different list could be obtained.

The occurrence of collisions in DAMAGE and other semi-stochastic IADC models [86] is simulated using random numbers. This gives rise to uncertainty in the forecasts of the future debris population, which was studied by e.g. Dolado-Perez et al. [26] and reported in section 1.3.2.2. To make sure that the conclusions of this work remain valid despite this uncertainty, research objective number 5 was formulated and addressed in section 4.3.1. It was found that Monte Carlo samples larger than used traditionally have to be employed to correctly capture the uncertainty of the semi-stochastic debris models and correctly represent the distributions of the number of object in orbit (Fig. 4.18b and Fig. 4.19). However, results of the past convergence studies, which determined the

minimum size of the sample needed to accurately represent the MC mean [90], were corroborated (Fig. 4.17). Despite the uncertainties associated with the evolutionary models, they can still reproduce the current state of the debris environment when projecting the initial conditions from 1989 to the present day [126]. This means that the results of the evolutionary debris models are not contrived and that JCA should have a beneficial effect on the environment if it is implemented.

The thesis that preventing high-P_C conjunctions can stop the growth of the number of debris was successfully tested in Chapter 4 to address the research objective number 6 (distributions in Fig. 4.27 moved towards fewer objects in orbit). It was shown that, if ephemeris accuracy of the space surveillance catalogue can be improved to be close to the current 5^{th} percentile level, cost-effective JCA systems could be deployed. Approximately 8 false alarms p.a. could be reached. Determining this number addressed research objective number 7 and is demonstrated in Fig. 4.30. The importance of ephemeris accuracy on the feasibility of JCA is not novel knowledge [99]. However, rigorous test of the potential effects of such a system on the evolution of the debris environment and quantification of the expected false alarm rate. The false alarm rates were estimated using the conjunctions found in orbit over 43 days. It is possible that more conjunctions will exceed a given $P_{C,TH}$ during different 43 days and thus the exact estimates of the number of false alarms cannot be relied upon strictly. These estimates can only be used to compare different JCA systems but research objective number 7 is still regarded as fulfilled because the order of magnitude of the number of false alarms should not change.

It was demonstrated that the cost-effectiveness of JCA is driven by ephemeris accuracy. Intuitively, it seems difficult to achieve ephemeris accuracy in the order of metres, which would make such a system feasible, especially based on the accuracy of two-line element sets presented in section 2.4. However, the analysis in section 4.2.2.2 showed that objects with larger masses have more accurate state vectors. The median RIC accuracy of the state vectors of objects from section 4.2.2.2 with mass larger than 459.4 kg and perigee altitude less than 2000 km was $\sigma_R = 6.7,\ \sigma_I = 16.3,\ \sigma_C = 6.4$ metres, i.e. is comparable to the 5^{th} percentile level ($\sigma_R = 1.6,\ \sigma_I = 5.4,\ \sigma_C = 1.7$ metres). This does not account for the growth of the state vector uncertainty with propagation time, and one standard deviation only represents part of the uncertainty region, where the objects might reside. What is more, half of the analysed objects had state vector accuracy worse than the quoted median values. However, if JCA is only performed hours to days before the time of the closest approach, as envisioned by McKnight et al. [99], it may be possible to refine the orbit knowledge of the potentially colliding objects to this level of accuracy. Thus, implementing such a system appears feasible with current technology. However, the cost of maintaining an accurate catalogue of space objects and performing daily conjunction screenings for all of them should be taken into account to assess the economical feasibility of JCA [130].

Apart from the impact of improving the ephemeris accuracy, incorporating mass as a JCA action criterion was demonstrated to reduce the false alarm rate. However, it was also shown that the m_{TH} threshold has to be low in order for JCA to have an effect on the long-term evolution of the debris environment, which will increase the number of false alarms. This was investigated further and the masses of the targets and projectiles from the DAMAGE collisions were plotted against the number of objects ≥ 10 cm at the end of the projection (2213) that their collisions gave rise to in Fig. 5.1. Collisions involving both large and low mass objects can give rise to many fragments in the final population, and collisions involving two large-mass objects are relatively rare. This signifies that, according to DAMAGE, the growth in the number of objects in orbit may not be caused by collisions of exclusively massive objects as suggested by McKnight et al. [98]; rather, it is many collisions involving smaller objects that cause the large derelicts to break up and the number of debris to increase. Even though collisions of two large-mass objects generated many fragments, the number of fragments produced in a collision did not correlate with the number of fragments that a given collision gave rise to in the final population, as shown in Fig. 5.2a. The effect of the collision altitude, shown in Fig. 5.2b, is clearer - many objects from the final population were generated at low altitudes. However, this is simply because the spatial density of objects at low altitudes is high and thus most of the collisions are expected to occur there [89]. Collisions that took place closer to the final epoch of the DAMAGE projection gave rise to more fragments in the final population than collisions that took place close to the beginning of the projection, as shown in Fig. 5.3c. This was expected because the effects of individual collisions can be discerned in the Monte Carlo samples for approximately 50 years after the fragmentation epoch [124]. However, the effects of such collisions on the conclusions drawn in this work were minimised by employing robust statistical methods to analyse the results as well as by using a relatively large Monte Carlo sample (two orders of magnitude larger than the projections in the IADC comparison study [86]). The earlier in the simulation a collision took place, the more follow-on collisions its fragments were involved in as shown in Fig. 5.3b. However, even if fragments from a collision were involved in many follow-on collisions, this collision did not necessarily give rise to many fragments in the final population as shown in Fig. 5.3a. This shows that the "Kessler syndrome" did not initiate in any MC run.

It was suggested by Pardini and Anselmo [116] that the documented debris-intact collisions did not generate as many fragments as predicted by the breakup model, which is implemented in DAMAGE and other evolutionary debris models. Hence, they suggested that the number of fragments generated in collisions simulated in evolutionary debris models could be overestimated because, even if a collision has enough energy to

be catastrophic [51], the disparity in the sizes of the involved objects, object structural properties and collision geometry could lead to few fragments actually being produced in the event [100, 109, 159]. However, Fig. 5.1 and Fig. 5.2a show that even if the number of fragments generated in a collision is relatively low, this collision could give rise to many fragments at some census epoch through introducing follow-on collisions.

The population of the debris in orbit is claimed to be unstable from a mathematical point of view [9]. Even if the debris environment is stable, collisions will cause the number of debris in orbit to increase and spacecraft operations to be hindered. Collisions are also required to provide the feedback mechanism needed to sustain the "Kessler syndrome", regardless of whether it has begun or not. It is impossible to say how many collisions are needed to trigger an exponential, self-perpetuating growth of the number of debris in orbit. Nor is it possible to predict what objects will take part in those collisions - collisions involving small objects might give rise to many fragments in the future debris population, as shown in Fig. 5.1, and unpredictable high-P_C conjunctions might result in collisions as demonstrated in Chapter 3.

If not all derelicts are removed from orbit, collisions could still occur and the "Kessler syndrome" could take place. Therefore, preventing collisions appears to be the best approach to limiting the future number of debris. This could be done via a combination of ADR, JCA, mitigation, or other means. The fact that even JCA distributions in Fig. 4.27 have tails, where the number of objects is still large in spite of JCA, signifies that efforts have to be made to prevent all collisions in order to ensure that the debris population does not grow. Setting the JCA thresholds, e.g. m_{TH}, as low as possible and performing ADR increases the probability that the number of debris in orbit will not grow.

A gap in the number of objects in the final population snapshot plotted against the number of fragments generated in collisions can be observed around 6500 generated fragments in Fig. 5.2a. The origins of this discontinuity were investigated and a histogram of the number of fragments generated in collisions was plotted in Fig. 5.5. Relatively few collisions generated 6000 to 7000 fragments larger than 10 cm, which corresponds to the gap observed in Fig. 5.2a. The number of fragments generated in a collision depends on the mass of the objects that collided [51]. Therefore, this discontinuity was caused by the fact that few combinations of objects' masses could generate this range of the number of fragments. This is a manifestation of the fact that the distribution of the masses of the objects in orbit is not continuous, as was shown in Fig. 4.6.

It can also be noted in Fig. 5.1 that collisions between relatively low-mass objects occurred more frequently than massive-on-massive collisions. This is purely due to the fact that there are fewer large-mass objects in orbit and so collisions involving such objects are rare, because random numbers are used to seed collisions. Related to this is the fact that, for example, collisions involving two large-mass objects, which generate

many fragments, rarely lead to many follow-on collisions and thus do not contribute many objects to the final population as shown in Fig. 5.2a. Specifically, only 1290 collisions in Fig. 5.4 generated 7000 fragments or more, whereas 80 688 collisions generated 2000 or more fragments. The use of random numbers, collision detection algorithms, breakup modelling shortcomings, and the assumptions of the reference scenario listed in section 4.3.1 mean that the results of the JCA analysis can only be interpreted in a relative to sense. Specifically, it was shown that JCA can have a beneficial effect on the debris environment, which will not change regardless of the modelling assumptions and simplifications because collisions are needed to lead to a large increase in the number of objects in orbit. Similarly, it was shown that the JCA action thresholds have to be set low to prevent many collisions, because collisions involving even low-mass objects could eventually contribute to a large increase in the debris population. However, the exact threshold values and the number of objects in orbit for every JCA scenario would undoubtedly change if the assumptions of the reference scenario, e.g. the launch traffic, were different or even the same scenario was re-run but with a new random seed. This means that the research objective number 8 was not addressed in full because definite JCA action thresholds were not established.

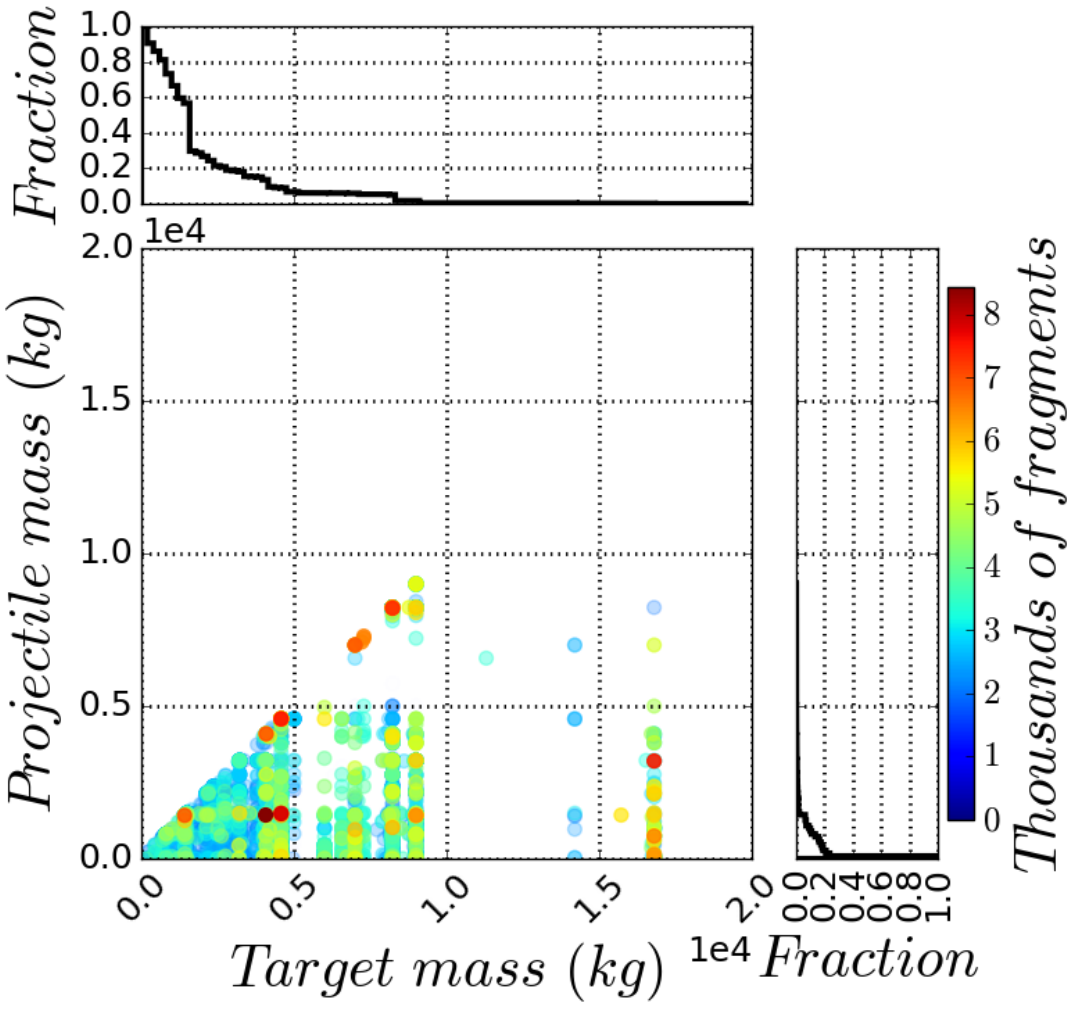

Figure 5.1: Relationship between projectile and target masses from DAMAGE collisions, and the numbers of objects in the final population snapshot that these collisions gave rise to. 15 000 MC runs of the "mitigation only" scenario from section 4.3.1. Investigating the number of fragments ≥ 10 cm at the beginning of 2213. Also showing the histograms of the projectile and target masses that correspond to the main scatter plot.

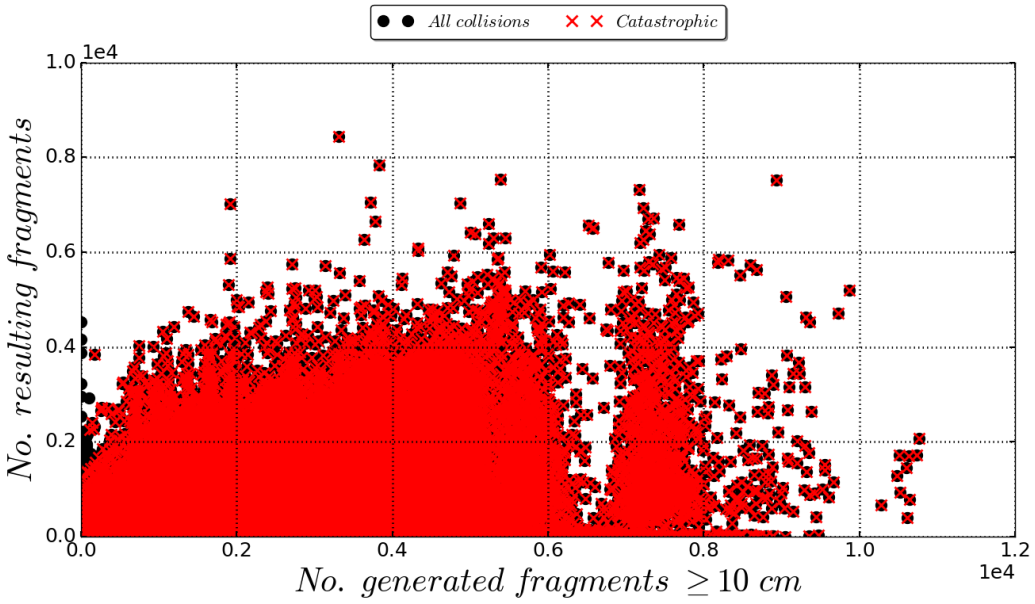

(a) No. fragments $\geq$ 10 cm generated in the collision

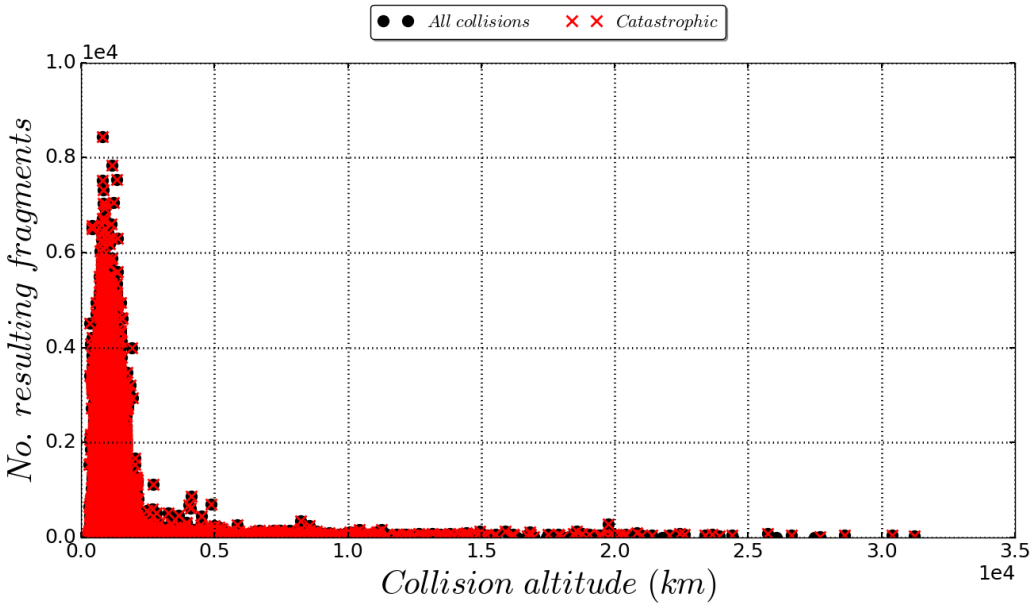

(b) Collision altitude

Figure 5.2: Relationship between the number of fragments larger than 10 cm in the final population snapshot and properties of the collisions they originated from. 15 000 Monte Carlo runs of "mitigation only" scenario from section 4.3.1.

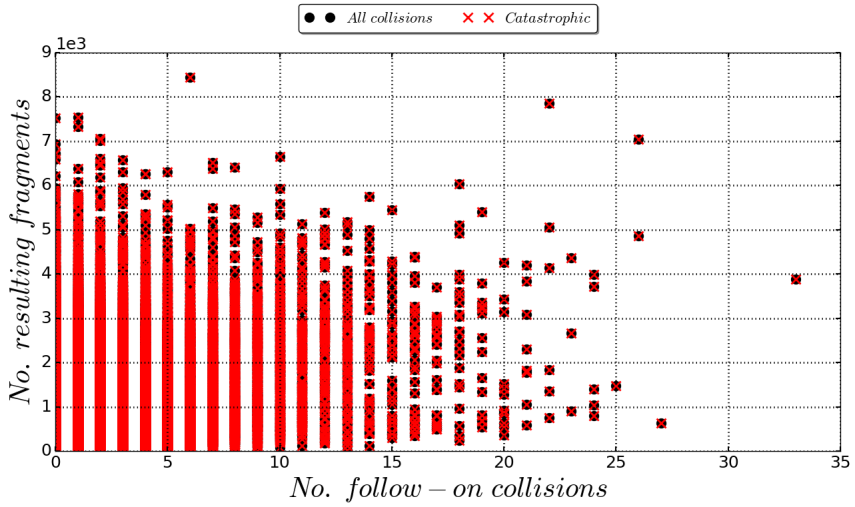

(a) No. follow-on collisions

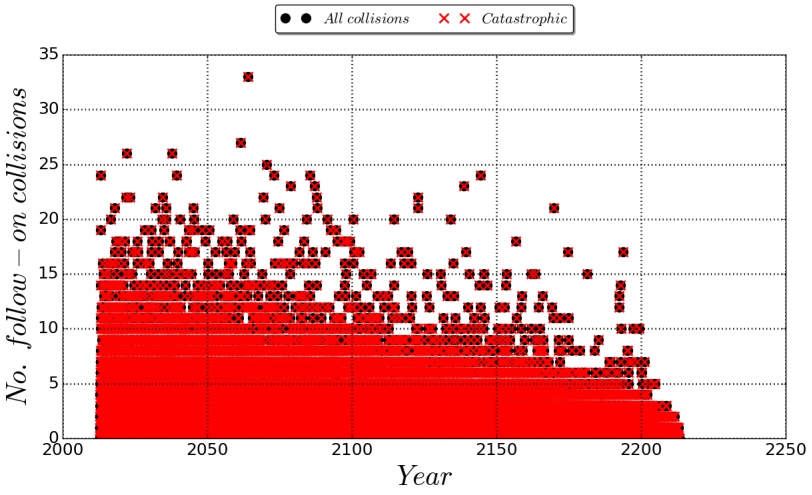

(b) No. follow-on collisions as a function of collision epoch

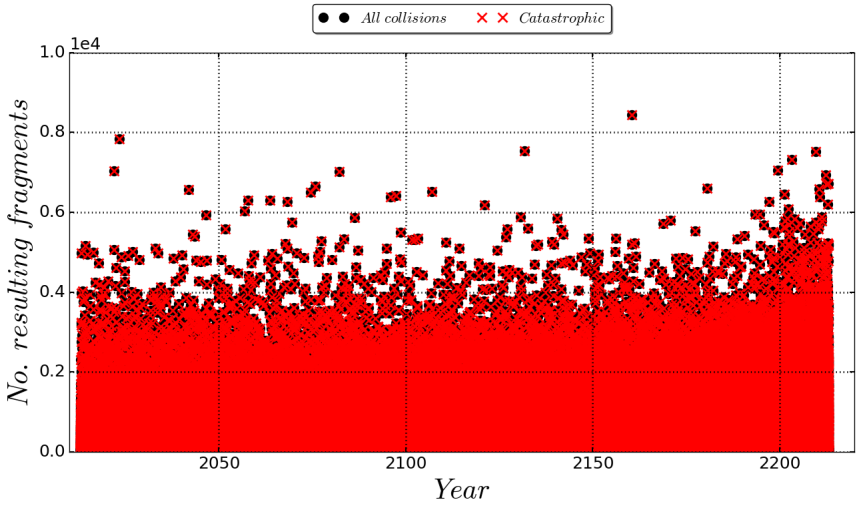

(c) Collision epoch

Figure 5.3: Relationship between the number of fragments in the final population snapshot, epochs of the collisions they originated from, and the number of follow-on collisions that these collision gave rise to. 15 000 Monte Carlo runs of "mitigation only" scenario from section 4.3.1.

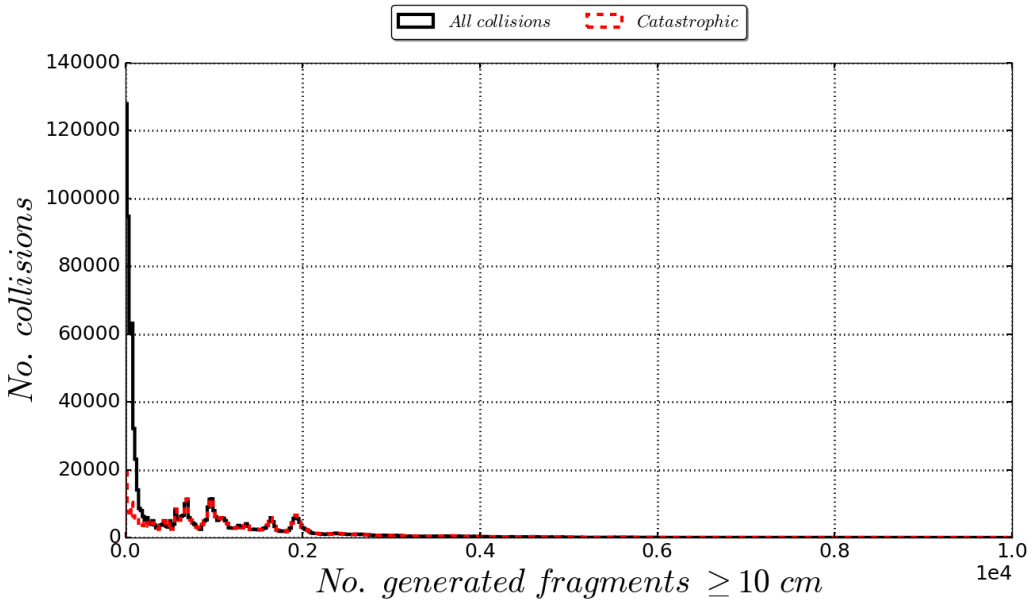

Figure 5.4: Histogram of the number of fragments ≥ 10 cm generated in collisions. Data from 15 000 Monte Carlo runs of "mitigation only" scenario from section 4.3.1.

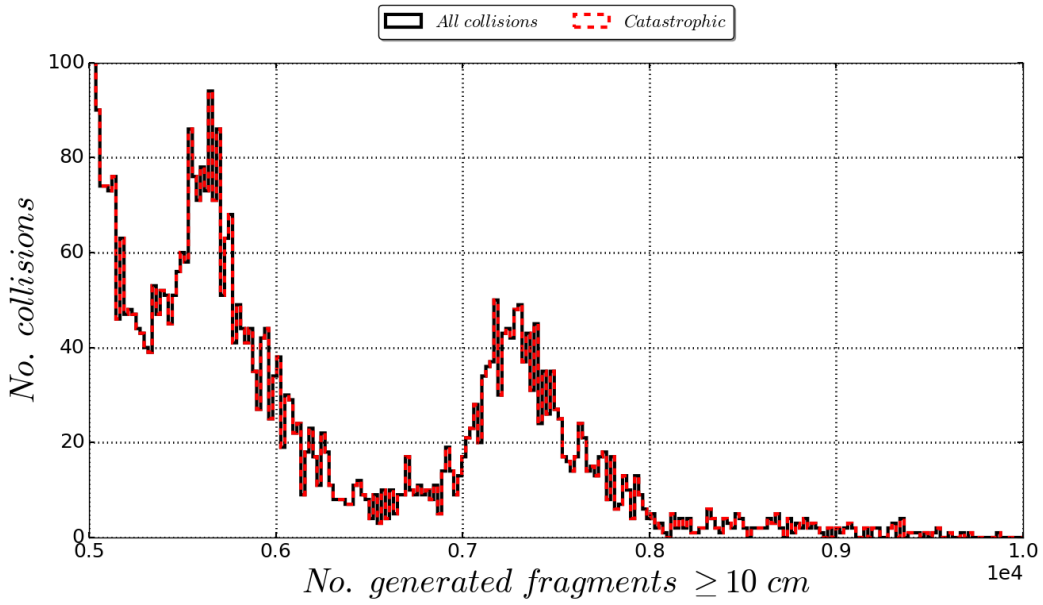

Figure 5.5: Histogram of the number of fragments ≥ 10 cm generated in collisions. Focusing on a subset of data from Fig. 5.4.

Chapter 6

Summary and Conclusions

6.1 Summary

This work was aimed at testing whether it is possible to accurately estimate the long-term collision probability of objects and thus select a subset to be removed via ADR to reduce the collision probability in orbit. It was hypothesised that rare, high-P_C conjunctions, which cannot be forecast far in advance, would make such long-term collision probability estimates incapable of accurately identifying the subset of objects that have the highest collision probability in a given period of time. Thus, it was also intended to test whether *ad hoc* collision prevention can stop the growth of the number of objects in the presence of such conjunctions, which can only be forecast at a short notice. This research goal was formalised into eight specific objectives set out in section 1.6 (not repeated here for brevity)

To address the objectives 1, 2 and 3, a high-resolution debris simulation tool was developed. This tool uses conjunction detection and collision probability estimation algorithms more accurate than the evolutionary debris models and operates at higher spatial and temporal resolutions. It was used to find the collision probabilities, and criticalities based on those, of all the objects in four different scenarios using two snapshots of the public two-line element set catalogue. It was noticed that particular conjunctions, with collision probabilities several orders of magnitude higher than most of the events, contribute as much as 14.5% to the final collision probability accumulated by 81% of the objects over a time window of one month. Moreover, 50% of the probability of any collision taking place in orbit in those time periods was caused by only 234, 268, 405 and 466 conjunctions. These constituted 0.007%, 0.008%, 0.014% and 0.015% of the total numbers of conjunctions recorded in those time windows.

While addressing the objective number 3, these particular, high-P_C conjunctions were also shown to define what objects had the highest collision probability in the analysed time window. Variations in solar activity, cannot be forecast accurately far in advance, were shown to affect the collision probability of individual objects through introducing new, high-P_C conjunctions. This was shown to change collision probabilities of certain objects by up to two orders of magnitude. These changes in P_C were shown to position objects, which would normally be regarded as unlikely to be involved in a collision, close to the top of a list of highest-risk objects in the given time interval. Objects that are found likely to be involved in collisions, i.e. are located in densely-populated orbital regimes, and have large cross sectional area and mass, were also found amongst the ones with the highest criticalities in the analysed time windows. Such objects would likely be chosen for removal via ADR.

The existence of such particular, high-P_C conjunctions was confirmed through analysis of the results of an evolutionary debris model, namely DAMAGE. Even though the high collision probabilities were obtained using different algorithms and represent slightly different quantities, this confirms that the presence of such events and their impact is not an artefact generated by the method adopted here. Moreover, it was suggested that these high-P_C conjunctions may be the cause of more future collisions than the conjunctions with lower collision probabilities. This fulfilled the research objective number 4.

The objective number 5 was addressed in section 1.3.2.2, where the distributions of the MC projections obtained with DAMAGE were analysed. However, the MC samples were found to be too small to reliably capture the future distributions of the number of objects. Thus, a larger MC sample (25 000 instead of 140 MC runs) was analysed in section 4.3.1 and larger uncertainty in the future number of objects was observed than has been reported in the IADC comparison study [86]. These two analyses fully addressed the objective number 5.

The objectives number 6, 7 and 8 were addressed in Chapter 4. A framework, which simulates preventing orbital collisions on an *ad hoc* basis, when they can be forecast reliably, was developed. Then, 50 scenarios of such derelict collision prevention (also referred to as JCA) were simulated and their effects on the debris environment were investigated. The high-resolution conjunction detection and assessment algorithms described in Chapter 2 were used to assess the number of false alarms that JCA might experience. It was shown that reducing the number of JCA false alarms conflicted with attempts to reduce the mean number of objects in orbit in 2213, and thus these two quantities need to be traded off. It was shown how such a trade-off could be conducted and cost-effective JCA solutions were found. However, in the presence of debris modelling uncertainties and high computational cost of analysing JCA systems, full optimisation of JCA was not performed. It was also shown that collisions, which generate few fragments, relative to other events, themselves can initiate a sequence of collisions that gives rise to many objects in the final population.

These findings provide a new understanding of what events might lead to orbital collisions and hence the growth of the number of debris in orbit. It was only possible to gain this new knowledge by applying established collision detection and assessment methods, albeit with certain modifications that improve their accuracy and computational speed, in a new area of space debris research. It is hoped that these findings will enable development of systems that will reduce mankind's impact on the space environment and, ultimately, make spaceflight sustainable.

6.2 Conclusions

It was shown that certain evolutionary debris models identify approximately as many conjunctions in 200 years in 100 Monte Carlo runs as take place in orbit in approximately three months. Every such "conjunction" in these models accounts for many close approaches a given pair of objects might have over a period of time. This is because the temporal resolution of these models is in the order of days, which enables multiple long-term Monte Carlo analyses to be performed. Even though the collision probabilities accumulated by different objects found in this fashion appear consistent with the ones obtained using approaches with high spatial and temporal resolutions [73], many actual conjunctions are missed and their details are different to what would be obtained operationally. The debris models that do not identify close approaches and use other collision probability estimates, e.g. like those described by Bastida-Virgili [14], cannot reflect the impact of individual conjunctions on the collision probabilities accumulated by the objects by definition.

Details of individual conjunctions were shown to be important, however. For 10% of the objects, a particular conjunction with high P_C contributed 58% or more to the P_C accumulated in a given short time window. At most 0.015% of conjunctions closer than 20 km were responsible for 50% of the probability of any collision taking place in orbit over the analysed periods of one month.

Regardless of the model in use, conjunctions cannot be forecast reliably more than several days or at most weeks ahead. This is, for example, due to the fact that the daily solar activity can lead to unpredictable changes in the atmospheric density. It was shown that such variations can lead to conjunctions with high collision probabilities and thus to a different set of objects being the most likely to be involved in a collision than what could be predicted far in advance.

Moreover, those high-P_C events can involve objects that are not large or located in densely populated orbital regimes and thus are not often quoted as "risky" in the context of increasing the number of space debris. This is because these objects do not accumulate high collision probabilities on a daily basis or in simulations.

High-P_C close approaches found using evolutionary debris models might impact ADR target selection based on the results of such models. If an object takes part in one or several high-P_C close approaches in DAMAGE, it could be brought close to the top of the potential ADR target list if P_C is included in the ADR target selection metric. However, these events might not represent what will happen in reality and therefore the collision probability accumulated by the hypothetical object could be several orders of magnitude higher than what could be found when performing daily conjunction screenings. This could cause the object to be unnecessarily removed by ADR because it is not going to take part in a collision. This effect is not necessarily going to affect ADR target selection if many Monte Carlo runs are combined to agree on the list of the targets to remove in reality. However, the top several objects that have the highest collision probability in individual MC runs have collision probability orders of magnitude higher than the rest [153]. Therefore, high-P_C events affect the objects that are removed in those MC runs, which causes ADR to be unsuccessful in those runs.

The above findings mean that, unless all the derelicts are removed from orbit, collisions might happen despite the efforts to prevent them through active removal of objects that are likely to accumulate a high P_C.

The possibilities for the future of the debris environment are to remove all the objects, remove only some objects and accept that collisions are going to happen, do not remove any objects and accept that more collisions will take place, or to prevent the collisions in an *ad hoc* fashion, when they can be forecast reliably. It was shown here that preventing collisions between derelicts reduced the mean, median and variance of the number of objects larger than 10 cm in 2213. Several false alarms (extrapolating from a sample of 43 days to one year gave 8 false alarms) were expected annually when conducting such derelict collision avoidance. The simulated state vector accuracies, which resulted in so few false alarms, are in the range of what is currently achievable, although only at short lead times that do not allow the state vector uncertainty to grow significantly during propagation. A methodology, which enables the number of false alarms to be traded off against the expected number of objects in orbit was also developed; this could readily be used to define collision prevention thresholds when deploying such a system.

It was found that improving ephemeris accuracy from several hundreds of metres to several metres reduced the number of false alarms of just in-time collision avoidance by two orders of magnitude. Incorporating the mass of the objects as another criterion, which has to be met for a collision to be prevented, reduced the number of false alarms by two further orders of magnitude (from 17 932 to 571).

However, this study found that many objects that take part in high-P_C conjunctions are the ones with large cross sectional areas and are located in densely populated orbital regimes, i.e. will be found to have high P_C in long-term collision probability assessments. Examples of such object include SL-16 and SL-8 rocket bodies or Envisat (see Letizia et al. [71] and references therein for further details). Permanently removing those from

orbit might be more cost-effective than preventing the conjunctions they take part in. Therefore, a mixed approach where ADR is used to remove the objects that will take part in many high-P_C conjunctions, and JCA to ensure that the collisions, which cannot be forecast far in advance, are avoided, is recommended to constrain the number of objects in Earth orbit. Otherwise the high-P_C conjunctions and the resulting collisions may thwart any debris remediation efforts.

Therefore, it is recommended to conduct development of JCA technologies in parallel to ADR. If the number of ADR missions is to be reduced to the absolute minimum, thus lowering its cost, but as many collisions as possible are to be prevented, JCA has to be used in the first instance. This is because it is impossible to predict which objects, from the ones likely to be involved in a collision, are going to collide first and thus should be removed with the highest priority. If an object repeatedly takes part in high-P_C conjunctions, it should then be removed by means of ADR, thus lowering the running cost of JCA.

We cannot gain support for removing all of the derelicts, thereby removing the potential to generate many new fragments. Consequently, we need to look for alternative or complementary means to preserving the space debris environment. It was shown here that JCA can be used to the same end as ADR, and that the number of false alarms, and also cost, of JCA can be tailored to the expected number of objects in orbit that we *are ready to accept*.

6.3 Recommendations for the future lines of study

This work showed that deployment of a JCA system is likely to improve the sustainability of space activities. Consequently, techniques to conduct post-JCA conjunction screenings before altering the trajectories of the objects should be developed because new, high-P_C conjunctions could be introduced when mitigating the collision probability of other events, which could cause collisions. To this end, modelling of the interaction of laser light [95] and gas particles [103] with derelicts needs to be improved. Similarly, our capabilities to propagate uncertainty and compute collision probabilities that reflect uncertainty in the objects' positions at the TCA need to be improved [50, 106, 147]. This only re-emphasises the importance of conducting such research, which was originally highlighted by other authors.

The findings of this work have revealed new lines of inquiry, which should be followed to improve our understanding of the space debris environment. First of all, it was shown that the currently used space debris models lack spatial and temporal resolutions to identify individual conjunctions. The details of single conjunctions were shown to dominate many others as far as the collision probability of the objects is concerned, however.

The algorithms used here are incapable of projecting an entire debris population hundreds of years into the future due to computational time constraints, which the current space debris models are capable of. Merging the two approaches, e.g. by improving the computational speed of the methods described in Chapter 2 and incorporating a breakup model into the developed framework, would produce an evolutionary debris model capable of investigating the importance of single conjunctions on timescales of decades to hundreds of years. The algorithms that estimate the P_C described in Chapter 2 appear to offer the most room for improvement in the computational speed because this work made sacrifices in speed to gain higher precision. It is likely that the P_C estimation accuracy will be compromised if the algorithms are made faster, but it could be acceptable when projections are made for hundreds of years.

A number of assumptions were made when generating the DAMAGE projection on which the effects of JCA were analysed, as listed in section 4.3.1. This work showed that JCA is a viable means to debris remediation and thus could be analysed in more details on other projections. Understanding the sensitivity of JCA to e.g. the launch traffic or post-mission compliance rate could help deploy such a system.

Comprehensive, all-on-all conjunction screenings of all the derelicts in orbit could readily be conducted. Performing such screenings over a period of months to several years should generate a large enough sample to identify derelicts that often have high-P_C conjunctions and thus are good candidates for ADR. Such long-term conjunction screening data could be used to interpret the space debris environment in the context of a network, as suggested by Lewis et al. [75]. This could reveal objects that are going to have recurring close approaches with many others, and thus accumulate P_C quicker than most other objects. Such objects, which act as 'hubs' of the network, would make good targets for ADR not only because of the fact that they are likely to be involved in collision due to their high P_C, but also because they would facilitate follow-on collisions should any other objects in orbit break up. Finding such 'hub' objects should be performed based on conjunctions identified using higher-fidelity algorithms than in the work by Lewis et al. [75] to correctly reflect the impact of particular conjunctions, however. Also, once a network of objects in orbit is modelled, its sensitivity to atmospheric density and object attitude should be studied, because such variations were shown to change the high-P_C conjunctions in this work, and thus they might also redefine the 'hubs' of the network. This work could be carried out by conducting the analyses done in Chapter B over a longer period of time.

Appendix A

Conjunction Detection and Assessment

A.1 Investigation of the trajectory interpolation accuracy

The four interpolation schemes developed in section 2.1.1 were tested to establish their accuracies depending on the spacing of the interpolation nodes and the interpolating polynomial's order. The effect of including velocity data in formulation of the polynomials was also investigated.

The interpolation accuracy is normally computed by comparing the interpolated positions of objects to their reference positions obtained by propagating them directly on a fine time grid [3, 111]. Each of the objects from Table 2.1 was propagated from the TLE's epoch for the duration of one orbital period using the SGP4 [56] propagator at one second intervals to generate reference ephemerides. Various node spacings were then used with every interpolation scheme of interest and the ephemerides were interpolated at the reference epochs. This was repeated for a number of interpolating polynomial orders in cases of Lagrange and power series interpolation schemes.

A constant time spacing between the interpolation nodes was used because no *a priori* knowledge of the optimum interpolation nodes' locations was available and because computing these locations would be required for every object (adaptive quadrature [123]). This would increase the computational time thus offsetting the benefit of being able to propagate the objects at a larger time interval. This was considered important as a preliminary study revealed that evaluating object's state using the SGP4 propagator required a comparable amount of time to performing such complex algebraic operations. Lastly, using a constant propagation time step for all the objects considerably simplified the development of the conjunction detection algorithms without impacting the accuracy in any way.

It was decided to perform the testing of the sensitivity to polynomial order and node spacing using the representations of the interpolating polynomials that do not utilise gradient information, i.e. Lagrange and power series, due to the simplicity of the underlying mathematics and little computational time required. The effect of including velocity data in the interpolation accuracy could only be performed using Hermite and modified power series approaches. Only piecewise cubic polynomials were used in this case because this was the most desired polynomial type, because it made the algorithm, which finds the time of the closest approach, the most computationally efficient.

The differences between the reference and interpolated ephemerides and their 2-norms were computed and are presented in Fig. A.1b and Fig. A.1a for the LEO and the GTO cases, respectively. The accuracy of piecewise-cubic interpolation obtained using the Hermite and modified power series approaches is also shown as a reference for every investigated polynomial order, even though the order of these schemes was constant. The accuracy of the Hermite and modified power series schemes can be examined in more detail in Figures A.2a and A.2b.

As expected, the Lagrange and power series, and Hermite and modified power series find the same interpolating polynomials [123]. Interpolation accuracy decreases as the node spacing increases. This is particularly severe for the GTO case, where the interpolating polynomials stop representing the orbit well for node spacing of more than 600 seconds. The interpolation accuracy is retained for longer if the polynomial order is higher (up to 900 seconds for 8^{th}-order polynomials in A.1b). However, at low interpolation node spacings the low-order polynomials perform just as well as higher-order ones.

This hints that low-order polynomials may suffice when used with interpolation nodes spaced by up to approximately 400 seconds. However, the interpolation time step may be dictated by the algorithms used to prefilter objects during the conjunction screening process, which is be described in section 2.2 [1].

Furthermore, the power series approaches perform just as well as Lagrange or Hermite schemes, whilst offering the ability to use the coefficients of the polynomials interpolating the position for other means. This has considerable advantage of reducing the computational time needed for the analysis as the velocity can be interpolated using the coefficients of the polynomials interpolating the position.

Lastly, including the velocity information, through the modified power series or Hermite approaches, improves the interpolation accuracy while ensuring that the object's velocity is continuous between the neighbouring intervals. This can be observed in Figures A.3a and A.3b that compare the interpolation accuracies of cubic splines of four kinds. The methods that use the gradient data (Hermite and modified power series) are more accurate than those that use the values only (Lagrange and power series).

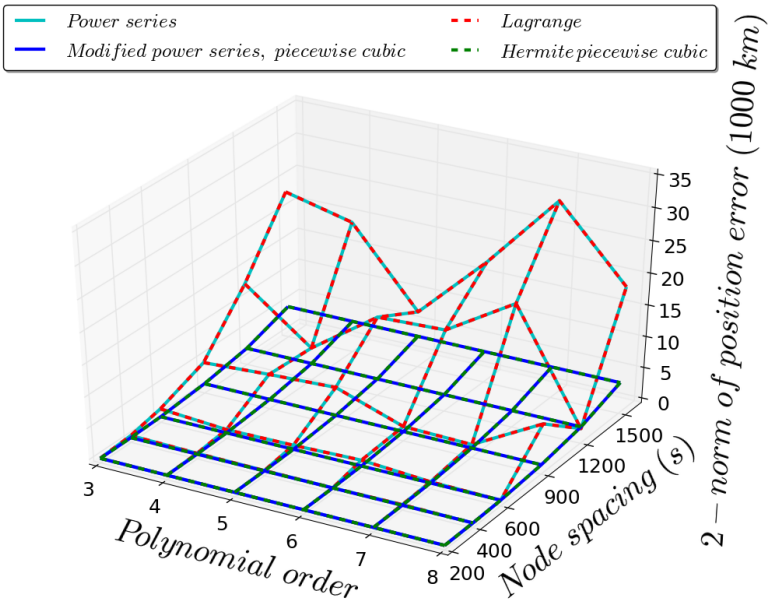

(a) GTO test case

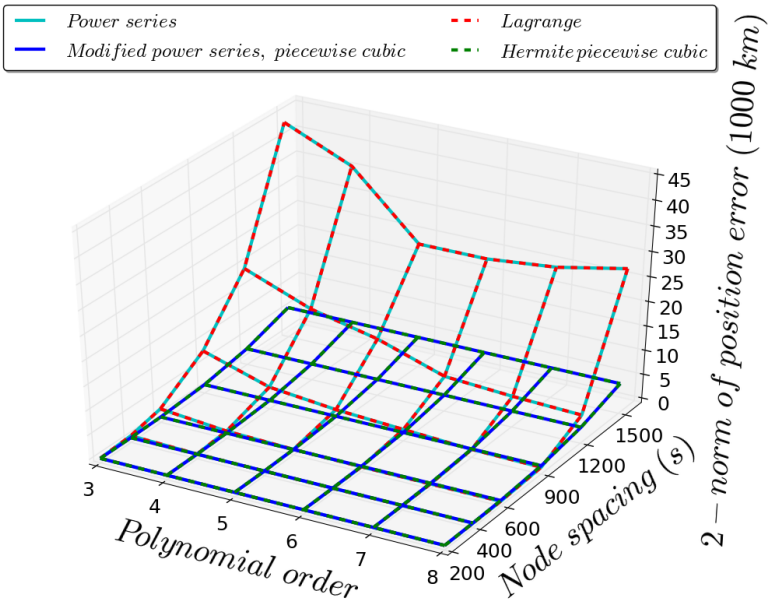

(b) LEO test case

Figure A.1: The effects of the interpolation node spacing and interpolating polynomial order (Lagrange and power series only) on the interpolation accuracy. Two-norm of error computed with respect to the nominal orbit of both objects progagated using SGP4 at 1 second intervals.

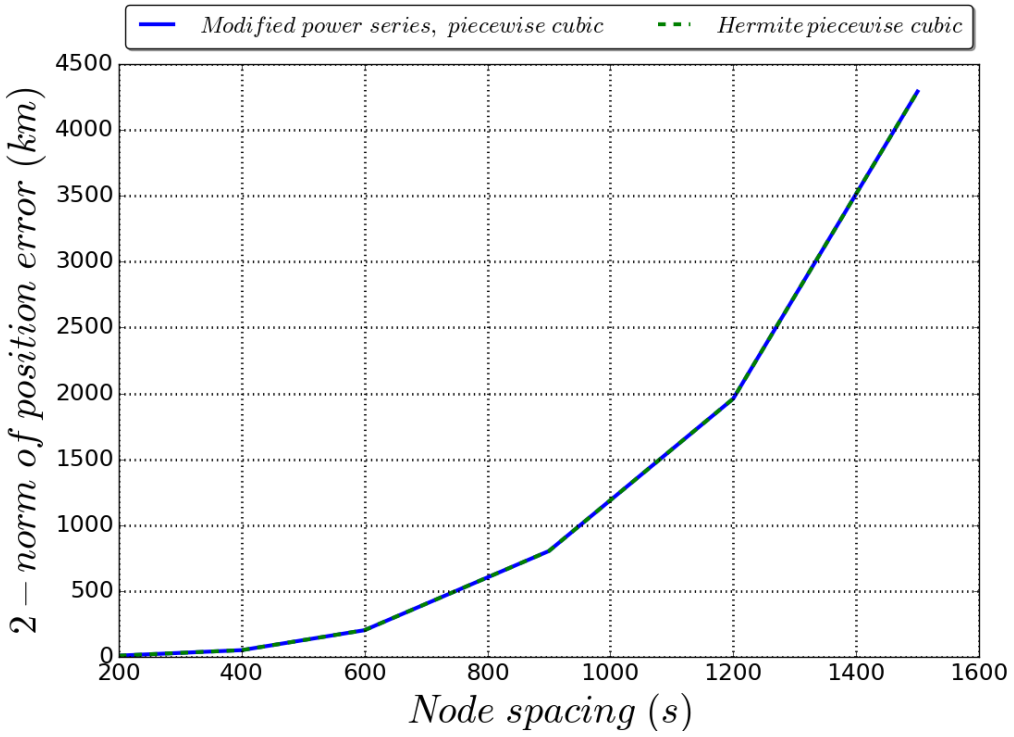

(a) GTO test case

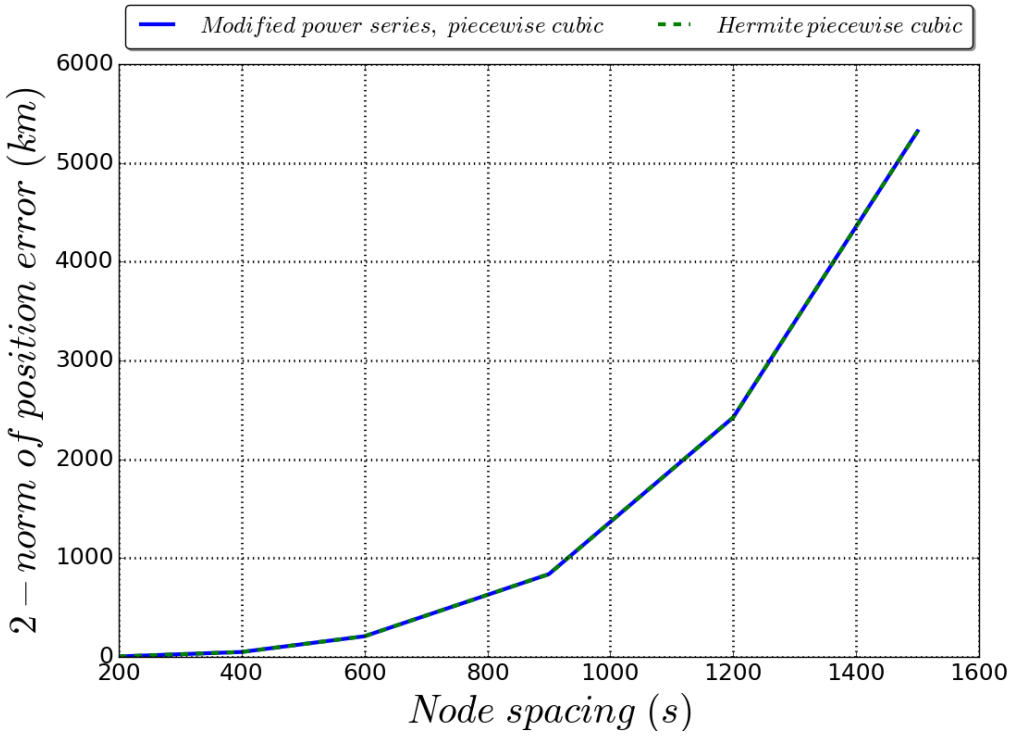

(b) LEO test case

Figure A.2: The effects of the interpolation node spacing on the interpolation accuracy for piecewise cubic spline interpolation. Two-norm of error computed with respect to the nominal orbit of both objects propagated using SGP4 at 1 second intervals.

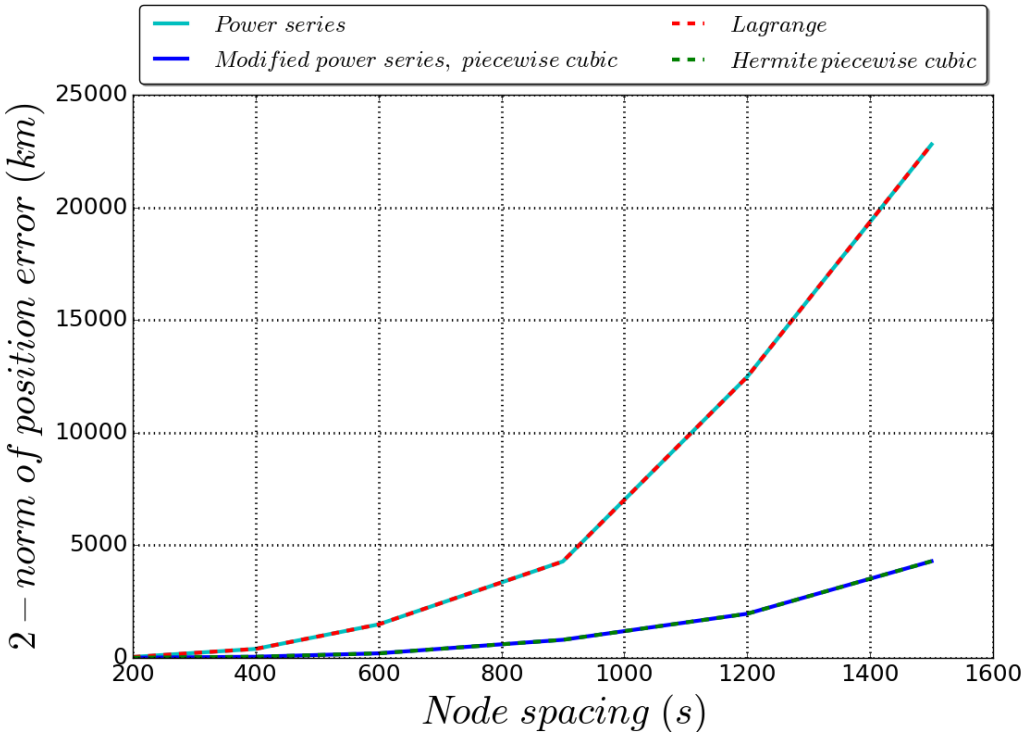

(a) GTO test case

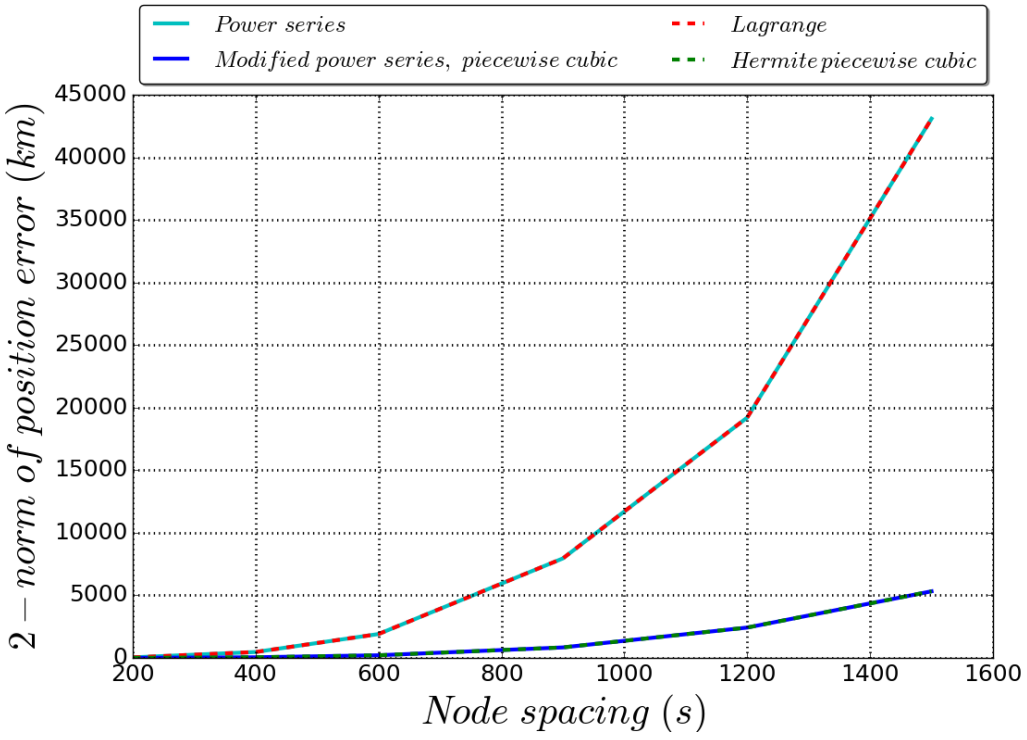

(b) LEO test case

Figure A.3: Comparison of the piecewise cubic spline interpolation accuracy for four investigated schemes, showing the impact of using gradient data to formulate the interpolating polynomials. Two-norm of error computed with respect to the nominal orbit of both objects propagated using SGP4 at 1 second intervals.

This is why a power series approach that uses the velocity information was decided upon. The maximum error of this scheme (∞- norm) for position interpolation is presented in Fig. A.4a and Fig. A.4b for the GTO and LEO cases, respectively. The corresponding precision of the velocity interpolation, performed using the interpolating polynomial coefficients, is presented in Fig. A.5a and Fig. A.5b.

A.2 Conjunction detection algorithm development

A.2.1 "Smart sieve" steps

Limiting the problem of identifying conjunctions between Earth-satellites allows simplifications to be made, firstly by observing that no objects can move with respect to each other faster than twice the surface escape velocity at any time [1]. If the analysis interval, in which the conjunctions are sought, ΔT, is known, a distance R_{th} referred to as the threshold radius in [1], may be defined as

$$R_{th} = R_{conjunction} + v_{escape}\Delta T. \tag{A.1}$$

If the distance between the two objects at the beginning of the analysis interval is greater than R_{th}, the two objects cannot get within the conjunction distance threshold, $R_{conjunction}$, during this analysis interval [1]. Furthermore, if a given object pair is separated by more than R_{th} at the beginning of the given time interval, a number of subsequent intervals may be skipped as

$$N_{skip} = int\left(\frac{r - R_{th}}{2}\right), \tag{A.2}$$

where r is the actual separation distance between the objects at the beginning of the analysis time step, and $int()$ denotes the integer part of a number.

Equation A.1 does not account for the effects of gravity, i.e. it assumes linear relative motion. The maximum acceleration between a pair of objects can never exceed twice the surface value, g_0 [1]. Hence, a maximum distance, R_{acc}, can be established that ensures that the secondary object, if it does get within $R_{conjunction}$ from the primary in the current time step, will be picked up in the same fashion as with the R_{th} but accounting for the acceleration effects:

$$R_{acc} = R_{conjunction} + g_0\Delta T^2. \tag{A.3}$$

The classical "smart sieve " [1] consisted of the following steps:

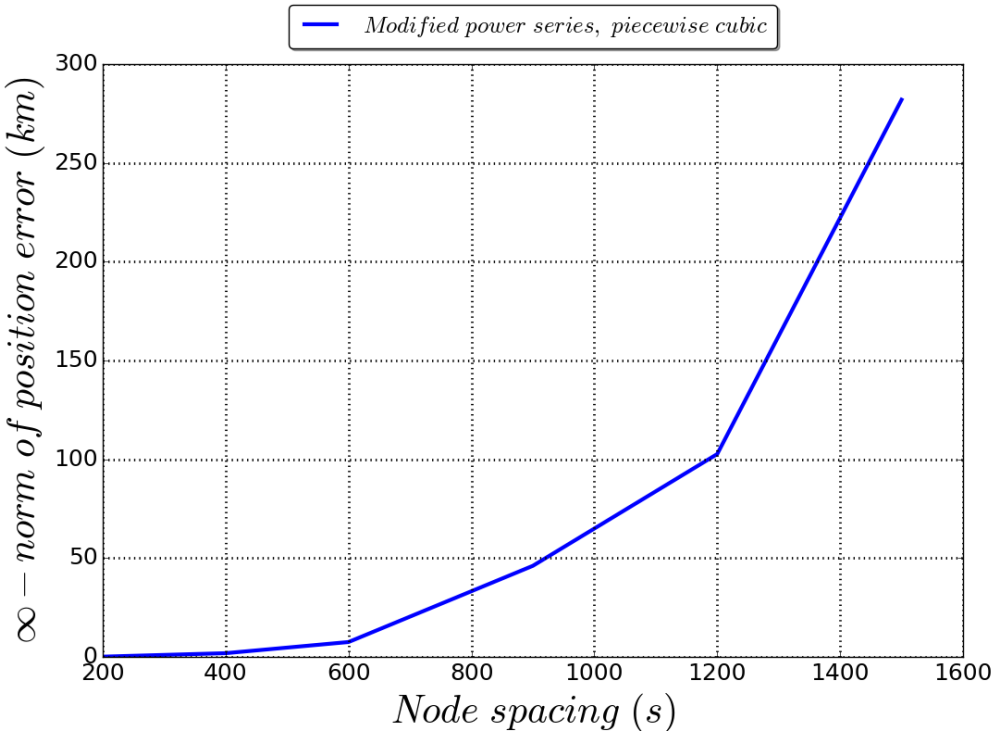

(a) GTO test case

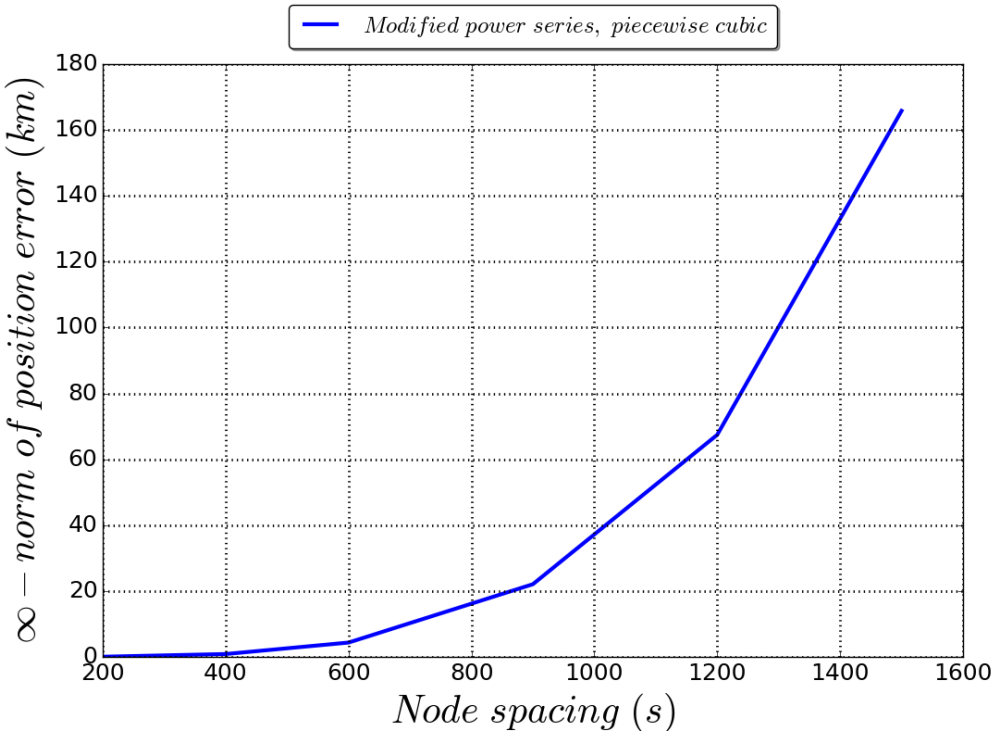

(b) LEO test case

Figure A.4: The effects of the interpolation node spacing on the position interpolation accuracy for piecewise cubic spline interpolation. Infinity-norm of error (maximum error over one orbit) computed with respect to the nominal orbit of both objects propagated using SGP4 at 1 second intervals.

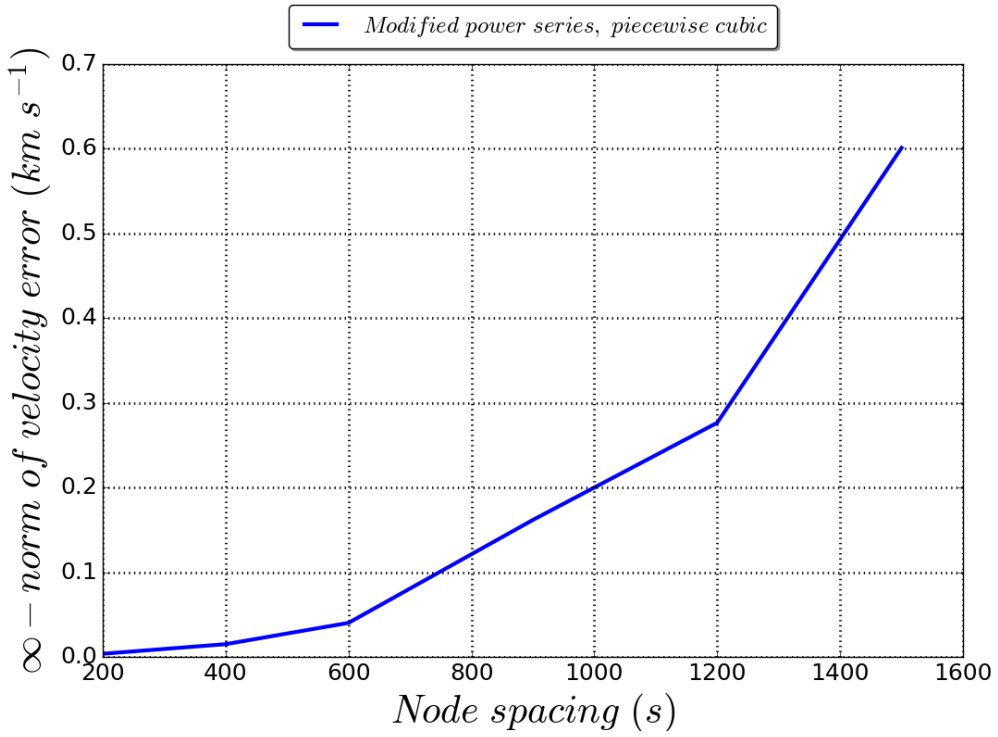

(a) GTO test case

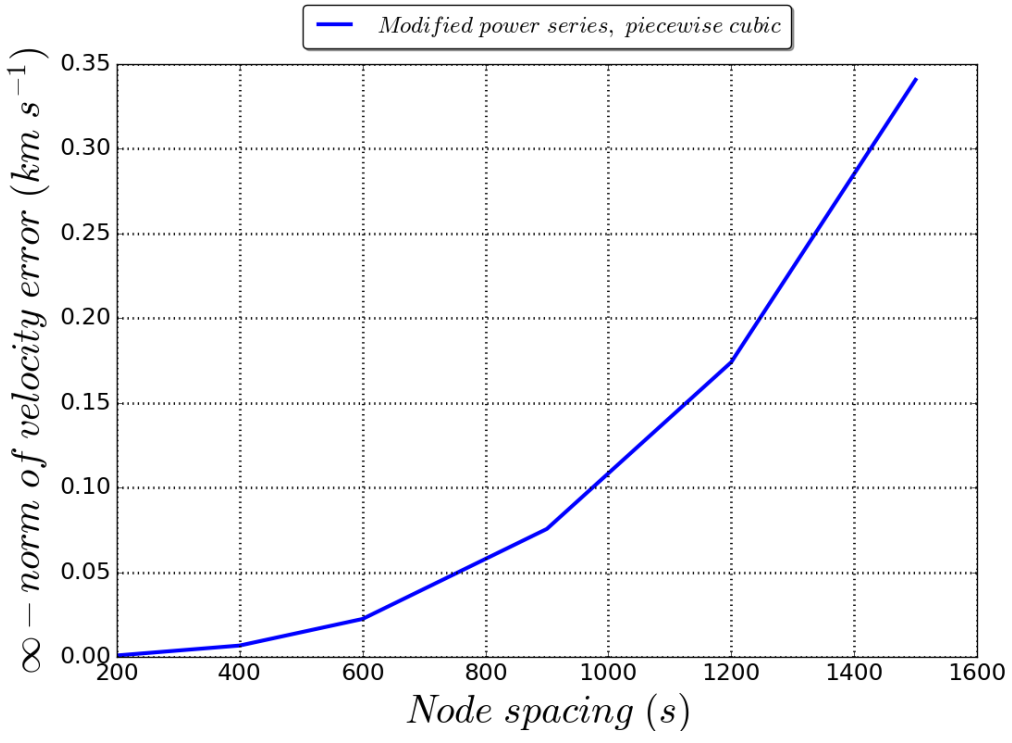

(b) LEO test case

Figure A.5: The effects of the interpolation node spacing on the velocity interpolation accuracy for piecewise cubic spline interpolation. Infinity-norm of error (maximum error over one orbit) computed with respect to the nominal orbit of both objects propagated using SGP4 at 1 second intervals.

1. Apogee/perigee filter - it is the most robust of the classical pre-filters developed by [9] and hence has been implemented in the "smart sieve" scheme as well.

2. X, Y, Z sieve - this part of the "smart sieve" used the threshold distance R_{th}, given in Eq. A.1, to filter object by their position coordinates according to Eq. 2.9. If this filter has not been passed a number of subsequent steps would be skipped as per Eq. A.2.

3. r^2 sieve - the object pairs with the square of the separation distance at the beginning of the analysis interval greater than the R_{th}^2 would not be analysed further in a given time step. Square of the distance was used rather than the standard 2-norm of the vector in order to avoid repetitively calling the square root operator, which reduced the computational time.

4. Minimum distance (MD) sieve - this pre-filter rejected the secondary from further analysis in the current time step if the square of the minimum separation distance between the two objects in a given analysis interval was greater than R_{acc}^2. The minimum distance, r_{min}, was computed using the actual relative velocity, $\overrightarrow{v_{rel}}$, and separation, $\vec{r}$, between the objects at the beginning of the analysis interval as per Eq. A.4.

$$r_{min}^2 = |\overrightarrow{r}|^2 - \left(\vec{r} \times \frac{\overrightarrow{v_{rel}}}{|\overrightarrow{v_{rel}}|}\right)^2. \tag{A.4}$$

5. Fine r^2 sieve - this pre-filter was similar to the r^2 sieve but used the actual relative velocity between the objects, $\overrightarrow{v_{rel}}$, rather than the surface escape velocity, as well as the acceleration radius, R_{acc}, instead of R_{th}. It rejected object pair if the square of their distance from the primary at the beginning of the time step, r^2, was greater than $R_{th,fine}$ given in Eq. A.5.

$$R_{th,fine}^2 = \left(R_{acc} + \frac{1}{2}\left|\vec{r} \times \frac{\overrightarrow{v_{rel}}}{|\overrightarrow{v_{rel}}|}\right| \Delta T\right)^2. \tag{A.5}$$

A.2.2 Conjunction detection algorithm testing and modifications

The chosen set of pre-filters, i.e. the classical "smart sieve" described in sections 2.2.1 and A.2.1, was implemented together with an algorithm that identifies the times of closest approaches between objects detailed in section 2.2.2. All the "smart sieve" steps were tested individually, i.e. the effect of including every step on the number of false negatives (missed conjunctions) was investigated. Even though rigorous testing of all the parts of the sieve was undertaken, only the key decisions that had to be made and the related sieve levels will be described in more detail for brevity.

Envisat's TLE given in Table 2.1 was screened for conjunctions against a snapshot of the public TLE catalogue from the 23 Oct 2013. This snapshot contained 14 917 objects [135], thus the computational time needed to perform the conjunction screening was significant (order of hours using the prototype implementation of the pre-filters and TCA-finding algorithm). Therefore, it was decided to perform the screening for one day only because even such a short period produced many (52) conjunctions, thus giving a sample big enough to observe any trends introduced when enabling sieve stages.

The interpolation time step was the same as the conjunction detection time step in order to simplify the software architecture as well as to reduce the number of floating point operations and thus reducing the computational time. Time step of 600 seconds was chosen because during the development tests it was noticed that impacts of the filters of particular interest may not be visible when using very short analysis intervals.

The histogram of miss distances of all the conjunctions closer than 20 km, prefiltered with various parts of the "smart sieve", is shown in Fig. A.6. No reference results are presented because the more conjunctions are found the better the precision of the algorithm, i.e. the fewer conjunctions are missed.

When the original r^2 sieve is used, six out of 52 conjunctions are missed, including one closer than 1 km. This can only be avoided when the threshold radius given in Eq. A.1 is enlarged by adding a constant factor that acts as a contingency, effectively increasing the threshold radius. Several different contingency factors ranging between 1.0 and 4.0 were investigated, but the details will not be discussed here for brevity. The objective of this investigation was to keep this factor as low as possible in order to cause as few additional objects to pass this sieve stage, which would increase the computational time, while removing the false negatives. The smallest possible contingency factor that did not cause any false negatives was found to be 2.0, i.e. the original threshold radius from Eq. A.1 was multiplied by $\sqrt{2}$.

Original work by Alarcon Rodriguez et al. [1] did not mention any pads in the perigee/apogee sieve, but it has been found that not implementing any contingency here could lead to several percent of conjunctions to be missed [2]. A modification was therefore made to the original perigee/apogee filter implemented in the "smart sieve" and a pad of 50 km was added. Such a pad setting should produce almost no false negatives with conjunction threshold distances as large as 50 km. This comes at a price of somewhat increased computational time but, as long as the net computational time remained feasible, this was not considered an issue.

Lastly, the object pairs would be initially screened using the perigee/apogee filter based on their radii at the beginning of the analysis with a pad of 1000 km added to the conjunction threshold distance. This removed object pairs that did not stand a chance of naturally crossing each other's altitude bands, e.g. removed GEO and MEO objects from a conjunction screening for a primary object in LEO. This pad value is only a half

of what is defined as the LEO regime by the IADC [139]. However, in order for an object to enter a Hohmann transfer trajectory from a 1100 km, circular orbit to an altitude of 100 km, a ΔV of 267 ms^{-1} would be needed. It is not expected that such large orbital energy changes could naturally occur for spacecraft, especially in the relatively short analysis windows anticipated in this study (order of several weeks). Big orbital energy and thus also altitude changes could only take place if manoeuvres are performed, but these were ignored in this study as no data about manoeuvres performed by various spacecraft is made publically available.

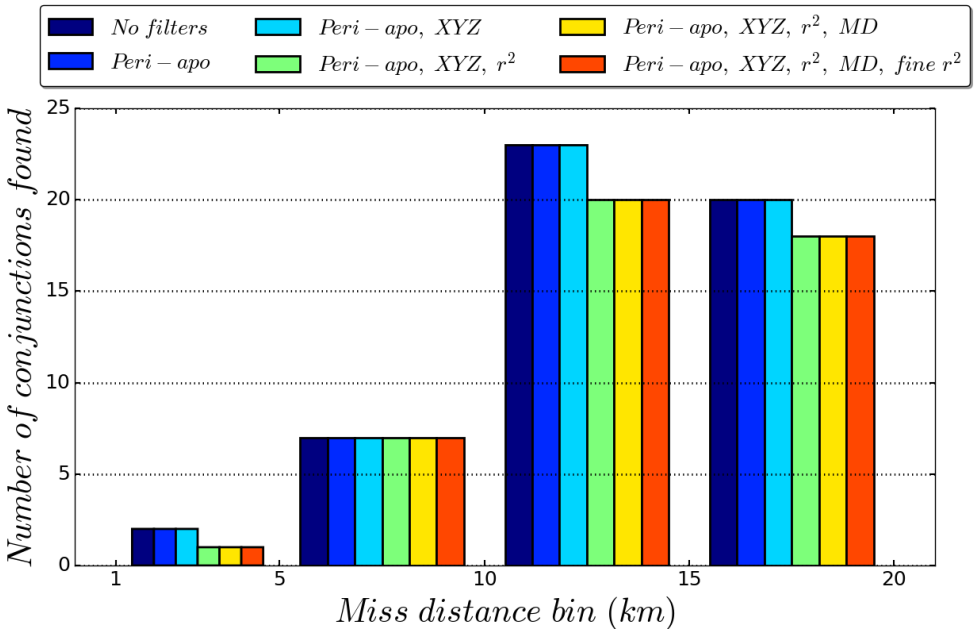

Figure A.6: Histogram of conjunctions closer than 20 km found for Envisat against the public TLE catalogue from 23 Oct 2013 over one day. Different series show how the number of conjunctions found in every miss distance bin varies when implementing further "smart sieve" steps described in section 2.2.1.

A.2.3 Conjunction detection algorithm time step choice

It was mentioned in section A.1 that varying the time step used to generate the state vectors, which are then interpolated, affects the resulting interpolation accuracy and thus also the miss distance of the identified conjunctions and the corresponding collision probabilities. From the accuracy point of view, the smallest possible time step should be used.

Several steps of the algorithm selected to pre-filter object pairs during the conjunction screening depend on the analysis time step, ΔT, e.g. the threshold radius through Eq. A.1. This means that the computational speed of the "smart sieve" as well as its accuracy depend on ΔT and the time step has an optimum value [1]. Specifically, the larger the analysis time step, the fewer times the pre-filters need to be computed and hence the faster the analysis. However, as the time step increases beyond the optimum value, more objects pass all the pre-filters and more root finding has to be executed, and hence the analysis becomes slower. If ΔT is too big, many false negatives take place and therefore algorithm accuracy is compromised.

It is, in principle, possible to keep the interpolation and conjunction screening time steps separate. This would, however, increase the number of floating point operations that would have to be performed to screen an object pair for conjunctions, thus increasing the computational time. Therefore, it was decided to use only one time step for both pre-filtering the object pairs and interpolating individual objects' trajectories.

A study was conducted to find the optimum time step that produces the fewest false negatives but also offers the best computational time savings. In order to do this, Envisat's TLE given in Table 2.1 was screened for conjunctions closer than 20 km for a period of one year using public TLE catalogue snapshot from 23 Oct 2013 while varying ΔT. The number of conjunctions found and the required computational time for every ΔT, together with reference data generated using STK CAT, are shown in Fig. A.7. The histogram of the miss distances found with every time step is shown in Fig. A.8 to verify that no systematic error, e.g. missing very close conjunctions, is present.

As ΔT is increased from 60 seconds, the computational time required decreases but, beyond approx. 600 s, it begins to increase. Further increase beyond 1200 s reduces the computational time somewhat but is accompanied by a considerable decrease in the number of false negatives. This speed-up beyond 1200 seconds was most likely caused by conducting collision probability estimations fewer times.

In section A.1, the interpolation accuracy was found to decrease significantly if the time step was increased beyond 400 seconds. For interpolation nodes spaced by 400 s, the infinity-norm of interpolating a low-Earth orbit was 0.87 km, and 1.88 km for a geostationary transfer orbit. When examining Fig. A.7, it appears likely that the optimum time step, which results in the highest computational speed of the entire conjunction detection framework, is between 400 s and 500 s. Notably, the developed conjunction detection algorithm performed better than STK CAT for time steps up to 900 s.

Therefore, a time step of 400 s was decided upon because it offered good computational speed of the conjunction detection framework and acceptable trajectory interpolation accuracy. With this time step, 19 541 conjunctions were found while STK CAT identified 19 485, meaning that the developed algorithm produced fewer false negatives. Moreover, it can be noted in Fig. A.8 that no trend is exhibited between the miss distance and the number of conjunctions found, meaning that there is no systematic error that results in missing e.g. all the very close conjunctions but finding more distant ones.

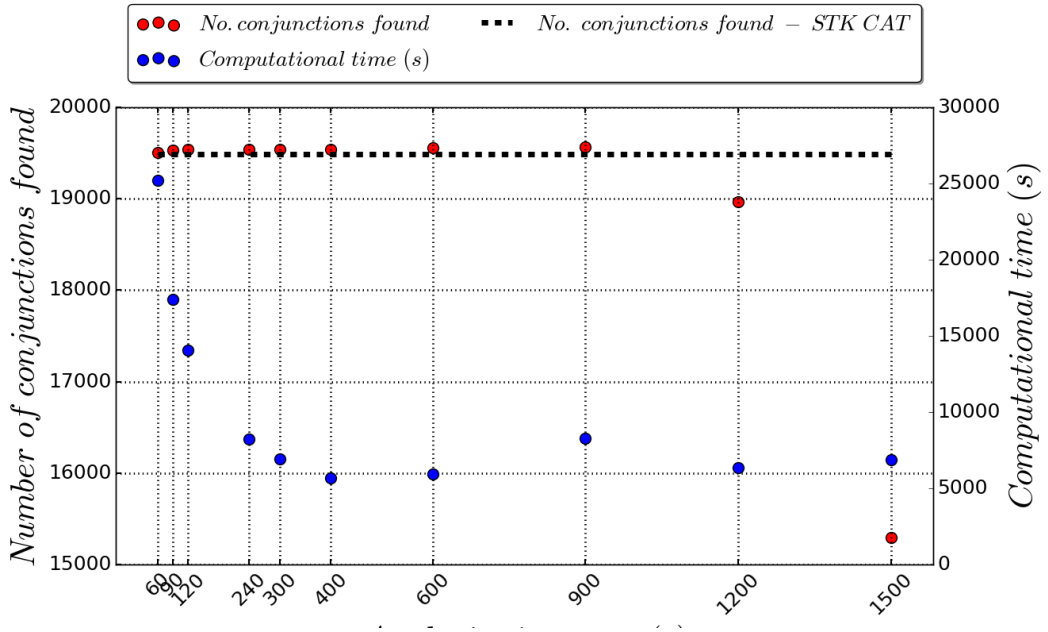

Figure A.7: Algorithm performance for various analysis time steps together with reference results obtained using STK CAT. Conjunctions closer than 20 km found for Envisat screened against the public TLE catalogue obtained on the 23 Oct 2013.

A.3 Verification of the collision probability estimation

The adopted collision probability estimation method was verified against Monte Carlo method. This was done in the regime where the assumptions made by the adopted P_C estimation method are true. The verification and algorithm tuning was performed on a set of exemplar conjunction geometries that will be presented first. Then the details of the collision estimation approach will be examined and numerical parameters, specifically the number of terms in the series expansion of the collision probability integral given in Eq. 2.21 as well as the number of points needed to numerically integrate it, will be chosen. Lastly, scaling the covariance matrix to the worst case will be verified.

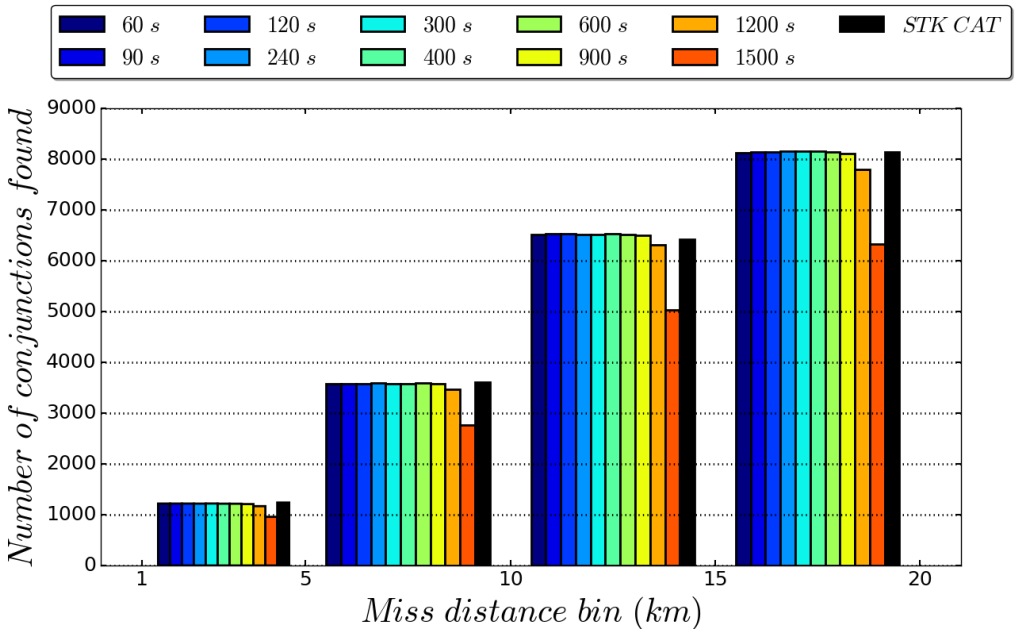

Figure A.8: Number of conjunctions found in various miss distance bins for various analysis time steps together with reference results obtained using STK CAT. Conjunctions closer than 20 km found for Envisat screened against the public TLE catalogue obtained on the 23 Oct 2013.

A.3.1 Test cases

Several test conjunctions that investigate extreme potential conjunction geometries are shown in Fig. A.9. These have been chosen to investigate the extrema of the spectrum of the shapes of the uncertainty projected on the B-plane. This is to guarantee that any other conjunction would result in an intermediate geometry bound by the test cases. The projections of the combined uncertainty ellipsoids onto the B-plane for every test case are shown in Fig. A.10.

In all cases, separation along only one axis of the inertial coordinate system was used with the relative velocity aligned with the separation. Every time the uncertainty of position of both objects was assumed to be $\begin{bmatrix} 0.089 & 0.0 & 0.0 \\ 0.0 & 4.014 & 0.0 \\ 0.0 & 0.0 & 0.028 \end{bmatrix}$ km^2 in the radial, in-track, cross-track reference frame. This was established by estimating the covariance of the Envisat's TLE from Table 2.1 using the method described in section 2.4.

The exact separation distance was varied in every test, whereas relative velocity was kept at $2.0\,km\ s^{-1}$ in all cases. This is because the relative velocity has to be non-zero in order for the B-plane to be defined. The lower the relative velocity, the less rectilinear the relative motion will be and so the assumption that allows the combined uncertainty to be projected onto the B-plane will be invalid in certain cases [106]. McKinley [96] showed that relative velocities of $0.013\,km\ s^{-1}$ are sufficient for the rectilinear relative motion assumption to hold, thus $2.0\,km\ s^{-1}$ was also sufficient.

Y axis in the B-plane is pointing at the point of the closest approach, therefore certain separation between the objects has to be present in this direction in order to be able to define such a coordinate system. Also, position of the secondary could not be along the relative velocity vector to test covariance matrix scaling to the worst case. This is because if the primary and secondary are placed along the relative velocity vector, they end up at the same point in the B-plane, and hence the maximum collision probability is 1.0. This was found to obscure the influence of the separation distance between the objects on the maximum collision probability, therefore displacing the secondary by the same amount in both the relative velocity direction and Y direction in the B-plane was decided upon. This guaranteed that certain separation between the objects was present, thus allowing the B-plane to be defined, as well as allowed investigation of all the behaviours of the maximum collision probability.

It is expected that cases A.9a and A.9b, A.9c and A.9d, as well as A.9e and A.9f will have almost identical collision probabilities because the objects are at the same distances from one another and the alignments of the uncertainty regions are the same. However, the conjunction geometry in case A.9a might challenge the rectilinear relative motion assumption if the relative velocity is not high enough and thus make its P_C different to that of case A.9b.

The fact that only three of the example geometries need to be examined will be proven in section A.3.4. But first the number of series expansion terms and relative position PDF evaluations to use in direct numerical integration will be chosen based on these three geometries. Only three of the test cases will be presented instead of all six for brevity.

A.3.2 Direct integration - the choice of the number of integration points

Direct numerical integration of Eq. 2.21 was tested on test conjunction geometries shown in Figures A.9b, A.9d and A.9e. Different numbers of interpolation intervals in Equations 2.23 and 2.24 were investigated for a number of separation distances and a range of covariance scaling factors, which accounts for different sizes of the uncertainty ellipsoids.

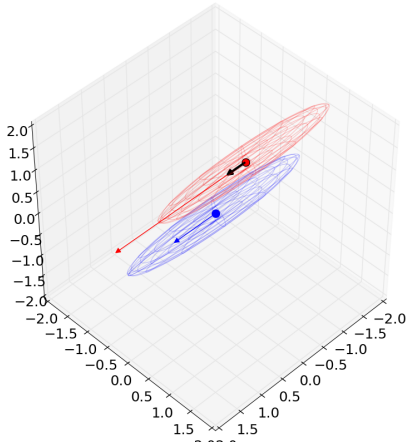

(a) Test conjunction 1: overtaking

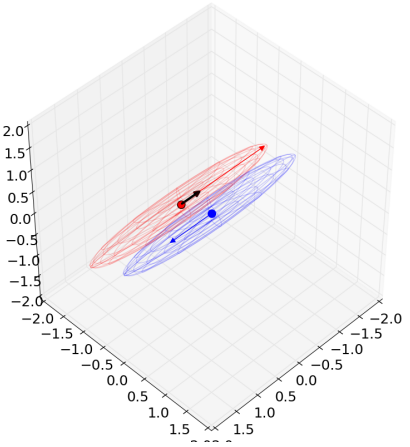

(b) Test conjunction 2: head-on

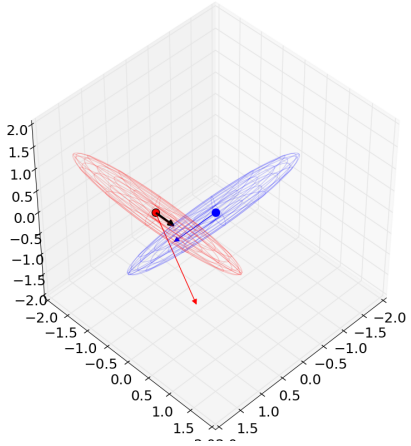

(c) Test conjunction 3: right-to-left

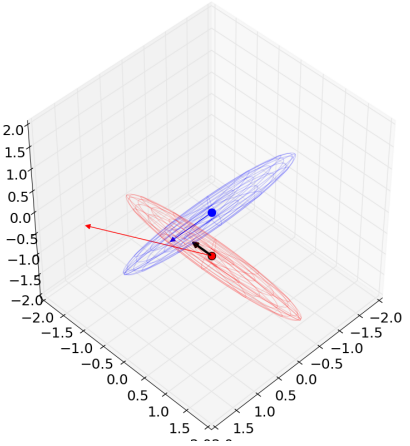

(d) Test conjunction 4: left-to-right

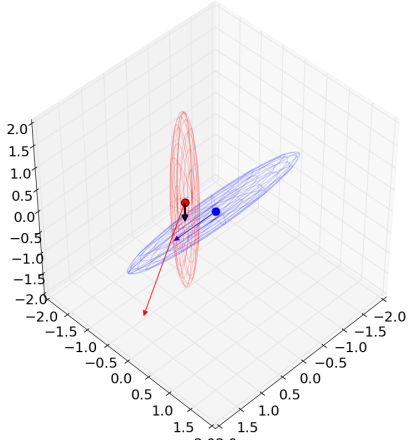

(e) Test conjunction 5: top-to-bottom

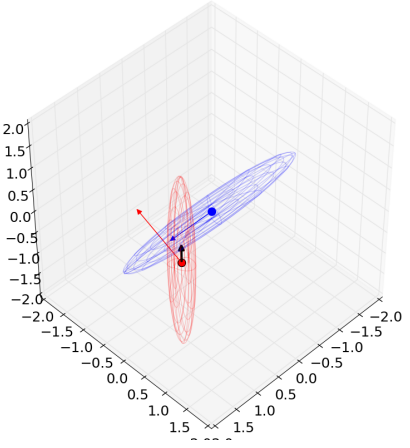

(f) Test conjunction 6: bottom-to-top

Figure A.9: Conjunction geometries that investigate extreme conjunction cases. Primary marked with a blue dot and secondary with a red one. Their respective velocities are indicated with blue and red arrows whereas the relative velocity is indicated with a black arrow. One standard deviation uncertainty ellipsoids of both objects are also marked with the respective colours.

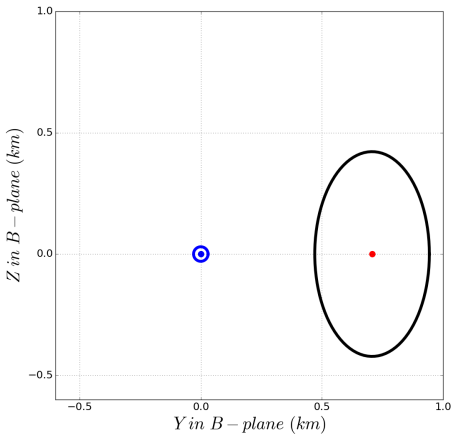

(a) Test conjunction 1: overtaking

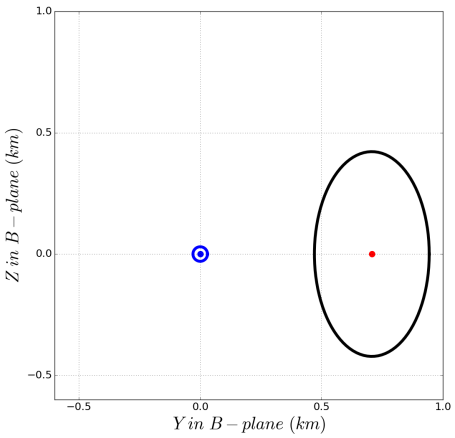

(b) Test conjunction 2: head-on

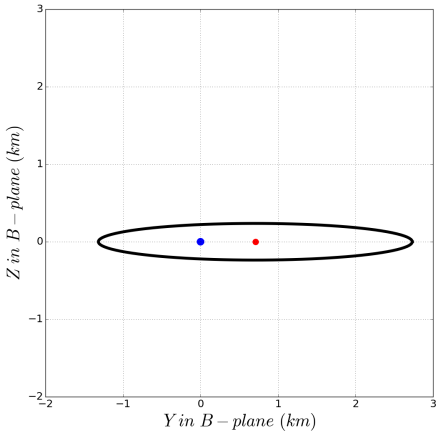

(c) Test conjunction 3: right-to-left

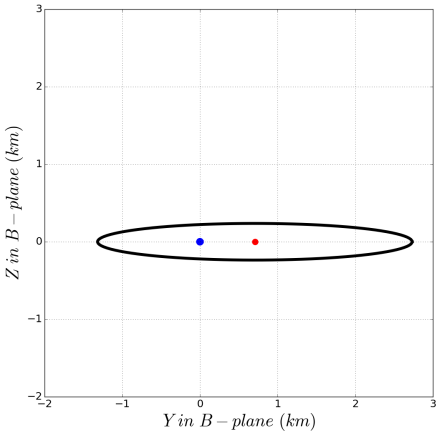

(d) Test conjunction 4: left-to-right

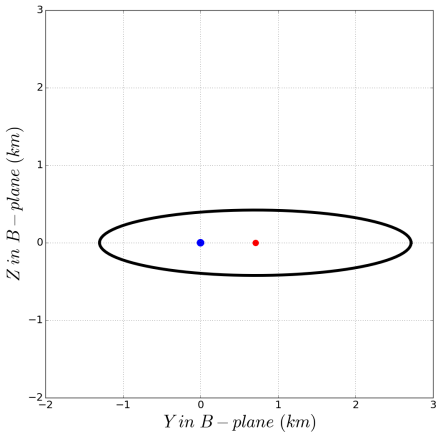

(e) Test conjunction 5: top-to-bottom

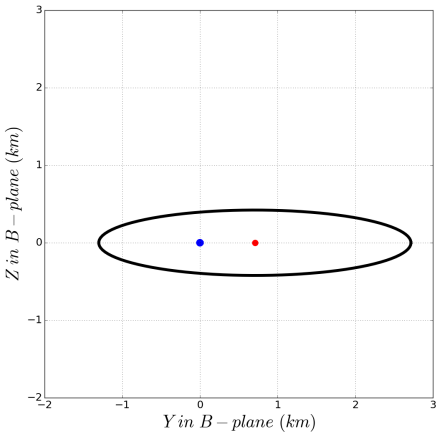

(f) Test conjunction 6: bottom-to-top

Figure A.10: Projection of the secondary's position (red), the collision circle (blue), and combined one standard deviation uncertainty envelope (black) onto the B-plane for the conjunction geometries from Figure A.9.

Double Simpson's rule with 50, 100, 1000, 2500, 5000 and 10 000 interpolation intervals was tested. The same number of intervals was used to estimate the integrals in both equations - the optimum number of intervals in both directions could be different but establishing those would not produce any accuracy gains and complicate the parametric study. The results for the three tested geometries are presented in Figures A.11, A.12 and A.13.

The "head-on" geometry in Fig. A.11 shows the impact of the number of integration integrals on the collision probability in the most prominent fashion. In cases where the separation distance between the two objects is equal to or less than their combined radius, when the maximum collision probability should be equal to 1.0, 50 and 100 interpolation intervals do not provide sufficient precision to capture this behaviour. This is because it requires the covariance scaling factor, k^2, to be zero and thus the probability density of the relative position to be zero as well. If too few interpolating intervals are used the truncation errors, T_y and T_z, in equations 2.23 and 2.24 are greater than the actual probability density and thus dominate the collision probability that is computed. The same behaviour is expected and was observed for relatively distant conjunctions where the probability density within the collision circle is low.

Almost no improvement (less than one percent change in the maximum collision probabilities) can be seen when the number of terms is increased from 2500 to 5000 for all the tested geometries and miss distance to collision radius ratios. However, in order to provide margin and thus ensure precision of the results, 5000 terms were used.

A.3.3 Series expansion - choice of the number of series expansion terms

Figures A.14, A.15 and A.16 present the dependence of the collision probability on the scaling factor, k^2, used to scale the covariance matrix according to Eq. 2.31. These values are shown for a number of ratios between the collision radius and the minimum distance between the objects' centres of mass, $\frac{r}{|p_{mean}|}$, and for three test cases A.9b, A.9d and A.9e. These results were obtained by computing the collision probability according to Eq. 2.29 with different numbers of terms used in the series expansion.

Some of the conjunctions have separation distance equal to or less than the objects' combined radius, and their maximum collision probability should be equal to 1.0. This is because scaling to the worst-case covariance matrix should remove any uncertainty that allows the objects not to collide. For any ratios $\frac{r}{|p_{mean}|}$ less than 1.0, a clear maximum of the collision probability is expected [4].

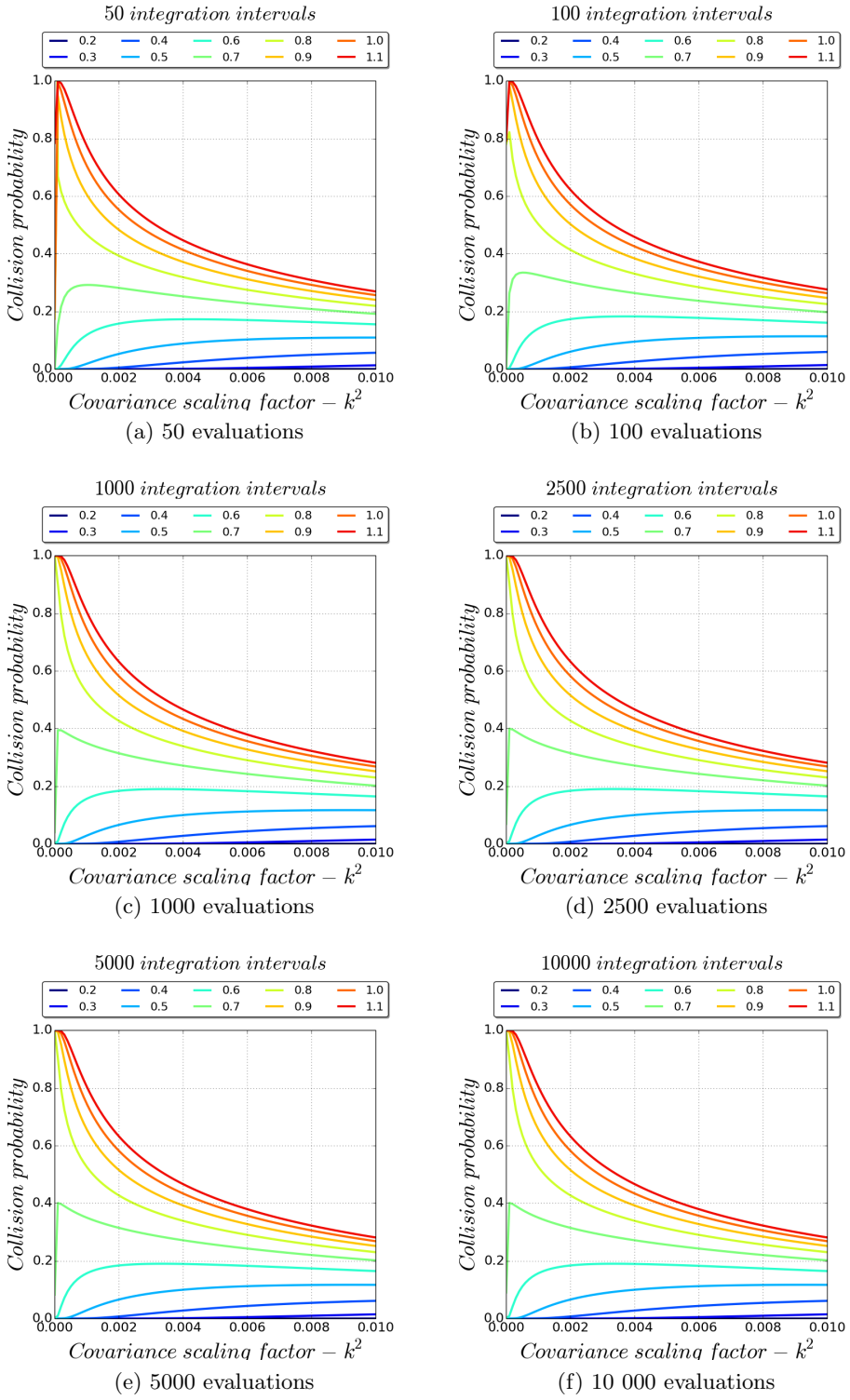

(a) 50 evaluations (b) 100 evaluations

(c) 1000 evaluations (d) 2500 evaluations

(e) 5000 evaluations (f) 10 000 evaluations

Figure A.11: Collision probability as a function of the covariance scaling factor for various ratios of the combined object radius to the miss distance. Computed for varying numbers of evaluations used to numerically integrate the probability density function of the relative position using the Simpson's rule. "Head-on" conjunction geometry from Fig. A.9b.

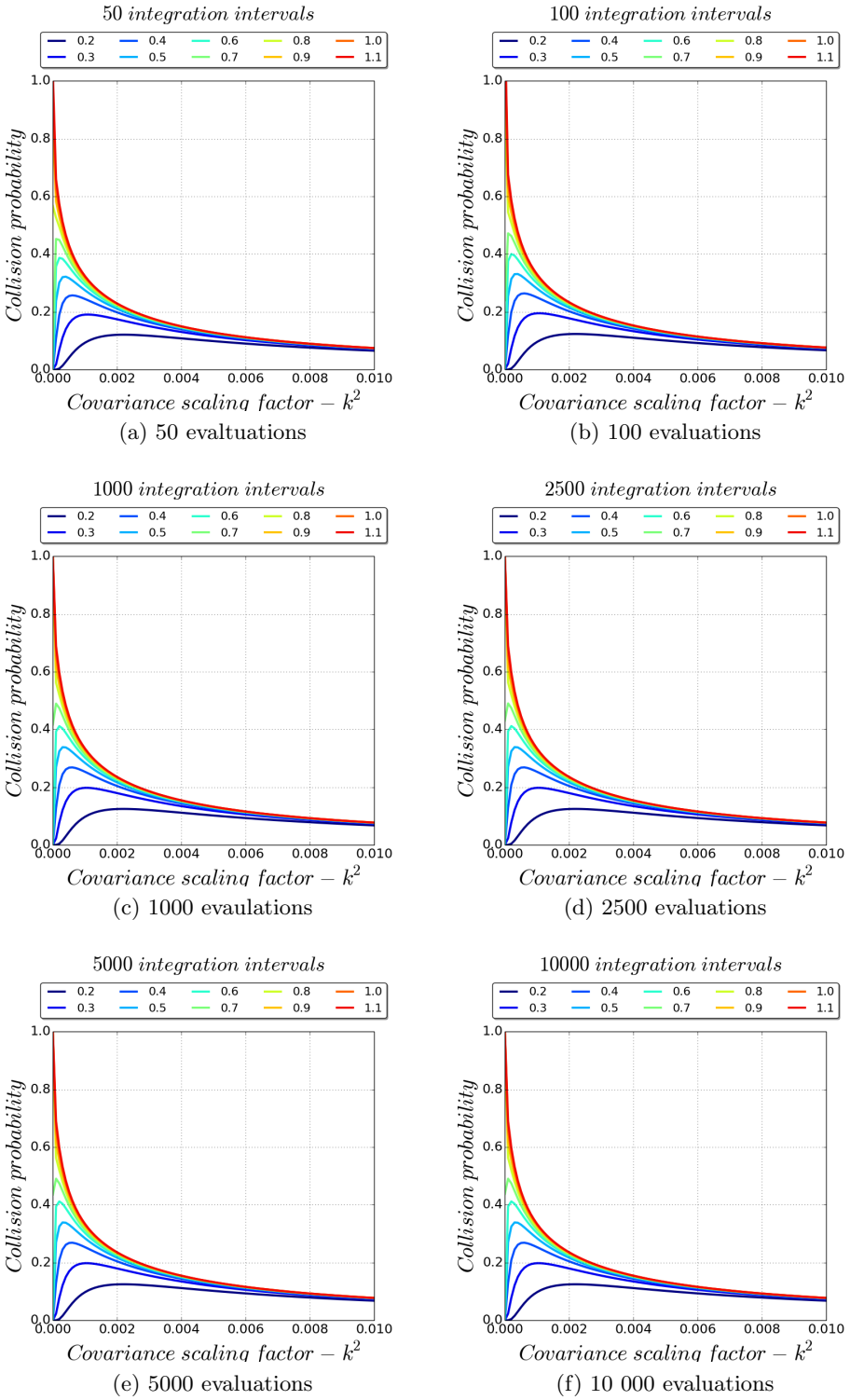

(a) 50 evaltuations (b) 100 evaluations

(c) 1000 evaulations (d) 2500 evaluations

(e) 5000 evaluations (f) 10 000 evaluations

Figure A.12: Collision probability as a function of the covariance scaling factor for various ratios of the combined object radius to the miss distance. Computed for varying numbers of evaluations used to numerically integrate the probability density function of the relative position using the Simpson's rule. "Left-to-right" conjunction geometry from Fig. A.9d.

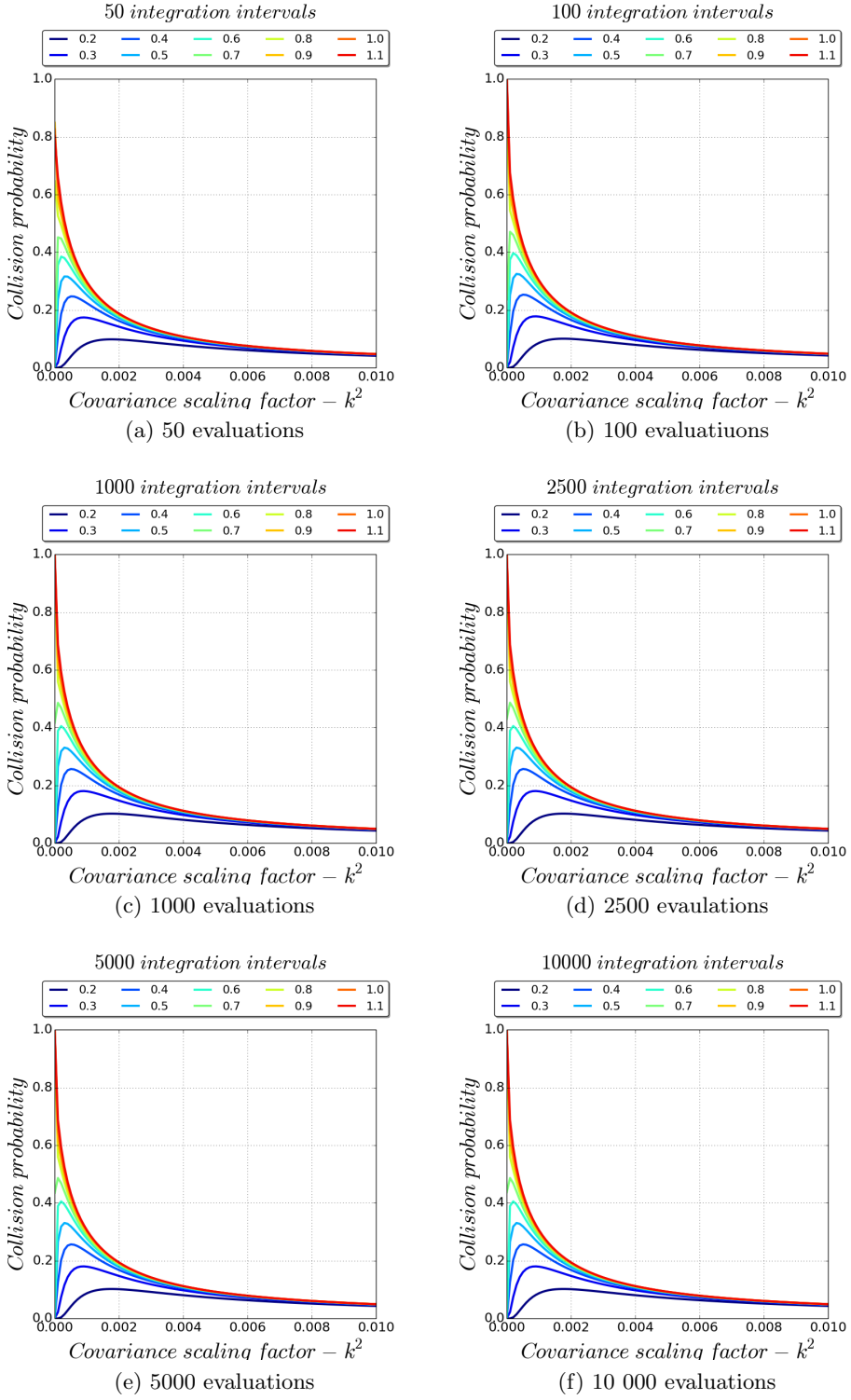

(a) 50 evaluations (b) 100 evaluatiuons

(c) 1000 evaluations (d) 2500 evaulations

(e) 5000 evaluations (f) 10 000 evaluations

Figure A.13: Collision probability as a function of the covariance scaling factor for various ratios of the combined object radius to the miss distance. Computed for varying numbers of evaluations used to numerically integrate the probability density function of the relative position using the Simpson's rule. "Top-to-bottom" conjunction geometry from Fig. A.9e.

For relatively distant conjunctions with $\frac{r}{|p_{mean}|}$ less than approximately 0.2, little increase in the precision of the P_C estimation is observed as the number of terms increases from 1 to 50. This behaviour is the same in all three test cases. However, as conjunctions get closer and $\frac{r}{|p_{mean}|}$ increases, the number of terms in the series expansion begins to play a role in how accurately the dependence of P_C on the scaling factor k^2 is modelled. This will also impact the $P_C|^{MAX}$ value that can be found with this method. The closer the conjunction the more terms are needed to accurately represent the behaviour of its P_C.

However, using more than 50 terms becomes computationally expensive and difficult. Specifically, computing $e^{\frac{-u}{2}}$ and $e^{\frac{-v}{2}}$ in Eq. 2.28 with large dimensionless u and v variables can exceed the range of real numbers that can be represented as double precision floating point numbers. This is not necessarily an issue when computing $P_C|^{TRUE}$ because for most conjunctions u and v will be small enough. However, when one tries to compute maximum collision probability, the standard deviations of position uncertainty decrease thus causing u and v to increase, which can be deduced from Eq. 2.28. Empirically, 50 terms was established as the highest number of terms that can be used in most of the cases.

This number of terms is only precise for $\frac{r}{|p_{mean}|}$ less than 1.0 - in Fig. A.16f collision probability of 1.0 was not reached even for conjunctions with separation less than the combined radius of the objects. This is not desired because very close conjunctions should be allowed to have $P_C|^{MAX}$ as close to what they could achieve with Monte Carlo P_C estimation. Therefore, it was decided to use 50 terms for $\frac{r}{|p_{mean}|} < 0.8$ and direct numerical integration of Eq. 2.21 elsewhere. Using such a combination of the two methods allowed reducing the computational time by using the fast to evaluate P_C estimation algorithm wherever it is accurate, while modelling the extremely close conjunctions correctly.

A.3.4 Verification

The direct numerical integration of Eq. 2.21 and the series expansion from Eq. 2.29 were tested against Monte Carlo probability estimation on the six test cases presented in Fig. A.9 with miss distance of 1.0 km.

Monte Carlo P_C estimation was performed by seeding pairs of conjunction geometries from the covariance matrix that had been rotated and combined in the B-plane. The ratio of the number of pairs where the two objects' centres of mass were within the collision radius to the total number of samples was regarded as the collision probability [106]. The entire process was repeated for 10^6, 10^7 and 10^8 sample pairs to verify that the collision probability did not change with the number of samples and thus that sufficiently many Monte Carlo samples had been taken.

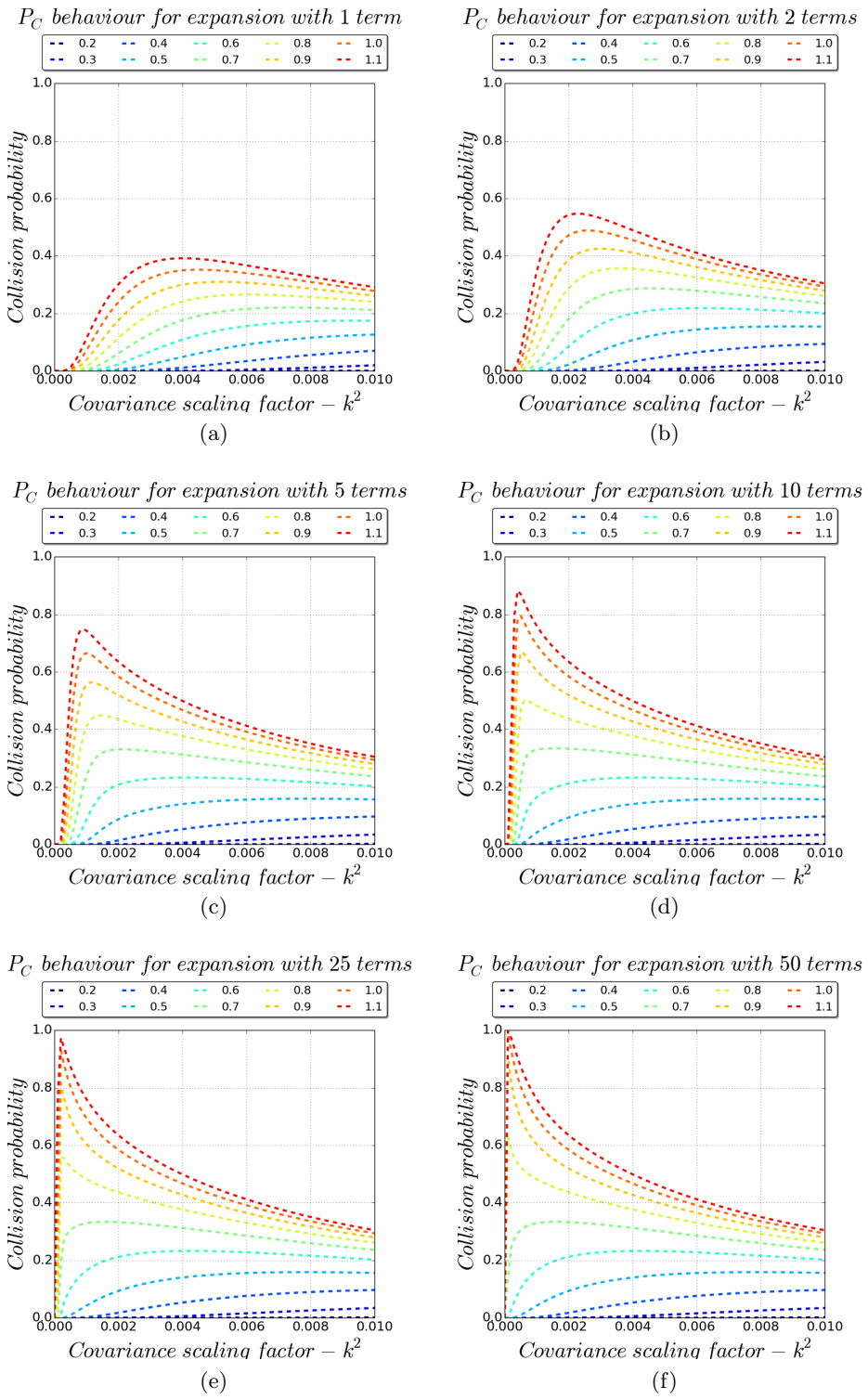

Figure A.14: Collision probability as a function of the covariance scaling factor for various ratios of the combined object radius to the miss distance. Computed for varying numbers of terms used to evaluate the integral of the relative position probability density using the series expansion algorithm. "Head-on" conjunction geometry from Fig. A.9b.

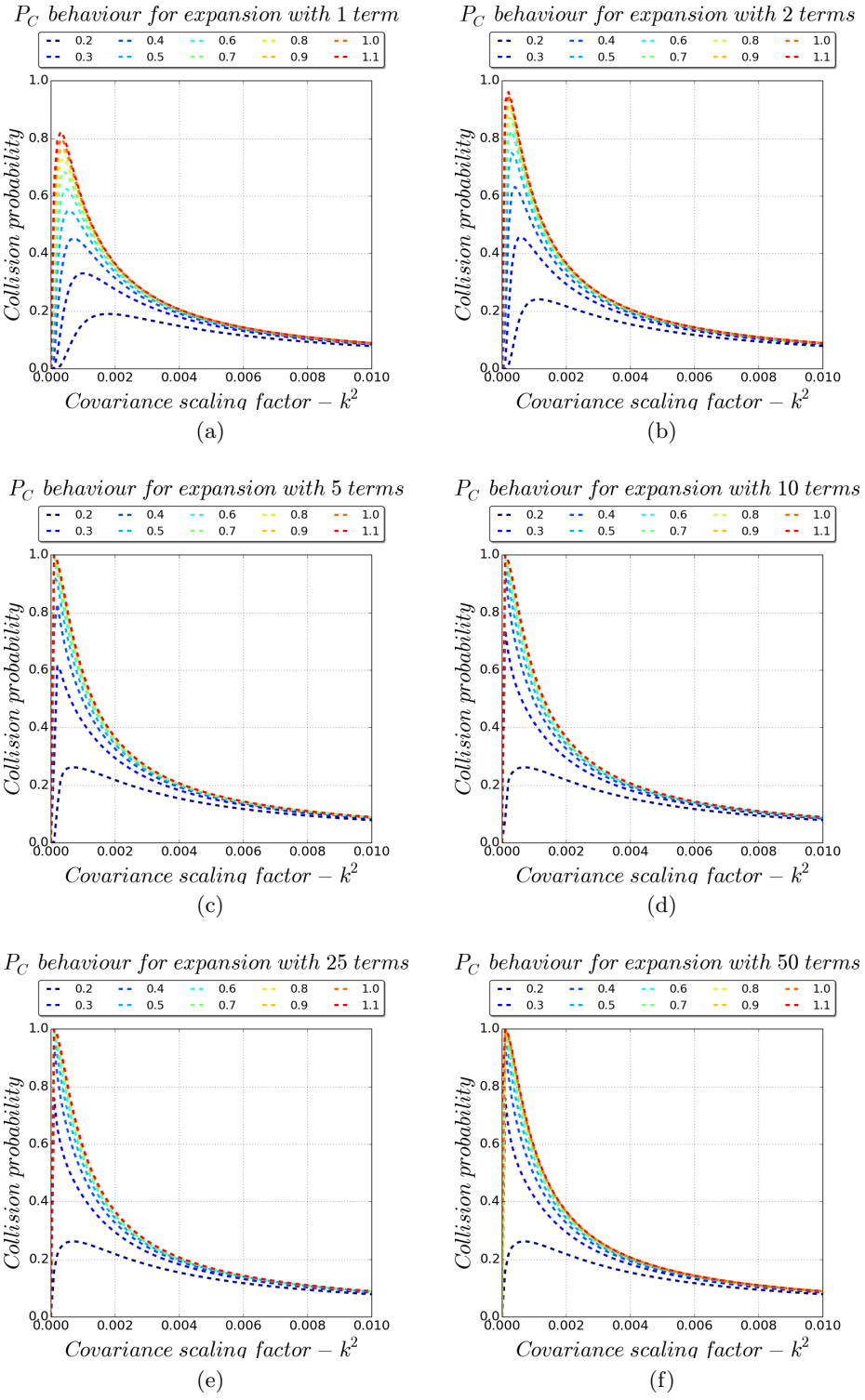

Figure A.15: Collision probability as a function of the covariance scaling factor for various ratios of the combined object radius to the miss distance. Computed for varying numbers of terms used to evaluate the integral of the relative position probability density using the series expansion algorithm. "Left-to-right" conjunction geometry from Fig. A.9d.

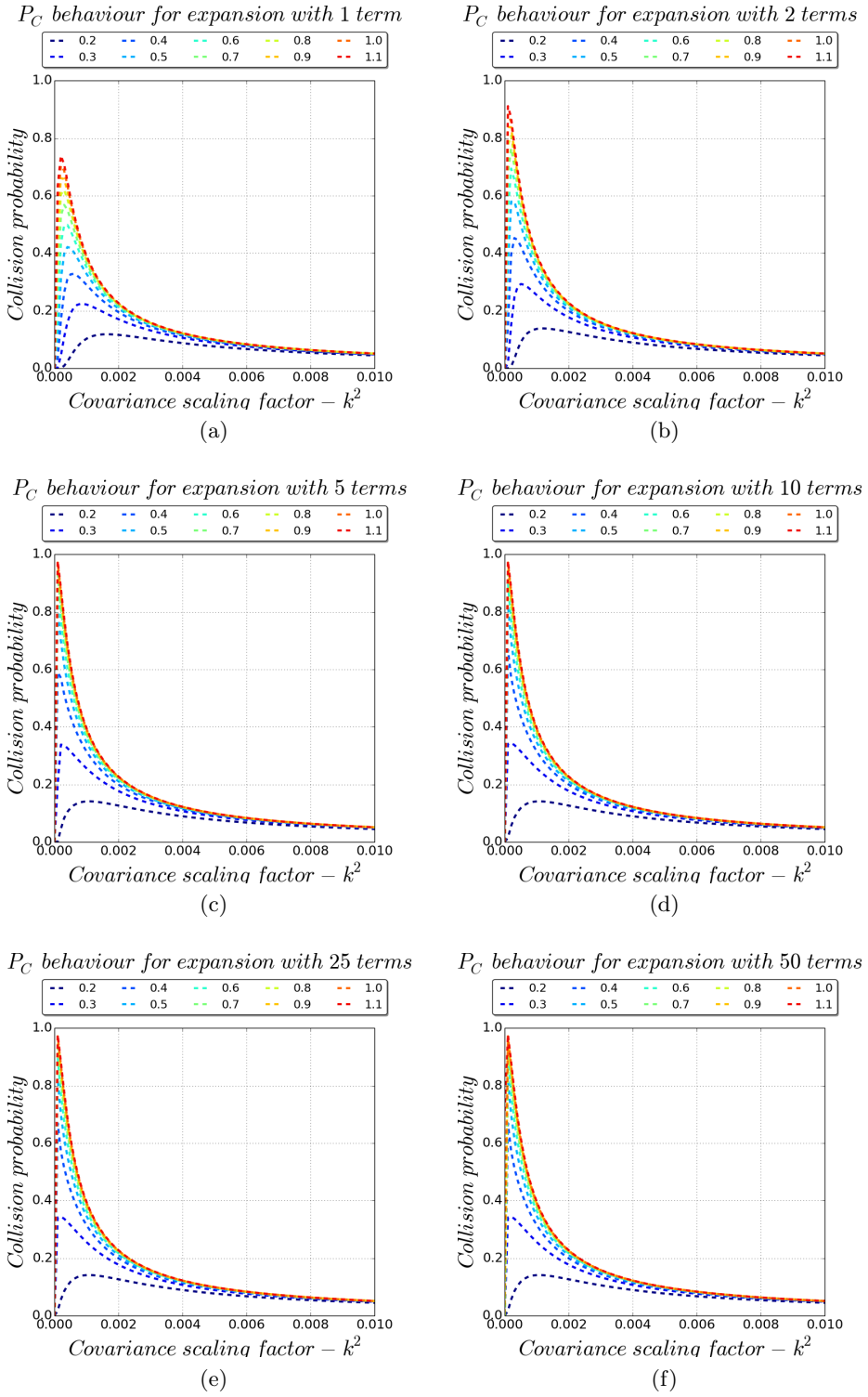

Figure A.16: Collision probability as a function of the covariance scaling factor for various ratios of the combined object radius to the miss distance. Computed for varying numbers of terms used to evaluate the integral of the relative position probability density using the series expansion algorithm. "Top-to-bottom" conjunction geometry from Fig. A.9e.

Direct integration method used 5000 function evaluations in Equations 2.23 and 2.24 whereas the series approach used 50 terms. The resulting Monte Carlo (MC), direct integration (DI) and series expansion collision probabilities for every conjunction geometry are presented in Fig. A.17.

First of all, cases A.9a and A.9b, A.9c and A.9d, as well as A.9e and A.9f have the same collision probability when computed using the semi-analytical algorithms. This is expected because the relative velocity was set high enough ($2.0\,km\ s^{-1}$) not to cause the recitlinear assumption to break down in case A.9a. Therefore performing the previous investigations only on cases A.9b, A.9d and A.9e did not affect the generality of the findings.

The Monte Carlo collision probability varied by 21% when increasing the number of samples from 10^6 to 10^8. However, the difference between 10^7 and 10^8 samples was at most 5.48%. Therefore, it is believed that the number of Monte Carlo samples was sufficient. Hereafter, all the comparisons will be made to Monte Carlo P_C values obtained with 10^8 samples.

Direct integration agrees with MC to within 0.92%, and series expansion to within 0.85% for cases A.9c to A.9f. The discrepancy when the secondary approaches the primary along the in-track direction, i.e. cases A.10a and A.10b, is greater. Direct integration is accurate to within 0.74% but the series expansion to within only 360%, i.e. it differs by two orders of magnitude c.f. Monte Carlo in cases A.17a and A.17b. This difference can be explained by the fact that the collision probability is low in these two cases, that is 5.21×10^{-5} and 5.27×10^{-5} when using the Monte Carlo method. This causes the series approach not to be able to reproduce the very low probability density of the relative position and result in incorrect estimates of the collision probability. The extents to which this affects the results will be quantified when examining the combined conjunction detection and assessment framework. However, the accuracy of the collision probability estimation can be deemed sufficient, especially when performed using the direct numerical integration.

A.3.5 Covariance matrix scaling to maximum collision probability

An analytical estimate of the covariance scaling factor k, which maximises the collision probability, was given in Eq. 2.30. This analytical scaling factor was tested on test conjunction geometries shown in Figures A.9b, A.9d and A.9e. The collision probabilities as functions of the scaling factor, together with the maximum P_C found using the analytical estimate of the scaling factor, are shown in Fig. A.18 for the three conjunction geometries.

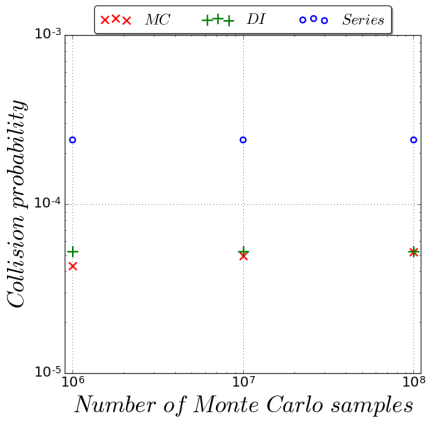

(a) Test conjunction 1: overtaking

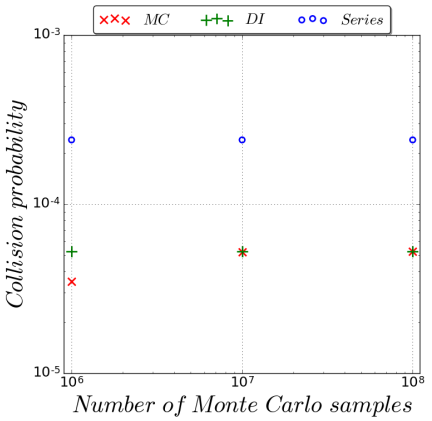

(b) Test conjunction 2: head-on

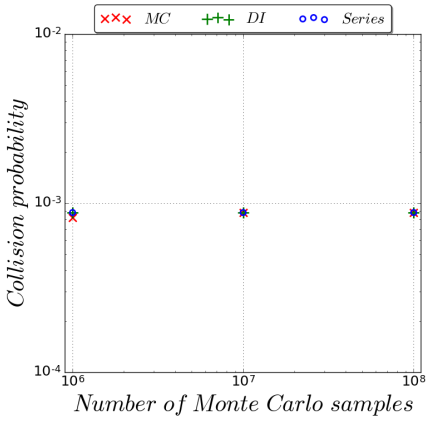

(c) Test conjunction 3: right-to-left

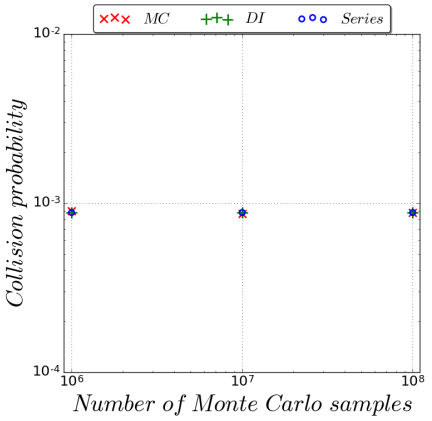

(d) Test conjunction 4: left-to-right

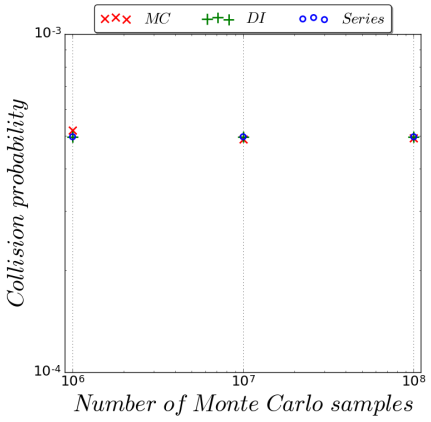

(e) Test conjunction 5: top-to-bottom

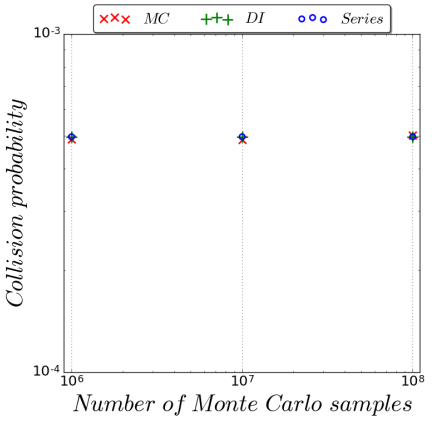

(f) Test conjunction 6: bottom-to-top

Figure A.17: Comparison of the collision probabilities obtained using direct numerical integration of Eq. 2.21 (DI), series expansion of the integral, and direct Monte Carlo (MC) with the number of MC samples for the six test conjunction geometries. The Monte Carlo samples were seeded from the covariance matrix rotated and combined in the B-plane.

The analytical k produces the maximum collision probability accurately for $\frac{r}{|p_{mean}|}$ less than 0.1. This is to say that it is accurate for distant conjunctions. However, for the lower miss distances, the analytical covariance scaling factor is overestimated thus leading to the collision probability being underestimated. Moreover, the analytical estimate of k is incapable of resulting in $P_C|^{MAX} = 1.0$. In order to avoid this, a simple numerical search [123] was employed to find the correct scaling factor k for close conjunctions. The analytical estimate of the worst-case scaling factor, k_A, is higher than the one that produces the true $P_C|^{MAX}$ in all the tested cases. Therefore, the sought k is located in the interval $[0,\ k_A]$ ($[0,\ 1.5k_A]$ was used here to increase confidence in the search). The algorithm of the golden ratio search, together with C++ source code, is given by Press et al. [123]. The search is terminated when k is found with accuracy of 1% or when 100 iterations have elapsed.

This golden ratio search was employed for conjunctions with $\frac{r}{|p_{mean}|} \geq 0.8$. This is because this search requires repetitive estimation of $P_C|^{MAX}$ during every iteration, which increases the computational time. The analytical estimate k_A may be inaccurate in the $0.1 \leq \frac{r}{|p_{mean}|} \leq 0.8$ regime. However, $P_C|^{MAX}$ is still going to be in the order of tens of percent even when using k_A directly in this regime, which is expected to be considerably higher than $P_C|^{MAX}$ of most of the conjunctions. This search was only employed to ensure that $P_C|^{MAX} \approx 1.0$.

A.4 Verification of the public catalogue covariance estimation

The adopted algorithm used to estimate the uncertainty of the two-line element sets, described in section 2.4, was verified. Firstly, a comparison was made to several test cases used by the algorithm's author, largely to ensure that it was implemented correctly. Then, the algorithm was compared to TLE uncertainties, which were estimated using a different algorithm, to verify that the obtained results are not contrived. Lastly, the evolution of the estimated TLE covariance with time was qualitatively compared to propagating the state uncertainty using state transition matrices.

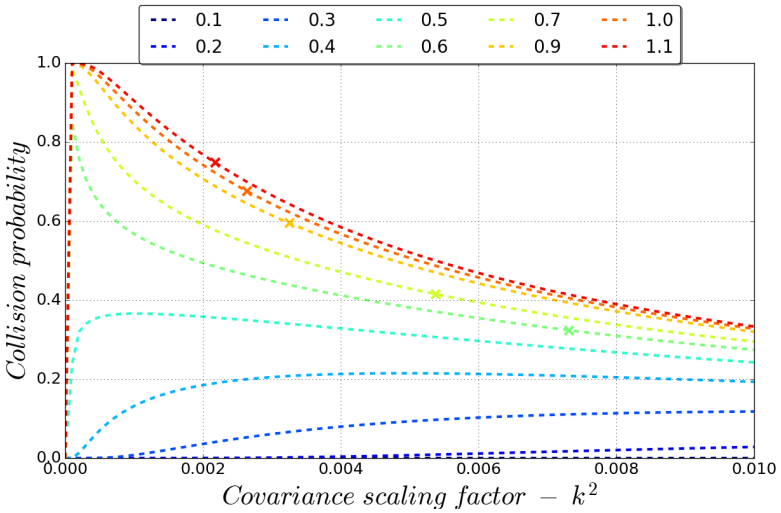

(a) Test conjunction 2: head-on

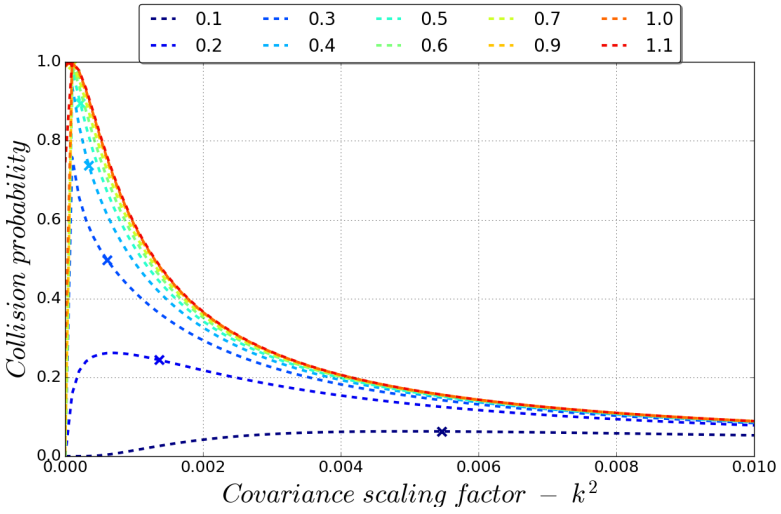

(b) Test conjunction 4: left-to-right

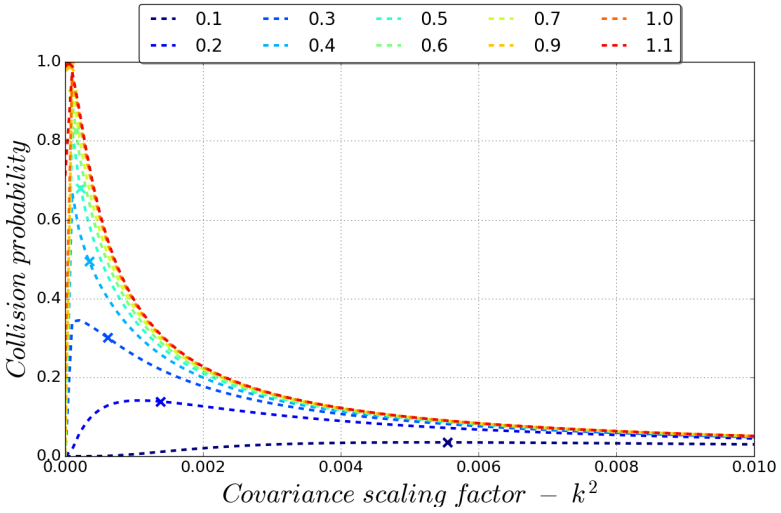

(c) Test conjunction 5: top-to-bottom

Figure A.18: Collision probability as a function of the covariance scaling factor for various ratios of the combined object radius to the miss distance. Computed for various conjunction geometries from Fig. A.9e. The worst-case covariance scaling factor computed using Eq. 2.30 and the corresponding collision probability are also marked.

Table A.1: Comparison of the position covariance matrices obtained by Osweiler [114] to the algorithm implemented herein. Presented in the velocity, normal, co-normal (VNC) reference frame. Relative errors with respect data by Osweiler [114] computed using Eq. A.6 are also given.

Lageos 1

	Original (km^2)			**Reproduced** (km^2)			**Relative error**		
	V	N	C	V	N	C	V	N	C
V	3E-1	2E-2	5E-2	3E-1	8E-3	6E-2	12%	−52%	18%
N	2E-2	3E-3	5E-3	8E-3	6E-3	-1E-3	−52%	125%	−123%
C	5E-2	5E-3	2E-2	6E-2	-1E-3	2E-2	18%	−123%	25%

FAST

	Original (km^2)			**Reproduced** (km^2)			**Relative error**		
	V	N	C	V	N	C	V	N	C
V	3E+3	-4E+1	5E+0	3E+3	-4E+1	5E+0	−7%	9%	−6%
N	-4E+1	7E-1	-2E-1	-4E+1	9E-1	-2E-1	9%	42%	16%
C	5E+0	-2E-1	9E-2	5E+0	-2E-1	10E-2	−6%	16%	15%

A.4.1 Comparison to original test cases

Osweiler [114] gives covariance matrices estimated for 18 TLEs. However, only the corresponding most recent TLEs rather than complete sets spanning the two-week windows are supplied, thus making direct verification of the implemented algorithm difficult. Two test cases will be presented here nevertheless for completeness' sake and to show that the algorithm was implemented correctly. These are cases 4 and 3 for Lageos 1 and FAST, respectively [114]. These were chosen because the smallest discrepancies between the reference results exist for these cases.

Table A.1 compares position covariance matrices for these two test cases estimated by Osweiler [114] to the ones obtained here. The relative errors in the variance, Δ_V, of position in the velocity, normal, co-normal reference frame were computed using Eq. A.6, where V_E is the variance estimated here and V_{REF} is the reference variance from the work by Osweiler [114]. The absolute magnitude of the error was not used to indicate whether the uncertainty is being over or underestimated. The relative error is at most 125%, which is considered acceptable given the fact that the exact sets of the TLEs used to obtain the reference covariance matrices are unknown.

$$\Delta_V = \frac{V_E - V_{REF}}{V_{REF}}. \tag{A.6}$$

A.4.2 Comparison to higher-fidelity algorithms

A set of estimated TLE covariances for objects spanning 18 orbital regimes in the eccentricity-inclination-perigee altitude space was compared to the results obtained with the implemented algorithm. These objects have been selected by Krag et al. [63] as a representative sample that categorises varying levels of accuracy of TLEs in different orbital regimes. An overview of the orbital regimes and the exemplar object in each is given in Table A.3.

These reference data had been obtained by propagating the TLE state and generating pseudo-observations hence. Then orbit determination was performed on these simulated observations and the resulting orbit propagated numerically. Comparison of the numerically propagated states to the ones generated with the original TLE yielded covariance. This process is detailed in [36]. The reference data were intended to quantify the discrepancies between TLEs and reality. This is different from the goals of this work that is interested primarily in variability in the TLE sets themselves. Comparing the results of the used algorithm to higher-fidelity data and thus verifying that the uncertainties it estimates are not entirely contrived was still considered important, however.

Inclination, perigee altitude and eccentricity are only some of the factors that affect orbit determination uncertainty. They also might not have as much impact as, for example, orbit maintenance being performed by some of the objects, their radar cross section, type of the object and alike [53]. Therefore, using other criteria to parametrise uncertainties of the TLEs could be more appropriate. However, the set of the exemplar objects from Table A.3 was used to compare the accuracy of TLE uncertainty estimation for those objects only. The uncertainty of every TLE used in this study was estimated individually, therefore, if the estimation algorithm is sufficiently accurate for the exemplar objects, it should also be for any other one. The only way to extend this verification would be to compare estimated TLE covariances for a more exhaustive number of different types of objects in the catalogue, but such data were not available.

The approach adopted here was applied to the exemplar objects from Table A.3 at the epoch as close to the reference date (1 Jan 2008) as possible. The relative errors of the estimated to reference TLE position standard deviations in the radial, in-track, cross-track (RIC) reference frame, are presented in Table A.5. The relative error was computed using Eq. A.6, but with different reference data; also standard deviation rather than variance was used here. Unfortunately, for objects 23100, 27763 and 20944 the epochs of the TLEs were different by 7, 3, and 1 years, respectively, with respect to the reference epoch. This is because the TLEs for the representative objects were not available on Space-Track [135] in the desired period.

Table A.3: Orbital regimes in the eccentricity-inclination-perigee altitude space used to validate the TLE covariance estimation approach. The corresponding objects' catalogue numbers, and the numbers of two-line element sets are also given.

$e \leq 0.1$

	$\mathbf{h_P \leq 800\,km}$			$\mathbf{800 < h_P \leq 25000\,km}$			$\mathbf{25000\,km < h_P}$		
	$i \leq 30°$	$30° < i \leq 60°$	$60° < i$	$i \leq 30°$	$30° < i \leq 60°$	$60° < i$	$i \leq 30°$	$30° < i \leq 60°$	$60° < i$
SSC	27783	23100	23940	22176	24320	23736	24435	24435	24435
No. TLEs	13	24	30	17	19	16	12	12	12

$0.1 < e$

	$\mathbf{h_P \leq 800\,km}$			$\mathbf{800 < h_P \leq 25000\,km}$			$\mathbf{25000\,km < h_P}$		
	$i \leq 30°$	$30° < i \leq 60°$	$60° < i$	$i \leq 30°$	$30° < i \leq 60°$	$60° < i$	$i \leq 30°$	$30° < i \leq 60°$	$60° < i$
SSC	21223	14900	27763	21966	21833	20944	14069	14069	14069
No. TLEs	14	11	21	12	7	17	7	7	7

The epoch differences for objects 27763 and 20944 are less than 28% of the solar cycle and the $F10.7$ solar flux did not vary by more than 20 SFU [146] between these epochs and the reference date. The orbit determination accuracy depends on the accuracy with which the drag coefficient can be estimated. Accuracy of the drag coefficient estimation depends on the solar activity [117], which means that the orbit determination accuracy depends on the solar activity. Therefore, it can be expected that the epoch differences for objects 27763 and 20944 did not affect the orbit determination accuracy and so the covariance estimated for them should be similar to the reference data.

For the object 23100, however, the difference in the $F10.7$ solar flux was more than 100 SFU [146] and so the orbit determination accuracy could have been vastly different. Moreover, since autumn of 2012, the way in which at least some TLEs are generated has changed [46]. This makes a direct comparison between the estimated and reference covariance for 23100 questionable, because both sets of data could have been generated using different ephemerides.

The number of TLEs spanning the 14-day window, used to estimate the covariance of the most-recent TLE, was different for every object. For objects 23100, 27763 and 20944, however, similar numbers of TLEs were available, that is 24, 21, and 17, respectively. Therefore, this factor should not influence the relative accuracy of the results.

The difference between the in-track standard deviation in the orbital regime of the object 23100 and the reference data was investigated further. A different object, 25112, located in the same orbital regime was investigated because TLEs were available for it close to the reference epoch (one day difference). 25112 is a satellite as opposed to a rocket body, therefore it most likely experiences different drag, but objects in this orbital regime typically have position uncertainties in the same order of magnitude [36]. The results of this investigation, in the same form as in Table A.5 to enable direct comparison between the two, are given in Table A.7.

As in the case of eight out of 18 orbital regimes, over one order of magnitude difference in the in-track position standard deviation is present for object 25112. This discrepancy is considerably smaller than for object 23100, however, which may hint that part of the source of error for 23100 was the seven-year difference between the epochs at which the uncertainties were estimated.

The standard deviations of position uncertainties obtained with the adopted approach are typically in the same order of magnitude as the ones estimated using the more involved algorithm in [36]. The biggest differences can be seen in the in-track direction. This is not surprising as the Keplerian dynamics will cause the largest dispersion of the sample objects in this direction.

This natural stretching of the position uncertainty in the in-track direction will be further amplified by the atmospheric drag that affects in-track positions of the objects. It is difficult to accurately represent such non-conservative forces analytically [29]. Therefore, the simplifications made in the SGP theory are expected to cause dispersion of the sample TLEs to be the greatest in this direction [29, 57], thus resulting in even greater in-track position standard deviation. The effect of drag affecting the covariance estimation accuracy can be seen by observing that the in-track standard deviation estimation inaccuracies are the greatest at low altitudes.

A.4.3 Evolution of the estimated uncertainty over time

The evolution of position uncertainty for the highly-eccentric test case from Table 2.1, Delta 1 rocket body, was investigated. It was decided to investigate only this test case because the effects of non-linear orbital dynamics are expected to be the greatest for such orbits [149].

Evolution of the numerically computed eigenvalues of the position covariance matrix is shown in Fig. A.19. A cycle that correlates with the orbital period can be observed together with a secular growth of the uncertainty the longer the propagation. As can be seen in Fig. A.20b, the uncertainty is the largest close to the perigee and smallest at the apogee, as expected. Furthermore, according to Fig. A.20a, the largest uncertainty is present along the velocity direction.

Table A.5: Relative error of the estimated to reference TLE position standard deviations in every orbital regime in radial, in-track, cross-track (RIC) reference frame. One order of magnitude difference is indicated with light grey, and two orders of magnitude with dark grey.

$e \leq 0.1$

	$\mathbf{h_P \leq 800\,km}$			$\mathbf{800 < h_P \leq 25000\,km}$			$\mathbf{25000\,km < h_P}$		
	$i \leq 30°$	$30° < i \leq 60°$	$60° < i$	$i \leq 30°$	$30° < i \leq 60°$	$60° < i$	$i \leq 30°$	$30° < i \leq 60°$	$60° < i$
R	0.90	9.02	1.63	-0.74	0.70	1.25	0.34	0.34	0.34
I	0.43	270.34	3.01	5.58	90.36	27.22	4.60	4.60	4.60
C	2.82	8.97	2.77	0.85	14.24	-0.54	-0.17	-0.17	-0.17

$0.1 < e$

	$\mathbf{h_P \leq 800\,km}$			$\mathbf{800 < h_P \leq 25000\,km}$			$\mathbf{25000\,km < h_P}$		
	$i \leq 30°$	$30° < i \leq 60°$	$60° < i$	$i \leq 30°$	$30° < i \leq 60°$	$60° < i$	$i \leq 30°$	$30° < i \leq 60°$	$60° < i$
R	-0.64	3.79	10.36	2.34	0.67	67.90	0.69	0.69	0.69
I	0.96	7.80	27.73	2.18	1.12	58.80	25.50	25.50	25.50
C	-0.48	-0.15	-0.38	-0.29	-0.06	2.05	-0.28	-0.28	-0.28

Table A.7: Relative error of the estimated to reference standard deviations of position in the RIC frame, for another object with perigee altitude lower than 800 km, inclination between 30 and 60 degrees, and eccentricity less than 0.1. One order of magnitude difference is indicated with light grey, and two orders of magnitude with dark grey.

SSC	25122
No. TLEs	24
R	-0.39
I	34.04
C	6.98

Qualitatively similar behaviour was observed when propagating the covariance matrices using the state transition matrices as implemented in Analytical Graphics Incorporated's System Toolkit. Quantitative comparison was not conducted because the algorithms developed here are not implemented in STK. This proves that the covariance uncertainty estimation algorithm implemented here can be used to propagate the uncertainty in time in a fashion that is physically correct. This means that those conjunctions that have a high collision probability because the orbit knowledge is good will also have a high P_C here.

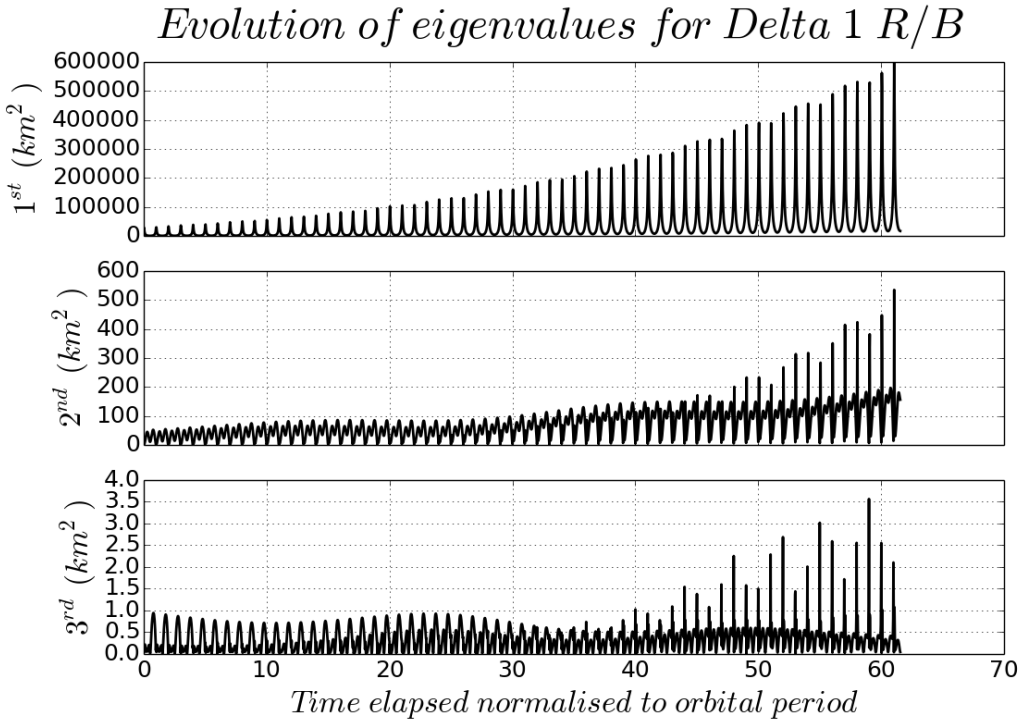

Figure A.19: Evolution of the 1^{st}, 2^{nd} and 3^{rd} largest eigenvalues of the position covariance matrix estimated for Delta 1 R/B's TLE from Table 2.1. Obtained by propagating a set of TLEs and estimating the covariance at every epoch. The first, largest eigenvalue is always aligned with the orbital velocity. The alignment of the second and third largest eigenvalues depends on the position of the object along the orbit.

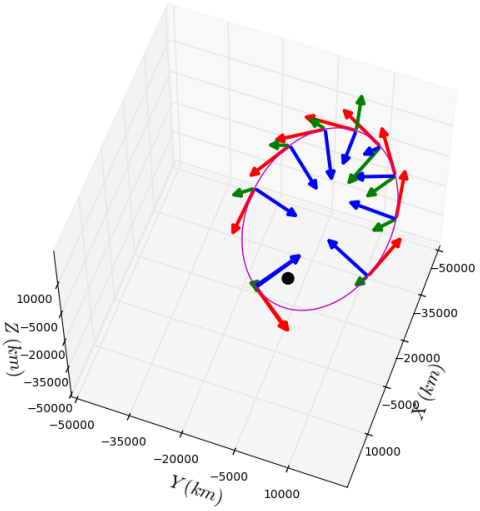

(a) Directions of eigenvectors

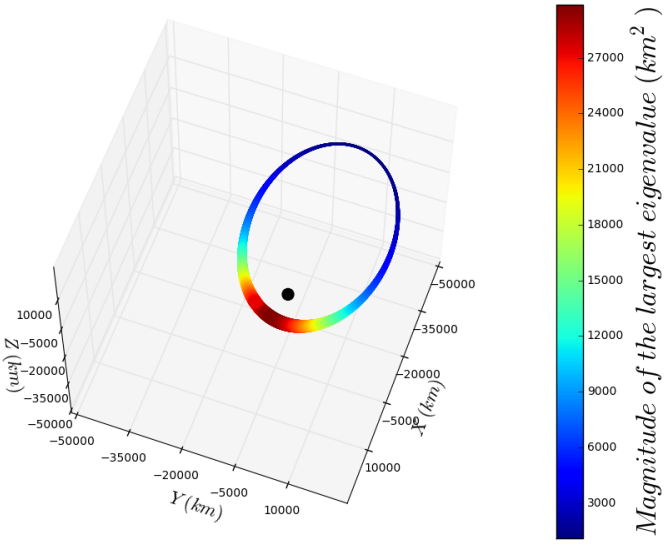

(b) Largest eigenvalue

Figure A.20: Evolution of the eigenvectors and the largest eigenvalue of the position covariance matrix estimated for Delta 1 R/B. Obtained by propagating a set of TLEs and estimating the covariance at every epoch. Black dot indicates the centre of the Earth. The eigenvector corresponding to the largest eigenvalue shown in red, second largest in green, and the smallest in blue.

Appendix B

Saturation of the collision probability in evolutionary debris models

It was considered insightful to investigate the time after which the probability of any collision taking place in orbit reaches 1.0. This duration marks a point when any discussion based on collision probability looses its meaning because any additional conjunctions, no matter how high their P_C, will not affect the accumulated collision probabilities of individual objects or the probability of any collision taking place in orbit. This is why work by Radtke et al. [125] used fluxes of objects, not the P_C calculated directly using the evolutionary debris models, to rank the objects according to their collision probability. Such an approach allows dealing with the fact that more than one collision could take place in orbit, which cannot be represented by a probability metric easily - $P_C \in [0, 1]$, as required by the second axiom of probability [25].

Evolution of the probability of any collision taking place in every Monte Carlo run from section 3.2 was plotted against its epoch and is shown in Fig. B.1. In most of the Monte Carlo runs, the likelihoods of collisions (collision probabilities of collisions that took place) did not reach 1.0. However, the probability of any collision taking place saturated in every Monte Carlo run when investigating close approaches, as shown in Fig. B.1a.

Quantitative analysis of the time it took for the accumulated collision probability to saturate was performed. For every Monte Carlo run, the time it took for the accumulated P_C to reach 99.99% was computed. The results are presented in Fig. B.2. This was only performed for close approaches, not collisions, because P_C of the latter events did not saturate in most of the MC runs.

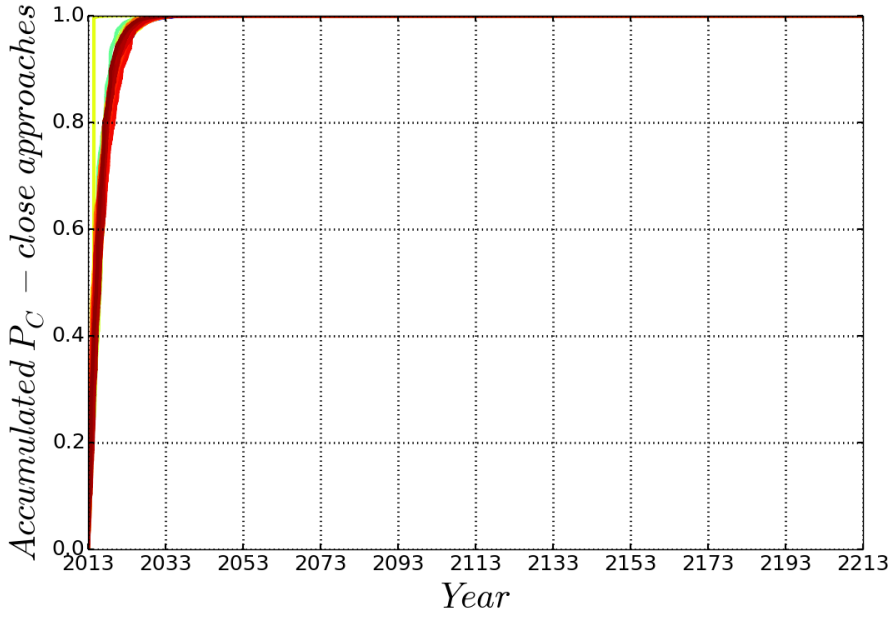

(a) Close approaches

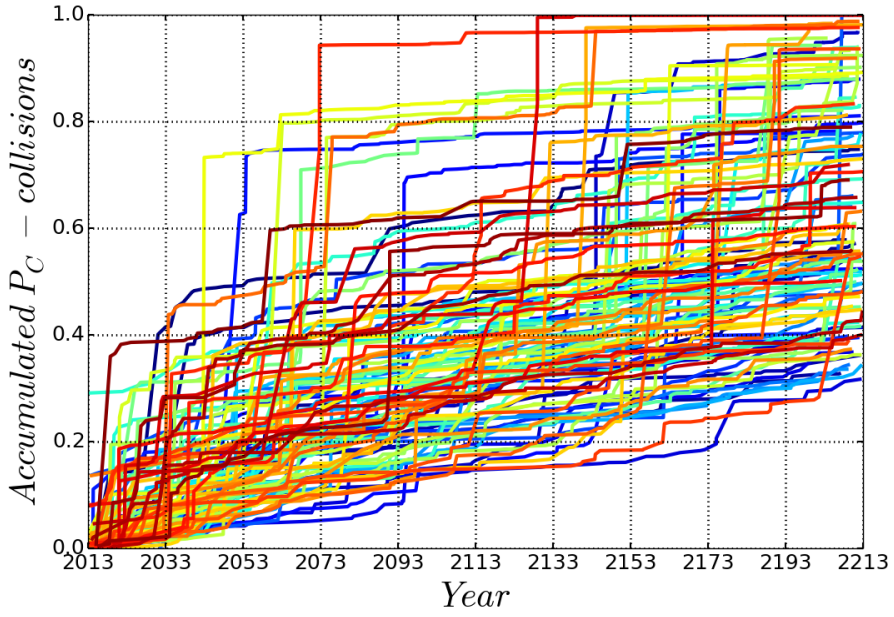

(b) Collisions

Figure B.1: Evolutions of the accumulated collision probabilities in the entire debris environment with time for all the Monte Carlo runs. Examining close approaches, which did not result in a collision, and collisions separately. Data from 100 runs obtained as part of the IADC comparison study mentioned in section 1.3.1. "Mitigation only" scenario from Table 1.1. Data provided by Dr Hugh G. Lewis.

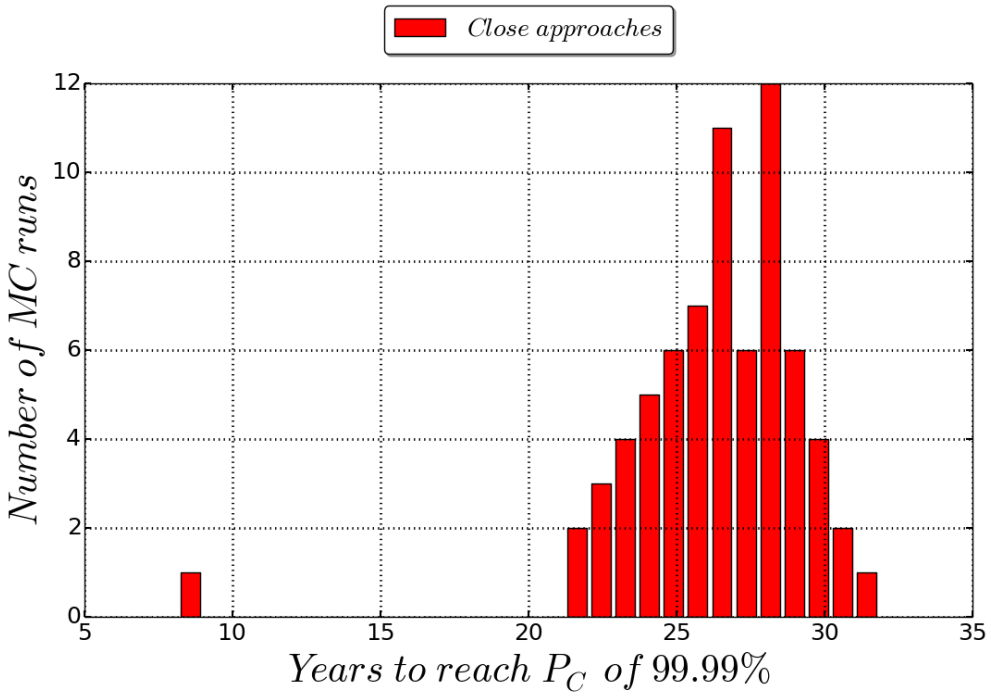

Figure B.2: Histogram of the number of years it took for the collision probability in the entire debris environment to saturate in various Monte Carlo runs. As can be noted in Fig. B.1, collision probabilities from the collisions did not saturate in most of the Monte Carlo run and thus these events were not included in this figure. Data from 100 runs obtained as part of the IADC comparison study mentioned in section 1.3.1. "Mitigation only" scenario from Table 1.1. Data provided by Dr Hugh G. Lewis.

On average, the accumulated P_C exceeds 99.99% after 26.34 years. However, in some MC runs it was as little as 8.39 or as long as 31.34 years. In the Monte Carlo run where the P_C saturated after 8.39 years, it was a particular conjunction with P_C of 61.2%, which took place 1.52 years after the beginning of the analysis, that caused the accumulated P_C to saturate 9.75 years sooner than in any other MC run.

Appendix C

JCA sensitivity study

C.1 JCA Monte Carlo sample bootstrap study

This section presents the convergence study of simulations of just in-time collision avoidance. The bootstrap of the statistical parameters of the final distribution of the number of objects in the Monte Carlo sample is presented for selected permutations of the JCA parameters from Table 4.3. This approach to convergence verification is detailed in section 4.3.1. In every presented case, varying numbers of Monte Carlo runs were used as the complete sample, starting at 50 and finishing at 15 000 with increments of 50. For each MC sample size, the individual MC runs were randomly selected from the pool of 15 000 and the statistical parameters of the distribution recomputed. This random selection was repeated 2000 times, thus giving distributions of the shape parameters for every sample size. Percentiles of these distributions were computed, and the MC sample size was incremented and the process repeated until all desired sample sizes were investigated.

C.2 JCA false alarm time step choice

The conjunction screenings using estimated TLE uncertainties presented in this work use time step, ΔT, of 400 s. This value was obtained in the the parameter study presented in section A.2.3. However, the state vector uncertainties used in the JCA false alarm study from section 4.3.2.2 are several orders of magnitude smaller than the estimated TLE covariances. Therefore, it was studied if ΔT should be reduced to increase the interpolation accuracy to improve the accuracy with which the miss distance and P_C

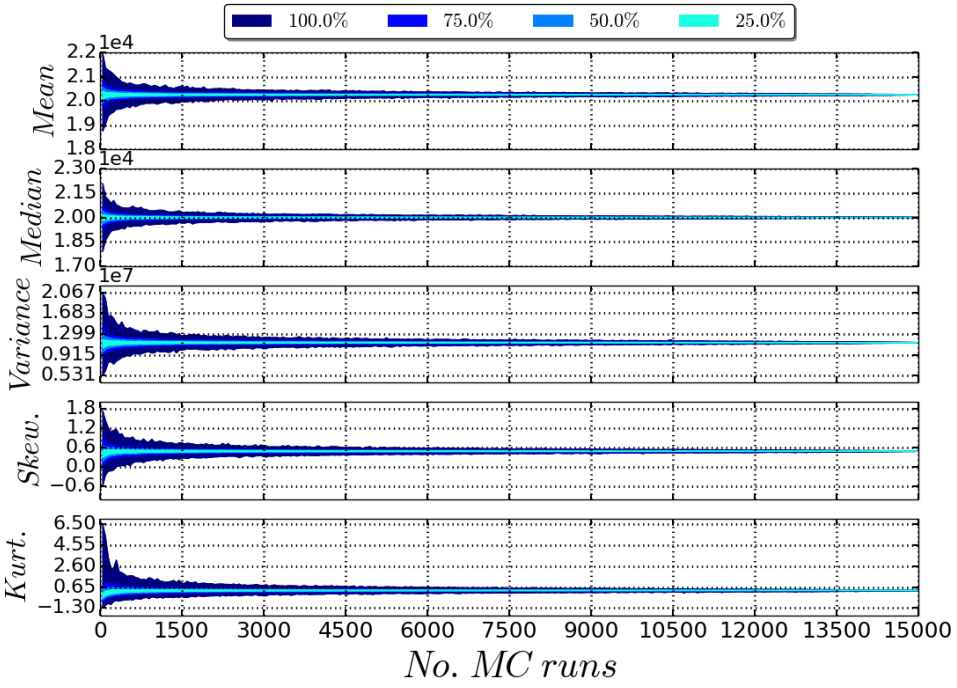

Figure C.1: Bootstrap of the statistical parameters of the distribution of the number of objects $\geq$ 10 cm at the end of the projection (2213) in the MC sample of the JCA settings number 9 from Table 4.3.

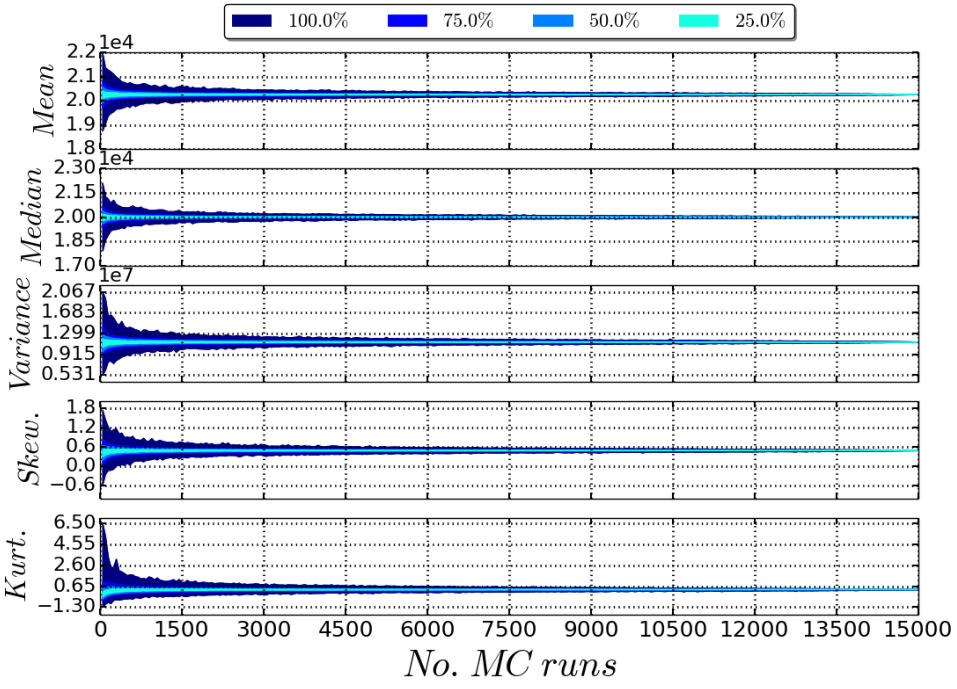

Figure C.2: Bootstrap of the statistical parameters of the distribution of the number of objects $\geq$ 10 cm at the end of the projection (2213) in the MC sample of the JCA settings number 11 from Table 4.3.

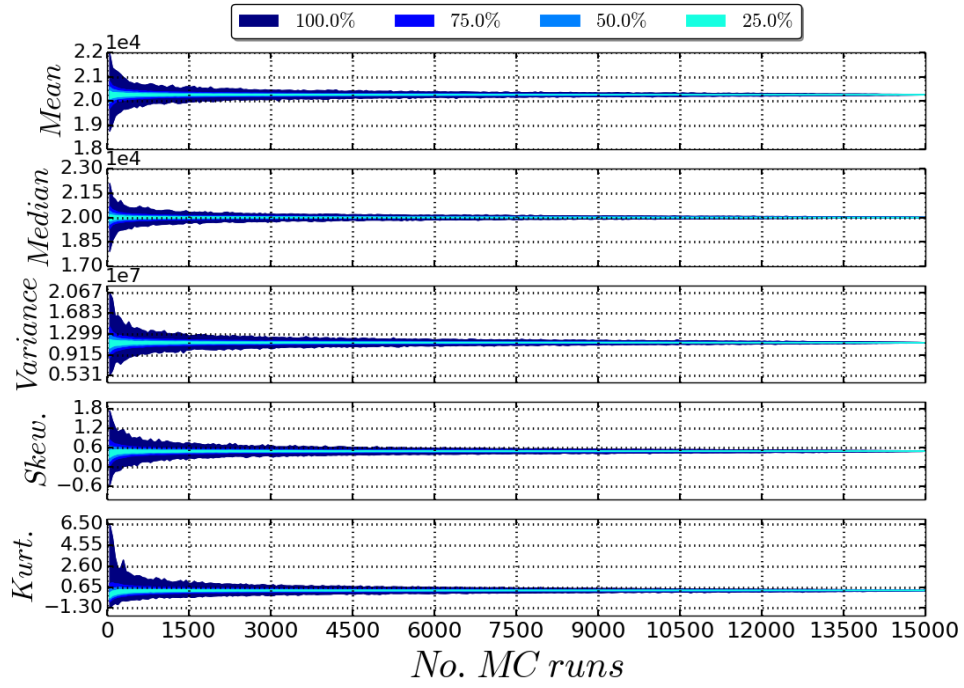

Figure C.3: Bootstrap of the statistical parameters of the distribution of the number of objects ≥ 10 cm at the end of the projection (2213) in the MC sample of the JCA settings number 21 from Table 4.3.

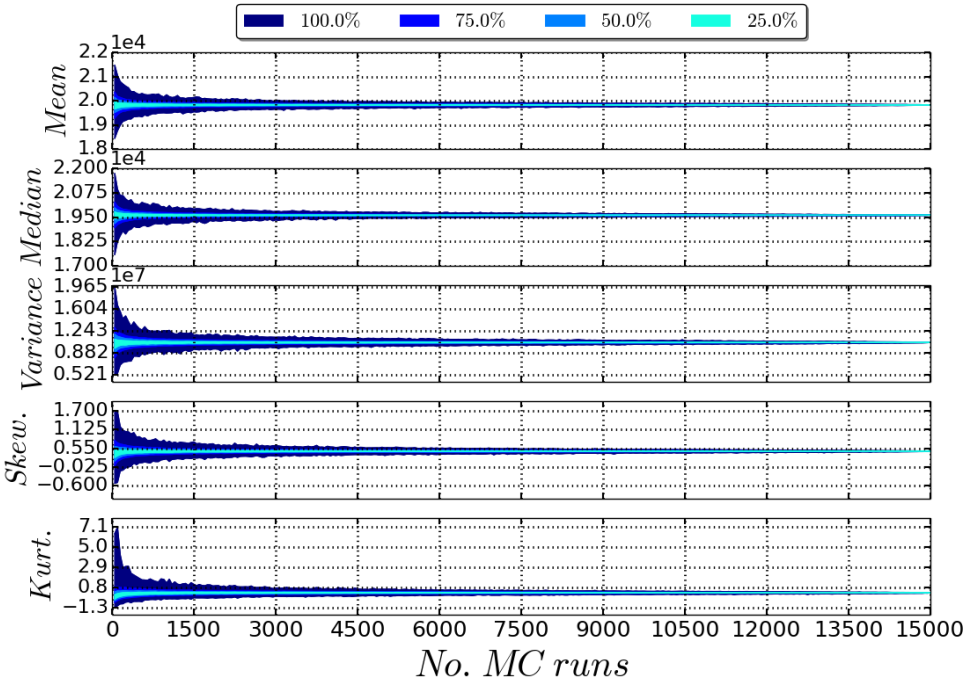

Figure C.4: Bootstrap of the statistical parameters of the distribution of the number of objects ≥ 10 cm at the end of the projection (2213) in the MC sample of the JCA settings number 22 from Table 4.3.

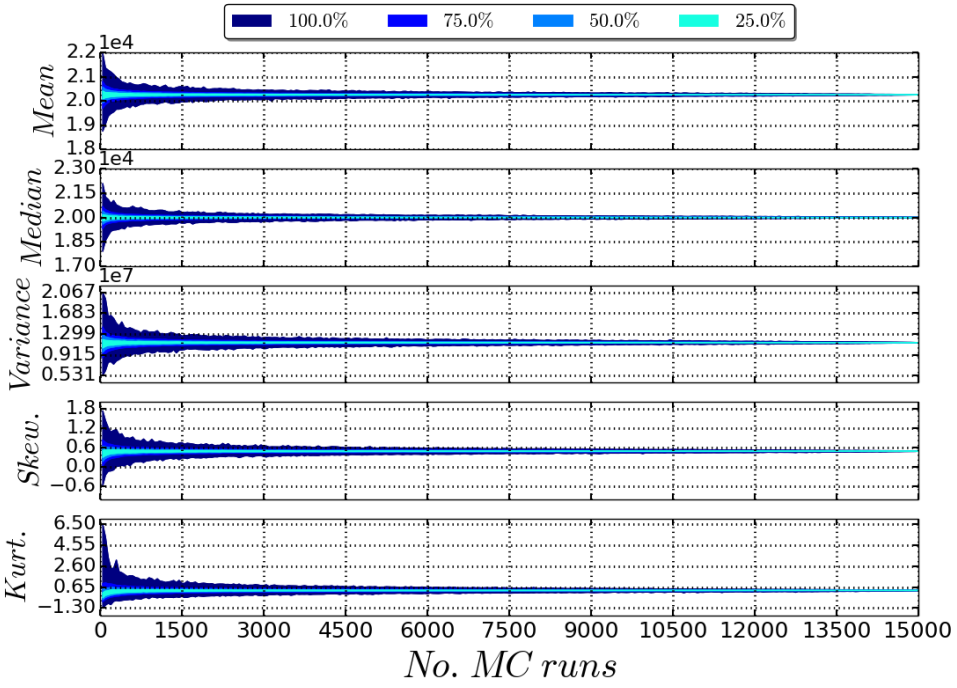

Figure C.5: Bootstrap of the statistical parameters of the distribution of the number of objects $\geq$ 10 cm at the end of the projection (2213) in the MC sample of the JCA settings number 28 from Table 4.3.

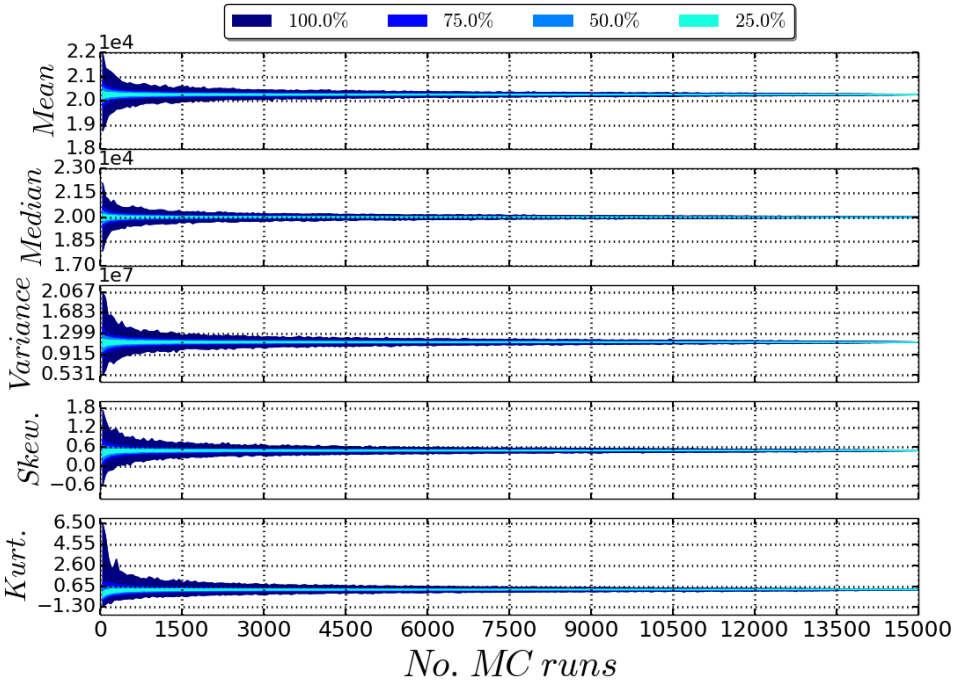

Figure C.6: Bootstrap of the statistical parameters of the distribution of the number of objects $\geq$ 10 cm at the end of the projection (2213) in the MC sample of the JCA settings number 33 from Table 4.3.

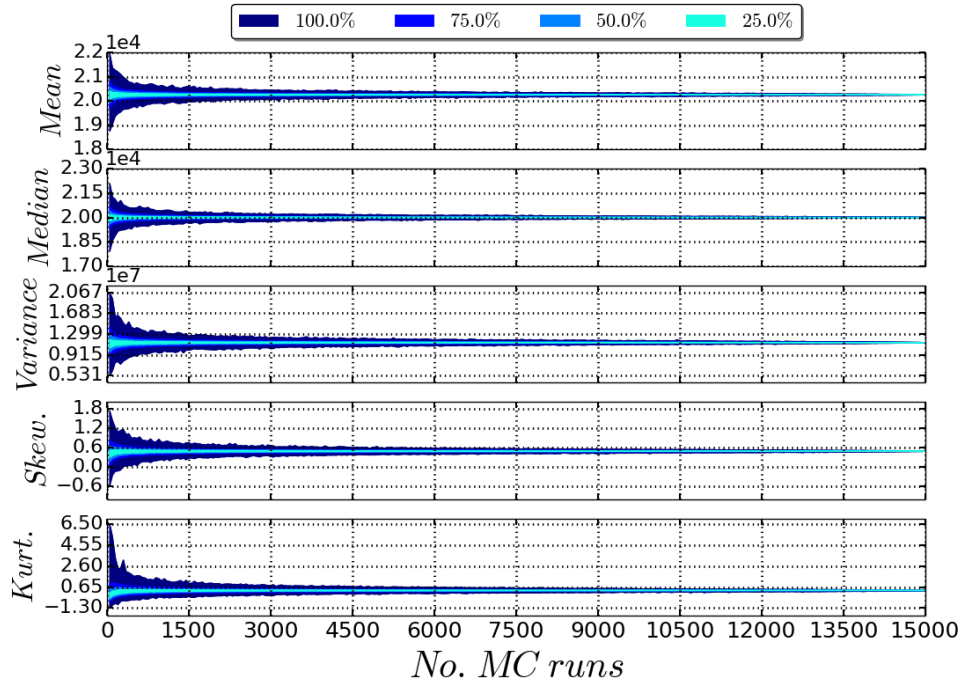

Figure C.7: Bootstrap of the statistical parameters of the distribution of the number of objects $\geq$ 10 cm at the end of the projection (2213) in the MC sample of the JCA settings number 34 from Table 4.3.

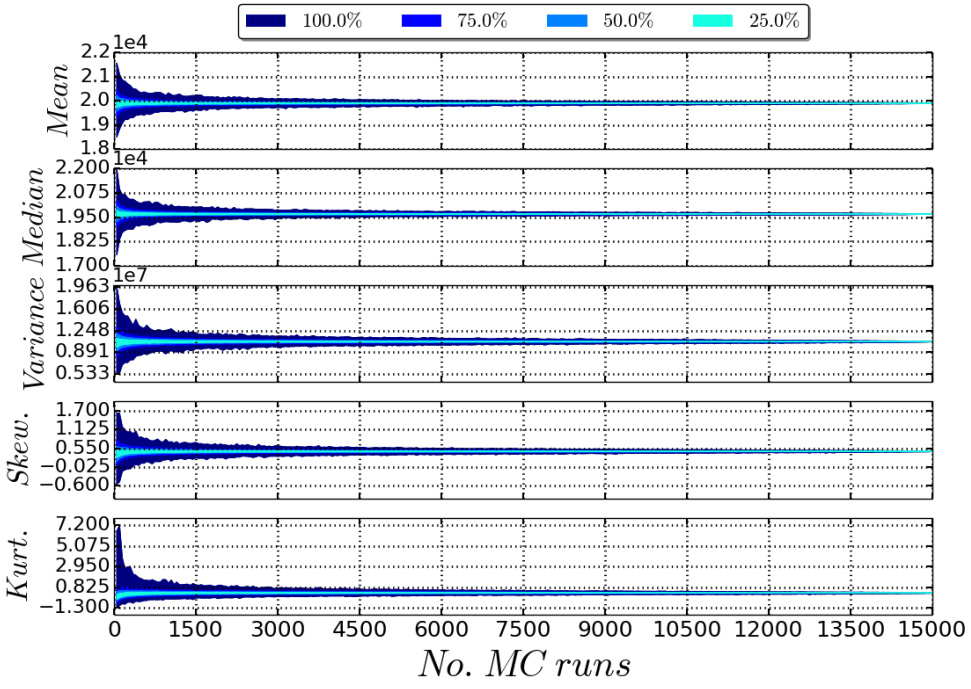

Figure C.8: Bootstrap of the statistical parameters of the distribution of the number of objects $\geq$ 10 cm at the end of the projection (2213) in the MC sample of the JCA settings number 40 from Table 4.3.

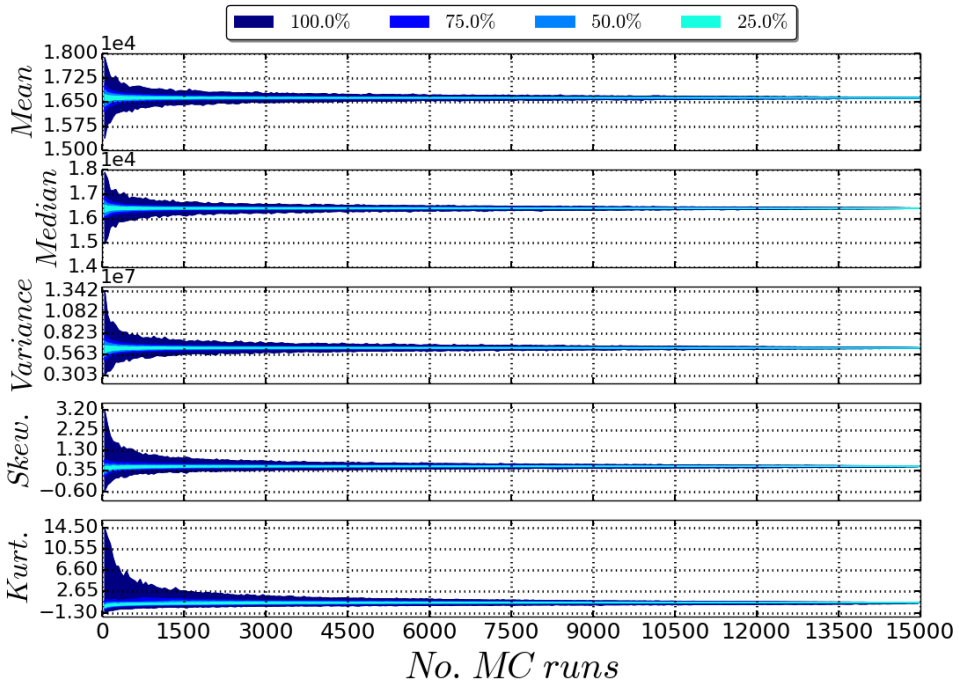

Figure C.9: Bootstrap of the statistical parameters of the distribution of the number of objects ≥ 10 cm at the end of the projection (2213) in the MC sample of the JCA settings number 47 from Table 4.3.

are estimated. This could be the case because the the interpolation error had to be low, relative to the ephemeris uncertainty, for the estimated P_C not to be contrived. This is also why STK CAT, used in other verification studies in this work, was not use here because the effects of the SGP4 discrepancies were more profound for smaller ephemeris uncertainties and so STK was not considered a reliable reference.

The two test cases from section 2.1, i.e. Envisat and Delta 1, were screened for conjunctions closer than 1 km over one year, between 23 Oct 2013 and 23 Oct 2014. Time-invariant position standard deviations of 10 m in all RIC directions were assumed for all the objects. Such uncertainty was comparable in magnitude to the lowest uncertainties used in the JCA sensitivity study from section 4.3.2.2. Delta 1 experienced no conjunctions closer than 1 km in this period of time, while the time history of the $P_C|^{TRUE}$ accumulated by Envisat for the investigated ΔT values is shown in Fig. C.10. The accumulated $P_C|^{TRUE}$ was similar in all cases except of $\Delta T = 400$ s. When the relative errors in the final accumulated $P_C|^{TRUE}$ were compared, as shown in Fig. C.11, the errors relative to the median were -3.1%, -2.2%, -2.2% and 169.2% for $\Delta T \in \{50, 100, 200, 400\}$, respectively. Even though refining ΔT beyond 200 s did not improve the accuracy of P_C estimation for Envisat, it was decided to use $\Delta T = 100$ s to ensure that the time step was not too small for other orbits. It was found in section A.1 that finer time steps always improved the accuracy of state vector interpolation. Therefore, it using $\Delta T = 100$ s

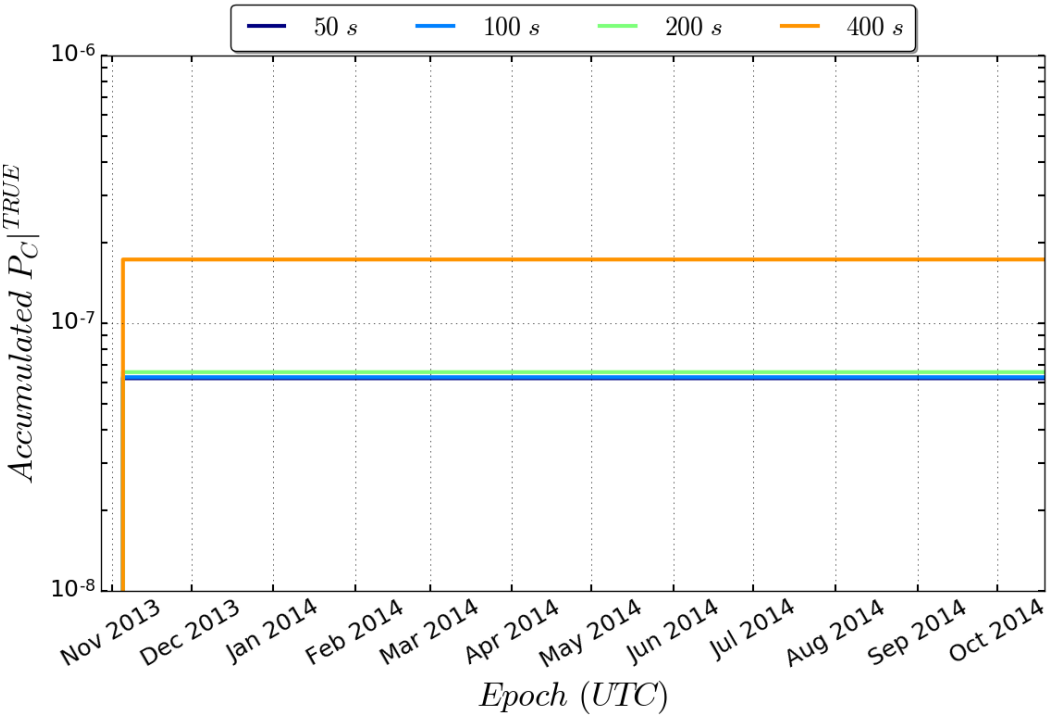

Figure C.10: Time history of the $P_C|^{TRUE}$ accumulated by Envisat between 23 Oct 2013 and 23 Oct 2014 for the investigated ΔT values. Conjunctions closer than 1 km and assuming time-invariant position standard deviations of 10 m for all the objects.

instead of 200 s should not deteriorate the results. The respective ∞-norms of position interpolation with $\Delta T = 100$ s for Envisat and Delta 1 were 3.37 and 23.8 m, which was in the same order of magnitude as the lowest expected position standard deviations. Such interpolation accuracy was deemed sufficient not to cause the estimated P_C to be contrived.

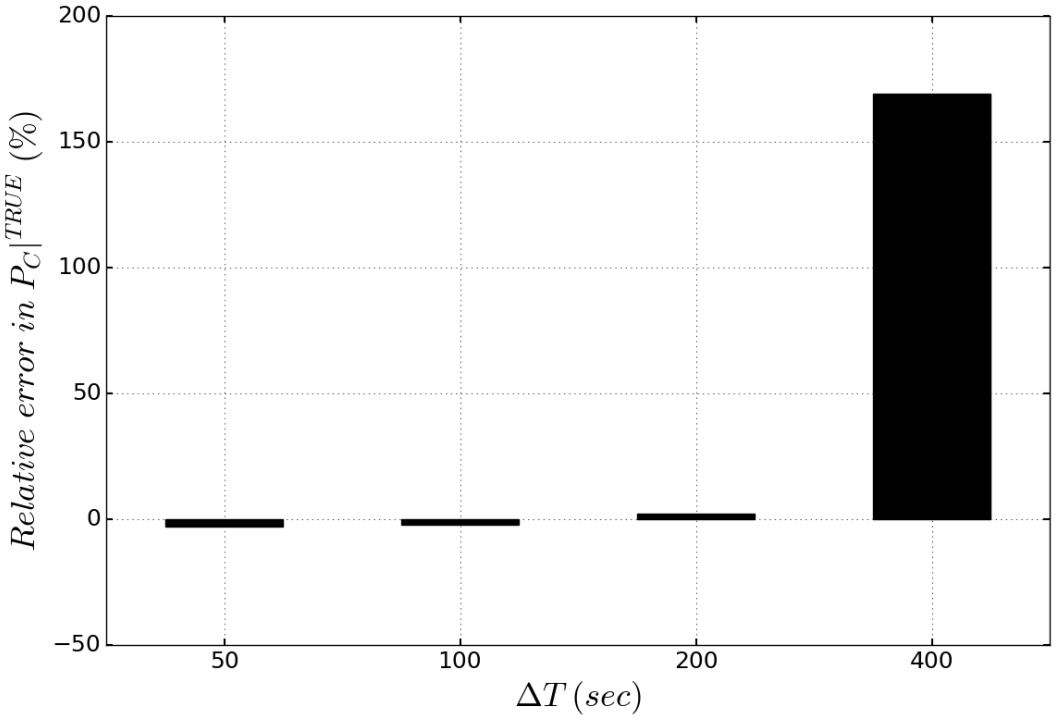

Figure C.11: Error in estimating the final $P_C|^{TRUE}$ accumulated by Envisat between 23 Oct 2013 and 23 Oct 2014 for the investigated ΔT values, relative to the median. Conjunctions closer than 1 km and assuming time-invariant position standard deviations of 10 m for all the objects.

References

[1] Alarcon Rodriguez, J., Martinez Fadrique, F., and Klinkrad, H. (2002). Collision risk assessment with a 'smart sieve' method. In *Joint ESA-NASA Space-Flight Safety Conference*, volume 2002, Noordwijk, the Netherlands.

[2] Alfano, S. and Finkelman, D. (2014). On Selecting Satellite Conjunction Filter Parameters. *Acta Astronautica*, 99:193–200.

[3] Alfano, S. (1994). Determining Satellite Close Approaches, Part II. *The Journal of the Astronautical Sciences*.

[4] Alfano, S. (2005). Relating Position Uncertainty to Maximum Conjunction Probability. *The Journal of the Astronautical Sciences*, 53(2):193–205.

[5] Alfano, S. (2007). Review of Conjunction Probability Methods for Short-term Encounters. In *Proceedings of the AAS/AIAA Space Flight Mechanics Meeting*, volume 2007, Sedona, AZ, USA.

[6] Alfano, S. (2012). Toroidal path filter for orbital conjunction screening. *Celestial Mechanics and Dynamical Astronomy*, pages 321–334.

[7] Anderson, P. and Schaub, H. (2014). Local debris congestion in the geosynchronous environment with population augmentation. *Acta Astronautica*, 94:619–628.

[8] Anselmo, L. and Pardini, C. (2004). The end-of-life disposal of the Italian geostationary satellites. *Advances in Space Research*, 34:1203–1208.

[9] Anselmo, L. (2001). The long-term evolution of the space debris environment. In *Proceedings of the 3rd European Conference on Space Debris*, volume 2001, Noordwijk, the Netherlands.

[10] Ariyoshi, Y. and Hanada, T. (2009). GEODEEM 4.0: Updated Model for Better Understanding GEO Debris Environment. In *Proceedings of the 27th International Symposium on Space Technology and Science*, volume 2009, Tsukuba, Japan.

[11] Armellin, R., Di Lizia, P., Berz, M., and Makino, K. (2010). Computing the critical points of the distance function between two Keplerian orbits via rigorous global optimization. *Celestial Mechanics and Dynamical Astronomy*, 107:377–395.

[12] Ash, R., O'Donoghue, P., Chambers, E., and Raney, J. (1993). A methodology for selective removal of orbital debris. *Advances in Space Research*, 13:243–247.

[13] Bai, X.-Z., Chen, L., and Tang, G.-J. (2013). Explicit expression of collision probability in terms of RSW and NTW components of relative position. *Advances in Space Research*, 52(6):1078–1096.

[14] Bastida-Virgili, B. (2016). DELTA (Debris Evolution Long-Term Analysis). In *Proceedings of the 6th International Workshop on Astrodynamics Tools and Techniques*, Darmstadt, Germany.

[15] Berend, N. (1999). Estimation of the probability of collision between two catalogued orbiting objects. *Advances in Space Research*, 23.

[16] Blake, R. and Lewis, H. (2014). The effect of modelling assumptions on predictions of the space debris environment. In *Proceedings of the 65th International Astronautical Congress*, volume 2014, Toronto, Canada.

[17] Braun, V., Luepken, A., Flegel, S., Gelhaus, J., Moeckel, M., Kebschull, C., Wiedemann, C., and Voersmann, P. (2013). Active debris removal of multiple priority targets. *Advances in Space Research*, 51:1638–1648.

[18] Budianto-Ho, I nad Alberty, C., Scarberry, R., Johnson, S., and RM, S. (2014). Scalable Conjunction Processing Using Spatialotemporally Indexed Ephemeris Data. In *Proceedings of the Advanced Maui Optical and Space Surveillance Technologies Conference*, volume 2014, Wailea, HI, USA.

[19] Cerf, M. (2013). Multiple Space Debris Collecting MissionDebris Selection and Trajectory Optimization. *Journal of Optimization Theory and Applications*, 156(3):761–796.

[20] Chamot, B., Richard, M., Salmon, T., Pisseloup, A., Cougnet, C., Axthelm, R., Saunders, C., Dupont, C., and Lequette, L. (2013). Technology combination analysis tool (TCAT) for Active Debris Removal. In *Proceedings of the 6th European Conference on Space Debris*, volume 2013, Darmstadt, Germany.

[21] Chan, K. (2009). International space station collision probability. `http://aero.tamu.edu/sites/default/files/faculty/alfriend/S4.2%20Chan.pdf`. Accessed: 18 Feb 2014.

[22] Coppola, V., Dupont, S., Ring, K., and Stoner, F. (2009). Assessing satellite conjunctions for the entire space catalog using COTS multi-core processor hardware. In *Proceedings of the AAS/AIAA Astrodynamics Specialist Conference*, volume 2009, Pittsburgh, PA, USA.

[23] Coppola, V. and Woodburn, J. (1999). Determination of Close Approaches Based on Ellipsoidal Threat Volumes. *Advances in the Astronautical Sciences*, 102:1013–1024.

[24] Cougnet, C., Brooker, L., David, M., Gergonne, B., Putzar, R., Stokes, H., , and Bourke, P. (2013). Protecting the LEO space systems against small debris particles. In *Proceedings of the 64th International Astronautical Congress*, volume 2013, Beijing. China.

[25] DeGroot, M. and Schervish, M. (2014). *Probability and Statistics: Fourth Edition*. Pearson Education Limited, Harlow, UK.

[26] Dolado-Perez, J., Pardini, C., and Anselmo, L. (2015). Review of uncertainty sources affecting the long-term predictions of space debris evolutionary models. *Acta Astronautica*, 113:51–65.

[27] Dominguez-Gonzalez, R. and Sanchez-Ortiz, N. (2014). Classification of TLE-catalogue objects in regard to their long-term collision probabilities. In *Proceedings of the 3rd European Workshop on Space Debris Modelling and Remediation*, volume 2014, Paris, France.

[28] Duncan, M. and Long, A. (2006). Realistic Covariance Prediction for the Earth Science Constellation. In *Proceedings of the AIAA/AAS Astrodynamics Specialist Conference*, volume 2006, Keystone CO, USA.

[29] Easthope, P. (2014). Examination of SGP4 along-track errors for initially circular orbits. *IMA Journal of Applied Mathematics*, on-line:1–15.

[30] Emmert, J., Warren, H., Segerman, A., Byers, J., and Picone, J. (2016). Propagation of atmospheric density errors to satellite orbits. *Advances in Space Research*, Available online.

[31] Ericson, Nancy, E. Jaszkowiak, D. K. (2012). Assessing Ephemerides for Conjunction Assessment. In *CSM/SSA Sharing Workshop*, Tokyo, Japan. Air Force Space Command.

[32] European Space Agency (2014). Esa budget 2014. `http://www.esa.int/For_Media/Highlights/ESA_budget_2014`. Accessed: 11 Feb 2015.

[33] Farinella, P. and Cordelli, A. (1991). The Proliferation of Orbiting Fragments: a Simple Mathematical Model. *Science and Global Security*, 2:365–378.

[34] Flohrer, T., Klinkrad, H., Krag, H., Bastida Virgili, B., and Merz, K. (2011). Operational Collision Avoidance for LEO Satellites at ESA. In *Proceedings of the 28th International Symposium on Space Technology and Science (ISTS)*, volume 2011, Okinawa, Japan.

[35] Flohrer, T., Krag, H., Klinkrad, H., Virgili, B. B., and Früh, C. (2009b). Improving ESA's Collision Risk Estimates by an Assessment of the TLE orbit Errors of the US SSN Catalogue. *Proceedings of the 5th European Conference on Space Debris*.

[36] Flohrer, T., Krag, H., and Klinkrad, H. (2008). Assessment and Categorization of TLE Orbit Errors for the US SSN Catalogue. In *Proceedings of the Advanced Maui Optical and Space Surveillance Technologies Conference*, volume 2008, Wailea, HI, USA.

[37] Flohrer, T., Krag, H., and Klinkrad, H. (2009a). ESAs process for the identification and assessment of high-risk conjunction events. *Advances in Space Research*, 44(3):355–363.

[38] Frigm, R. and Rohrbaugh, D. (2008). Relative Velocity as a Metric for Probability of Collision Calculations. In *Proceedings of the 59th International Astronautical Congress*, volume 2008, Glasgow, Scotland.

[39] Furuta, S., Hanada, T., Fujita, K., and Takezono, K. (2014). Discussion on the Necessity of Orbital Debris Removal in the Geostationary Region. In *Proceedings of the 65th International Astronautical Congress*, Toronto, Canada.

[40] Garber, S. (2007). Sputnik and the dawn of the space age. `http://history.nasa.gov/sputnik`. Accessed: 23 Dec 2014.

[41] Grassi, L and Tiboldo, F and Destefanis, R and Donath, T and Winterboer, A and Evans, L and Jankovsky, R and Kempf, S and Rudolph, M and Schaefer, F, and Gelhaus, J (2014). Satellite vulnerability to space debris - an improved 3D risk assessment methodology. *Acta Astronautica*, 99:283–291.

[42] Greene, B. (2002). Laser tracking of space debris. In *Proceedings of the 13th International Workshop on Laser Ranging Instrumentation*, volume 2002, Washington DC, USA.

[43] Haines, L and Phu, P (2011). Space Fence PDR Concept Development Phase. In *Proceedings of the Advanced Maui Optical and Space Surveillance Technologies Conference*, Wailea, Maui, HI, USA. The Maui Economic Development Board.

[44] Hausmann, G., Bellido, E., Haarmann, R., and Richter, L. (2014). Kayser-Threde Space Debris Remediation Concepts. In *Proceedings of the 3rd European Workshop on Space Debris Modelling and Remediation*, volume 2014, Paris, France.

[45] Healy, L. (1995). Close Conjunction Detection on Parallel Computer. *Journal of Guidance, Control, and Dynamics*, 18:824–829.

[46] Hejduk, M., Casali, S., Cappellucci, D., Ericson, N., and Snow, D. (2013). A Catalog-Wide Implementation of General Perturbations Orbit Determination Extrapolated From Higher Order Orbital Theory Solutions. In *Proceedings of the 23rd AAS/AIAA Spaceflight Mechanics Conference*, volume 2013, Kauai, HI, USA.

[47] Hoots, F., Crawford, L., and Roehrich, R. (1984). An Analytic Method to Determine Future Close Approaches. *Celestial Mechanics*, 102:143–158.

[48] Hoots, F. and Roehrich, R. (1988). Spacetrack Report No. 3-Models for Propagation of NORAD Element Sets. Technical report, Aerospace Defense Center, Peterson AFB, CO, USA.

[49] Horstman, M. and Mulrooney, M. (2007). An analysis of the orbital distribution of solid rocket motor slag. In *58th International Astronautical Congress*, Hyderabad, India.

[50] Horwood, J. and Aristoff, J. (2014). Beyond covariance realism: a new metric for uncertainty realism. *SPIE - Signal and Data Processing of Small Targets*, 9092:1–14.

[51] Johnson, N., Krisko, P., Liou, J., , and Anz-Meador, P. (2001). NASA's new breakup model of evolve 4.0. *Advances in Space Research*, 28:1377–1384.

[52] Johnson, N. (2005). The Historical Effectiveness of Space Debris Mitigation Measures. In *Proceedings of the 56th International Astronautical Congress*, volume 2005, Fukuoka, Japan.

[53] Kaya, D. and Snow, D. (2000). Element set accuracy assessment. *Advances in the Astronautical Sciences*, 103:1937–1946.

[54] Keane, A. and Nair, P. (2005). *Computational Approaches for Aerospace Design: The Pursuit of Excellence*. John Wiley & Sons, Ltd, Chichester, UK.

[55] Kebschull, C., Krag, H., Braun, V., Hesselbach, S., Radtke, J., and Scheidemann, P. (2014). Simulation of the space debris environment in LEO using an analytical approach. In *Proceedings of the 40th COSPAR Scientific Assembly*, Moscow, Russia.

[56] Kelso, T. (2000). Satellite tracking software. `www.celestrak.com/software/tskelso-sw.asp`. Accessed: 26 Apr 2014.

[57] Kelso, T. (2007). Validation of SGP4 and IS-GPS-200D Against GPS Precision Ephemerides. In *Proceedings of the 17th AAS/AIAA Spaceflight Mechanics Conference*, volume 2007, Sedona, AZ, USA.

[58] Kessler, D. and Cour-Palais, B. (1978). Collision frequency of artificial satellites: The creation of a debris belt. *Journal of Geophysical Research*, 83(A6):2637–2646.

[59] Kessler, D. (1981). Derivation of the Collision Probability between Orbiting Objects: The Lifetimes of Jupiter's Outer Moons. *Icarus*, 48:39–48.

[60] Khutorovsky, Z., Boikov, V., and Kamensky, S. (1993). Direct method for the analysis of collision probability of artificial space objects in LEO: techniques, results and applications. In *Proceedings of the First European Conference on Space Debris*, volume 1993, Darmstadt, Germany.

[61] Klinkrad, H. (1997). One Year of Conjunction Events of ERS-1 and ERS-2 with Objects of the Usspacecom Catalog. In *Proceedings of the Second European Conference on Space Debris*, volume 1997, Darmstadt, Germany.

[62] Klinkrad, H. (2006). *Space Debris: Models and Risk Analysis*. Praxis Publishing, Ltd, Chichester, UK.

[63] Krag, H., Klinkrad, H., and Alarcón-Rodriguez, J. (2007). Assessment of orbit uncertainties for collision risk predictions at ESA. In *Second IAASS conference Space safety in a global world"*.

[64] Krag, H., Lemmens, S., and Klinkrad, H. (2012). Consideration of Space Debris Mitigation Requirements in the Operation of LEO Missions. In *Proceedings of the 12th International Conference on Space Operations*, volume 2012, Stockholm, Sweden.

[65] Krishnaiah, P. (1980). *Handbook of statistics 1: Analysis of Variance*. Elsevier North-Holland, Inc., New York, NY, USA.

[66] Krisko, P., Flegel, S., Matney, J., Jarkey, D., and Braun, V. (2015). ORDEM 3.0 and MASTER-2009 modeled debris population comparison. *Acta Astronautica*, 113:204–211.

[67] Krisko, P. (2007). The predicted growth of the low Earth orbit space debris environment - an assessment of future risk for spacecraft. *Journal of Aerospace Engineering*.

[68] Krisko, P. (2011). Proper Implementation of the 1998 NASA Breakup Model. *NASA Orbital Debris Quarterly News*, 15:4–5.

[69] Lang, T., Kervarc, R., Bertrand, S., Carle, P., Donath, T., Destefanis, R., Grassi, L., Tiboldo, F., Schaefer, F., Kempf, S., , and Gelhaus, J. (2015). Short and long term efficiencies of debris risk reduction measures: Application to a European LEO mission. *Advances in Space Research*, 55:282–296.

[70] LaPorte, F. and Sasot, E. (2008). Operational management of collision risks for LEO satellites at CNES. *Space Operations Communicator*, 5(4):1–13.

[71] Letizia, F., Colombo, C., Lewis, H., and Krag, H. (2016). Assessment of breakup severity on operational satellites. *Advances in Space Research*, 58:1255–1274.

[72] Levit, C. and Marshall, W. (2011). Improved orbit predictions using two-line elements. *Advances in Space Research*, 47:1107–1115.

[73] Lewis, H. and Lidtke, A. (2014a). A Collision Conundrum: Investigation of Envisat Collision Hazard. In *Proceedings of the 32nd Inter-Agency Space Debris Coordination Committee Meeting*, Beijing, China.

[74] Lewis, H. and Lidtke, A. (2014b). Active Debris Removal: Consequences of Mission Failure. In *Proceedings of the 65th International Astronautical Congress*, volume 2014, Toronto, Canda.

[75] Lewis, H., Newland, R., Swinerd, G., and Saunders, A. (2010). A new analysis of debris mitigation and removal using networks. *Acta Astronautica*, 66:257–268.

[76] Lewis, H., Swinerd, G., Newland, R., and Saunders, A. (2009). The fast debris evolution model. *Advances in Space Research*, 44:568–578.

[77] Lewis, H., Swinerd, G., Williams, D., and Gittins, G. (2001). Investigating the long-term evolution of the debris environment in high earth orbit using the damage model. In *International Astronautical Congress*, Toulouse, France.

[78] Lewis, H., White, A., Crowther, R., and Stokes, H. (2012a). Synergy of debris mitigation and removal. *Acta Astronautica*, 81:62–68.

[79] Lewis, H., White, A., and Stokes, H. (2012b). Debris mitigation capability and capacity to reduce orbital debris. In *Proceedings of the 63rd International Astronautical Congress*, volume 2012, Naples, Italy.

[80] Lewis, H., White, A., and Stokes, H. (2012c). The effectiveness of space debris mitigation measures. In *Proceedings of the ISU's 16th Annual International Symposium*, volume 2012, Strasbourg, France.

[81] Lidtke, A., Gondelach, D., Armellin, R., Colombo, C., Lewis, H., Funke, Q., and Flohrer, T. (2016). Processing two line element sets to facilitate re-entry prediction of spent rocket bodies from geostationary transfer orbit. In *Proceedings of the International Conference on Astrodynamics Tools and Techniques*, volume 2016, Darmstadt, DE.

[82] Lidtke, A., Lewis, H., and Armellin, R. (2014a). A deterministic approach to active debris removal target selection. In *Proceedings of the Advanced Maui Optical and Space Surveillance Technologies Conference*, volume 2014, Wailea, HI, USA.

[83] Lidtke, A., Lewis, H., and Armellin, R. (2015). Impact of high-risk conjunctions on Active Debris Removal target selection. *Advances in Space Research*, 56:1752–1764.

[84] Lidtke, A., Lewis, H., and Blake, R. (2014b). Deterministic method for Active Debris Removal target selection. In *Proceedings of the 3rd European Workshop on Space Debris Modelling and Remediation*, volume 2014, Paris, France.

[85] Lidtke, A. and Lewis, H. (2014). Collision Probability Assessment for Active Debris Removal Missions. In *Proceedings of the 65th International Astronautical Congress*, volume 2014, Toronto, Canda.

[86] Liou, J., Anilkumar, A., Bastida Virgili, B., Hanada, T., Krag, H., Lewis, H., Raj, M., Rao, M., Rossi, A., and Sharma, R. (2013). Stability of the Future LEO Environment - an IADC Comparison Study. In *Proceedings of the 6th European Conference on Space Debris*, volume 2013, Darmstadt, Germany.

[87] Liou, J. and Johnson, N. (2006). Risks in Space from Orbiting Debris. *Science*, 311:340–341.

[88] Liou, J. and Johnson, N. (2008). Instability of the present LEO satellite populations. *Advances in Space Research*, 41:1046–1053.

[89] Liou, J. (2006). Collision activities in the future orbital debris environment. *Advances in Space Research*, 38:2102–2106.

[90] Liou, J. (2008). A statistical analysis of the future debris environment. *Acta Astronautica*, 62:264–271.

[91] Liou, J. (2011). An active debris removal parametric study for LEO environment remediation. *Advances in Space Research*, 47:1865–1876.

[92] Liou, J. (2014). personal communication.

[93] Liou, J.-C. and Johnson, N. (2009). A sensitivity study of the effectiveness of active debris removal in LEO. *Acta Astronautica*, 64(2-3):236–243.

[94] Martin, C., Walker, R., and Klinkrad, H. (2004). The sensitivity of the ESA DELTA model. *Advances in Space Research*, 34:969–974.

[95] Mason, J., Stupl, J., Marshall, W., and Levit, C. (2011). Orbital debris-debris collision avoidance. *Advances in Space Research*, 48:1643–1655.

[96] McKinley, D. (2002). Development of a Nonlinear Probability of Collision Tool. In *AIAA/AAS Astrodynamics Specialist Conference*, Monterey, CA, USA.

[97] McKnight, D., Di Pentino, F., Kaczmarek, A., and Dingman, P. (2012a). System engineering analysis of derelict collision prevention options. *Acta Astronautica*, 89:248–253.

[98] McKnight, D., DiPentino, and Knowles, S. (2014). Massive Collisions in LEO - a catalyst to initiate ADR. In *Proceedings of the 65th International Astronautical Congress*, volume 2014, Toronto, Canada.

[99] McKnight, D., DiPentino, F., Musekamp, D., and Dingman, P. (2012b). System Engineering Analysis of Derelict Collision Prevention Options. In *Proceedings of the 63rd International Astronautical Congress*, volume 2012, Naples, Italy.

[100] McKnight, D., Maher, R., and Nagl, L. (1995). Refined Algorithms for Structural Breakup due to Hypervelocity Impact. *International Journal of Impact Engineering*, 17:547–558.

[101] McKnight, D. (2013). US Active Debris Rremoval (ADR) efforts. In *UN COPUS meeting*, Vienna, Austria.

[102] McKnight, D. (2015a). Engineering and Operational Issues Related to Just-In-Time Collision Avoidance. In *Proceedings of the 6th European conference for aeronautics and space sciences (EUCASS)*, volume 2015, Krakow, Poland.

[103] McKnight, D. (2015b). Op-ed— orbital debris remediation: A risk management problem. `http://spacenews.com/op-ed-orbital-debris-remediation-a-risk-management-problem/`. Accessed: 9 Feb 2015.

[104] Montgomery, D. and Runger, G. (2006). *Applied Statistics and Probability for Engineers: Fourth Edition*. John Wiley and Sons, Inc., Hoboken, JN, USA.

[105] Morris, M. and Mitchell, T. (1992). Exploratory designs for computational experiments. `http://web.ornl.gov/info/reports/1992/3445603672345.pdf`. Accessed: 8 Jan 2016.

[106] Morselli, A., Armellin, R., Di Lizia, P., and Bernelli Zazzera, F. (2015). A high order method for orbital conjunctions analysis: Monte Carlo collision probability computation. *Advances in Space Research*, 55:311–333.

[107] Morselli, A. and Armellin, R. (2014). A high order method for orbital conjunctions analysis: Sensitivity to initial uncertainties. *Advances in Space ...*, 53(3):490–508.

[108] National Aeronautics and Space Administration (2014). Nasa fiscal year 2016 budget request. `http://www.nasa.gov/sites/default/files/files/Agency_Fact_Sheet_FY_2016.pdf`. Accessed: 11 Feb 2015.

[109] Nock, K., Aaron, K., and McKnight, D. (2013). Removing Orbital Debris with Less Risk. *Journal of Spacecraft and Rockets*, 50:365–379.

[110] Oepik, E. (1952). Collision probabilities with the planets and the distribution of interplanetary matter. *Proceedings of the Royal Irish Academy. Section A: Mathematical and Physical Sciences*, 54:165–199.

[111] Oltrogge, D., Kelso, T., and Seago, J. (2011). Validation of SGP4 and IS-GPS-200D Against GPS Precision Ephemerides. In *Proceedings of the AAS/AIAA Spaceflight Mechanics Meeting*, volume 2011, New Orleans, LA, USA.

[112] Oltrogge, D nad Ramrath, J. (2014). Parametric Characterization of SGP4 Theory and TLE Positional Accuracy. In *Proceedings of the Advanced Maui Optical and Space Surveillance Technologies Conference*, volume 2014, Wailea, HI, USA.

[113] Olympio, J. e. a. (2010). Towards a better understanding of active debris removal options. In *Proceedings of the European Workshop on Active Debris Removal*, volume 2010, Paris, France.

[114] Osweiler, V. (2006). Covariance estimation and autocorrelation of NORAD two-line element sets. Master of science, Air Force Institute of Technology.

[115] Oxford University Press (2015). Definition of sustainable in english. `http://www.oxforddictionaries.com/definition/english/sustainable`. Accessed: 16 Feb 2015.

[116] Pardini, C. and Anselmo, L. (2014). Review of past on-orbit collisions among cataloged objects and examination of the catastrophic fragmentation concept. *Acta Astronautica*, 100:30–39.

[117] Pardini, C., Kent Tobiska, W., and Anselmo, L. (2006). Analysis of the orbital decay of spherical satellites using different solar flux proxies and atmospheric density models. *Advances in Space Research*, 37:392–400.

[118] Pas, N., Lousada, J., Terhes, C., Bernabeu, M., and Bauer, W. (2014). Target selection and comparison of mission design for space debris removal by DLR's advanced study group. *Acta Astronautica*, 102:241–248.

[119] Patera, R. (2001). General method for calculating satellite collision probability. *Journal of Guidance, Control, and Dynamics*, 24(4):716–722.

[120] Patera, R. (2005). Calculating Collision Probability for Arbitrary Space Vehicle Shapes via Numerical Quadrature. *Journal of Guidanance, Control and Dynamics*, 28:1326–1328.

[121] Patera, R. (2008). Space Event Detection Method. *Journal of Spacecraft and Rockets*, 45:554–559.

[122] Portelli, C., Alby, F., Crowther, R., and Wirt, U. (2010). Space Debris Mitigation in France, Germany, Italy and United Kingdom. *Advances in Space Research*, 45:1035–1041.

[123] Press, W., Flannery, B., Teukolsky, S., and Vetterling, W. (2002). *Numerical Recipes in C++: 2nd edition*. Cambridge University Press, Cambridge, UK.

[124] Radtke, J., Flegel, S., Gelhaus, J., Moeckel, M., Braun, V., Kebschull, C., Wiedemann, C., Krag, H., Merz, K., and Voersmann, P. (2013). Revision of statistical collision analysis for objects inside of satellite constellations. In *Proceedings of the Proceedings of the 64th International Astronautical Congress*, volume 2013, Beijing, China.

[125] Radtke, J., Flegel, S., Roth, S., and Krag, H. (2014). Deriving the Spacecraft Criticality from Monte-Carlo Simulations of the Space Debris Environment. In *Proceedings of the 65th International Astronautical Congress*, volume 2014, Toronto, Canada.

[126] Radtke, R. and Stoll, E. (2016). Comparing long-term projections of the space debris environment to real world data looking back to 1990. *Acta Astronautica*, 127:482–490.

[127] Reed, J. and Barraclough, S. (2013). Development of a Harpoon System for Capturing Space Debris. In *Proceedings of the 6th European Conference on Space Debris*, volume 2013, Darmstadt, Germany.

[128] Rossi, A., Valsecchi, G., and Alessi, E. (2015). The Criticality of Spacecraft Index. *Advances in Space Research*.

[129] Rossi, A. (2006). NASA Breakup Model Implementation Comparison of Results. In *Proceedings of the 24th Inter-Agency Space Debris Coordination Committee Meeting*, Tsukuba, Japan.

[130] Schaub, H., Jasper, L., Anderson, P., and McKnight, D. (2014). Cost and risk assessment for spacecraft operation decisions caused by the space debris environment. In *Proceedings of the 65th International Astronautical Congress*, volume 2014, Toronto, Canada.

[131] Schenwerk, M. (2003). A brief review of basic GPS orbit interpolation strategies. *GPS Solutions*, 6:265–267.

[132] Schmitz, M., Fasoulas, S., and Utzmann, J. (2015). Performance model for space-based laser debris sweepers. *Acta Astronautica*, 115:376–383.

[133] scikit-learn (2014). Epsilon-support vector regression. `http://scikit-learn.org/stable/modules/generated/sklearn.svm.SVR.html`. Accessed: 26 May 2016.

[134] Soucek, A. (2014). Active Debris Removal and questions of export control. In *Proceedings of the 3rd European Workshop on Space Debris Modelling and Remediation*, volume 2014, Paris, France.

[135] Space-Track (2013). `https://www.space-track.org`. Accessed: 4 Mar 2014.

[136] Stupl, J., Mason, J., Marshall, W., and Levit, C. (2010). Debris-debris collision avoidance using medium power ground-based lasers. In *Proceedings of the 2010 Beijing Orbital Debris Mitigation Workshop*, volume 2010, Beijing, China.

[137] Talent, D. (1992). Analytic Model for Orbital Debris Environmental Management. *The Journal of Spacecraft and Rockets*, 29:508–513.

[138] Tanygin, S. (2006). Ephemeris & Attitude Interpolation. `http://www.agi.com/downloads/events/2006-agi-user-exchange/9_Ephemeris_Attitude_Interpolation_Tanygin2.pdf`. Accessed: 26 Feb 2015.

[139] The Inter-Agency Space Debris Coordination Committee (2002). Iadc space debris mitigation guidelines. `http://www.iadc-online.org/Documents/IADC-2002-01,%20IADC%20Space%20Debris%20Guidelines,%20Revision%201.pdf`. Accessed: 4 Feb 2015.

[140] The Scipy community (2015). scipy.stats.describe. `www.docs.scipy.org/doc/scipy/reference/generated/scipy.stats.describe.html`. Accessed: 21 September 2015.

[141] The Space Foundation (2013). The space report 2013.

[142] Ting, W. and Hai, H. (2008). New method to determine close approaches between satellites. In *Proceeding of 3rd IAASS Conference*, Rome, Italy.

[143] UK Space Agency (2015). Outer space act database of standards. `https://www.gov.uk/apply-for-a-license-under-the-outer-space-act-1986`. Accessed: 4@Feb 2015.

[144] UN Office for Outer Space Affairs (2016). Compendium of space debris mitigation standards adopted by States and international organizations. In *55th UN Office for Outer Space Affairs Legal Subcommittee session*, Vienna, Austria. Accessed: 19 Sep 2016.

[145] Utzmann, J., Oswald, M., Stabroth, S., Wagner, A., and Retat, I. (2012). Ranking and characterisation of heavy debris for active removal. In *Proceedings of the 63rd International Astronautical Congress*, volume 2012, Naples, Italy.

[146] Vallado, D. and Finkelman, D. (2014). A critical assessment of satellite drag and atmospheric density modelling. *Acta Astronautica*, 95:141–165.

[147] Vallado, D. and Seago, J. (2009). Covariance Realism. *Advances in the Astronautical Sciences*, pages 1–19.

[148] Vallado, D. (2013). *Fundamentals of Astrodynamics and Applications, 4th ed.* Microcosm Press.

[149] Valli, M., Armellin, R., Di Liziza, P., and Lavagna, M. (2013). Nonlinear Mapping of Uncertainties in Celestial Mechanics. *Journal of Guidanance, Control and Dynamics*, 36:48–63.

[150] Vance, L. and Mense, A. (2013). Value analysis for orbital debris removal. *Advances in Space Research*, 52:685–695.

[151] Wade, T. (1951). *The algebra of vectors and matrices.* Addison-Wesley Press, Inc., Cambridge, MA, USA.

[152] White, A. and Lewis, H. (2014). The many futures of active debris removal. *Acta Astronautica*, 95:189–197.

[153] White, A. (2014). *An Adaptive Strategy to Control the Space Debris Population.* Doctor of philosophy, University of Southampton.

[154] Wiedemann, C., Oswald, M., Stabroth, S., Klinkrad, H., and Voersmann, P. (2008). Mathematical description of the NaK model for MASTER-2005. *Advances in Space Research*, 41:1063–1070.

[155] Windall, S. (2009). Vectors, matrices and coordinate transformations. `http://ocw.mit.edu/courses/aeronautics-and-astronautics/16-07-dynamics-fall-2009/lecture-notes/MIT16_07F09_Lec03.pdf`. Accessed: 2 Mar 2015.

[156] Woodburn, J., Coppola, V., and Stoner, F. (2009). A description of filters for minimizing the time required for orbital conjunction computation. In *Proceedings of the AAS-AIAA Astrodynamics Specialist Conference*, volume 2009, Pittsburgh, USA.

[157] Wormnes, K., Le Letty, R., Summerer, L., Schonenborg, R., Dubois-Matra, O., Luraschi, E., Cropp, A., Krag, H., and Delaval, J. (2013). ESA technologies for space debris remediation. In *Proceedings of the 6th European Conference on Space Debris*, Darmstadt, Germany.

[158] Yasaka, T. (2011). Can We Have an End to the Debris Issue? In *Proceedings of the 62nd International Astronautical Congress*, volume 2011, Cape Town, South Africa.

[159] Zaccariotto, M., Francesconi, A., and Galvanetto, U. (2014). A New Method To Predict the Catastrophic Disintegration of Spacecraft Upon Collision with Large Orbital Debris. In *Proceedings of the 65th International Astronautical Congress*, volume 2014, Toronto, Canada.

[160] Zuiani, F. and Vasile, M. (2012). Preliminary design of Debris removal missions by means of simplified Low-Thrust, many-revolution transfers. *International Journal of Aerospace Engineering*, 2012:836250.